THE UNIVERSITY OF SHEFFIELD

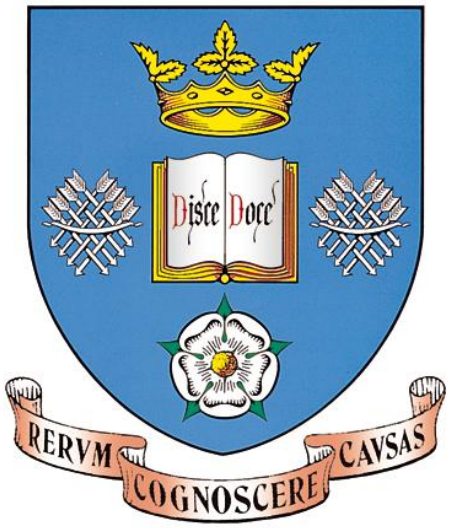

HIGH TEMPERATURE EMBEDDED ELECTRICAL MACHINES FOR AEROSPACE TURBINE APPLICATIONS

By

Leon Rodrigues

A Thesis submitted for the degree of Doctor of Philosophy in the Department of Electronic and Electrical Engineering, The University of Sheffield.

MAY 2013

Abstract

This thesis describes research contributions in the field of electrical machines for operation at elevated temperatures. High temperature operation of electrical machines is considered critical for the realisation of the ‘more-electric aircraft’ concept, which involves electrical machines embedded directly on to the shafts of the aircraft gas turbine. The particular machine of interest for this thesis is a switched reluctance machine for operation on the high pressure shaft. The hostile environment, mainly due to the high temperatures (~350°C ambient) introduces several challenges in the modelling, design and manufacture of electrical machines.

In order to aid selection of materials and collect necessary data for the machine design, detailed analysis of the published magnetic and electrical data for key materials at high temperatures has been carried out. Further measurements on the high strength 50% Cobalt Iron materials were also conducted, which supplement the understanding of the materials behaviour at high temperatures, specifically in terms of the effects of the long term thermal ageing on the individual loss mechanisms in the material.

The design optimisation of an SR machine for 350°C operation is also described in detail. The design procedure illustrates how the high temperature material properties influence machine performance and achievable power densities. In order to more reliably predict the performance of machines at elevated temperatures several modelling techniques have been developed. A method to calculate instantaneous core loss was introduced, which was formulated such that it could be used in circuit simulations to ensure power balance. Extensive validation of this model has also been carried out.

Acknowledgements

I would like to express my sincere thanks to Geraint Jewell for his invaluable guidance, encouragement and support during the course of the research and the writing of this thesis.

I would also like to thank the Engineering Physical Sciences and Research Council and Rolls Royce for the award of a research studentship and financial support. I would like to thank the staff at Rolls Royce, especially John Cullen and Ellis Chong for their support and enthusiasm.

I would also like to thank the technical staff in the Electrical Machines and Drives group, who were particularly helpful in the construction and installation of the test-rig. Thanks are also due to my colleagues in the UTC and Electrical Machines and Drives Group, for both their technical advice and for providing a lively and friendly atmosphere.

Finally, I would like to thank my family for their consistent support and encouragement throughout my life, and my friends for the great times which helped me keep my sanity during the course of this PhD.

Contents

Chapter 5 : High temperature switched reluctance machine design

Chapter 6 : High temperature machine demonstrator and testing

List of figures

List of Acronyms

CFD	Computational fluid dynamics
FE	Finite element
HP	High pressure
IP	Intermediate pressure
LP	Low pressure
MEA	More electric aircraft
MEE	More electric engine
PDF	Preisach distribution function
PID	Proportional integral derivative
PM	Permanent magnet
PWM	Pulse width modulation
SR	Switched Reluctance
UAV	Unmanned aerial vehicle
VAC	Vacuumschmelze

Nomenclature

Symbol	Definition	Unit
A	Cross sectional area of the toroidal core sample	m^2
A_2	Cross sectional area of the sense coil	m^2
A_{load}	Electric loading	A/m
B	Flux density	T
B_{hyst}	Hysteretic flux density	T
B_{load}	Magnetic loading	T
B_p	Peak Flux density	T
C	Stienmetz's material specific loss constant	-
D_{bore}	Machine bore diameter	m
D_m	Mean bearing diameter	mm
D_{rot}	Rotor outer diameter	rads/s
E	Electrical field	V/m
H	Applied magnetic field	A/m
H_{bias}	DC bias applied to demagnetisation curve	A
H_{hyst}	Hysteretic magnetisation field	A/m
H_m	Last reversal point on magnetic excursion	A/m
Hm_i	Peak applied field of individual minor loop	A
H_s	Slot depth	m
H_{sat}	Field intensity at which core is completely saturated	A/m
J	Current density	A/m^2
L_{bore}	Machine axial length	m
L_c	Characteristic length of fluid flow	m
L_{ext}	Leakage inductances	H
L_{ph}	Phase inductance	H
M	Core magnetisation	A/m
N	Maximum rotating speed for bearing	rpm
N_2	Number of turns on the sense coil	-
N_s	Number of stator slots	-
N_u	Nusselt number	-

Symbol	Definition	Unit
P_h	Hysteresis loss	W
P_{cl}	Classical eddy current loss	W
P_{exc}	Excess loss	W
P_r	Prandtl number	-
P_{st}	Core loss as calculated using the Stienmetz equation	W
P_{total}	Total core loss	W
Q	Energy lost over a magnetic excursion	J/kg
R_e	Reynolds number	-
R_{ph}	Phase resistance	Ω
T_{SRM}	Average torque of a switched reluctance machine	N-m
$T(\alpha, \beta)$	Everett integral	-
W_c	Width of rectangular coil	m
a	Material specific loss parameter for flux density	-
b	Material specific loss parameter for frequency	-
c_{ff}	Coil fill factor	m
d	Lamination thickness	m
d_u	Distance between the stator and rotor tooth tips	m
f	Frequency of excitation	Hz
h_r	Rotor tooth hieght	m
h_s	Surface heat transfer coefficient	W/m^{2}K
h_{shaft}	Heat transfer coefficient on rotor shaft	W/m^{2}K
$h_{surface}$	Heat transfer coefficient on rotor exposed surfaces	W/m^{2}K
i	Currents at which flux linkages are and torque predicted	A
i_{an}	Lossless or anhysteretic current	A
i_{loss}	Current due to core losses	A
i_{ph}	Phase current	A
i_{ph}	SRM phase current	A
k_{cl}	Eddy current loss coefficient	-
k_{exc}	Excess loss coefficient	-
k_f	Thermal conductivity of coolant	W/mK
k_h	Hysteresis loss coefficient	-

Symbol	Definition	Unit
k_i	Loss coefficients for modified excess loss formula	-
k_{lam}	Thermal conductivity of lamination	W/mK
k_{stack}	Thermal conductivity of stator stack in axial direction	W/mK
k_t	Machine torque constant	N-m/A
k_{var}	Thermal conductivity of stator varnish	W/mK
k_σ	Rotor stress constant	-
l_{sb}	Arc length of back iron between two teeth	m
l_{so}	Arc length of slot opening	m
p_{core}	Instantaneous power flow into the core	W
p_i	Coefficients for power term in excess loss formula	-
r_{loss}	Equivalent parallel core loss resistance across coil	Ω
v_{coil}	Voltage across coil	V
v_{ph}	Phase voltage	V
α	Upper switching point of unit hysteretic switch	A/m
α_c	Temperature co-efficient of resistance	/°C
α_{sf}	Stacking factor	-
β	Lower switching point of unit hysteretic switch	A/m
δ_p	Skin depth	m
θ	Set of rotor positions at which flux linkage and torque are predicted	deg.
μ	Permeability	H/m
$\mu(\alpha,\beta)$	Preisach density function	-
μ_o	Permeability of air	$H{\cdot}m^{-1}$
ρ_{rot}	Density of rotor lamination	kg/m^3
ϱ_c	Resistivity of conductor	Ω-m
σ	Electrical conductivity	Ω-m
σ_{max}	Maximum allowable stress in the rotor laminations	MPa
σ_{rot}	Peak rotor stress	MPa
$\emptyset$	Flux	Wb
ψ	Finite element predicted flux linkage	Wb

Symbol	Definition	Unit
ψ_{an}	Flux linkage calculated using the materials anhysteretic B vs. H relationship	Wb
ψ_{ph}	Phase flux linkage	Wb
ω_e	Frequency of excitation	rad/s
ω_{mech}	Rotor mechanical speed	rad/s

Chapter 1 : Introduction

1.1 More-Electric Aircraft

The more-electric aircraft (MEA) concept is based around the principle of replacing many of the existing mechanical, hydraulic and pneumatic systems with a single globally optimized electrical system[1]. This concept has been driven by advancements in power electronics and electrical machines that can provide improved system integration, performance, fault tolerance and overall power density. The increase in aircraft electrical loads as part of the MEA concept requires a step change in the on-board electrical generation system, leading to the development of the so called more-electric engine (MEE).

The MEE design draws it electrical power from a series of high power density, high speed motor generators embedded on the different shafts of the gas turbine engine. Figure 1.1 shows a schematic of a three-shaft design of a turbo-fan engine. In this particular example, three motor/generators are integrated, one on each of the shafts which are commonly referred to as the low pressure (LP), intermediate pressure (IP) and high pressure (HP) shafts. There are numerous benefits of having electrical machines embedded directly on the shafts such as the reduction in weight and operating costs, increased reliability and improved fuel efficiency, which make it a very attractive option for the future aero engines[2]. Some of the requirements for embedded machines are high power density to minimize weight and high reliability in variable operating conditions. The operating conditions on the three shafts vary considerably. Arguably, the most severe conditions exist on the HP shaft in which ambient temperatures range from 350~400°C in the regions into which an electrical machine would be embedded. This thesis is focussed on addressing the design considerations for an electrical machine operating in this environment.

An electrical machine driven by the HP shaft would usually be required to both start the engine, and when the engine attains its ignition speed operate as a generator supplying power to the aircraft electrical network. In conventional engine architectures, such as the Trent 1000 engine on the Boeing 787[3], the starter-generator is positioned outside the main core of the engine and is connected to the IP shaft through a take-off shaft and the main accessory gearbox as shown in Figure 1.2. A machine mounted directly on the HP shaft will

do away with the need for a take-off shaft (at least in terms of driving the electrical machine) with consequent weight savings and reduced maintenance requirements. However, the technical challenges in terms of designing and manufacturing a functional and reliable electrical machine to operate at such temperatures are extremely challenging. This thesis addresses several of the main issues which are raised by high temperature operation and considers the design methodology and the development of a laboratory demonstrator.

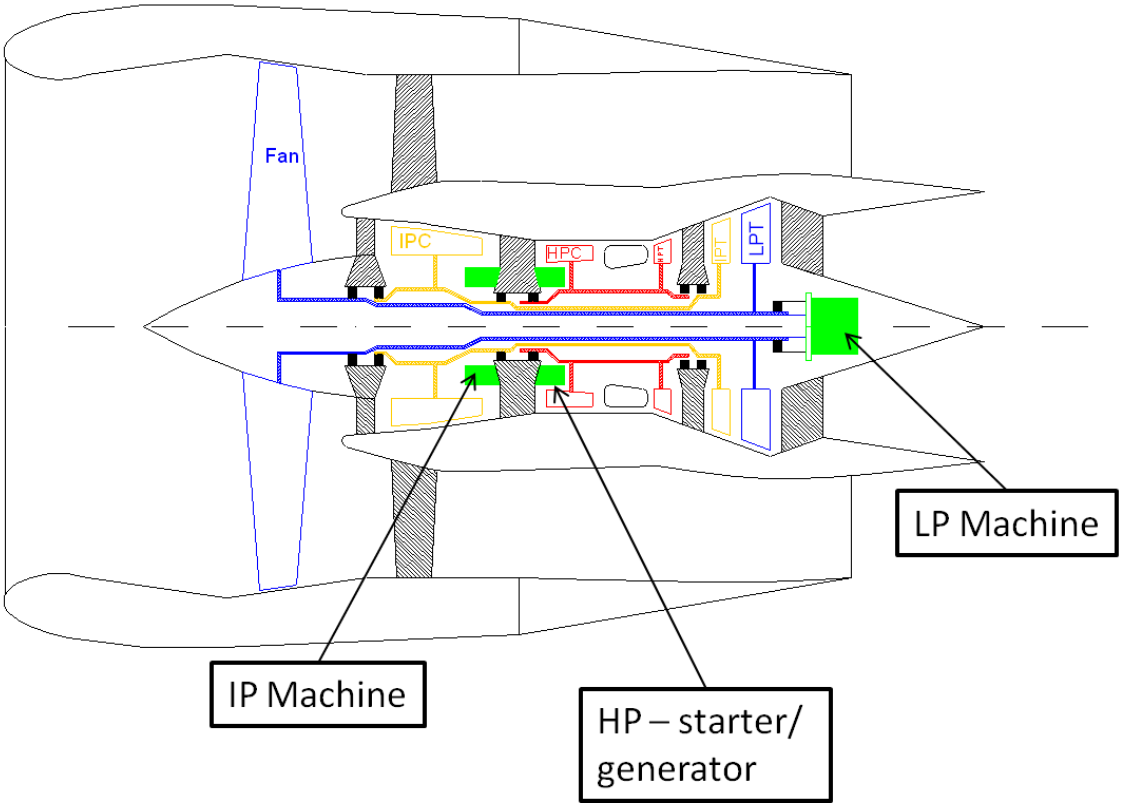

Figure 1.1: Cross-section through a three-shaft aero-engine gas turbine with shaft-line mounted electrical machines. (source: [4])

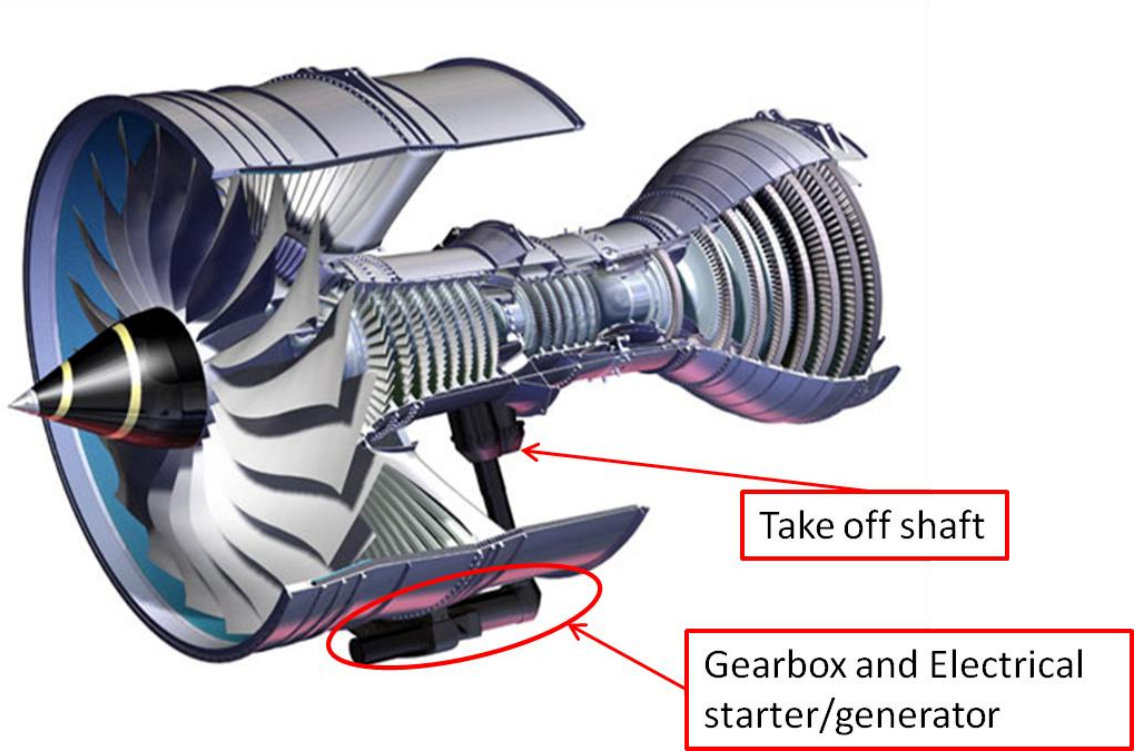

Figure 1.2: Rolls Royce Trent 1000 engine showing take off shaft and starter generator.

1.2 Challenges for high temperature operation of electrical machines

The main challenges of operating electrical machines at high temperatures, i.e. above 300°C or so, are mainly related to the material properties at temperature, specifically:

- Materials exhibit increased corrosion and oxidation at high temperatures.
- The full temperature range varies from -40°C for a cold start to a peak hotspot temperature of 450°C. Therefore it is important that materials used have similar coefficients of thermal expansion.
- Due to the long expected working lifetime of highly embedded engine components (orders of 10s of thousands of hours) thermal ageing effects are a concern as material properties tend to degrade over time.
- Magnetic materials lose their magnetic properties as they approach their Curie temperatures, and only a few soft magnetic materials have Curie temperatures above the 400-450°C. Permanent magnets tend to have lower Curie

temperatures and exhibit significant levels of degradation in performance with temperature.

- Soft magnetic materials exhibit some degree of reduction in saturation flux density with increase in temperature.

- The temperature co-efficient of electrical resistance copper is about 40% per 100°C which gives a resistivity at 450°C of ~2.8 times that at room temperature. This has a direct consequence on the copper loss, and consequently the peak temperature within the coil.

- Soft magnetic materials exhibit an increase in electrical resistivity with increasing temperature. This is however advantageous in terms of reducing eddy current losses.

All these drawbacks have a dramatic effect on the machine design and pose significant challenges in terms of achieving acceptable operational reliability. As an example, the copper loss in the windings is proportional to the resistance of copper and the square of the current density, and hence an increase in copper resistance would have to be compensated for by reducing the current density, which in turn incurs a penalty in power density. The reliable design of electrical machines also requires a significant amount of magnetic material data in order to select the most appropriate material and in the design stage to accurately predict machine performance and losses. To further improve the understanding of important aspects of material behaviour, this thesis includes extensive measurements on specific soft magnetic grades at temperature.

1.3 Challenges of incorporating an electrical machine on the HP shaft

In addition to the high temperatures, the HP shaft machine poses several challenges in terms of electrical machine design. The HP shaft has the highest rotational speed of the three shafts which can have a significant effect on the mechanical stresses incurred in the rotor. There are also severe space envelope constraints around the HP compressor. The HP shaft also has the largest diameter of the three shaft (the other two passing through its bore), and hence the electrical machine rotor core tend to have large inner diameters which can often dictate the need for high pole numbers to fit within the machine within a narrow annulus[5].

The power density is usually limited by the cooling techniques available to dissipate losses from the coils. In order to maximise power density, machines often incorporate elaborate cooling methods varying from forced air cooling to direct liquid cooling of windings. Due to the location of the HP shaft, there are several limitations with respect to employing such cooling systems as it might entail significant modifications to engine structures, and may not be considered feasible.

As the machine is directly mounted on the engine shaft, the rotor will be subjected to vibrations and rotor dynamic effects of the main HP shaft. This may require a larger radial clearance between the rotor and stator than would be necessary in a stand-alone machine with its own bearings. Similarly, the need to avoid exciting resonant frequencies in the shaft may place limits on torque ripple and/or radial unbalance. Secondary issues such as routing the cables through to the HP inter-case and terminating coils at high temperatures also pose a significant challenge.

In summary, there are many challenges that must be overcome before electrical machines can be considered as a ready technology for embedded operation on the HP shaft a commercial gas turbine aero-engine. This thesis addresses some of these challenges, particularly those related to electromagnetics, and aims to improve the understanding of materials and machine operation in such environments.

1.4 Switched Reluctance machines for HP shaft integration

Switched reluctance (SR) machine have emerged as the favoured electrical machine type option for embedding on the HP shaft [4, 5]. The main advantages of SR machines cited for the HP shaft application are its ability to operate at elevated temperatures, rugged mechanical construction, high torque density, reliability, inherent fault-tolerance and ability to operate over a wide speed range.

Permanent magnet (PM) machines have historically been largely discounted for such operating environments due to modest properties of the available permanent magnets at elevated temperatures. Synchronous reluctance machines and induction machines have also been considered as alternative options. The main advantage of synchronous reluctance machines is that they can employ solid rotors which are more robust and have lower rotor

losses as compared to the SR machine. Achieving low rotor losses is however reliant on maintaining low harmonics content in the air gap flux distribution, which require complex distributed winding configurations which are not necessarily well-suited to high temperature wires. The existing high temperature wire technologies are limited to encapsulated ex-situ wound concentrated coils. The harmonics introduced by short pitched concentrated coils would cause rotor losses to increase substantially and reduce the performance of synchronous reluctance machines. SR machines on the other hand require concentrated short pitched coils. In comparison to PM machines, SR machines generally have lower efficiencies and at low speeds generally tend to be copper loss dominated. This is in large part because of their singly excited nature. Since the resistivity of Copper increases by ~40% for every 100°C rise in temperature, copper loss is likely to be the critical factor for high temperature operation.

Previous studies on the integration of an SR machine onto the HP shaft of a gas turbine[6] focussed on modelling rotor mechanical stresses although the issues of electromagnetic and thermal modelling were performed in the context of a generating requirement of 100kW at 13,500 rpm. Several issues concerned with designing a high power SR machine within a specified space envelope of a gas turbine were addressed, however many high temperature material properties were not considered and the machine constructed was not intended for tests at high temperature. The specification considered on this thesis will not target a specific turbine application and power rating, but rather will a more generic machine as a proof of concept, with the aim developing generic procedures for design and optimisation of machines for high temperatures.

1.5 Modelling of electrical machines

The modelling techniques used for electrical machines have improved significantly over the last 20 years with the need to extract higher performance and efficiencies at the narrowest of margins. These improvements have been largely driven by finite element (FE) techniques which are a powerful tool for design and analysis. These allow the designer to optimize machine geometry, winding configuration and operating conditions, to suit the demands of a particular application. However, simulating machine performance under dynamic operating conditions pose several challenges, such as core loss estimation, eddy current screening and rotor dynamics. Due to the high speed of the HP shaft, an improved

understanding of machine performance under dynamic conditions is critical to the design of such machines.

Advanced thermal modelling techniques have also been gaining significant importance in electrical machine design. Knowledge of the machine temperatures is essential in terms of understanding the limits of machine performance, especially as high power dense machines tend to be designed to operate at, or near, to their thermal limit. As the power density of machines increase and more complex methods of cooling need to be employed, the accurate a-priori modelling of machine temperatures becomes more important. In the case of the high temperature machines considered in this thesis, the extreme environment in the vicinity of the HP shaft application requires effective management of losses.

1.6 Summary of thesis structure

As described in section 1.2, many of the challenges for the HP shaft machine are related to material behaviour at elevated temperatures. This application requires materials to operate beyond the temperature ranges over which they are normally used. One consequence is that material data at elevated temperatures is usually very limited. Therefore, it was proved necessary to undertake a literature review of available material data at representative temperatures to enable selection of appropriate materials and collect necessary data for the machine design and analysis. Chapter 2 summarizes the data available in the literature along with some basic material characterisation for loss parameters using the available data.

The high specific core loss of the material selected for the machine cores when in combined with the high speed and pole number of the SR machine, dictated that the core losses would form a significant proportion of the total power. Chapter 3 considers methods of modelling electrical machines under dynamic conditions with the main focus being on core loss prediction. It is shown the common practice of excluding core loss in the dynamic circuit simulations can lead to significant over-estimates of output power and under prediction of copper loss when the machine is supplied by a given voltage pulse. A method to include core losses in the circuit simulations which involves modelling instantaneous core losses is developed in chapter 3.

Chapter 4 outlines a simplified method to characterise core materials for the loss model described in chapter 3. The measurements are carried out on two ring samples of Vacodur S+ Cobalt Iron grades heat treated to achieve specific balances of electromagnetic and mechanical properties. Extensive validation of the loss model proposed in chapter 3 is also carried out using the same ring samples. The samples were also thermally aged at 400°C of up to 2000 hours and core loss data was collected at set intervals.

Chapter 5 describes a design methodology used for the HP shaft SR machine. The design procedure illustrates how the high temperature material properties influence machine performance and achievable power densities. The loss models developed in chapter 3 along with the material parameters estimated in chapter 4 are used to design the machine. The chapter also describes the thermal modelling techniques employed to aid the design of the machine.

Finally, chapter 6 describes the manufacture of the demonstrator machine, and illustrates the number of challenges faced in building a laboratory high temperature machine and an associated test-rig. The chapter also describes the testing carried out on the built machine at temperature and proposes a series of modifications to the current test-rig to achieve better testing conditions.

References

[1] M. J. Provost, "The More Electric Aero-engine: a general overview from an engine manufacturer," in *Power Electronics, Machines and Drives, 2002. International Conference on (Conf. Publ. No. 487)*, 2002, pp. 246-251.

[2] I. Moir, "More-electric aircraft-system considerations," in *Electrical Machines and Systems for the More Electric Aircraft (Ref. No. 1999/180), IEE Colloquium on*, 1999, pp. 10/1-10/9.

[3] "Trent 1000." Rolls Royce PLC. http://www.rolls-royce.com/civil/productslargeaircraft/trent_1000

[4] D. P. Geraint Jewell, Dave Howe, "Topologies of Switched Reluctance Machines for the More-Electric Aircraft Engine," presented at the New Topologies for Electrical Machines, 2002.

[5] R. Hall, A. G. Jack, B. C. Mecrow, and A. J. Mitcham, "Design and initial testing of an outer rotating segmented rotor switched reluctance machine for an aero-engine shaft-line-embedded starter/generator," in *Electric Machines and Drives, 2005 IEEE International Conference on*, 2005, pp. 1870-1877.

[6] D. J. Powell, "Modeling of High Power Density Electrical Machines for Aerospace," PhD, Electrical and Electrical Engineering, University of Sheffield, Sheffield, 2003.

Chapter 2 : Materials for high temperature machines

2.1 Introduction

This chapter discusses the influence of elevated temperature on the electrical and magnetic properties of key materials used in electrical machines, and the implications of these effects on electrical machine design. The upper limit on operating temperatures in conventional electrical machines using well-established technology and materials is of the order of 200°C for long-term operation. Hence, applications in which machine components are exposed to temperatures of 350-450°C necessitate a fundamental review of the materials used. Published literature and manufacturer's data sheet present a large amount of technical data to aid selection of suitable materials for more conventional operating temperatures. In such applications with modest ambient temperatures, maintaining the temperature within the prescribed limits of the materials is a matter of effectively managing the losses. In this application, operating temperature is the key driving factor in the selection of materials. Hence, this chapter reviews the published magnetic and electrical data for key materials at high temperatures. Although there is a significant amount of published data for a set of materials at the temperatures involved, several gaps remain to populate the knowledge base that would be required for effectively designing machines operating at such temperatures. In addition to the ambient temperature, there are several challenges introduced by the application such as the high speed, which necessitates good mechanical strength for the moving components.

The materials required to manufacture a machine can be separated into those required for active and structural components. Depending on the type of electrical machine, the active elements can comprise of, permanent magnets, soft magnetic core and coils, the structural components being the casing, shaft, bearings etc. This chapter focuses on candidate materials for the active components of the machine. The selection of structural components will be briefly described in chapter 6. The key enabling component for high temperature machine operation, and arguably the least developed and established, are the stator coils. Localised hotspot temperature and the mechanical loads imposed by vibrations and thermal cycling, dictate that the coils have to endure very harsh conditions while maintaining high mechanical

and electrical integrity. There are several challenges that must be overcome in order to manufacture high temperature coils several of which will be described in this chapter.

Permanent magnets have in the past been largely discounted for operation at high temperatures. The absence of permanent magnets in switched reluctance (SR) machines is one of the mains reason for them being favoured for high temperature operation. Nonetheless, over the past 15 years or so, there have been significant advances in permanent magnet materials, with grades now available that are rated at temperatures up to 550°C. Thus, it is important to re-evaluate the state-of-the-art high temperature permanent magnets and their properties so as to assess the viability of a permanent magnet PM machine option for a HP shaft starter/generator.

The main focus of this chapter however is the effects of temperature on soft magnetic materials. Although in the short term high temperature operation of soft magnetic materials show some benefits such as lower eddy current losses, long term operation has several limitations due to ageing effects as was found through the literature review. These ageing related issues will be outlined in this chapter with an aim to select the materials required for the machine design.

2.2 High temperature coils

Operating an electrical machine in an ambient temperature of 350°C requires coils that can withstand considerably higher localised temperatures in order to accommodate internal heating generated by ohmic losses. Although the ultimate temperature will depend on the design constraints and performance requirements, it is likely that regions of the coil may be required to operate at ~450°C. Despite Copper having a relatively high temperature coefficient of resistance (increasing by some 40% per 100°C) it still offers the highest volumetric electrical conductivity at around 400-450°C and hence is still considered the leading core conductor material for wires operating at these temperatures.

Copper tends to oxidise at relatively low temperatures. Unalloyed Copper can start to oxidise at 200°C in 25 minutes and at 350°C in as less as 5 minutes[1]. Copper oxidation rates also increase very rapidly as the temperature increases [2]. Commercially available high temperature wires have plated or clad a Nickel coating which forms a protective barrier for the Copper at the expense of some increase in wire resistivity. A comparison of the oxidation

rates of pure Copper and Nickel coated Copper at high temperatures of 600-800°C showed a tenfold reduction in mass gain for the Nickel coated material [3]. The commercially available Nickel coated Copper wires have rated temperature ranges of about 400-500°C, though several different options are being considered for applications at 600°C and above[4].

Although Nickel is useful for enhancing oxidation resistance, long-term exposure of Nickel coated Copper to elevated temperature wires gives rise to diffusion of Nickel into Copper conductor due to grain boundary diffusion[5]. A study carried out in [6] considered at the effect of the Nickel diffusion on the electrical resistivity of potential commercially available high temperature wires. The Nickel diffusion causes an increase in the resistivity of the conductor which over a period will have a marked effect on the copper loss. Very extensive diffusion of Nickel into Copper core may result in some Copper reaching the surface and hence exposed to oxidation. Thus the use of Nickel coated Copper at temperatures of 400-450°C for extended periods will require that careful consideration is given to the thickness of Nickel coatings. Other options such as silver coatings or pure silver conductors could also be possible contenders for this application.

Conventional insulated wires dominate the manufacture of electrical machines for almost all applications. The insulation systems on conventional wire typically consist of organic materials that are limited to maximum operating temperatures of around 250°C, beyond which they increasingly and rapidly degrade with temperature. They can be used beyond their long-term rated temperature but at the expense of rapidly reducing lifetime. A useful rule-of-thumb is a halving of lifetime with every 10°C of temperature increase. In some short-term applications such as missiles, motor-sport components they may be pushed up to 280-300°C. Commercially available high temperature wires, i.e. wires with a long-term temperature capability of >250-300°C tend to have non-organic based insulations such as conformal ceramics, glass fibre braided sleeving of ceramic/glass fibre tapes. Wires with conformal ceramic coatings tend to be fragile, are limited to relatively large bend radii and are prone to cracking during coil forming.

To overcome some of these drawbacks, some high temperature wires such as ‘Fujikura Fujithermo A’ have a hybrid organic-ceramic coating which starts off as a flexible insulation with properties similar to organic coatings which can be formed more or less with standard methods. Once heated to a certain temperature (600°C in the case of the Fujithermo A) converts into a rigid ceramic coating. Although these commercially available wires are

notionally rated for the temperatures of 400°C and above, little data exists on their behaviour at temperature, either in terms of key electrical indicators or long-term stability. A study by [7] compared the dielectric properties of two commercially produced wires the Ceramawire and Fujithermo M. The results showed a significant difference in the dielectric strengths with the Fujithermo wire having breakdown voltages orders in magnitude higher than the Ceramawire at rated temperatures.

In addition to the primary insulation on the wire itself, an encapsulation material is required to ensure good thermal contact between the individual turns within the coil and the stator core. It also provides some secondary insulation and mechanical support to maintain coil integrity. The encapsulation materials require good mechanical strength to withstand thermal cycling and vibrations. The thermal conductivity of the encapsulant also helps dissipate the coil losses through the core which in many machines may be the dominant mechanism for dissipating the losses. It is also important that the potting compounds have similar thermal expansion coefficients as the core and wire to avoid cracking during thermal cycling. Due to the high viscosity of the encapsulation materials, methods such as vacuum impregnation cannot be used effectively as any voids or air capsules formed may compromise the mechanical integrity of the coils. Therefore the coils need to be pre-formed or manufactured or ex-situ and then placed in the stator, as opposed to in-situ winding of individual turns into the slot. The high temperature encapsulate is applied between layers during the manufacturing process to provide a good consistency. Pre-formed coils offer several benefits in term of:

- Ease of stator assembly
- High coil packing factor
- Reduced repair turn-around time for example stator rewound after a stator fault
- May be the only means of forming a coil for some wire insulation types which do not have the abrasive resistance to tolerate in-situ winding

Pre-forming coils however imposes several constraints on the manufacturing process. These include:

- Requirement to employ parallel sided stator core teeth with no tooth tips (In machines which require flared teeth, semi-permeable slot wedges can be

employed. However the maximum operating temperature of these materials is likely to be the limiting factor)

- The coils must pass the adjacent coil when inserted into the stator slot
- There will be little or no deformability in the coil once formed

These constraints tend to incur penalties in the proportion of the final slot which is occupied by actual conductor as opposed to voids and space between individual conductors which is often referred to as the 'packing factor'. The packing factor has a significant impact on the machine design as it dictates the slot area required to accommodate a given ampere-turns which has a knock-on effect on the size of the core.

There are several commercially available insulated Nickel coated Copper wires with rated temperatures of 400-500°C. The simulated results reported in [6] suggests that these may not possess the long term capability for ~30,000 hours of continuous operation, due to effects of Nickel diffusion. Nonetheless, they remain the leading candidates for this design study although their introduction into service would be contingent on establishing a detailed understanding of long term stability. Commercially available high temperature wires can be used with a variety of encapsulation materials. However, manufactures tend to suggest specific encapsulates for the wires based on experience. In selecting an optimal combination of wire and encapsulate to produce a reliable high temperature coil, there are several electrical and mechanical tests that sample coils should be subjected to such as voltage breakdown capability, susceptibility to partial discharge, mechanical and electrical integrity with thermal cycling of coils and exposure to vibration.

In this machine a combination of a commercially available wire SK650 by Von Roll and No. 10 encapsulate by Sauereisen was selected. Previous studies, conducted at the University of Sheffield, including a high temperature actuator demonstrator, have identified this combination as the best available at present in terms of electrical and mechanical robustness[8, 9]. As part of these previous investigations, a series of commercially produced wires and encapsulates were systematically evaluated using simple test coils. The combination of SK650 and Sauereisen No. 10 encapsulant showed a high voltage breakdown compared to the other combinations on test, and also had a better net cross sectional thermal conductivity with the encapsulate combination.

However, the data produced in these previous studies, is not sufficient to unequivocally state that this option is superior to the other combinations for such

applications. The main disadvantage of this wire is its comparatively thick insulation layer, which reduces the achievable packing factor, i.e. the proportion of the total coil cross-section which is occupied by the core Copper conductor. For the 1mm diameter SK650 wire under consideration, the insulation thickness of ~0.1mm results in only 62% of the wire cross section being composed of conductor. Although in practice slightly better packing is achieved due to a level of compressibility in the wire insulation, this factor in combination with the 78% fill factor for circular conductors in a rectangular slot suggests that the maximum packing factor geometrically possible is at best 48%. Previous experience of constructing coils using this combination yielded packing factors of no more than 30%. The implications of this modest packing factor on the machine design are discussed in detail in chapter 5.

2.3 Hard magnetic materials

Table 2-1 lists some of the common grades of high performance hard magnetic materials used in electrical machines together with key magnetic properties which have been drawn from manufacturer datasheets. There are many different measures of the effectiveness of hard magnetic materials. Three commonly used measures which are useful in the context of assessing suitability of different grades for electrical machines are the remanence, energy product calculated as $(BH)_{max}$ and the maximum service temperature. The lowest cost and most commonly used permanent magnet is hard ferrite, but it has both a low Curie temperatures and very modest magnetic properties. In ferromagnetic materials the Curie temperature is the temperature at which the material becomes completely non-magnetic. However for most practical purposes these materials have to be operated at temperatures reasonably lower than the Curie temperature. Certain magnetic materials such as Alnico have much higher curie temperatures (850°C) but have quite low demagnetising fields. In applications which demand high power density such as electrical machines, the rare earth materials such as Neodymium Iron Boron (NdFeB) and Samarium Cobalt (SmCo) are more commonly used due to their higher energy products. NdFeB have higher energy products and are relatively cheaper but have low Curie temperatures and peak operating temperatures of under 200°C. Thus the SmCo magnets have been preferred for higher operating temperature ranges [10].

Table 2-1 : Temperature limits of magnetic materials.

Magnet Material	Remanence (T)	Energy product $(BH)_{max}$ (kJ/m^3) at room temperature	Maximum operating temperature (°C)	Curie temperature (°C)
Hard Ferrite	0.40	27	200	450
AlNiCo	1.12	35	450	860
Samarium Cobalt ($SmCo_5$)	0.85	143-59	250	725
Neodymium Iron Boron (NdFeB)	1.43	382-398	80	310
Neodymium Iron Boron-HT (NdFeB)	1.20	223-239	200	310
Samarium Cobalt (Sm_2Co_{17})	1.15	159-175	300	800
Samarium Cobalt -UHT (Sm_2Co_{17})	0.85	167	500	800

Figure 2.1 shows the demagnetisation curves for a high temperature grade of Sm_2Co_{17}, which is rated for operation up to 550°C [11]. These magnets start with a lower remanence than their conventional grade counterparts at room temperature. As is common with all grades of $Sm_2Co_{17,}$ as temperature increases, the performance decreases further. The $(BH)_{max}$ for the grade EEC 16-T550 drops from 134 kJ/m^3 at 25°C to 71 kJ/m^3 at 450°C. Due to the lower coercivities at elevated temperature, the risk of demagnetisation increases, and the electric loading must be compromised. Exposure to high temperatures for extended periods showed that the material is susceptible to oxidation, which causes irreversible

damage to magnetic properties[12]. Methods such as protective coatings or doping with Silicon [13] can significantly reduce oxidation, but are still a long way from solving the problem of oxidation completely.

Other than the magnetic properties, there are other issues with permanent magnet machines such as magnet containment on high speed rotors. At high rotational speeds surface mount magnet rotors tend to use a mechanical retaining sleeve for magnet containment, based on materials such as carbon fibre or high strength metals. Carbon fibre bandings have a much higher strength to weight ratio and almost no losses and hence is becoming more prevalent. However the temperature limits for the carbon fibre and the bonding resins used are fairly low (~150°C). Metal based bandings are capable of temperature but have additional eddy current losses and weight. The interior permanent magnet rotor option may be more promising for such an application, however the centrifugal stresses acting on the magnets at high speeds need to be alleviated, as the materials tend to have poor mechanical strength. Therefore, many challenges remain to be overcome before permanent magnetic materials can be readily employed in applications of power dense high temperature machines.

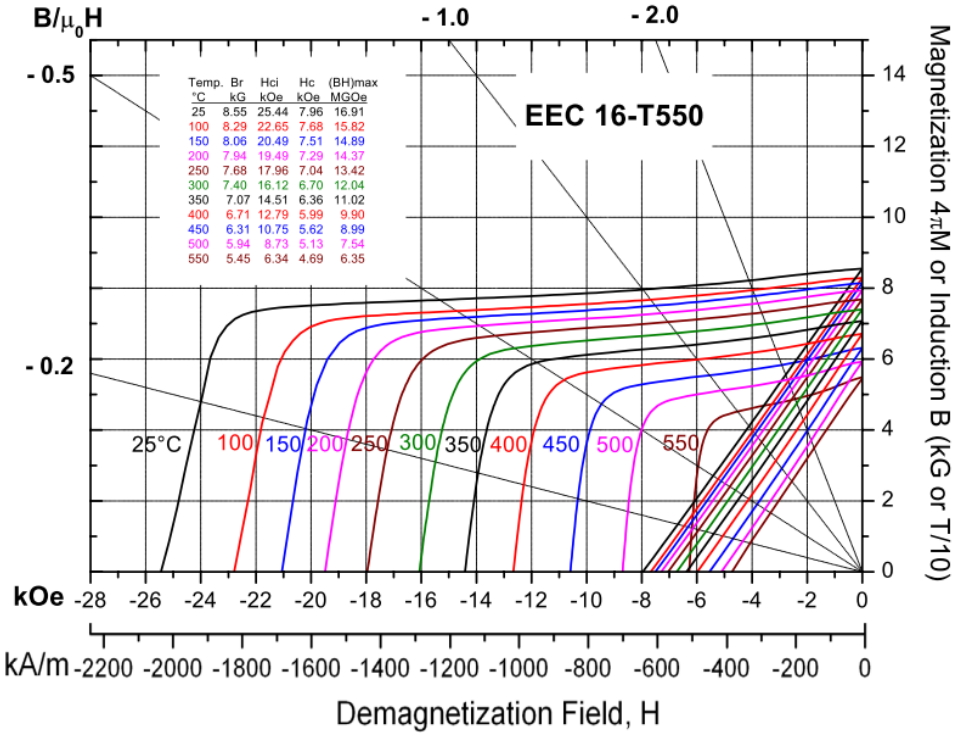

Figure 2.1: Demagnetisation curves of Sm-Co UHT grade at high temperatures [Source:[11]].

2.4 Soft magnetic materials

The choice of soft magnetic material for either the stator or rotor cores is an important factor in determining the performance of electrical machines. The dominant soft magnetic material in industrial electrical machines is Silicon steel (Si-Fe) with grades having typical Silicon contents of between 3-6%. In very low cost machines with modest performance, plain low-carbon steels are sometimes used despite their relatively poor electromagnetic performance. The comparatively low cost, high saturation flux density and low loss characteristics of Si-Fe grades with 3-3.5% Silicon make them the preferred material choice for many medium to high performance applications.

In applications which the very highest level of performance, particularly in terms of reduced weight, such as aerospace or motorsport, Cobalt Iron (Co-Fe) is often preferred despite its very high cost (can be 80-100 times the cost of Si-Fe depending on volume etc). The main benefit of using Co-Fe in such applications is the higher saturation flux density which leads to savings in weight as the volume of core required to carry a given flux is reduced. For an aerospace HP shaft machine considered in this thesis, the key requirements are high power density and high temperature capability, Co-Fe grades offer advantages in both these regards compared to Si-Fe.

Table 2-2 lists the range of Curie temperatures exhibited by soft magnetic materials used in magnetic cores. The Silicon and Cobalt steels have Curie temperatures much higher than the proposed operating temperature of the HP machine. Nickel iron also has a Curie temperature of 480°C, however has a much lower saturation flux density. Nevertheless, it is considered as a potential candidate for low power actuator applications. It is important to note that although a material retains some degree of magnetism up to its Curie temperature, it is usually necessary to maintain a considerable margin from the operating temperature in order to retain useful levels of performance.

Figure 2.2 shows the saturation flux density of the different commercially available soft magnetic alloys manufactured by Vacuumschmelze (VAC) [14]. Co-Fe grades show the highest saturation flux density which is largely maintained even at 400°C. The high cost of Co-Fe makes it a seldom used material, even though it has superior magnetic properties. In the HP shaft application, since power density is at such a premium, this higher cost can be justified.

Table 2-2 : Curie temperatures of typical soft magnetic materials.

Material	Curie Temperatures (°C)
NiZn ceramic ferrites	150
MnZn ceramic ferrites	200
Amorphous Metallic Glass (80%Fe-20%B)	375
77% Nickel Iron (Permalloy)	480
3% Silicon Steel	720
Pure Iron	770
49% Cobalt Iron (Permendur)	950
Pure Cobalt	1121

The addition of silicon reduces the Curie temperatures of iron but this increases the electrical resistivity so as to achieve lower losses. Nevertheless, the susceptibility to oxidation in silicon steels at even modest temperatures is a fundamental shortcoming for the material in this application. Conversely, Co-Fe exhibits good resistance to oxidation and has been used in applications for temperatures above 400°C [15]. Other benefits include high strength capability and relatively low losses. Commercially available laminations use a variety of protective coatings for insulation which could be either a simple organic varnish or in cases where higher resistance and temperatures are required inorganic coatings. Co-Fe laminations have a magnesium based oxide layer, a few microns thick, which acts as insulation between successive laminations. This coating is well suited to high temperatures. In machines operating at more conventional temperatures, lamination stacks can be adhesively bonded to form a high integrity single piece stack. However, in the case of high temperature machines, the stack must be either simply clamped, welded or bonded with a high temperature ceramic adhesives, should a suitable adhesive be identified (which would need both high strength at high temperature and be capable of being applied in very thin layers so as not to diminish the achievable stack factor).

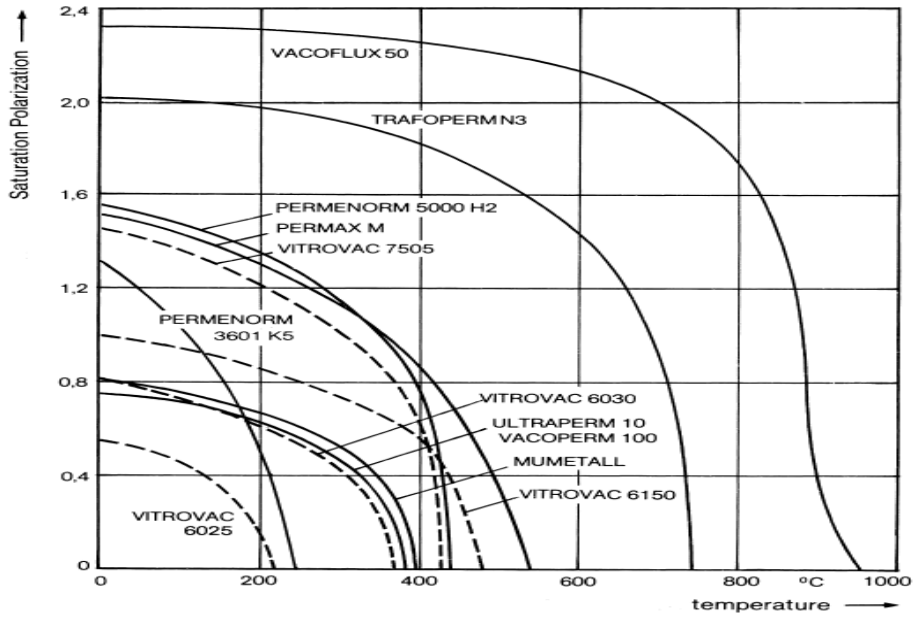

Figure 2.2: Saturation flux density of various Vacuumschmelze soft magnetic materials as a function of operating temperature [Source:[14]].

Co-Fe is produced in various grades providing a range of magnetic and mechanical properties. Even for a given alloy composition, the final properties can be tailored by varying the heat-treatment schedule. It is possible to trade-off magnetic and mechanical properties by selecting a particular heat-treatment schedule. Several studies have been published on the high temperature properties of three different grades of Co-Fe manufactured by Carpenter viz., Hiperco 50, Hiperco 50-HS and Hiperco 27 [16-21]. The Hiperco 50 and 50-HS grades (which both have Cobalt content of ~49%) have a higher permeability and saturation flux density than Hiperco27 (which has a Cobalt content of 27%). However the lower Cobalt content results in a lower cost alloy which makes it attractive in some applications, notably high value automotive components such as fuel injector actuator.

The most significant body of data on the performance of Co-Fe is published in [16]. This includes measurements of thermal ageing effects of magnetic and mechanical properties due to long term exposure to high temperatures. The studies indicate that the materials show evidence of significant degradation in mechanical and magnetic properties over the test period of 5000 hours of ageing in 500°C air. A reduction in mechanical strength of some 36% was observed over this period, which would need to be factored into the rotor design to avoid mechanical failure. The materials also showed an increase in core losses over time which

reduces efficiency and necessitates improved management of heat dissipation to accommodate this ageing effect into the design. As the operating periods of application may be of the order of 30000 hours, such significant degradation in relatively small operating times is undesirable. If some of the known degradation rates can be taken into account in the design stage, failures in the long term due to ageing effects can be avoided. In the next part of this chapter the basis for selecting the materials using the published data is discussed.

2.5 Properties of Cobalt-Iron

2.5.1 Mechanical properties

The SR machine rotor comprises a stack of thin Co-Fe laminations (typically 0.1 mm-0.5mm thick). At high rotational speeds, the rotor is subjected to centrifugal loading which can result in large hoop stresses which tend to be most pronounced at the base of the rotor teeth[22]. For a given maximum speed, the peak stresses are a function of the rotor outer diameter and the radial length of the rotor teeth. Hence, if the maximum stress that the material can sustain is low, the maximum rotor diameter is constrained, which consequently compromises the torque per unit length. Since the SR rotor is subjected to time varying flux excursions which generate core loss, it is also important to achieve better magnetic properties. Optimal mechanical and magnetic properties cannot be achieved simultaneously as the microstructures that benefit better mechanical strength impede the motion of magnetic domains required for magnetisation[23]. However, for the rotor core of the SR machine in the HP shaft, the mechanical properties will tend to be the overriding consideration, and the increased core losses will need to be carefully managed.

Of the three grades, Hiperco 50-HS has the best mechanical properties, specifically in terms of having a higher yield strength (0.2%) at all temperatures, ranging from 550 MPa at room temperature to 480 MPa at 480°C. The Hiperco 50 and Hiperco 27 grades have much lower strengths, and showed high failure rates in the creep tests [16]. Hence they were not considered as being viable options for the rotor design.

The yield strengths of Hiperco 50-HS showed degradation with ageing and after 2000 hours in 500°C air the yield strengths drops to 350MPa [16]. For ageing durations greater than 2000 hours Hiperco50-HS exhibited an increase in yield strength. This was attributed to the material hardening after some initial corrosion effects. For ageing times greater than 5000

hours it has been speculated that there might be a further increase in mechanical strength, but there is no published data to support this. If long term aged material does indeed exhibit stability to ageing at elevated temperature, there may be some scope to deploy pre-aged materials to minimise in-service variation, but this would come at a significant cost. The creep tests in [16]were carried out using a load of 300MPa which was close to the materials aged yield strengths at 2000 hours, and so unsurprisingly, creep rates increased after 2000 hours of ageing. From the various experimental findings in [16] it is apparent that the most likely case for potential mechanical failure would be due to creep effects as a result of the reduced strength of the rotor due to long term ageing. Drawing on these findings, the maximum rotor stress specified for the design study in this thesis was limited to half the worst case yield stress of 350MPa, which corresponds to 175MPa. This was deemed to provide a safety margin which should be sufficient to reliably accommodate thermal ageing.

2.5.2 Magnetic properties

The stator core is not subjected to high mechanical loads, and hence magnetic properties are the overriding consideration. Figure 2.3 shows the DC magnetisation curves of the three materials at room temperature taken from manufacturer's datasheets [14]. Hiperco 50 shows the highest saturation flux density at room temperature, followed by Hiperco 50-HS and Hiperco 27. At higher temperatures, the saturation flux density reduces but only at a modest rate. The thermal ageing of the materials in 450°C air showed that the magnetic permeability values degraded over the first 200 hours but reached more stable values after 1000 hours[20]. All material grades maintain a saturation flux density above 2T even after long term ageing (i.e. hundreds of hours). Hence, the flux carrying capability remains largely unaffected when the material is exposed to high temperatures for extended periods.

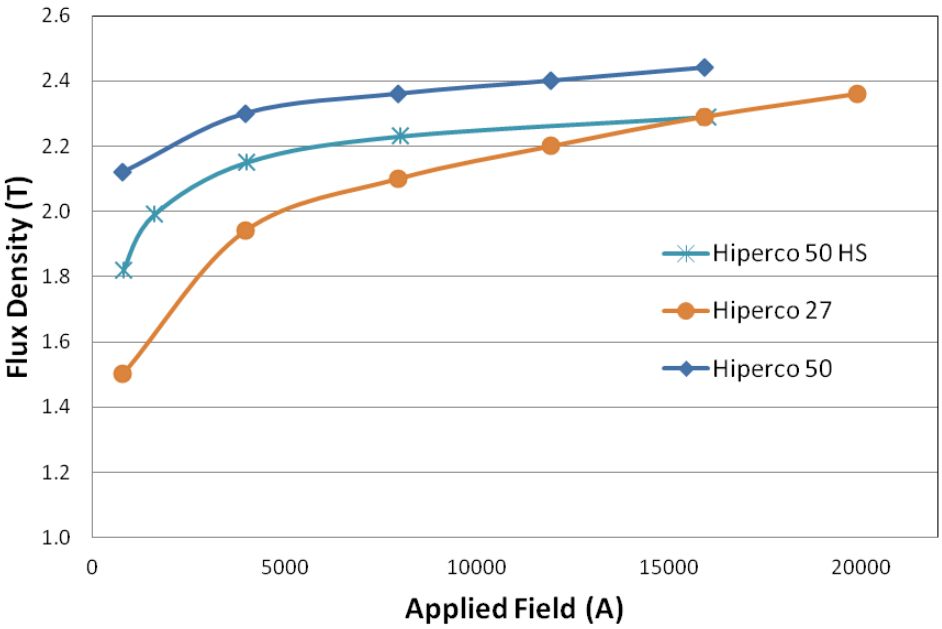

Figure 2.3: Manufacturer supplied magnetisation curves of Hiperco 50, Hiperco 50-HS and Hiperco 27 [Source: [24]].

As is the case in all electrical machines, employing materials with low core losses is beneficial in terms of minimising temperature rise and enhancing efficiency. The specific core loss of the three materials shows rather different behaviour with temperature and ageing. The eddy current losses in the core are inversely proportional to the electrical resistivity of the core material, and hence the increase in resistivity with temperature is beneficial in terms of reducing core losses. All the three materials have positive temperature coefficients of electrical resistivity with Hiperco 27 having the highest as seen in Figure 2.4. Figure 2.5 show the losses of three grades at an operating point of 1 kHz with a peak flux density of 1.8T as a function of temperature. In Hiperco 27, the losses reduce significantly with temperature, whereas the grades containing 50% Cobalt do not exhibit a significant variation in losses with temperature. This can in large part be attributed to the fact that the eddy current losses at the outset is a smaller fraction of the total losses for the 50% Cobalt grades.

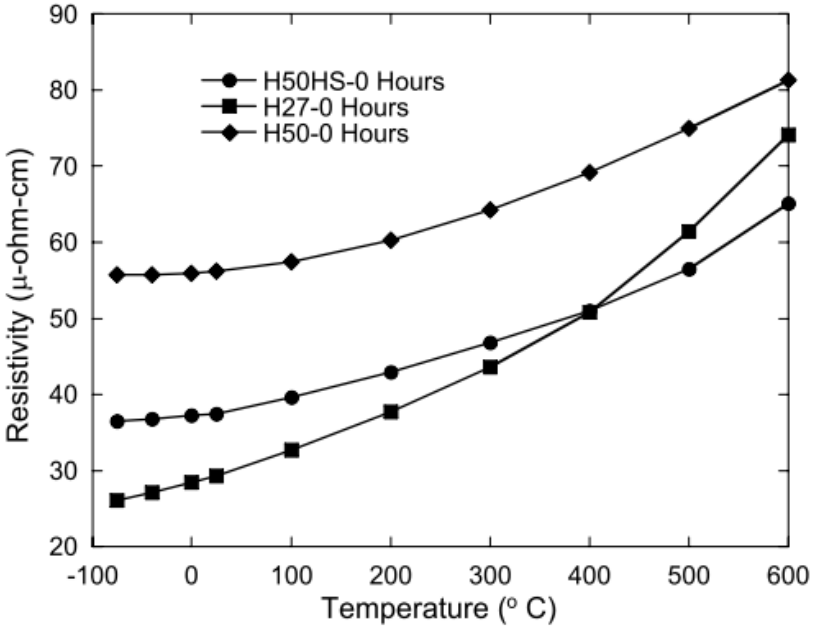

Figure 2.4: Measured resistivity as a function of temperature for the three Hiperco grades [Source: [16]] .

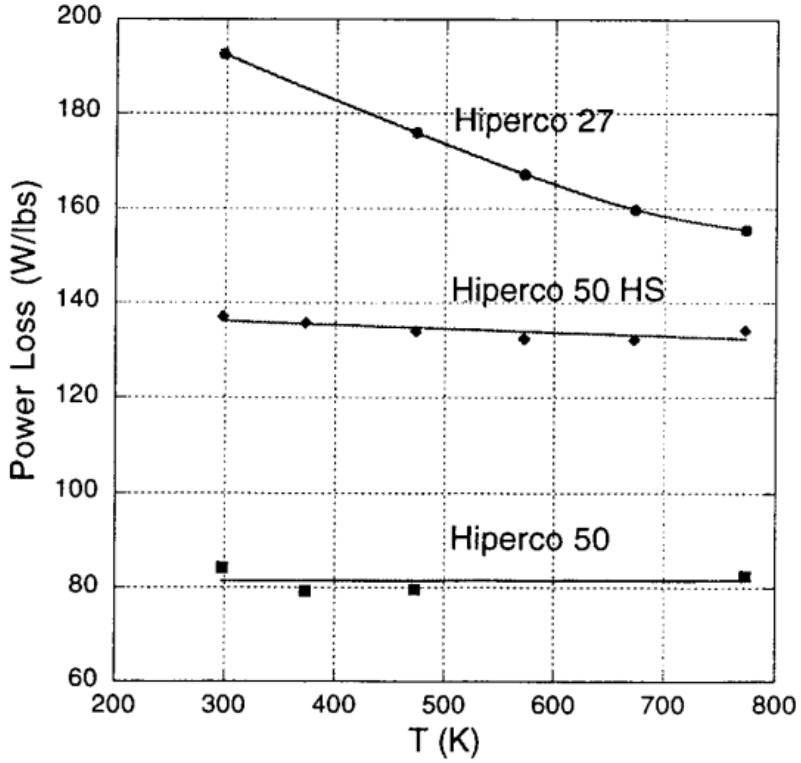

Figure 2.5: Measured core loss as a function of temperature for the three Hiperco grades at B=1.8T and f=1kHz [Source: [25]].

The Hiperco 50 grade exhibits the lowest losses across the full range of temperature, and would appear to be the leading candidate for the stator core. However, the electrical resistivity of all materials decreased with ageing at 500°C, as illustrated in Figure 2.6. The effect on Hiperco50, which has the highest electrical resistivity at 0 hours, is most pronounced, dropping by 34% over 5000 hours, whereas the Hiperco 50-HS material shows much better long-term stability. At 5000 hours the resistivity of these two grades converges. Hence, considerable increases in eddy current losses will occur with the Hiperco 50 as the material ages, in turn eroding its apparent superiority. This is illustrated in Table 2-3 which shows a comparison of core losses at 2 kHz and 2T, for Hiperco 50 and Hiperco 50-HS at the outset of testing and following 2000 and 5000 hours of ageing at 500^0C. It can be seen that the loss for Hiperco 50 exceeds that of the 50-HS grade before 2000 hours of ageing. The high flux density and frequency were selected for comparison as being representative of the operating range of the machine.

Although Hiperco27 material was shown to relatively stable to ageing, the absolute losses remain higher as compared to those of the 50% grades. Thus, for long term operation, Hiperco 50-HS appears to be the most suitable material for the stator core. The materials used in [16] were heat treated at the lower end of the heat treatment range (730°C) which tends to result in improved mechanical properties. Annealing at higher temperatures (up to 820°C) results in better magnetic properties, but at the expense of mechanical strength. For the stator, a heat treatment schedule at the upper end of the range is likely to provide the best performance.

Table 2-3: Room temperature core loss density in W/kg at 2 kHz and 2T for the un-aged, 2000 hours aged and 5000 hours aged samples (aged in air at 500°C) as read from [Source:[16]].

Grade	Un-aged	2000 hours aged	5000 hours aged
Hiperco 50	650	1370	1690
Hiperco 50-HS	780	1080	1330

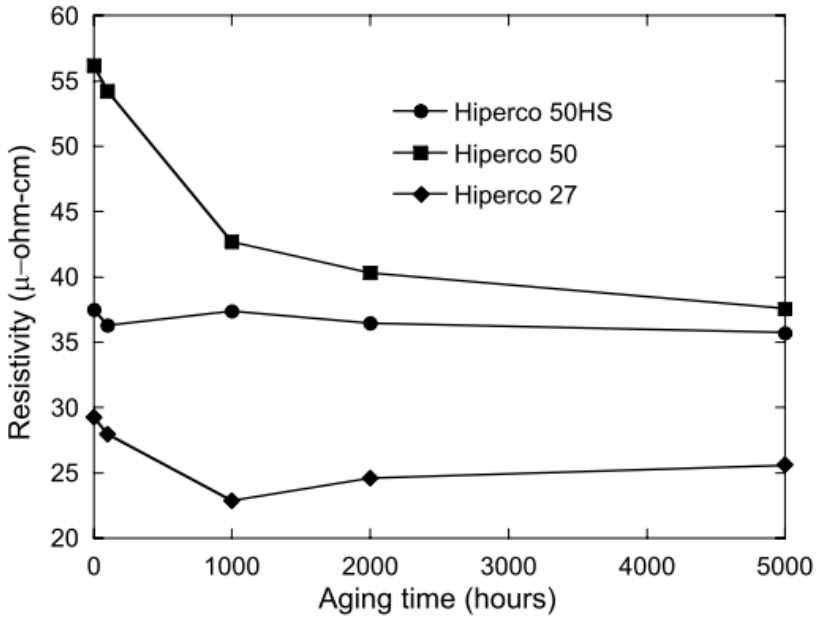

Figure 2.6: Room temperature resistivity as a function ageing duration at 500°C [Source: [16]].

2.6 Selection of rotor and stator materials

The degradation of the core materials with ageing, although not desirable, can be accounted for in the design process. Mechanical creep effects can be managed by limiting the rotor size and hence the stress levels, whereas the increase in core loss can be accounted for by either increasing the cooling provision or by reducing the flux levels in the core, although the latter would increase the machine size. The core loss shows a steep increase due to ageing at 2 kHz and 2T for Hiperco50-HS as well, almost doubling at 5000 hours of ageing. As the resistivity of the Hiperco50-HS appears to be relatively stable with ageing, the observed increase in losses cannot be attributed to classical eddy current losses, and is likely to be due to a change in the hysteresis and excess loss which indicates changes to the material microstructure. In order to improve the understanding of these variations, it is useful to fit the data to a loss separation model, which can then describe the effects of temperature and ageing on the individual loss components. Section 2.7 describes the method to characterise the materials with the limited data available.

Although published literature is predominantly based on the properties of the Hiperco range of alloys from Carpenter Technology, similar grades manufactured by Vacuumschmelze GmbH (VAC) were preferred for this project due to a combination of

availability in small batches and cooperation with VAC on data sharing. VAC manufactures two similar high strength grades of ~50% Cobalt content alloys, Vacodur 50 and Vacodur S+. The Vacodur 50 uses Niobium additions similar to the Hiperco 50-HS to achieve its mechanical properties, whereas the Vacodur S+ uses Tantalum and Zirconium additions. The Vacodur S+ can achieve a wider range of mechanical strengths but they are also not immune from degradation due to thermal ageing as described in [26]. Figure 2.7 shows the range of properties that can be achieved for different heat treatments of Vacodur 50 and Vacodur S+. The Vacoflux 50 grade is similar to Hiperco50, which has the better magnetic properties.

The Vacodur S+ material was selected for the rotor material due to its higher strength. The rotor laminations were annealed at 720°C to provide 0.2% yield strengths of 600MPa. Although higher strengths could be achieved with this material, the exponential increase in coercivity with strength which is shown in Figure 2.7 was undesirable. For the stator, Vacodur S+ laminations were selected and heat treated at 820°C to provide enhanced magnetic properties and a more modest 0.2% yield strength of ~390MPa. The manufacturer's material datasheets for Vacodur S+ only included limited core loss data, which was not sufficient to reliably fit to core loss models. As the selected materials had slightly different composition, and heat treatment schedules as compared to the Hiperco grades reported in the literature, the Hiperco data could not be reliably used. Hence, samples of Vacodur S+ were obtained to carry out loss measurements at temperature so as to characterise the materials for the two different heat treatments, including ageing data for comparison with the trends observed by Fingers et al. In the next chapter a loss model is developed for estimating losses in switched reluctance machines. The details of the measurement techniques used to characterise the materials for the loss model are described in chapter 4.

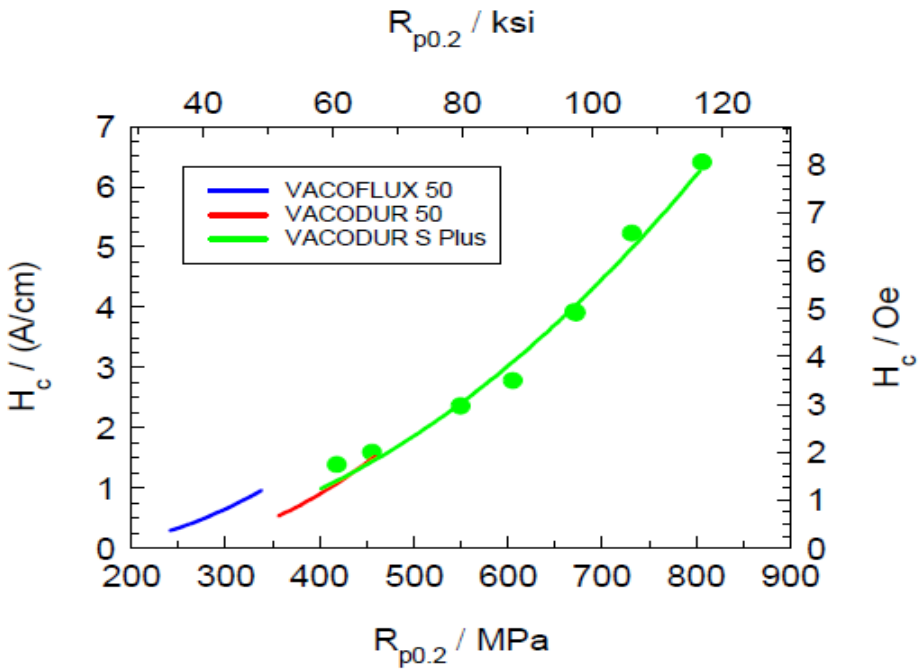

Figure 2.7: Coercivity vs. yield strength resulting from different annealing temperatures [Source: [13]].

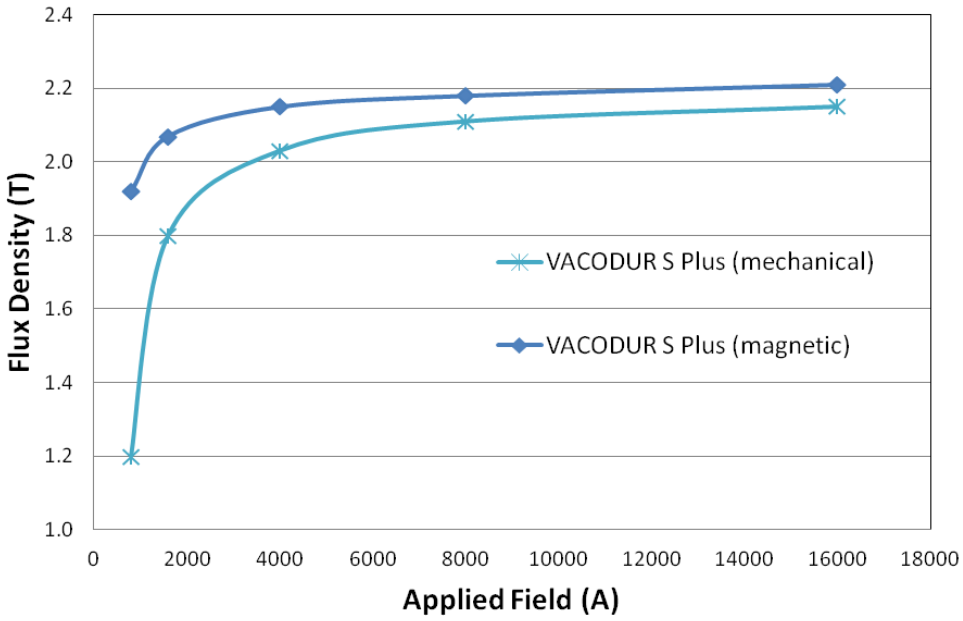

Figure 2.8: BH curves of Vacodur S+ from datasheet.

2.7 Material loss characterisation

In order to predict losses for the preliminary machine design studies, the published core loss measured data in [16] was used to fit parameters to a standard loss separation model. Since core loss changes markedly with temperature and ageing, some temperature dependency of the model parameters is inevitable. A widely used technique for predicting losses in electrical machines is that of loss separation. It is based on arriving at the total losses by the summation three constituent components, viz. classical eddy current loss, excess loss and hysteresis loss [27]. The standard loss formulation in the frequency domain is given as

$$\boldsymbol{P_{total} = k_{cl}B^2f^2 + k_{exc}B^{1.5}f^{1.5} + k_hB^{\alpha+\beta B}f} \quad \textbf{(2.1)}$$

The parameters of the loss model are k_{cl}, k_{exc}, k_h, α and β. The coefficient for classical eddy current losses k_{cl} is a function of the lamination electrical conductivity (σ) and thickness (d). The hysteresis energy loss per cycle is the frequency independent term, which is calculated as the energy lost within the static hysteretic loop. The hysteresis loss term is curve fit to an exponential curve whose coefficients are k_h α and β. The β term adds nonlinearity required to represent magnetic saturation effects. Excess losses arise due to the concentration of losses around magnetic domains. The parameter associated with excess loss k_{exc} is a function of the micro structural features of the material and, as such, is difficult to mathematically quantify on an a-priori basis. Thus k_{exc} is usually predicted by curve fitting the value of ($P_{total} - P_{cl} - P_h$) for a set of AC loss measurements. In this case, only the classical losses could be separated from the total losses as the only parameter available is the conductivity. As there were no hysteresis loop measurements published, it was not possible to separate the hysteresis losses directly. Therefore the hysteresis loss and excess loss parameters had to be curve fitted to the remaining loss by trial and error. This is far from ideal, but is the most pragmatic approach when there is little in the way of independent hysteresis measurements available.

The hysteresis loss coefficients were first selected to give good fit at the lower frequencies where they are at their most dominant. The residual losses at higher frequencies were incorporated into the excess loss coefficient. These were then tuned to give a good fit over the whole measurement spectrum. Figure 2.9 shows the loss predicted by this method for Hiperco 50-HS at room temperature 200 and 400°C using published data as the basis for

the coefficients. Table 2-4 shows the values of these coefficients estimated for the un-aged Hiperco50-HS as a function of temperature. The hysteresis losses which are a function of the material coercivity reduced marginally at temperatures around 400°C but there was an increase in the excess loss. However these were not sufficiently significant to gain any insight into the detailed behaviour of the excess loss with temperature. However, it can be inferred that the large contribution to the drop in loss with increasing temperature was due to the classical eddy current component.

Table 2-4 : Variation in parameters of loss model with temperature for Hiperco 50-HS

Temperature (°C)	**Room Temperature**	**200**	**400**
Resistivity (μΩ-m^{-1})	**38**	**43**	**51**
k_{exc}	**2x10^{-5}**	**3x10^{-5}**	**7 x10^{-5}**
k_h	**0.095**	**0.095**	**0.085**
a	**2.0**	**1.9**	**1.9**
b	**-0.15**	**-0.20**	**-0.20**

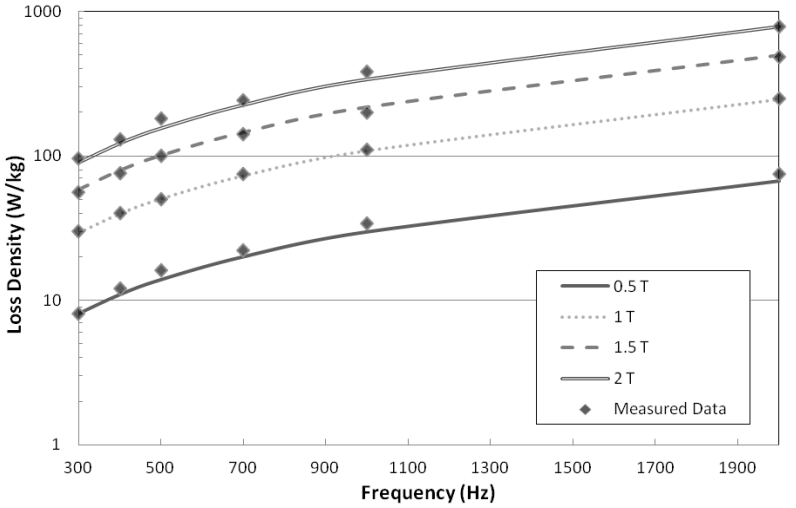

Room temperature

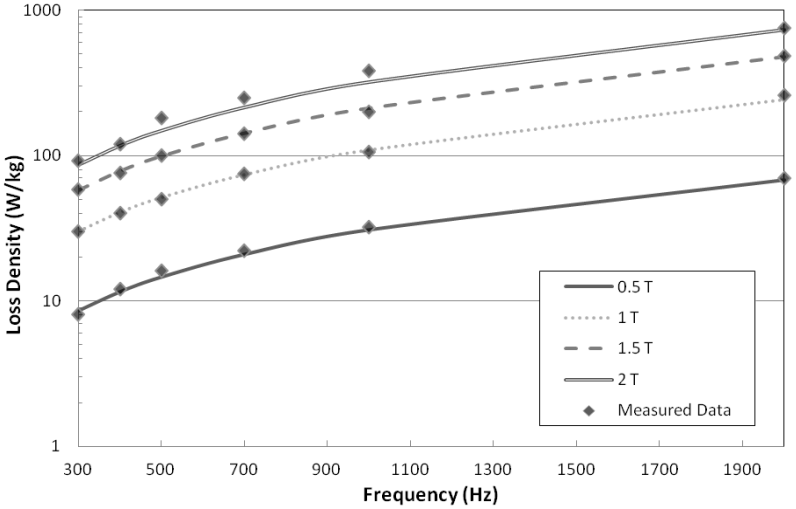

200°C

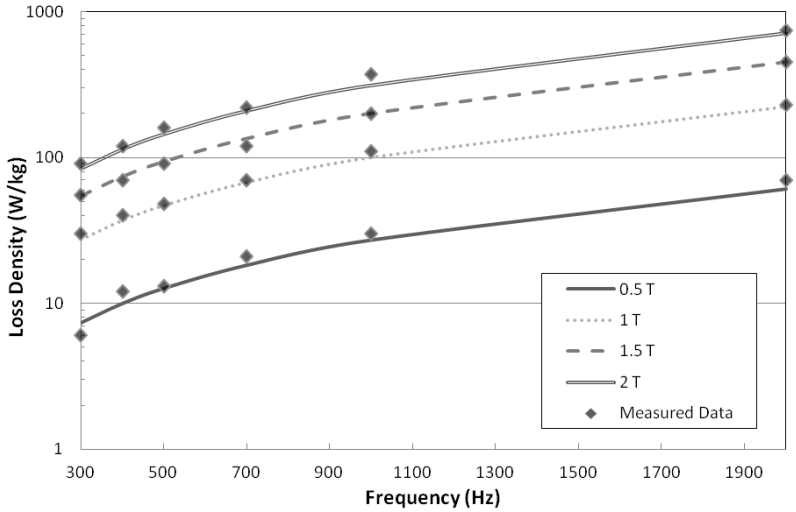

400°C

Figure 2.9 : Curve fit of loss model to Hiperco50-HS prior to ageing.

This curve-fitting technique was also used to fit parameters for aged Hiperco 50-HS. The graphs of the curve fits and the parameters used are included in Appendix A for completeness. The data showed a significant increase in losses at high frequencies and flux densities for the aged material. As the resistivity of the material remained relatively unchanged with ageing, the increase in loss could not be reliably attributed to classical eddy current losses. At high frequencies skin effect has the tendency to reduce the eddy current losses and hence this effect can also be ruled out as well. As a result, the vast majority of the increase in losses had to be incorporated into the hysteresis and excess loss components. However, when the hysteresis losses were fitted at the lower frequencies, there was a significant under prediction of loss at high frequencies, which hints that a large proportion of the temperature sensitivity of the loss was coming from the excess loss component.

The formulations used for excess losses described by Bertotti in [27] were based on statistical analysis of losses in the low to medium frequencies of around 400Hz, which are well below the frequencies considered in this case. At higher frequencies rate dependent hysteresis effects are more dominant which may have a power relationship with frequency of greater than the unity power adopted by Bertotti. These losses were incorporated into the excess loss co-efficient which showed a five-fold increase at 5000 hours ageing. It should be noted that the curve fits here, are only approximations and for a better understanding of the contributions from the various components and improved models for design purposed, detailed hysteresis loss data is required. Therefore, the samples obtained for characterisation were also aged at 400°C for 2000 hours. These results are described in detail in chapter 4.

2.8 Summary

This chapter has demonstrated that the magnetic and electrical materials used in high temperature machines have several limitations. Material ageing is considered as the main obstacle for long term operation at these temperatures. The mechanical ageing can be taken into account while setting the maximum stress level in the rotor, although the increases in losses have to be dealt with by the cooling system. If the diffusion of Nickel in Copper can be reliably predicted the ideal thickness of the nickel coating can be gauged for the length of operation. An attempt of modelling this is described in [6], which provides a useful starting point for specifying conductor dimensions. The increase in resistance and copper loss due to this must be accounted for in aged thermal models.

Although the core materials can withstand the 450°C temperatures and operate with a significant fraction of their room temperature capability, long term degradation remains a concern. From the data published in [26] it appears that the ageing accelerates at temperatures above 350°C. Thus, for long term operation it may be beneficial if core temperatures could be maintained under 350°C. This would require special cooling techniques the feasibility of which remains unknown at this point. From the published data on commercially available materials it was found that the high strength 50% Co-Fe grades were more stable with long term operation. However, these materials have much higher losses at the outset of service. To improve stator magnetic properties the material can be heat treated at the higher temperatures to deliver the optimal magnetic properties. A significant amount of published data exists on the Co-Fe materials, however due to the range of grades and heat treatments available, characterising the materials for loss models requires very specific measurements on the particular grade being used. In the case of the current application, further loss measurements for the heat treatment are described in chapter 4.

References

[1] M. Honkanen, M. Vippola, and T. Lepisto, "Low temperature oxidation of copper alloys - AEM and AFM characterization," *Journal of Materials Science,* vol. 42, pp. 4684-4691, Jun 2007.

[2] Y. F. Zhu, K. Mimura, J. W. Lim, M. Isshiki, and Q. Jiang, "Brief review of oxidation kinetics of copper at 350 degrees C to 1050 degrees C," *Metallurgical and Materials Transactions a-Physical Metallurgy and Materials Science,* vol. 37A, pp. 1231-1237, Apr 2006.

[3] U. V. Aniekwe and T. A. Utigard, "High-temperature oxidation of nickel-plated copper vs pure copper," *Canadian Metallurgical Quarterly,* vol. 38, pp. 277-281, Oct 1999.

[4] S. Jumonji, J. Senoo, K. Ueda, S. Chabata, S. Amano, and A. Ono, "Super heat resistant ceramic insulated wire," in *Electrical Electronics Insulation Conference, 1995, and Electrical Manufacturing & Coil Winding Conference. Proceedings*, 1995, pp. 557-563.

[5] J. S. Loos and B. A. Terhaar, "Influence of Heat-Treatments on the Electrical-Resistance of Thin-Film Copper Electroless Nickel Microcircuit Interconnections," *Thin Solid Films,* vol. 188, pp. 247-258, Jul 15 1990.

[6] A. Powell, "Impact of nickel diffusion on high temperature electrical conductors," Rolls-Royce DNS 166029, 2010.

[7] I. Timoshkin, R. Fouracre, S. MacGregor, M. Given, and T. Starke, "Dielectric Evaluation of Ceramic Insulated Wires," in *Solid Dielectrics, 2007. ICSD '07. IEEE International Conference on*, 2007, pp. 688-690.

[8] S. Gibson and D.Powell, "Phase 1: Down-selection of commercial high temperature wires," Rolls-Royce University Technology Centre in Advanced Electrical Machines and Drives RR/HEAT/TR/2008/03, 2008.

[9] B. Gysen, S. Gibson, R. Clark, and G. Jewell, "High temperature permanent magnet actuator for fail-safe applications," *IEEJ Transactions on Industry Applications*, vol. 128-D, pp. 1198 - null, 2008 2008.

[10] D. A. Williams, "Permanent Magnets for High Temperature Applications," presented at the High Temperature Magnetic Materials and Components, Oxford, 2009.

[11] "Ultra-high temperature Samarium Cobalt magnets and magnet assemblies." Electron Energy Corporation. http://www.electronenergy.com/products/samarium-cobalt-uht.htm

[12] C. H. Chen, M. S. Walmer, M. H. Walmer, L. Sam, and G. E. Kuhl, "Thermal stability of Sm-TM high temperature magnets at 300-550°C," *Magnetics, IEEE Transactions on*, vol. 36, pp. 3291-3293, 2000.

[13] L. Liu, T. Jin, and C. Jiang, "High-temperature oxidation resistance and magnetic properties of Si-doped Sm2Co17-type magnets at 500 °C," *Journal of Magnetism and Magnetic Materials*, vol. 324, pp. 2310-2314, 2012.

[14] "Datasheet, Soft Magnetic Materials and Semi-Finished Products," vol. Vacuumschmelze, 2002

[15] N. Sidell and G. W. Jewell, "The design and construction of a high temperature linear electromagnetic actuator," *Journal of Applied Physics*, vol. 85, pp. 4901-4903, Apr 15 1999.

[16] Z. T. Richard Fingers, John Horwath, "High Temperature properties and Aging - Stress related changes of FeCo Materials," Wright-Patterson Air force Base, Ohio AFRL-PR-WP-TR-2006-2176, 2006.

[17] P. E. Kueser, D. M. Pavlovic, D. H. Lane, J. J. Clark, and M. Spewock, "Properties of magnetic materials for use in space power systems," Westinghouse Electric Corporation1967.

[18] B. E. Lorenz and C. D. Graham, "High-temperature magnetostriction in polycrystalline Fe-Co alloys," *Ieee Transactions on Magnetics*, vol. 40, pp. 2751-2753, Jul 2004.

[19] R. H. Yu and J. Zhu, "Precipitation and high temperature magnetic properties of FeCo-based alloys," *Journal of Applied Physics*, vol. 97, pp. -, Mar 1 2005.

[20] L. Lin, "High temperature magnetic properties of 49%Co 2%V Fe alloy," *Journal of Applied Physics*, 1996.

[21] R. H. Yu, "High-temperature AC magnetic properties of FeCo-based soft magnets," *Journal of Magnetism and Magnetic Materials*, vol. 284, pp. 140-144, 2004.

[22] S. D. Calverley, "Design of a HIgh Speed Switched Reluctance Machine for Automotive Turbo-Generator Applications," PhD, Department of Electronic and Electrical Engineering, University of Sheffield, Sheffield, 2001.

[23] B. T. Hailer, "Effect of Heat Treatment on Magnetic and Mechanical Properties of an Iron-Cobalt-Vanadium-Niobium Alloy," 2002.

[24] Carpenter-Technology, "Cobalt-Iron Alloys Product Information," 1990

[25] R. T. Fingers, R. P. Carr, and Z. Turgut, "Effect of aging on magnetic properties of Hiperco (R) 27, Hiperco (R) 50, and Hiperco 50 HS (R) alloys," *Journal of Applied Physics*, vol. 91, pp. 7848-7850, May 15 2002.

[26] W. Pieper, "Soft Magnetic Cobalt-Iron Alloys at High Temperatures," presented at the High Temperature Magnetic Materials and Components, Oxford, 2009.

[27] G. Bertotti, *Hysteresis in magnetism : for physicists, materials scientists, and engineers*. San Diego, Calif. ; London: Academic Press, 1998.

Chapter 3 : Dynamic modelling of switched reluctance machines

3.1 Introduction

The operation of switched reluctance (SR) machines is characterised by being very dynamic and transient when compared to other machines such as induction machines, synchronous machines and permanent magnet which can often be modelled for most operating conditions using steady-state AC analysis. SR machine operation, even when operating at a fixed speed and load, involves a sequence of transient pulses of voltage, current and torque. Hence, numerical time-stepping simulation methods are usually adopted to predict even steady-state operation.

A key element in dynamic simulations of this type is the prediction of losses, this being a particular issue when power density is a major design objective. The reliable prediction of core losses in electrical machines remains possibly the most challenging aspect of their design. This is particularly the case for electrical machines in which the flux density excursions in various regions of the rotor and/or stator core are highly distorted. SR machines pose particular challenges as they include regions exposed to uni-polar flux density excursions, asymmetric bi-polar excursions, often with significant minor loops[1]. It has become common practice to calculate core losses as a post-processing operation and commercial finite element packages increasingly include core loss post-processing models based for example on the methods proposed in [2, 3].

The established approach is that a series of magneto-static finite element (FE) predicted magnetic field distributions spanning one complete cycle of the excitation are used to calculate time-varying flux density waveforms for all regions in the stator and/or rotor cores. This procedure is often performed on an element by element basis and the losses over one cycle in each finite element are aggregated to yield a total core loss for the machine. Various refinements and alternative approaches to this method have been proposed, for example in [4-7]. The method proposed in [7] for example, is based on enforcing the flux waveforms from the magneto-static FE calculations onto a separate one dimensional FE

model, in which the flux variation across the thickness is simulated to which can account for eddy current effects. Although these core loss models can predict accurate losses for a given flux density waveform, their post-processing nature means that they are unable to reflect the influence of the core loss on the electrical circuit and hence the field distribution itself.

In some machines, the combination of operating conditions and core magnetic properties are such that the core losses can constitute a significant fraction of the input power, which one could broadly regard as being 10-15% or above. Although such inefficiencies are undesirable, in cases where power density is the over-riding consideration, such losses may need to be accommodated. In cases where core loss constitutes such a significant fraction of input power, a failure to account for its influence on the electrical circuit behaviour can give rise to over-estimates of output power and under predict the copper loss when the machine is supplied by a given voltage pulse. Integrating a core loss model into the dynamic simulation of an electrical machine has the potential to improve the accuracy of performance predictions, it poses several challenges. The most obvious of these challenges is that the core loss must be predicted on an essentially instantaneous basis (or more strictly the energy in one simulation time step) as opposed to over a complete cycle. This is straightforward for eddy current and excess components of loss, as there are expressions for instantaneous loss readily available, and indeed integration of these expressions is used to calculate their contribution to the loss per cycle in well-established models. However, the need for dynamic models of instantaneous hysteresis loss is far from straightforward. This chapter describes the use of a Preisach based loss model which is capable of tracking hysteresis losses for arbitrary waveforms. Having calculated the various contributions to the instantaneous core loss at each time step, its influence can then be fed back into the circuit model to provide improved predictions of currents and hence magnetic fields in the machine and ensure power consistency in the simulations.

3.2 Overview of existing simulation techniques

When a series of simulations are to be performed on SR machines, for example to select optimum excitation angles, tune controllers etc, it is far more efficient in terms of computational time to pre-characterise the electromagnetic behaviour of the machine using magneto-static finite element analysis and produce a series of look-up tables which capture the various attributes of the machine, rather than perform specific time-stepped finite element

simulations for each conditions studied. By performing a series of isolated magneto-static calculations for all inclusive combinations of prescribed current and rotor angular position increments, the full dependency of the coil flux-linkage, electromagnetic torque and localised flux densities on the current and rotor angular displacement can be captured in look up tables.

In order to greatly reduce the number of field calculations, the characterisation is performed for a single phase, which makes use of the fact that in SR machines the mutual coupling between phases in terms of coil flux-linkage is small compared to self inductance effects and can therefore be neglected to a reasonable approximation.

The flux linkage and torque is calculated for a single phase using a set of currents over a set of rotor angular positions from unaligned to aligned. The predicted values of flux linkage are stored in a ψ-i-θ table making use of interpolation functions to estimate intermediate values. This table can be then rearranged to derive a value of current from the flux linkage and angular position. The static torque predicted using a virtual displacement method within the finite element package employed for each combination of phase current and rotor angular displacement is stored in a T-i-θ look up table. The two look up tables, i.e. i in terms of ψ-θ and T in terms of i-θ, are then be used in a dynamic circuit simulation to determine the current and torque for a given applied voltage waveform. The equivalent circuit used in the dynamic simulation is shown in Figure 3.1, and the corresponding equation for flux-linkage is given by

$$\boldsymbol{\psi_{ph}} = \int \left(\boldsymbol{v_{ph}} - \boldsymbol{i_{ph}} \boldsymbol{R_{ph}}\right) \boldsymbol{dt} \tag{3.1}$$

The effective voltage across the coil is integrated to calculate the flux linkage and the corresponding current is read from the look up table. The current can be subsequently used to recalculate the voltage across the coil and hence the flux, essentially iterating around this loop until convergence within a prescribed tolerance is achieved. However in many cases, for higher power machines, the voltage drop across the coil resistance is small compared to the applied voltage and hence this iteration stage can be excluded if a small time step is used. It is important to note that this simplification still accounts for the resistive volts drop in the circuit equations using the first derived values of current, but does not perform repeated iterations.

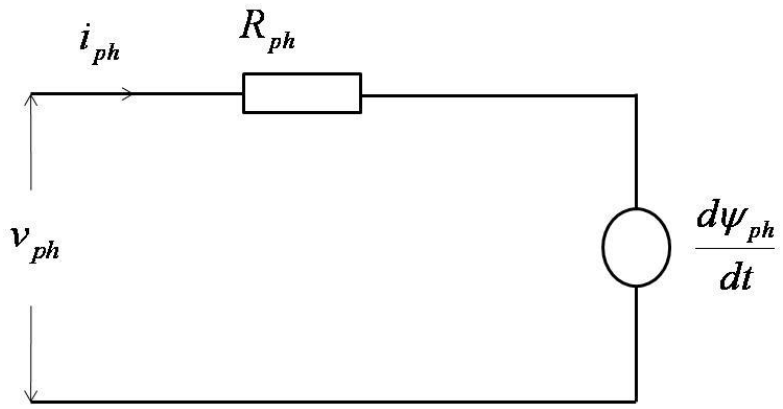

Figure 3.1 : Circuit diagram for dynamic simulations.

3.3 Representing core loss in circuit simulations

The inclusion of core loss in post-processing of simulations makes the dynamic circuit simulation inconsistent in power terms, as the core losses are not represented in the power flow in the model. In applications such as the high temperature machine considered in this thesis, the core losses are expected to be significant as a proportion of the overall dynamic power flow due to a combination of high speed, high pole number and the use of relatively lossy material grades due to reasons described in chapter 2. In a normal high-speed operating scheme in which the machine is supplied using pulses of a fixed DC voltage, if the same operating conditions are applied to the actual machine, the current drawn would be higher than predicted, whereas the power delivered to the converter in generation mode would fall short of the predicted value. In the case of core losses as high as 10% of rated power, such shortfalls may not be recoverable during commissioning by adjusting turn-on and turn-off angles, which in any case is achieved at the expense of a further increase in copper loss.

An increase in current due to core loss will impact on the predicted voltage drop across the coil resistance, in turn affecting the flux-linkage. This factor will be compounded in high temperature electrical machines because of the increase in coil resistance at elevated temperatures, e.g. the resistivity of copper is almost three times higher at 450^{o}C than at room temperature. Any underestimate of the current caused by neglecting core loss will also result in an underestimate of the copper losses, which could be significant in design terms as the margins between operating temperature and the limits imposed by materials are likely be fine.

Hence, for the particular combination of circumstances encountered in high-speed, high pole number and high temperature SR machines, integrating a dynamic core loss model into an FE based simulation of an electrical machine such that it more fully captures the various components of power flow, has the potential to improve the accuracy of performance predictions. However, as noted previously, such an approach poses several challenges, with arguably the greatest being the need to calculate instantaneous hysteresis loss.

FE based dynamic models which incorporate representations of core loss have been implemented and reported [8, 9] with the core loss represented as a component in the field equation using the equivalent elliptical loop approach[10]. In this method, the hysteresis characteristic of the core material is represented by equating the area within actual measured BH loops to an equivalent ellipse in the B-H plane whose extent is parameterised simply by the magnitude of the peak flux density. Once the extent of the ellipse is defined, its inherent geometrical form defines the accumulation of loss as it is traversed in the B-H plane. This method has been shown to be effective in describing instantaneous hysteresis loss for symmetrical centred BH loops with limited influence of minor loops. However, such methods have significant limitations in terms of predicting losses for highly distorted waveforms encountered in SR machines.

An analytical method described in [11] employs a ladder network to represent losses in different discrete layers within a lamination. The hysteresis loss in this case is represented by a nonlinear inductance in parallel with a resistance element which accounts for eddy currents. The multilayer lamination model has an added benefit that it can incorporate skin effect within a lamination, but cannot be easily incorporated in FE based models as it effectively requires a three dimensional lamination model. In this chapter, a Preisach based model is employed which is both capable of tracking hysteresis losses for any arbitrary waveform and can be employed in magneto-static time-stepped finite element simulation. An additional benefit of an instantaneous core loss model is its ability to provide detailed information regarding the distribution of losses over the cycle, which in principle, provides some insight on how machine geometry and control strategy can be optimised to minimise overall loss. Finally, since this approach to modelling ensures that the circuit is power consistent, which will assist in more reliable rating of drive circuit components.

3.4 Dynamic circuit model

As noted previously in section 3.2, there is little mutual coupling between phase windings in 3-phase SR machines with well-established stator and rotor tooth number combinations. By way of illustration, for the 12-8 SR machine designed in Chapter 5, the maximum and minimum values of phase self-inductances are 260μH and 44μH at low levels of excitation (i.e. below any meaningful level of saturation) whereas the maximum value of mutual inductance is only 8.1μH. Since each phase of an SR machine is driven from a separate full-bridge with a common coupling point of a reasonably stiff DC-link, it is usually adequate to model the electrical circuit behaviour and the variation in phase flux-linkage on a phase-by-phase basis using separate equivalent circuits for each phase. This approach remains valid even when current is flowing in more than one phase, which can occur for example either by deliberate overlap to minimise torque ripple or simply the dynamic behaviour at high speed in which the rise and fall time of current occurs over a significant angular displacement of the rotor.

Figure 3.2 shows the equivalent electrical circuit employed in the time-stepped simulation for one phase of a rotating electrical machine. The electrical resistance of the coil itself is represented by the fixed resistor R_{ph} although its resistance could be modified to reflect changes in coil temperature in a full electro-thermal simulation. The inductor L_{ext} represents any fixed values of inductance that reside outside the FE region, e.g. end winding inductance. The voltage source represents the FE model of the machine which generates a time-varying emf in response to a given combination of imposed current, rotor speed and rotor angular displacement. As the FE model captures the changing stored magnetic energy and the mechanical output power, it can act as a sink or source of power. This model of the field within the machine is lossless, with the core loss being represented by a separate circuit component, viz. the resistor $r_{loss.}$

During the solution of the governing field equations at each time step, the FE model employs an anhysteretic magnetisation curve to represent the magnetisation response of the core material. This provides a unique one-to-one mapping of flux density to magnetising field strength. Of the several possible means of establishing a single anhysteretic magnetisation curve a method based on horizontal averaging of a measured major B-H loop was adopted [12]. Hence, hysteresis is neglected in terms of predicting localised flux density variations in the core for a given combination of excitation currents, even though clearly hysteresis is a

factor that is considered in the subsequent loss calculation. Ultimately, it is entirely possible to include a hysteresis model into the finite element simulation, although this would be at the expense of a significant increase in the number of iterations required to solve the field and a greater number of time steps to remove start-up transients. Under dynamic conditions the eddy current effects also reduce the net permeability of the material and must be incorporated in the material model.

The core loss is represented in the electrical circuit by the variable resistor r_{loss} which is connected in parallel with the voltage source which represents the FE region. At each time-step, the value of the effective core loss resistance is re-calculated to ensure that the instantaneous loss in this resistance ($i_{loss}^2 r_{loss}$) is equal to the predicted core loss. The total power flow into the core at any instant is given by:

$$\boldsymbol{p_{core} = v_{coil}(i_{loss} + i_{an})} \tag{3.2}$$

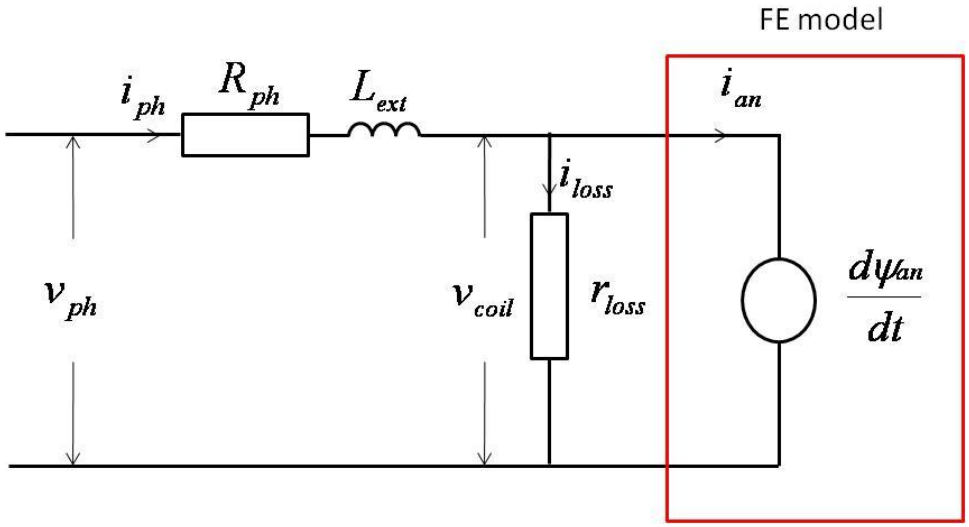

Figure 3.2: Equivalent circuit for a generic electromagnetic device supplied from a voltage source.

The instantaneous flux linkage of the machine coils are calculated using the anhysteretic BH curve for the material and hence is denoted as ψ_{an}. The current i_{an} can be calculated from the lossless flux linkage vs. current model in a similar manner to the SR machine model described in section 3.2. The loss current (i_{loss}) represents the additional

current drawn by the phase due to the instantaneous core loss in the machine. The flux linkage for the modified circuit is

$$\boldsymbol{\psi_{an}} = \int \boldsymbol{v_{coil}} \boldsymbol{dt} \tag{3.3}$$

where,

$$\boldsymbol{v_{coil}} = \boldsymbol{v_{ph}} - \boldsymbol{i_{ph}} \boldsymbol{R_{ph}} - \boldsymbol{L_{ext}} \frac{\boldsymbol{di_{ph}}}{\boldsymbol{dt}} \tag{3.4}$$

$$\boldsymbol{i_{ph}} = \boldsymbol{i_{loss}} + \boldsymbol{i_{an}} \tag{3.5}$$

Inspection of the circuit of Figure 3.2 and equations 3.3-3.5 suggests that iterations of the field and core loss calculations at each time step may be necessary to ensure circuit consistency since the voltage drop across the coil resistance and external inductance are dependent on the magnitude of the current drawn through r_{loss}. However, as explained earlier, the voltage drop associated with the coil resistance and external inductance is usually a very small proportion of the applied voltage and hence there is often little merit in undertaking such iterations. This said there is nothing inherent in the modelling approach adopted which would preclude iteration.

The circuit model of Figure 3.2 is a per-phase model and hence only represents the behaviour a single phase of a machine. Whereas this phase-by-phase approach can accommodate currents flowing in more than one phase at any given instant from the point of view of flux-linkage, when it comes to core loss, isolated consideration of each phase is more problematic. Despite the low mutual coupling between coils, some regions of the stator core, notably the back-iron, can have net flux densities with significant contributions from more than one phase. Since core loss is not linearly proportional to flux density, simple superposition cannot be readily applied. This poses a problem in that although the overall core loss can be derived from a combined finite element/loss model, it needs to be apportioned to individual equivalent circuits.

In a case where the currents in successive phases do no overlap, the current I_{loss} assigned to the conducting phase would correspond to the total machine loss. For cases of overlapping currents, the ratio of the flux linkages in the individual phases can be used as a

proxy measure to disaggregate the overall loss into individual phase losses. It is recognised that this involves some degree of approximation for regions of the stator and/or rotor cores with common flux paths, but it nevertheless provides a reasonable reflection of the likely contributions of different phases to the fluxing of the core.

3.5 Circuit implementation

Figure 3.3 shows a flowchart of the circuit simulation. The voltage v_{coil} can be calculated from the voltage v_{ph} which is derived from the state of the switching circuit and the current i_{ph} from the previous time step. Integrating v_{coil} gives the flux linkage ψ_{an} which in turn allows i_{an} to be estimated from a look table. The currents from all the machine phases are used as input to a two-dimensional finite element model, which calculates the flux density distribution throughout the core using the anhysteretic BH curve. This localised distribution of flux density along with the corresponding flux density distribution from the preceding time step provide the input required for the core loss model which has been developed and which is described in detail in section 3.6.

This loss model calculates the instantaneous core loss, p_{loss} for the entire machine. The core loss for each phase is then calculated using the ratio of flux linkages. The core loss current i_{loss} is then calculated from the phase core loss and voltage across the coil. The values of $i_{ph}$and v_{coil} are recalculated and the procedure is repeated until convergence within a prescribed tolerance is achieved. The disadvantage with this method is that for every time step several iterations may be required each with a finite element solution which can increase the solution times considerably. As mentioned before, in most cases, the voltage drop across the resistance R_{ph} and L_{ext} are relatively small compared to the applied voltages, and hence the iterative loop can be avoided and the total current from the previous step can be used to calculate the voltage for the next step. In this method the core loss current lags the voltage by one time step, and as a result smaller time steps are required to minimise error.

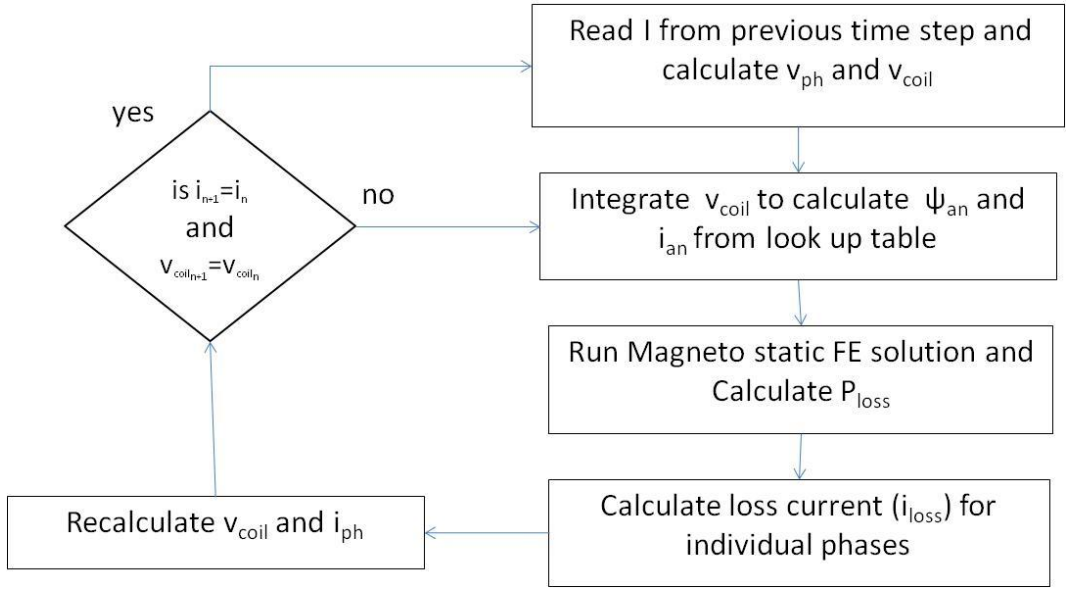

Figure 3.3: Flow chart of circuit simulation.

3.6 Core loss modelling

3.6.1 Introduction to core loss modelling

All soft magnetic materials exhibit core losses when subjected to time varying magnetic fields. The losses are generally a non-linear function of the magnitude and frequency of the imposed flux density. The Stienmetz equation is a straightforward and commonly used method for estimating core losses for the particular case of sinusoidal excitation. It employs a frequency domain approach in which an exponential curve fit is used to measured sinusoidal loss data.

$$\boldsymbol{P_{st} = C\mathrm{B_p^a f^b}} \tag{3.6}$$

The values of the material-specific constants C, a and b are those that best fit a set of loss measurements taken with sinusoidal excitations on test samples. Whereas the Steinmetz method has proved to be a useful approach in cases with well-defined sinusoidal excitation with low harmonic content, e.g. AC utility and power supply transformers, it is less suitable for the flux conditions that are encountered in SR machines. Figure 3.4 shows a typical series of flux waveforms in the different regions of a SR machine calculated by finite element analysis under single pulse operation. The waveforms in the stator teeth are uni-polar and are indicative of significant magnetic saturation, whereas the stator and rotor back iron contain

significant minor loops which are in some areas DC biased. In addition to these bulk regions, there are localised areas of very high saturation on the edges of tooth tips and rotational flux excursions in some areas.

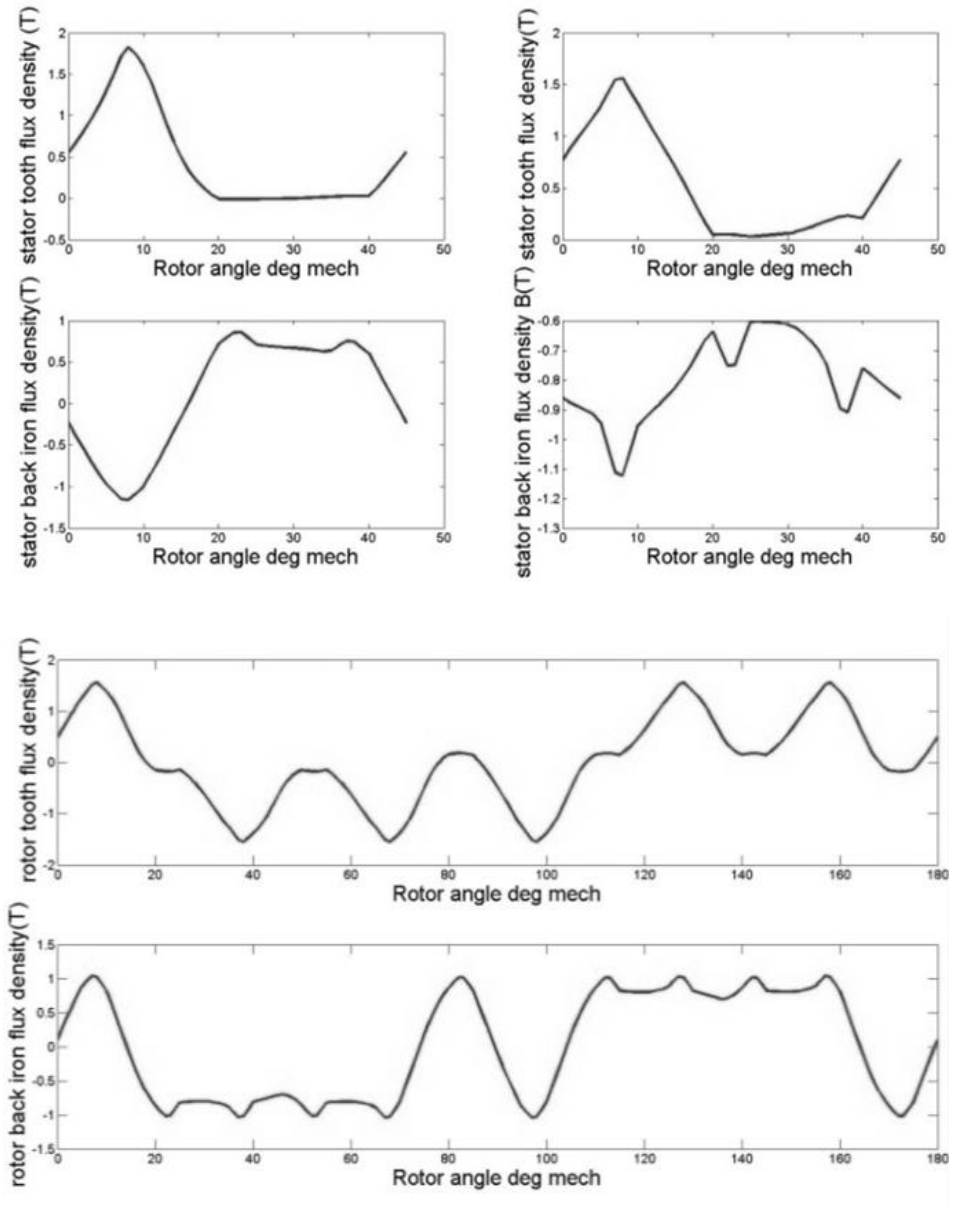

Figure 3.4: Typical flux density waveforms in SR machines calculated under single pulse operation using FE analysis.

Hence, in order to reliably calculate core losses in SR machines, it is necessary to employ a model that can accommodate essentially arbitrary flux density excursions rather than being limited to some sub-set of waveforms. The most widely used methods of core loss

estimation in electrical machines, and which can handle arbitrary flux density waveforms, are based on loss separation techniques which has been developed and championed by Bertotti[13]. In this method, the total core loss is considered to be the summation of three distinct components, viz. classical eddy current loss, hysteresis loss and excess loss.

$$\boldsymbol{P_{total} = P_{cl} + P_h + P_{exc}}$$

(3.7)

The underlying basis of the loss separation technique comes from the solution of Poyntings equation, which is a widely used general expression of the law of conservation of energy in magnetic fields, and is useful for describing power flow in many different applications.

$$-\oint_{s} (\boldsymbol{E} \times \boldsymbol{H}).\boldsymbol{ds} = \oint_{v} \boldsymbol{H}\frac{\boldsymbol{dB}}{\boldsymbol{dt}}\boldsymbol{dv} + \frac{\mathbf{1}}{\boldsymbol{\sigma}}\oint_{v} |\boldsymbol{J}|^2\,\boldsymbol{dv}$$

(3.8)

The left hand side term is referred to as the Pointing vector and describes the total energy through surface *s* per unit time. The terms of the right hand side of equation 3.8 describe how energy is stored or dissipated. When applied to the problem of core loss, the second term on the right side represents integral of joule losses produced by the eddy currents induced in the core due to a time varying flux. The main component of these losses is known as classical eddy current loss and can be calculated if the distribution of the induced current density across the core cross section is known, assuming the material is perfectly homogeneous. The instantaneous classical eddy current loss is given by:

$$\boldsymbol{P_{cl}} = \frac{\boldsymbol{\sigma d^2}}{\mathbf{12}}\left(\frac{\boldsymbol{dB}}{\boldsymbol{dt}}\right)^{\mathbf{2}}$$

(3.9)

The first term on the right side in equation 3.8 describes the energy stored in the magnetic field. The stored energy has reversible and irreversible components, the latter of which corresponds to the hysteresis loss. The hysteresis component is effectively a frictional type loss in the magnetisation process which is understood to be caused by so-called Barkhausen jumps. These Barkhausen jumps occur as magnetic domains reverse polarities and have typical time scales that are very short (typically of the order of a microsecond). Relative to frequency ranges encountered in electrical machines, these Barkhausen jumps can

be regarded as being instantaneous and hence the hysteresis power loss generated by a given number of Barkhausen jumps can be reasonably assumed to be linearly proportional to frequency[14].

The loss per cycle is typically calculated from the area within the static hysteresis loop which is traced by the variations in B and H. The form of hysteresis loops varies a great deal depending on the nature of the excitation, with minor loops caused by inflections in the variations of B and the influence of DC bias being particularly challenging. Many curve fitting techniques have been proposed and implemented using methods such as [15], in which the total loss from a set of minor loops are expressed as a function of their average peak flux density. Calverley [16] suggested using the ratio of the area enclosed by the different regions of the BH loop to the overall loop to calculate the losses due to the minor loops in those specific regions. These techniques have several limitations such as, the method described in [15] is only applicable for smooth harmonics with peak flux densities in the range of 1-2T. As these techniques use exponential curves to fit hysteresis loss, they are also poor at predicting loss when significant magnetic saturation is present. The equivalent elliptical loop method[10] is derived using curve fitting formulae and thus has similar limitations. Mathematical models such as Preisach or the Jiles-Atherton are better at predicting minor loops, and are becoming more commonly employed in finite element analysis[17]. In the model adopted in this thesis, the Jiles-Atherton model was not used as it is parameter intensive, requiring a great deal of material specific measurements. A Preisach type model was preferred as it allowed calculation of instantaneous hysteresis losses for arbitrary waveforms with a reduced reliance on material characterisation.

The third component of core loss in equation 3.7 is the less understood term, which is known as excess or anomalous loss. This component of loss is introduced in an attempt to cater for the inhomogeneity within the magnetic material caused by the presence of discrete magnetic domains. The movement of magnetic domains caused by changes in the applied field cause additional eddy current losses to be increased locally around the domain walls. Bertotti[13] argued that excess losses can be predicted by separating the classical eddy current losses as the average losses in a homogeneous material and the loss due to eddy current concentration on domain walls as excess loss. These losses were observed to broadly increase with a power of 1.5 type relationship with the rate of change of flux density. The instantaneous excess loss predicted by the Bertotti model is

$$P_{exc} = \sqrt{\sigma k_{exc}} \left(\frac{dB}{dt}\right)^{1.5}$$

(3.10)

The value of the co-efficient k_{exc} is an aggregation of constants related to the material cross sectional area and distribution of domains in the material. The numerical value adopted for k_{exc} for a given material grade if established by curve fitting measured loss data rather than by calculation from first principles.

3.6.2 Instantaneous hysteresis loss

The finite element model uses an anhysteretic BH curve to solve the governing field equations in the core; i.e. hysteresis is neglected in terms of predicting localised flux densities in the core for a given combination of excitation currents. As the FE solution outputs flux density, a modified Preisach model is used to calculate the hysteretic field H_{hyst} from the FE predicted flux density. The losses over a cycle are typically calculated as a function of the area traversed by the predicted hysteretic $B.H_{hyst}$ curve.

$$P_h = \int_0^T H_{hyst} \frac{dB}{dt} dt$$

(3.11)

The standard Preisach model is built on the notion of a number of parallel discrete hysteretic switches as shown in Figure 3.5 each with an upper (α) and lower (β) switching point. The distribution of the switches are defined on a two dimensional plane with the upper and lower switching points as its axis, by a probability distribution function $\mu(\alpha, \beta)$ known as the Preisach distribution function (PDF). The PDF essentially describes the number of switching domains per unit volume as a function of an increasing and decreasing magnetic field. The magnetisation at any time during the excursion can be calculated using the PDF as

$$M(t) = -\iint_T \mu(\alpha, \beta) d\alpha d\beta + 2 \iint_{s^+} \mu(\alpha, \beta) d\alpha d\beta$$

(3.12)

Figure 3.6 shows the plane over which the PDF is defined. From Figure 3.5 it is evident that $\alpha > \beta$, and the upper and lower limits are given by the applied field at which the

material gets saturated H_{sat}. Once the material is saturated, all the domains are oriented in the same direction and the incremental relative permeability of the material reduces to unity. Hence, no hysteresis losses are incurred beyond saturation and the material is effectively linear under quasi-static conditions. The region S+ is defined by the history of flux reversals in the magnetising field where every edge on the dotted line is defined by a flux reversal. An important feature of the Preisach model is the wiping out rule, which deletes stored reversal points when a larger magnitude of field is applied.

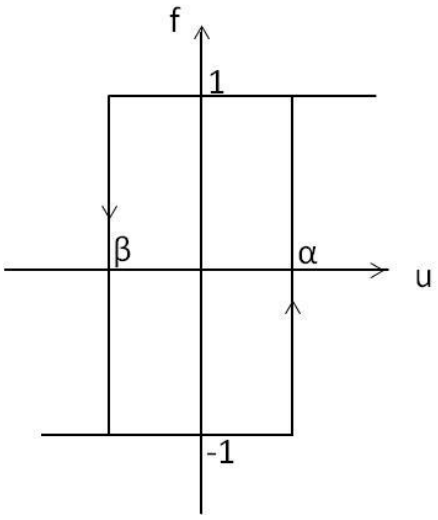

Figure 3.5: Rectangular unit hysteresis switch.

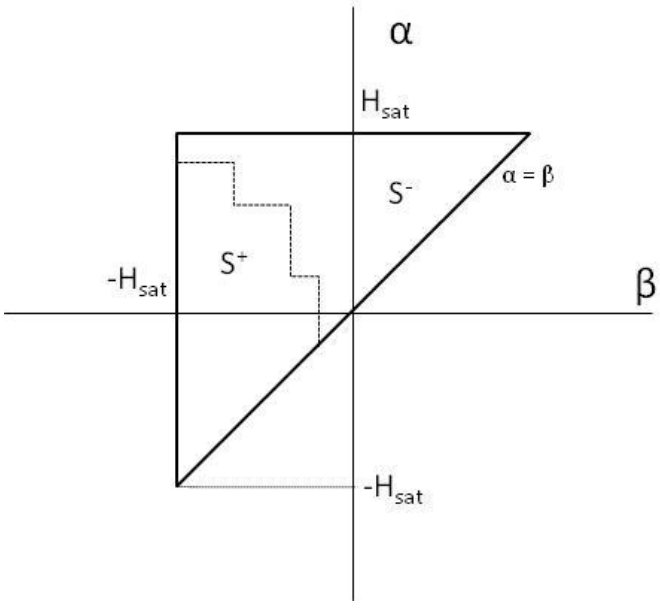

Figure 3.6: Triangle over which the Preisach model is defined.

Numerical implementation of the Preisach model using the PDF in eq. 3.12 is a computationally intensive process as it requires evaluating double integrals. In addition determining the PDF requires double differentiation of first order reversal curves. The more common implementation uses Everett integrals, which implements the double integrals of the PDF to calculate the magnetisation directly.

The Everett integral is defined as

$$\boldsymbol{T(\alpha', \beta') = \iint_{T(\alpha',\beta')} \mu(\alpha,\beta) d\alpha d\beta}$$

(3.13)

From the Everett integral the value of the flux density can be calculated as

$$\boldsymbol{B(H) = B(H_m) \pm 2T(H, H_m)}$$

(3.14)

Where, H_m is the applied field at the last reversal point and, $T(H,H_m)$ is the solution of the Everett integral for the excursion from H_m to H. The Preisach model requires an initial condition which can be assumed to be either ±saturation or alternatively as from an unmagnetised state at the origin of the B-H plane, in which case the flux density relationship for the flux density of the initial transient is

$$\boldsymbol{B(H) = T(H, -H)} \quad \textbf{for B > 0} \quad \textbf{or,}$$

$$\boldsymbol{B(H) = -T(-H, H)} \quad \textbf{for B < 0} \qquad \textbf{(3.15)}$$

A technique which draws on the method described by Mayergoyz[18] has been implemented to calculate the corresponding instantaneous hysteresis loss associated with each time-step of the simulation. The method is based around the assumption that a certain amount of loss can be associated with every switching transient in the Preisach model. The loss in any H excursion, however small, is given from a summation of the losses due to all the switches within that excursion. Consider the switching element in Figure 3.5, in which the loss incurred by the element is the area of the loop which is $2(\alpha - \beta)$. No losses are incurred in the horizontal parts of the loop as these are reversible. Therefore all the losses occur in the upward and downward transitions. If these are assumed to be equal, the loss in each transition

is $(\alpha - \beta)$. Using this as the basis, the energy loss within the region S+ due to an arbitrary waveform was calculated as

$$\boldsymbol{Q = \iint_{s+} \mu(\alpha,\beta)(\alpha-\beta)d\alpha d\beta}$$

(3.16)

The energy lost in an excursion from any reversal point *a* to a subsequent point *b*, *Q(a,b)* is calculated as:

$$\boldsymbol{Q(a,b) = (b-a)T(b,a) - \int_a^b T(b,\beta)d\beta - \int_a^b T(\alpha,a)d\alpha}$$

(3.17)

This equation requires the calculation of two line integrals every time step which incurs a penalty on the computational requirements of the model. The total number of switching transients in the upward and downward curve is the same, and hence the total losses are the same. The advantage of this method is that it can be used for any arbitrary waveform, and does not depend on the waveform being periodic which may be beneficial in predicting core loss during start up transients.

The essence of the method implemented is illustrated in Figure 3.7, which shows an arbitrary time variation in the magnetic field strength alongside the corresponding excursion on the Preisach probability α, β plane. Consider the excursion from point m_4 onwards, in which the localised region of the core under consideration has been exposed to previous peaks identified as m_1 m_2 and m_3. In the first time step after point m_4, the energy dissipated during the time step, which in turn determines the average power over the time-step, is derived from the shaded area identified in zoomed region 1 (ZR1). This process repeats itself on subsequent time steps past point b up until point m_3 is reached. For the next time step around point *c*, it is necessary to account for the 'wiping-out' of the influence of points m_3 and m_4. Hence, the energy dissipated in the next time step is derived from the shaded area shown in part in zoomed regions 2(ZR2). As will be evident, since the time-step straddles point *c*, it is necessary to account for the increase in area on the α, β plane part-way through the time step, as shown in zoomed region 3(ZR3).

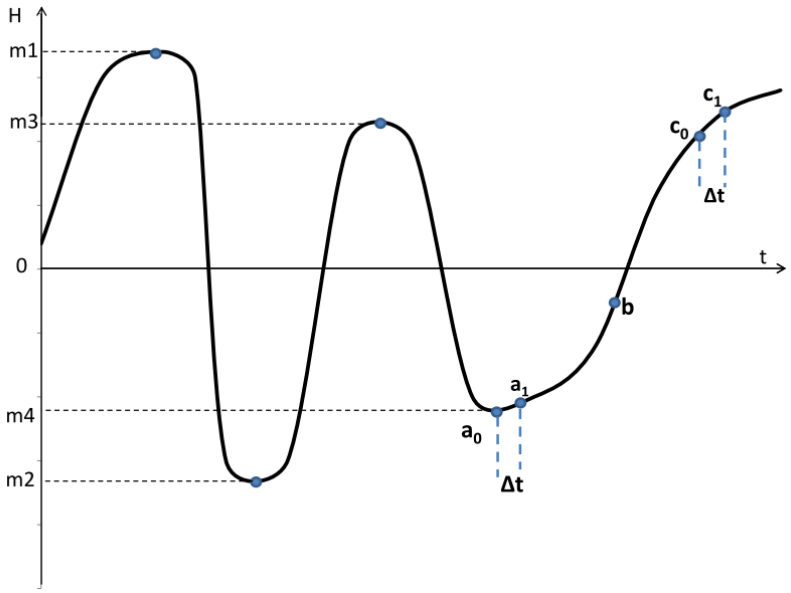

(a)

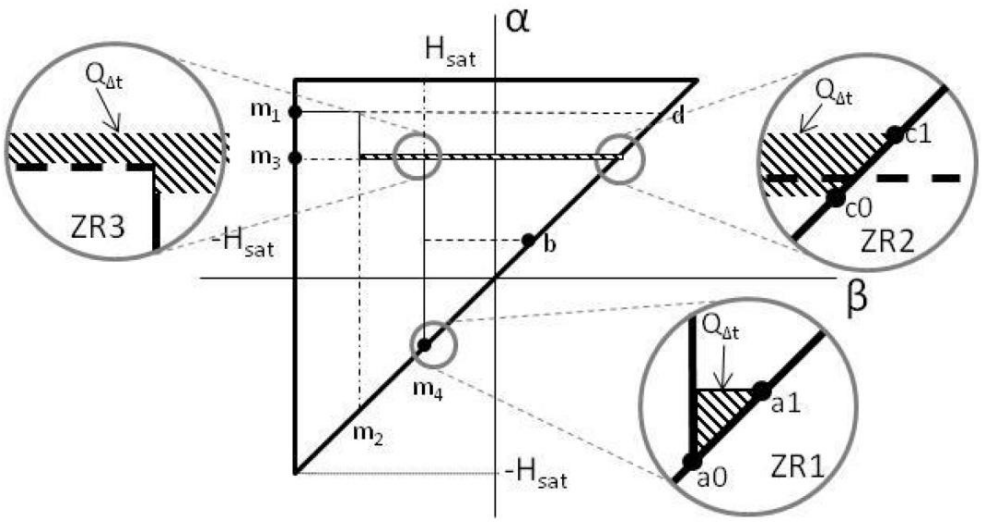

(b)

Figure 3.7: (a) Typical magnetisation curve. (b) Implementation on Preisach plane.

Figure 3.8 shows the predicted instantaneous loss for a Co-Fe grade Vacodur S+, for a sinusoidal flux density excursion with a peak flux density of 2 T i.e. a value for which there is a degree of magnetic saturation and hence appreciable non-linearity in the response of the core. As the core loss model assumes a symmetrical BH loop, it has an equal distribution of losses in the upward and downward flux density trajectories. As would be expected, the maximum value of instantaneous loss occurs when dB/dH is a maximum. This is because

the number of domains switching orientation are higher in this region. As the core begins to saturate, all the domains are oriented in the direction of magnetisation, and hence the loss reduces towards zero. The initial start-up transient in the model, which is evident in the first cycle or so of Figure 3.8. is a consequence of the need for the Preisach model to establish and update the reversal points, as the initial conditions are unknown and set at (0,0) in the α, β plane. Figure 3.9 shows the results for a sine wave flux density with a 50% third and 25% fifth harmonic. It should be noted that this waveform is similar to the flux excursions in the rotor back iron of a SR machine shown in Figure 3.4.

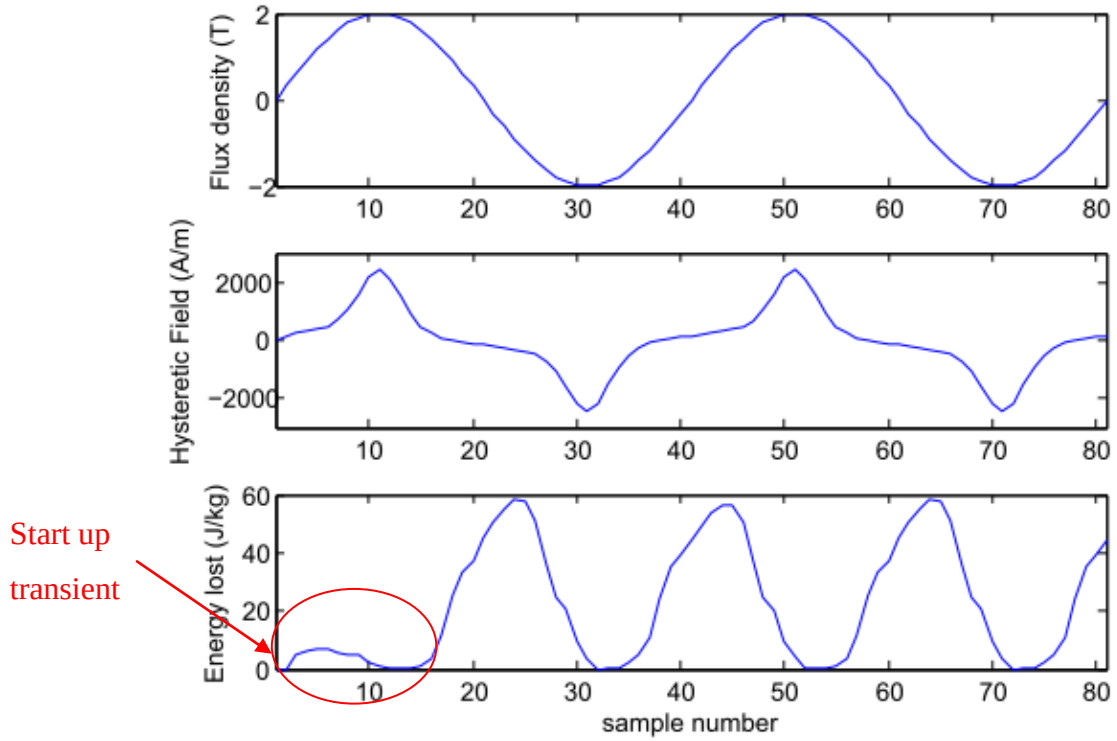

Figure 3.8: Predicted instantaneous hysteresis loss for a sinusoidal flux density waveform for a Vacodur S+ Co-Fe grade.

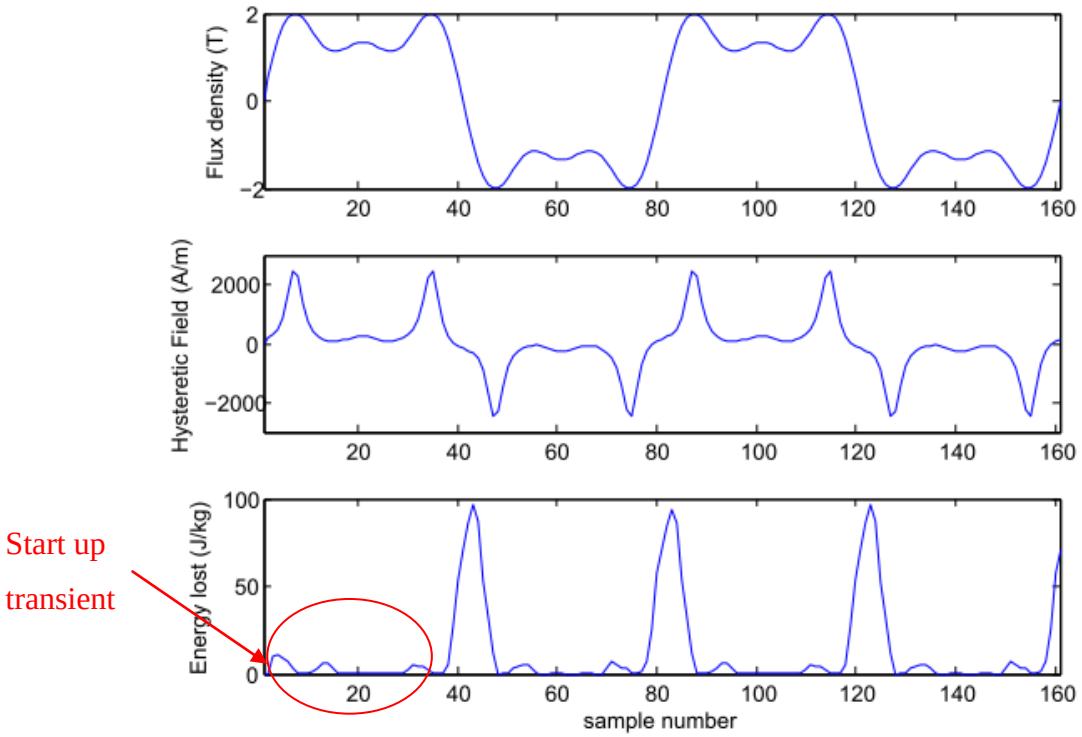

Figure 3.9: Predicted instantaneous hysteresis loss for flux density excursion with minor loops generated by third and fifth harmonic for a Vacodur S+ Co-Fe grade.

3.7 Summary

This chapter has described the development of a methodology which can be used to predict instantaneous core loss in a manner which makes is suitable for integration into a dynamic machine simulation. The overall core loss is predicted from a summation of the losses from an instantaneous hysteresis model whose elements have been selected and/or developed to cater for the specific conditions encountered in SR machine with well-established instantaneous eddy current and excess loss models. A detailed experimental validation of this methodology is described in chapter 4.

This methodology for predicting core loss has several advantages over the more established methods reviewed in section 3.6. Firstly, the distribution of loss over a given flux density excursion is based on material specific behaviour with a sound physical underpinning, as distinct from the convenient but rather generic elliptical representation of [10]. Secondly, it provides an improved representation of DC biased loops and minor loops because of the use of the Preisach model. Finally, it is a truly instantaneous model that is not reliant on periodicity, and hence could be used for predicting losses in machine start up

transients and in machines with a PWM voltage supplies in which there is no synchronisation between the fundamental and carrier frequency.

This methodology has two main drawbacks. Firstly, the time required for solving the model is much higher than a core loss calculation based on post-processing of a series of field solutions since model requires two line integrals for every finite element in each and every time step. Secondly, a larger data set is required to characterise the core of material, especially for the hysteresis and excess loss components. A method to simplify such measurements is described in Chapter 4.

References

[1] S. D. Calverley, G. W. Jewell, and R. J. Saunders, "Prediction and measurement of core losses in a high-speed switched-reluctance machine," *IEEE Transactions on Magnetics,* vol. 41, pp. 4288-4298, Nov 2005.

[2] M. Amar and R. Kaczmarek, "A General Formula for Prediction of Iron Losses under Nonsinusoidal Voltage Wave-Form," *IEEE Transactions on Magnetics,* vol. 31, pp. 2504-2509, Sep 1995.

[3] D. M. Ionel, M. Popescu, M. I. McGilp, T. J. E. Miller, S. J. Dellinger, and R. J. Heideman, "Computation of Core Losses in Electrical Machines Using Improved Models for Laminated Steel," *Industry Applications, IEEE Transactions on,* vol. 43, pp. 1554-1564, 2007.

[4] Y. Hayashi and T. J. E. Miller, "A New Approach to Calculating Core Losses in the Srm," *Ieee Transactions on Industry Applications,* vol. 31, pp. 1039-1046, Sep-Oct 1995.

[5] K. Nakamura, S. Fujio, and O. Ichinokura, "A Method for Calculating Iron Loss of an SR Motor Based on Reluctance Network Analysis and Comparison of Symmetric and Asymmetric Excitation," *Magnetics, IEEE Transactions on,* vol. 42, pp. 3440-3442, 2006.

[6] J. J. C. Gyselinck, L. R. L. Dupre, L. Vandevelde, and J. A. A. Melkebeek, "Calculation of no-load induction motor core losses using the rate-dependent Preisach model," *Magnetics, IEEE Transactions on,* vol. 34, pp. 3876-3881, 1998.

[7] A. Boglietti, A. Cavagnino, M. Lazzari, and M. Pastorelli, "Predicting iron losses in soft magnetic materials with arbitrary voltage supply: an engineering approach," *Magnetics, IEEE Transactions on,* vol. 39, pp. 981-989, 2003.

[8] H. Lin, T. S. Low, and S. X. Chen, "Investigation on magnetic saturation in switched reluctance motor using 2D hybrid finite element method," *IEEE Transactions on Magnetics,* vol. 32, pp. 4317-4319, Sep 1996.

[9] A. Belahcen and A. Arkkio, "Comprehensive dynamic loss model of electrical steel applied to FE simulation of electrical machines," *IEEE Transactions on Magnetics,* vol. 44, pp. 886-889, Jun 2008.

[10] D. Lin, P. Zhou, W. N. Fu, Z. Badics, and Z. J. Cendes, "A dynamic core loss model for soft ferromagnetic and power ferrite materials in transient finite element analysis," *IEEE Transactions on Magnetics,* vol. 40, pp. 1318-1321, Mar 2004.

[11] J. T. Charton, J. Corda, J. M. Stephenson, and S. P. Randall, "Dynamic modelling of switched reluctance machines with iron losses and phase interactions," *Iee Proceedings-Electric Power Applications,* vol. 153, pp. 327-336, May 2006.

[12] G. M. Shane and S. D. Sudhoff, "Refinements in Anhysteretic Characterization and Permeability Modeling," *Ieee Transactions on Magnetics,* vol. 46, pp. 3834-3843, Nov 2010.

[13] G. Bertotti, Hysteresis in magnetism : for physicists, materials scientists, and engineers. San Diego, Calif. ; London: Academic Press, 1998.

[14] K. Atallah, "Iron losses in brushless permanant magnet dc machines," PhD., Electronic and Electrical Engineering, University of Sheffield, Sheffield, 1993.

[15] J. D. Lavers, P. P. Biringer, and H. Hollitscher, "Simple Method of Estimating Minor Loop Hysteresis Loss in Thin Laminations," *Ieee Transactions on Magnetics,* vol. 14, pp. 386-388, 1978.

[16] S. D. Calverley, "Design of a HIgh Speed Switched Reluctance Machine for Automotive Turbo-Generator Applications," PhD, Department of Electronic and Electrical Engineering, University of Sheffield, Sheffield, 2001.

[17] M. Pasquale, G. Bertotti, D. C. Jiles, and Y. Bi, "Application of the Preisach and Jiles-Atherton models to the simulation of hysteresis in soft magnetic alloys," *Journal of Applied Physics,* vol. 85, pp. 4373-4375, Apr 15 1999.

[18] I. D. Mayergoyz, *Mathematical models of hysteresis*: Springer, 1991.

Chapter 4 : Characterisation of materials for core loss estimation

4.1 Introduction

The accurate prediction of core loss in electrical machines is reliant on extensive and precise characterisation of test samples of the core material in order to establish the various material specific constants and parameters. The datasheets produced by manufacturers tend to provide useful, but rather limited, data on core loss. This usually comprises average loss at a few standard combinations of sinusoidal frequencies and peak flux densities, invariably being limited to measurement performed at room temperature. In many cases, the complexity of a core loss model which is deployed can be limited by the availability of data from which to estimate the parameters for the loss models. As the complexity of loss models increase, the data required for characterisation exceeds that available from manufacturer datasheets.

For the model described in chapter 3 which is capable of estimating instantaneous core loss, extensive characterisation over wide range of flux densities, excitation frequencies and temperatures was required. The literature review in chapter 2 demonstrated that although a significant amount of published data exists on the three Co-Fe grades manufactured by Carpenter Technology, these could only be used to fit parameters for a standard frequency domain loss model at best. Although the published core loss data on 5000 hour aged samples measurements at temperatures [1] were useful in terms of selecting the preferred material grade, due to the absence of any applicable hysteresis loss measurements, these could not be accurately fit to the loss separation model. In addition the loss model proposed in chapter 3 necessitated a measured set of static BH loops in order to characterise the Preisach hysteresis model. The material ultimately selected for the machine was the Vacodur S+ grade manufactured by VAC which underwent different heat treatments for the rotor and stator. The heat treated materials exhibit different loss characteristics, the data for which does not exist in published literature.

This chapter describes a method to characterise the materials for the proposed loss model in chapter 3 using a simplified test setup. The measurements for characterising the

material were collected at temperatures up to 400°C and for 2000 hours of thermal ageing at 400°C. The established method for characterising materials involves curve fitting loss model parameters for sinusoidal flux density measurements. Inducing sinusoidal flux density waveforms in magnetic material samples requires a closed loop test system in order to contend with the non-linearity in the BH loop. The standard techniques developed for measuring losses such as [2, 3] employ proportional feedback control using a difference amplifier. The main setback of the analog method was that if the gain of the proportional control was high then the system risked turning unstable. The recent drive towards using digital control has improved the quality and bandwidth of measurements that can be achieved significantly. These methods typically use iterative closed loop feedback control techniques giving quick convergence while reducing the risk of oscillations[4]. An alternative option is to use iterative open loop methods [5], which use point by point correction on successive cycle's offline make the process of digital control easier, however they require multiple iterations to converge especially at higher frequencies. The loss model proposed in chapter 3 is capable of predicting losses for arbitrary waveforms. The method used to characterise materials for the loss model takes advantage of this facet by using a set of arbitrary (non-sinusoidal) waveforms to calculate the material parameters, and in turn avoiding the need to use the feedback mechanisms that complicate the measurement process.

4.2 Measurements required for characterising materials

The loss model described in chapter 3 uses a loss separation technique, and is based on arriving at the total losses by the summation of three constituent components, viz. classical eddy current loss, excess loss and hysteresis loss [6].

$$\boldsymbol{P_{total} = P_{cl} + P_{exc} + P_h} \tag{4.1}$$

The most straightforward of the material specific coefficients to establish are those required for classical eddy current losses, viz. the core material electrical conductivity (σ) and the individual lamination thickness (d). Room temperature values of electrical conductivity are readily found in manufacturer's datasheets, although the information is rarely available at elevated temperatures and hence must be measured from appropriate material samples. A typical coefficient of thermal expansion for Co-Fe is 10.1×10^{-6} per°C,

and hence a temperature rise of 400°C would only cause a change in lamination thickness of 0.4%. This change can be neglected in comparison with the many other temperature dependencies of core loss.

The Preisach model adopted is reliant on establishing the material specific Everett function, which in this case requires measurements of a set of quasi-static BH loops varying in magnitude as described in section 4.5. The very low frequency excitation used (typically 1Hz) means that the measured current and search coil emf loops are dominated by the hysteresis loss and hence the hysteresis parameters can be derived in isolation from any of the other loss coefficients.

The prediction of excess loss requires a material specific excess loss parameter k_{exc}. The value of this parameter is a function of micro-structural features of the material, notably behaviour around the grain boundaries, and as such is very difficult to quantify on a priori basis from measured material properties. Indeed, there is no recognisable experimental method for measuring this component in isolation. In practice, k_{exc} is usually established from the difference between the total measured loss and the classical eddy current and hysteresis loss predictions, i.e. $P_{exc} = (P_{total} - P_{cl} - P_h)$. This procedure is performed for a series of AC loss measurements spanning a range of flux densities and frequencies[6]. The main drawback of this approach is that the k_{exc} parameters are not derived from any physical basis but simply end up providing the best fit between the total loss and those components that can be predicted. Hence, any errors in the classical eddy current and hysteresis losses models, either in the derivation of the material coefficient or their assumed variation with frequency will give rise to variations in the value of k_{exc}. This problem is compounded in this grade of material, since the high hysteresis losses means that that the value of P_{exc} can be as low as 5-10% of the total loss, and hence any errors in P_{cl} and P_h, which account for the remaining 90% can produce a large variation in prediction of k_{exc}.

In the model adopted in this study, the value of both P_{cl} and P_{exc} are based on the actual instantaneous time derivative and P_h can be predicted for arbitrary waveforms. Hence, unlike some simplified loss separation models which are based on frequency domain data, the measurements performed to derive the material specific parameter need not be necessarily sinusoidal. Hence a set of AC measurements with non-sinusoidal waveforms can be used to estimate k_{exc}. In summary, in order to characterise any material at a given operating temperature for the proposed loss model, the following measurements are required:

- A series of static hysteresis loops centred about the origin.
- AC loss measurements for a set of arbitrary waveforms ranging in peak flux densities and cycle frequencies.
- Bulk electrical conductivity of the material if insufficient data is provided by the manufacturer.

4.3 Measurement technique

The apparatus employed for measuring the core loss in the test sample is shown schematically in Figure 4.1. The test sample is equipped with a search coil which is wound tightly around the core material and a drive coil which is wound on top of the search coil. The drive coil is supplied by a high-bandwidth 100V linear power amplifier, specifically a Techron 7570 which has a power bandwidth of 20 kHz. Since the methodology employed to extract the material specific constants is not reliant on achieving precise sinusoidal flux density waveforms, the control system which drives the power amplifier is rather straightforward in comparison with the closed-loop systems that are used to ensure sinusoidal flux density variations for frequency domain model characterisation. A series of sinusoidal current demands with varying peak magnitudes and cycle frequencies is generated using a waveform generator, and fed to the amplifier in constant current mode. The output current of the amplifier is measured as the actual drive current, which may differ from the current demand depending on the bandwidth and precision of the internal loop of the amplifier. At higher current demands and frequencies, the internal loop of the amplifier tends to give rise to oscillations. The instantaneous loss is calculated from the product of the measured primary current and secondary (search coil) voltage scaled by the appropriate turns ratio. A Voltech PM3000 digital wattmeter was used to supplement the measurements for order of magnitude checking of the loss per cycle. In addition a Magnet Physik EF14 integrating flux meter was used to read the flux directly from the search coil for the static hysteresis loop measurements.

Two toroidal test-pieces consisting of 80 laminations of 0.15 mm thick Vacodur S+ Co-Fe were prepared in accordance with dimensions specified in the ASTM A927 standard[7]. Each annular ring lamination is 0.15mm thick and has inner and outer diameters of 82mm and 90mm respectively. The diameter ratio of 0.91 reduces the variation in flux density across the sample width. In one test-piece, the Co-Fe was heat treated at 730°C to attain desired mechanical properties giving room temperature yield strengths of 620MPa

sample. The second sample was heat treated at 830°C for optimal magnetic properties and had room temperature yield strengths of 390MPa. Although all the measurements mentioned were carried out on both the samples (referred to as the 390MPa and 620MPa sample), in some cases, only the 390MPa sample results are presented in detail in the following sections of this chapter to reduce repetition.

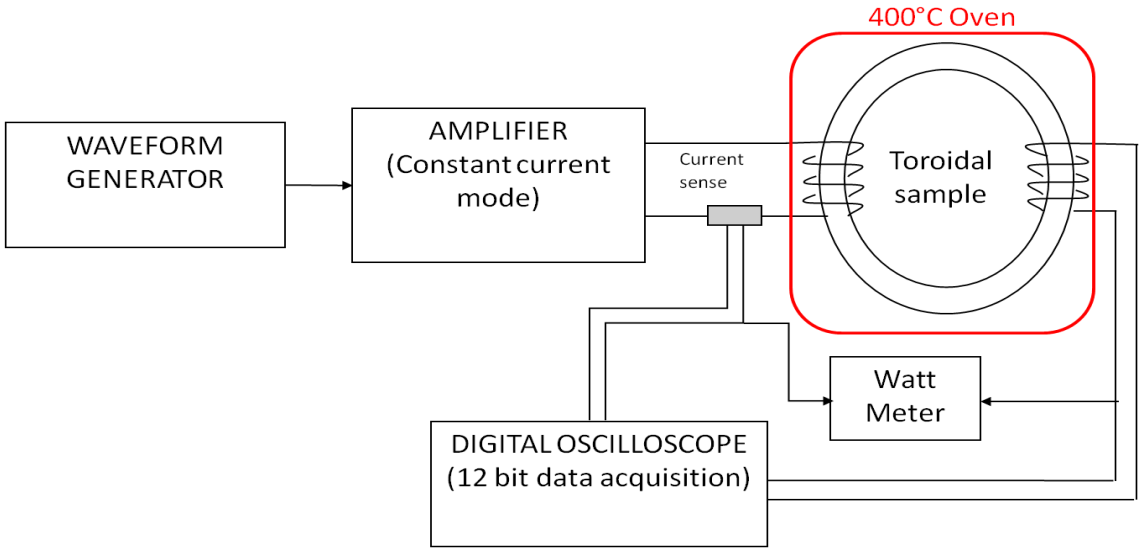

Figure 4.1: Experimental set up used for core loss measurements.

The stack of Co-Fe laminations was wrapped with a ceramic woven high temperature tape (0.8mm Cotronics 395) and wound with a 65 turn close-fitting search coil using 1mm diameter Cerafil 500 ceramic high temperature wire. The search-coil was then covered with a further layer of high temperature tape and then a double layered, toroidal drive coil was wound onto the test piece using Von-Roll SK650 1mm diameter high temperature wire. The first and last few of turns and leads of the coils were covered with a glass fibre sheathing to provide added protection at the entry and exits points. The prepared samples were placed in a Carbolite high temperature oven capable of temperatures up to 700°C as shown in Figure 4.2.

Due to the thickness of the Cotronics 395 tape, the sense coil is somewhat distant from the core, at least in comparison to normal arrangements for room temperature, where a very thin Kapton tape is used. Hence, it will sense some so-called 'air-flux', particularly if the saturation levels in the material are high. Air flux compensation tends to be a more significant matter in test methods such as the Epstein frame or single sheet tester where the thickness of the coils is much larger than the core sample. In these types of measurement systems, a common technique is to employ a mutual inductor to subtract any output when the specimen

is not present in the core. For the case of the ring specimens used in this study, a relatively simple compensation for air flux can be employed using [8],

$$\boldsymbol{B = \frac{\emptyset}{N_2 A} - \mu_o H \left(\frac{A_2 - A}{A} \right)} \quad \textbf{(4.2)}$$

Figure 4.2: Prepared core samples placed in a high temperature oven.

A set of hysteresis loops with varying peak flux densities at a quasi-static frequency of 1Hz were measured, to characterise the hysteresis loss. A carefully controlled demagnetising sequence was applied prior to every measurement in order to ensure all the loops were centred around the origin. A series of 32 AC measurements were performed on each test-piece, in each case with sinusoidal current demands having frequencies varying from 100 Hz to 4 kHz. At the high frequencies, the power dissipated in the samples could be sufficient to raise the temperature considerably. In the case of automated measurement systems, these high power measurements would be restricted to a few cycles that take a fraction of a second. In this case, the measurements were taken manually and hence it was important to establish the potential temperature rise due to the loss dissipation in the sample.

Table 4-1 shows the calculated temperature rise in the sample at a given level of power dissipation within the coil, based on a simple adiabatic temperature rise and the

manufacturer's published specific heat capacity. In this case a temperature rise of 10°C was selected to be the maximum allowable rise in temperature. The cells marked in red hence show the maximum time allowed for a given power loss, and losses greater than 150 W were not induced in the coil. The table were used as a guideline during measurements, and sufficient time was left in between the high frequency loss measurements to allow temperatures to return to the nominal setting, as a result increasing the time required for measurements.

Table 4-1: Expected temperature rise in °C for a corresponding loss in the core.

Time (s) / Loss (W)	1	3	5	10	20
10	0	1	1	2	4
20	0	1	2	4	9
50	1	3	6	11	22
100	2	7	11	22	45
150	3	10	17	33	67

During the course of this study, 12 full sets of hysteresis and AC loss measurements were performed on both coils, viz. nominally un-aged measurements at room temperature, 200°C and 400°C, and measurements at the three set temperatures following continuous 400°C temperature soaks of 500 hours, 1000 hours and 2000 hours. In each case, on reaching the set temperature, the samples were first allowed to soak at temperature for 2 hours after which measurements were taken over a period of some 24 hours allowing sufficient time between measurements.

4.4 Resistivity measurements

To characterise the two Co-Fe grades in terms of eddy current losses, electrical resistance measurements were carried out on serpentine samples of the core materials. The supplied lamination sheets used to manufacture the demonstrator machine and the core loss samples had two punched holes in order to allow the sheets to be individually hung during heat treatment. In order to maximise the length of the test sample, the test-piece was cut

around the punched holes in the specific shape shown in Figure 4.3. The resulting samples have a total mean path length of 1.8m and a cross-sectional area of 0.6mm^2, resulting in a sample resistance of 1.4Ω.

Three samples of each of the two heat treated grades samples were prepared and placed in the oven along with the toroidal core loss samples for the high temperature and ageing measurements. A Cropico DO5000 micro ohm meter was used along with a four-wire kelvin probe. The average of the three resistance measurements were scaled with due account of the cross-sectional area and path length to establish an estimate of the resistivity of the material. The measured resistivity of the two Vacodur S+ grades as a function of temperature prior to ageing is shown in Figure 4.4. The 390MPa samples showed a marginally higher resistivity at room temperature but at 400°C both materials showed the same resistivity.

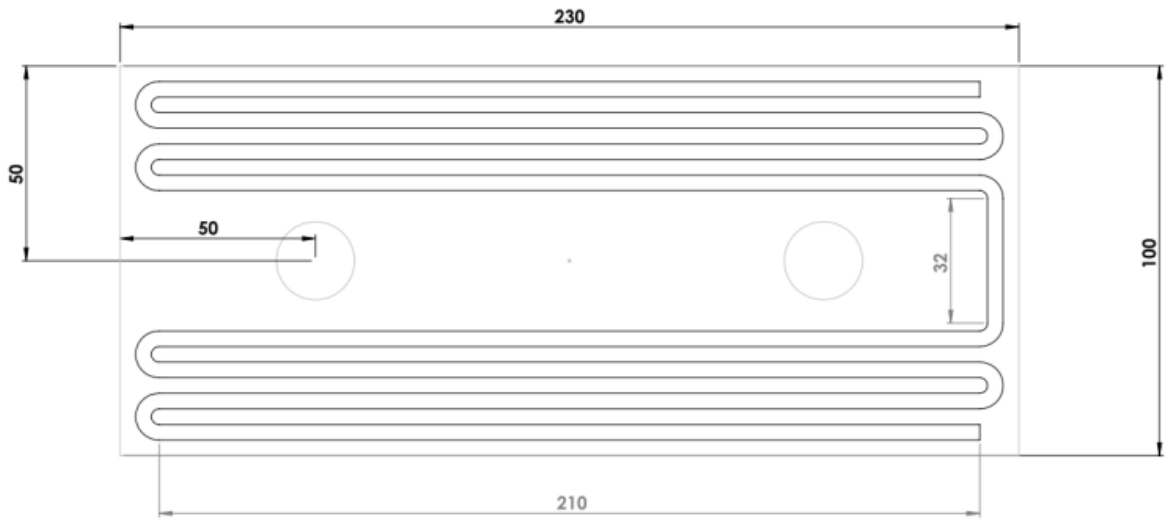

Figure 4.3: Drawings for wire erosion of lamination for resistivity measurements.

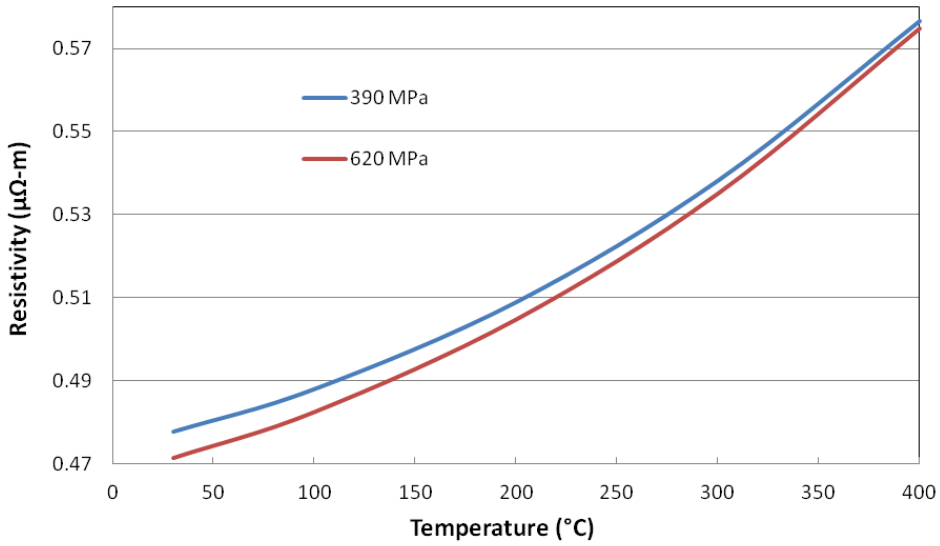

Figure 4.4: Measured resistivity as a function of temperature for the two Vacodur S+ samples.

4.5 Characterisation of hysteresis loss parameters using magneto-static measurements

4.5.1 Characterisation of the Everett function

There are several methods of determining the Everett function, such as using first order transition curves[9], least squares approximation[10]or Gaussian distribution[11]. The main drawback of these techniques is the extensive measurements required for characterising materials. To simplify the measurements required, a method of determining the Everett function from just the BH limiting loop was developed in[12]. The limiting loop can be defined as the BH loop obtained when the core is driven into complete saturation at both ends. This method was selected as the preferred option in this study, mainly due to the lower number of measurements required. The measured BH limiting loops for the two samples are shown in Figure 4.5. In order to provide some interim validation of the model, a set of BH loops were measured with varying peak flux densities and the Preisach model was used to reconstruct the BH loops.

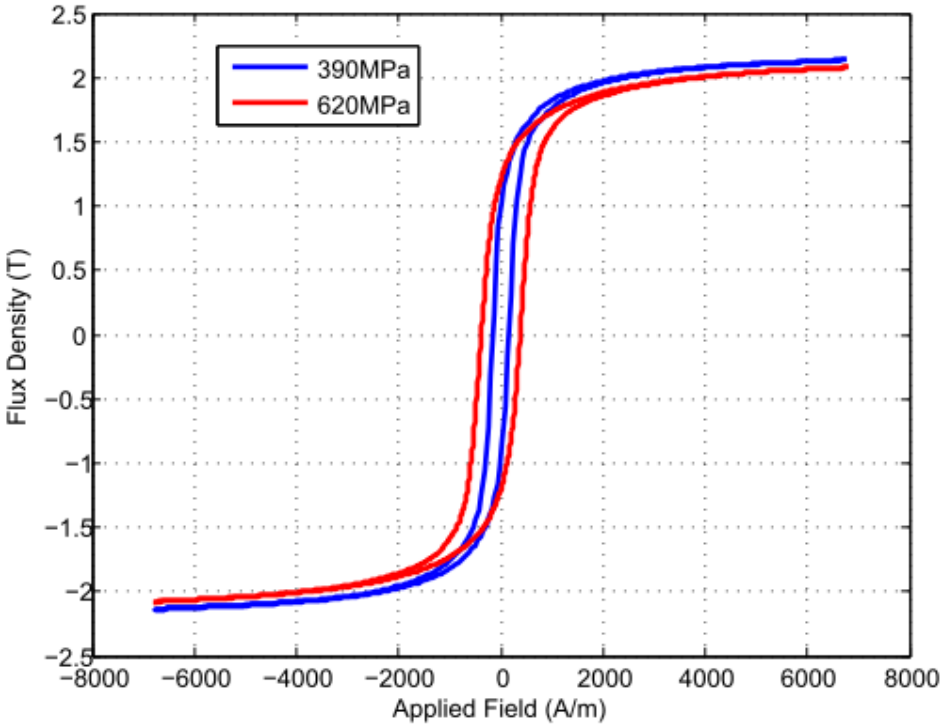

Figure 4.5: Measured limiting BH loops for the two samples.

A comparison of four of the measured and predicted loops is shown in Figure 4.6(a). It shows that the model generates significant errors for loops at lower peak flux densities, i.e. below ~1T. To overcome this problem, a method described in [13] was implemented which uses a further set of BH curves to generate a set of individual Everett functions. Linear interpolation is then used to calculate the Everett function for the whole set. Each centred loop with peak applied field Hm_i is used to calculate an Everett function $E(Hm_i,H)$, for values of H in the range $-Hm_i<H<Hm_i$, and is repeated for n loops with increasing applied magnetic fields. A set of 12 loops were used in this case. The final Everett function $E(Hm,H)$ is calculated by linear interpolation over the set of individual Everett functions $E(Hm_i,H)$ for $i=1:n$.

The static measurements were carried out using the same set up described in section 4.3 in conjunction with a Magnet Physik EF14 integrating flux meter on the secondary sense coil. The measurements were taken at cycle frequencies of 1Hz. Figure 4.6(b) shows a set of measured and predicted loops using this interpolation technique for Vacodur S+ (390MPa). The predicted loops (using the Preisach model and the measured Everett functions) track the measured loops accurately over the whole range of BH plane as can be seen in Figure 4.6 (b).

The drawback of this method however is that a larger number of hysteresis loops are required to be measured, which also need to be carefully centred around the origin in order to minimise error. Figure 4.7 shows the measured Everett functions for the two samples using the interpolation technique. The Everett functions are stored in look up tables to simplify the implementation. It should be noted that in the Everett functions for the selected materials, a significant proportion of the characteristic information is stored around the central region, in this case the region from $-1000<\alpha, \beta<1000$. For better accuracy a higher sampling may be used in this region of the look up table, however in practice this significantly increases complexity and solution times.

Figure 4.8 compares the measured and predicted static loop area for both samples. It can be seen that although the loops are followed very closely by the model there is an error in the overall area enclosed of 3-5%. This error is larger at higher peak flux densities. The source of error is partially a consequence of the linear interpolation used between successive loops to calculate the Everett function and offsets in the integration and procedure for centring the loops. It is also worth noting that the static loss for the 620MPa sample is almost twice that of the 390MPa, a finding which is consistent with the well-established trade-off between loss and mechanical strength. In order to verify the accuracy of the hysteresis model for minor loops, a test waveform with minor loops was generated using the arbitrary waveform generator. Figure 4.9 shows the comparison of the measured and predicted hysteresis loops for this test waveform. The measured flux density was used to predict the applied magnetic field which is shown in Figure 4.10. It can be seen that the model traces the main loop well, but shows some error in predicting some of the biased minor loops.

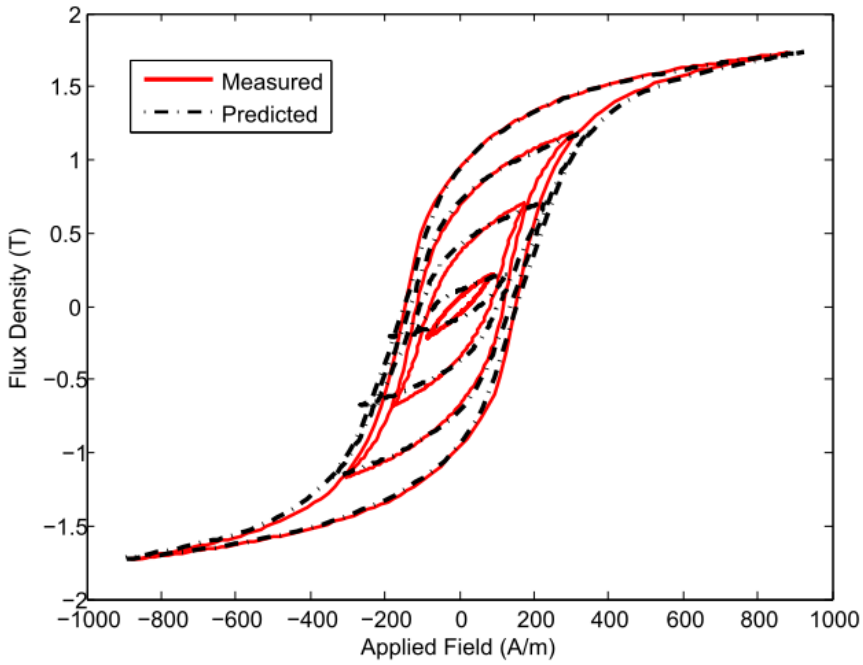

(a)

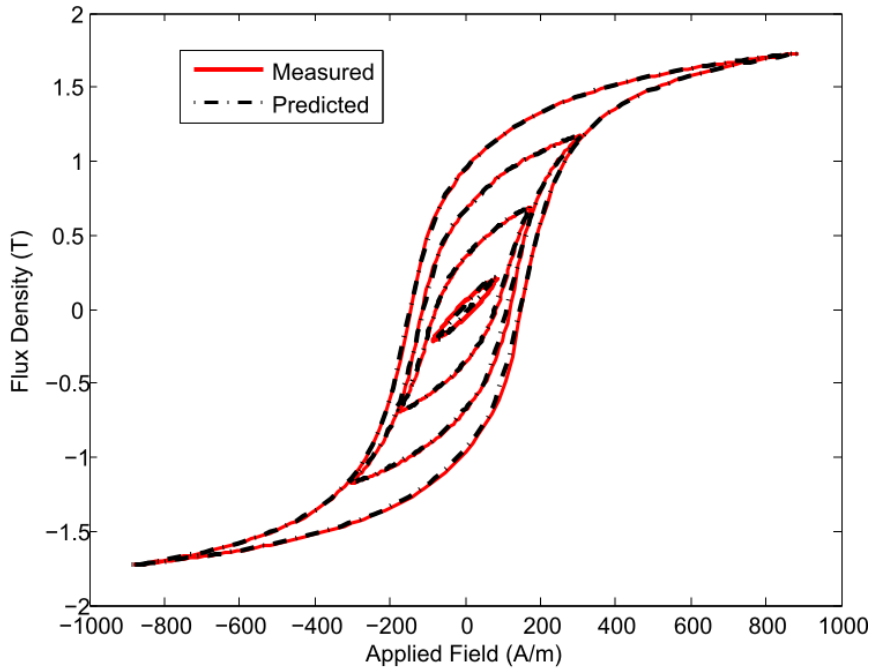

(b)

Figure 4.6: Hysteresis loops predicted using (a) limiting BH loop and (b) minor loop interpolation.

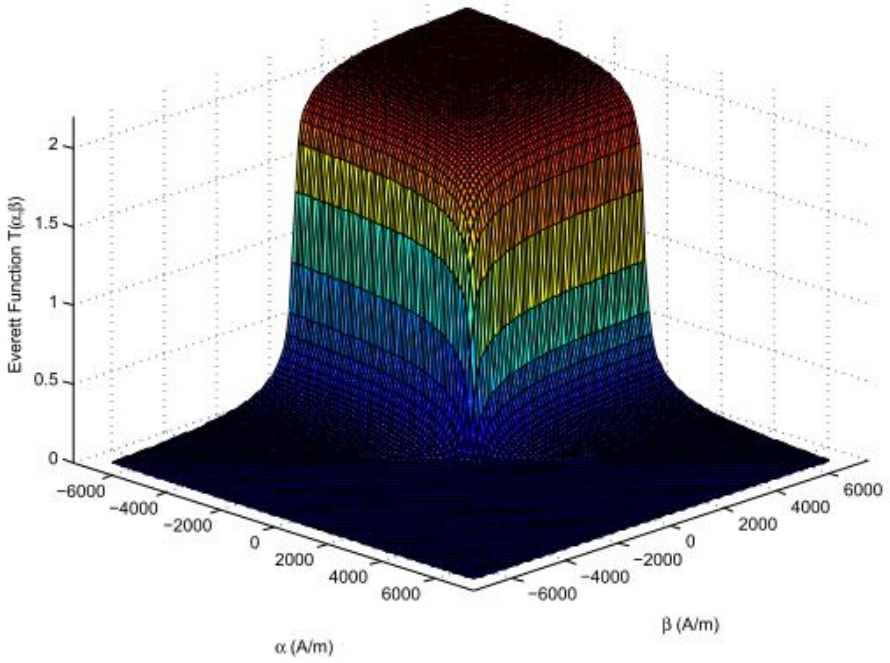

(a)

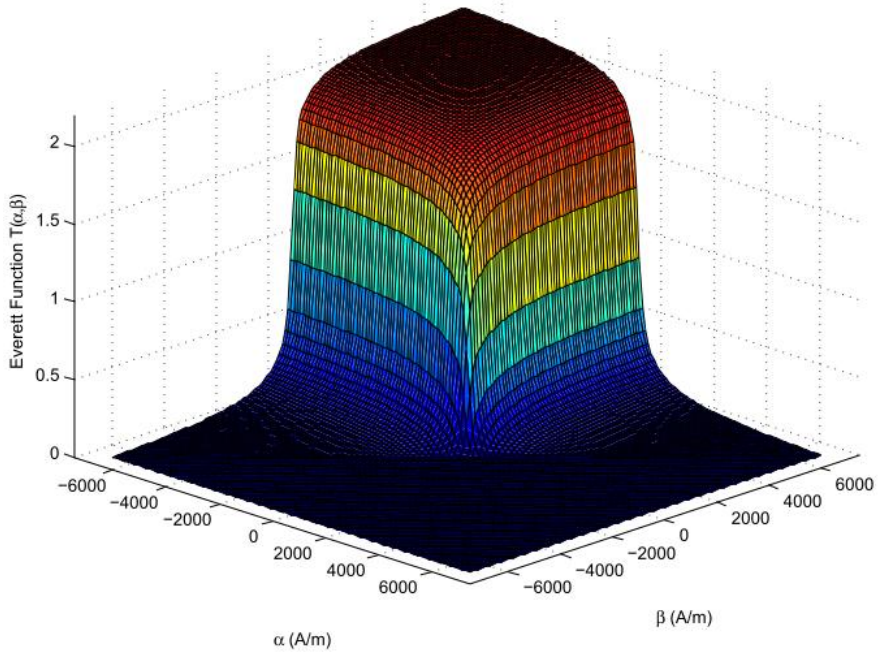

(b)

Figure 4.7 : Everett function for Vacodur S+: (a) 390MPa, (b) 620MPa.

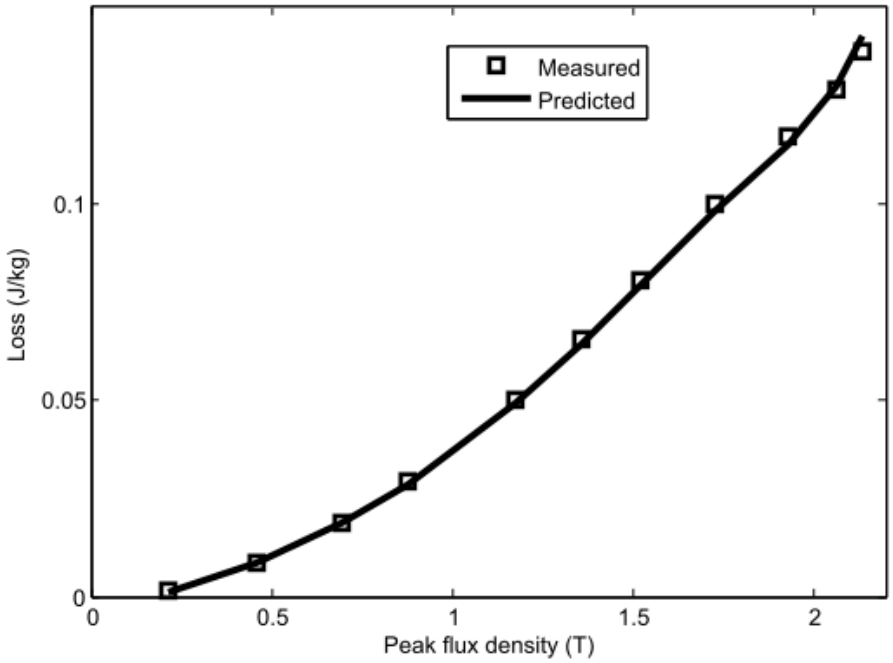

(a)

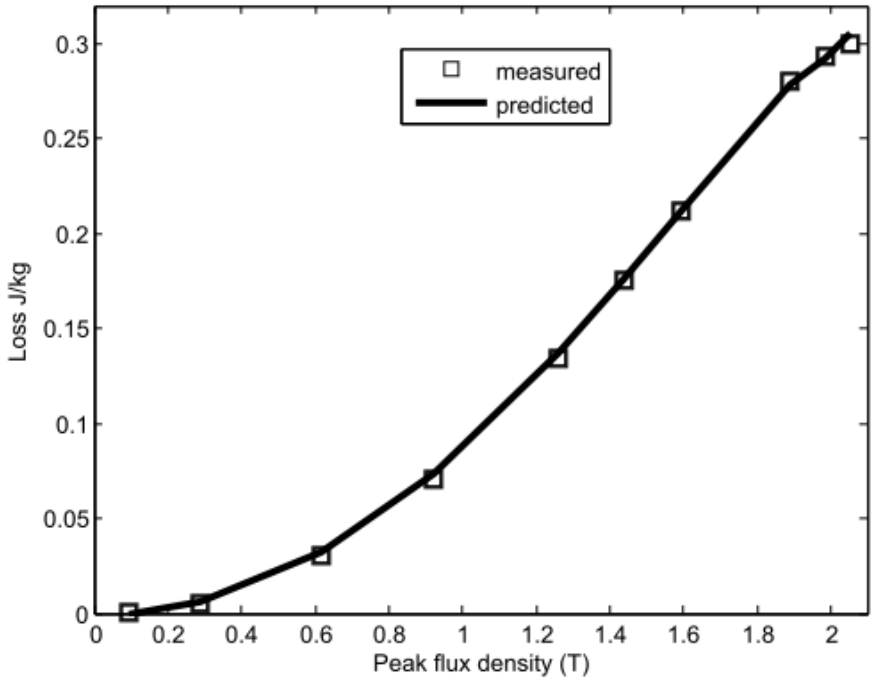

(b)

Figure 4.8. Measured and predicted hysteresis loss per cycle for BH loops containing no minor loops: (a) 390MPa, (b) 620MPa

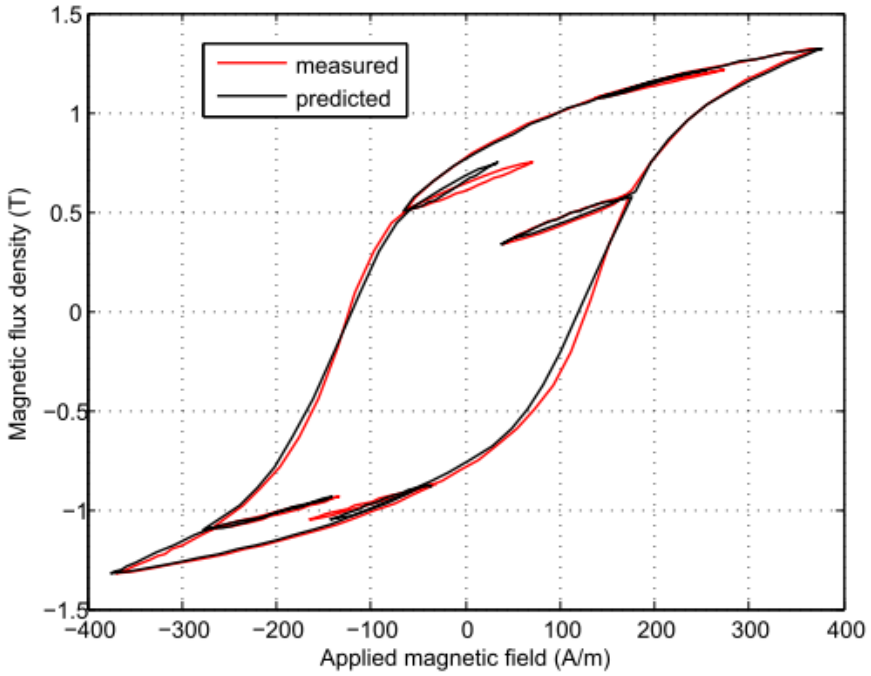

Figure 4.9: Measured and predicted BH loop including several DC biased minor loops.

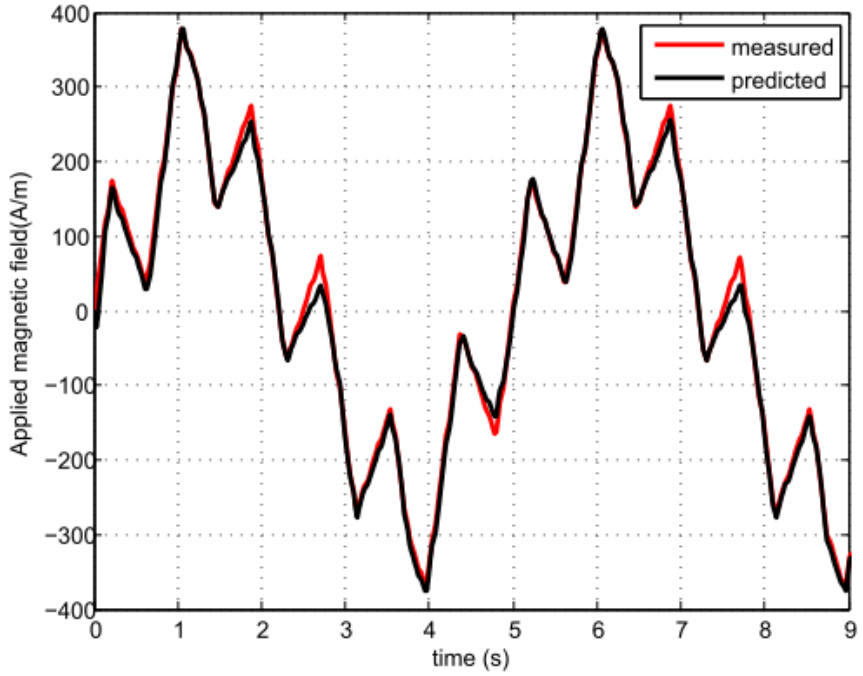

Figure 4.10: Measured and predicted applied magnetic field, using the Preisach model.

4.5.2 Anhysteretic magnetisation curve

The anhysteretic magnetisation curve provides a one to one mapping of the flux density to the applied field, and forms a lossless representation of the magnetisation process in the core material which passes through the origin of the B-H plane. This curve is often referred to as the normal BH characteristic curve or the initial magnetisation curve and is commonly used to represent the non-linearity of the core material during the numerical solution of finite element models. In chapter 3, the anhysteretic curve was used to model the instantaneous reactive power flow in the electromagnetic model. The initial magnetisation curve is generally one of the few characteristics provided by material manufacturers. In the case of the Co-Fe grades considered in this study, the information can be found in the VAC datasheet[14]. However, since data is only available for two specific heat treatments and at room temperature, it was necessary to measure the initial magnetisation curve for the samples with the specific heat treatments applied and at elevated temperatures.

There are several methods of establishing an anhysteretic curve from experimental measurements. The IEEE standard 393-1991 requires the measurement of a set of minor hysteresis loops, and defines the normal BH characteristic as the curve that joins the tips of these individual loops. An alternative method is to use the virgin magnetisation curve which is measured by first demagnetising the sample completely and then increasing the magnetic field to saturation and measuring the corresponding flux. A method to measure the anhysteretic curve is described in the Jiles Atherton model [15] which uses a set of DC biased demagnetising curves to measure the flux for the respective H_{bias}. This data is then curve fitted to a modified Langevin function in order to simplify the solver. A more recent method suggested in [16] calculates the measured anhysteretic curve by taking a horizontal average of the measured limiting BH loop. A similar curve can also be calculated by vertical averaging of the BH loop.

The Jiles Atherton method requires an extensive set of complicated measurements which would include controlled measurements on the induced flux waveforms in a closed loop circuit. As this could not be straightforwardly achieved using the existing experimental set-up, it was not considered as a viable option in this study. Of the remaining methods, viz. IEE 393-1991, initial magnetisation curve, horizontal and vertical averaging, they require the limiting BH loop and at most a set of minor loops and can be calculated from the set of BH loops measured for estimating the Everett function. Figure 4.11 shows a series of anhysteretic curves for Vacodur S+ 390 established using the four different methods. It can be seen that

all the curves have slightly varying initial permeability but as one would expect, they tend to converge as saturation is approached. Figure 4.12 shows the corresponding variations in the absolute relative permeability (i.e. B/H) as a function of the applied magnetising field strength established by the different methods.

The vertical averaging and IEE 393-1991 methods show lower initial permeability and are similar to the initial magnetisation curve, whereas horizontal averaging shows a much higher initial permeability. The initial magnetisation curve itself includes some hysteretic behaviour which can be observed as lower initial permeability and hence does not represent what should be the anhysteretic curve. On the other hand a higher initial permeability shown in the horizontal averaging method was considered to be more representative of the anhysteretic curve, as it does not exhibit a drop in permeability due to a hysteresis lag. Therefore the horizontal averaging method was selected to represent the anhysteretic BH curve for the model used in this study. However, it should be noted that the selection does not affect the outcome of the model by a significant margin and either of the described methods can also be used. The anhysteretic curves using horizontal averaging of measurements for the two materials with temperature are shown in Figure 4.13 and Figure 4.14. Although the saturation flux density in both the samples starts to reduce at 400°C, an increase in initial permeability is observed.

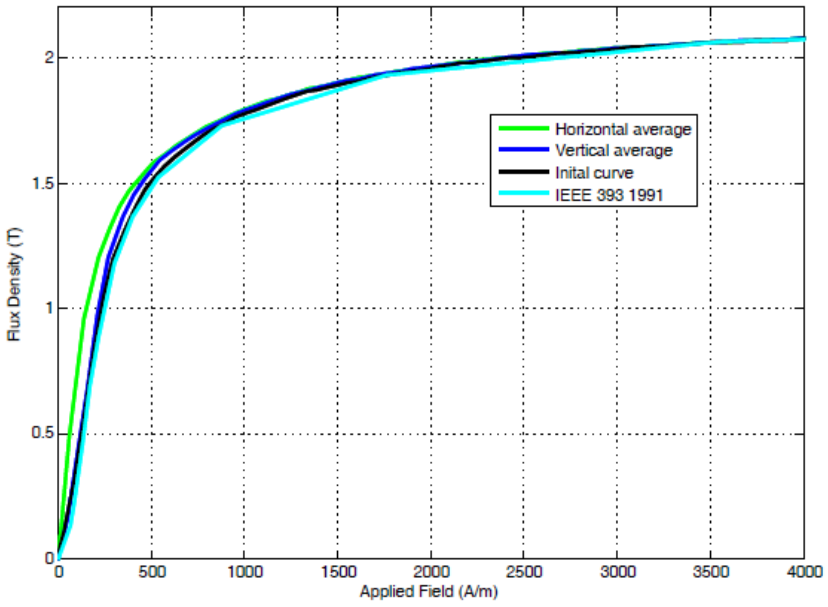

Figure 4.11: Measured anhysteretic curves for Vacodur S+ (390MPa).

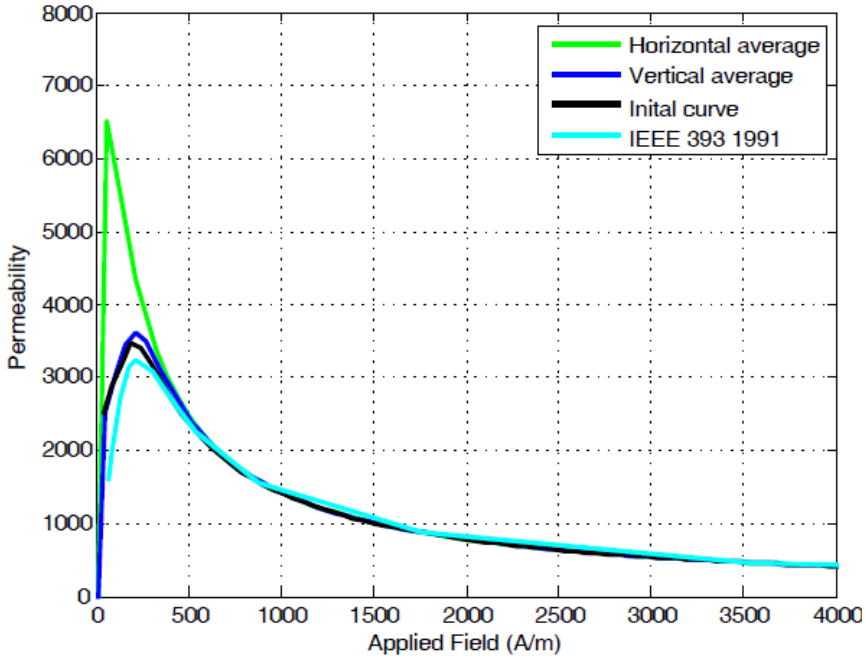

Figure 4.12: Variation in absolute relative permeability (B/H) as a function of magnetising field of Vacodur S+ (390MPa heat treatment regime).

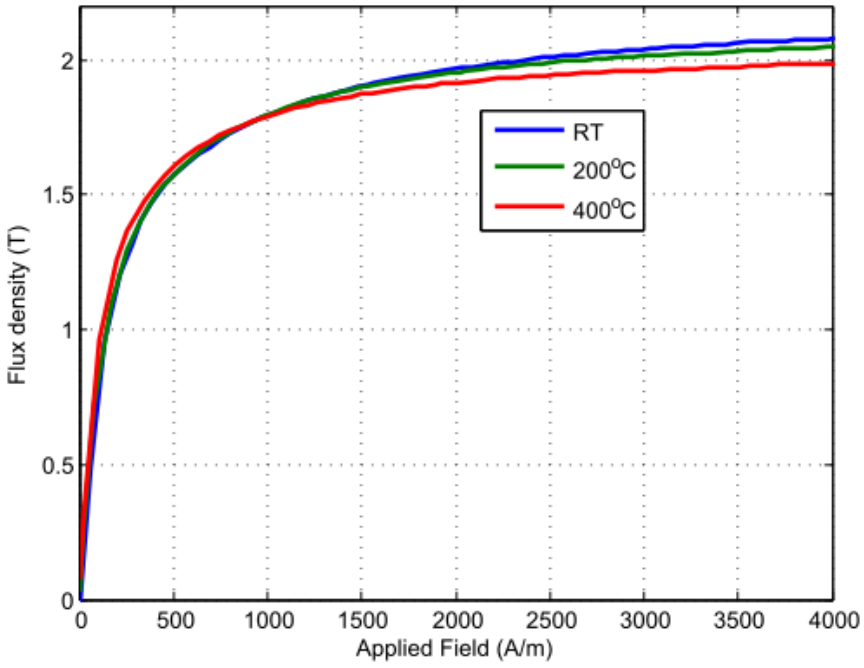

Figure 4.13: Anhysteretic curves for Vacodur S+ derived from horizontal averaging method (390MPa heat treatment regime).

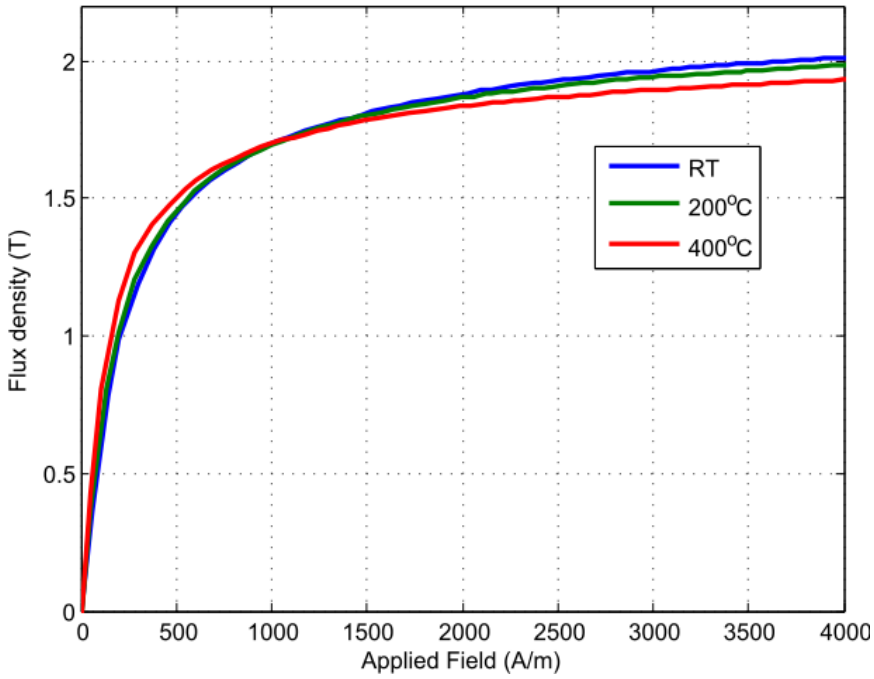

Figure 4.14: Anhysteretic curves for Vacodur S+ derived from horizontal averaging method (620MPa heat treatment regime).

4.6 AC core loss measurements

A series of AC measurements are necessary to estimate the excess loss coefficients. Whereas low frequency and low current operating points can result in reasonably sinusoidal current waveforms, at the higher currents and frequencies, some distortion of the flux density is inevitable due to the non-linear magnetisation behaviour of the core material. This is illustrated in Figure 4.15 which shows the measured current and flux density waveforms at a peak current of 16A for 100Hz and 800Hz, which correspond to peak flux densities of ~1.9T. In both cases, the amplifier (which is operating in current control mode) is fed by a sinusoidal input demand. The current waveform at 800Hz demonstrates the limited capability of the power amplifier to follow the current demand, which in turn has implications in terms of the flux density waveform. Although the method for extracting the material specific coefficients can cater for significant distortion of the current and flux density waveforms, ultimately there are issues of stability of the current control loop, which dictated that for high peak current demands, the fundamental frequencies that could be used were limited.

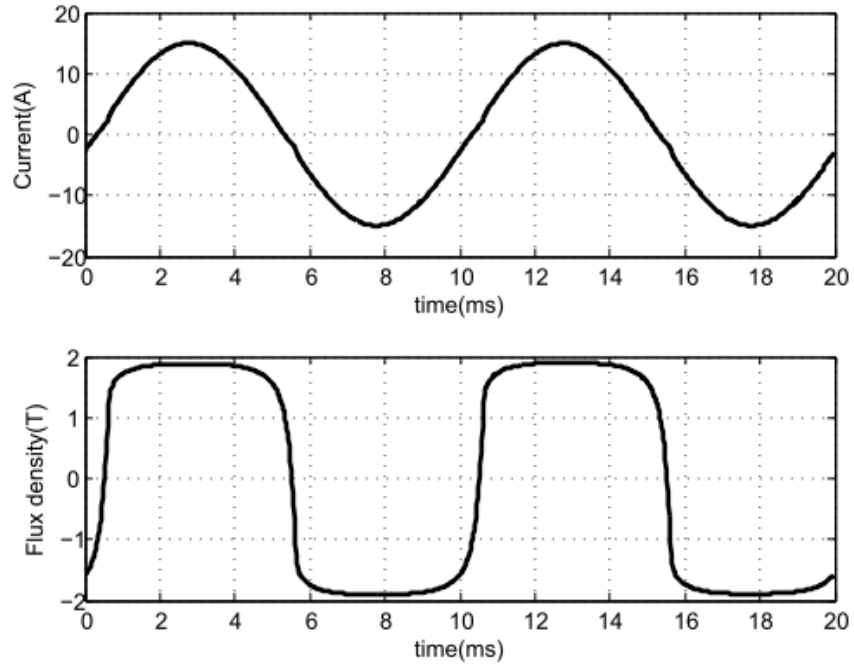

(a)

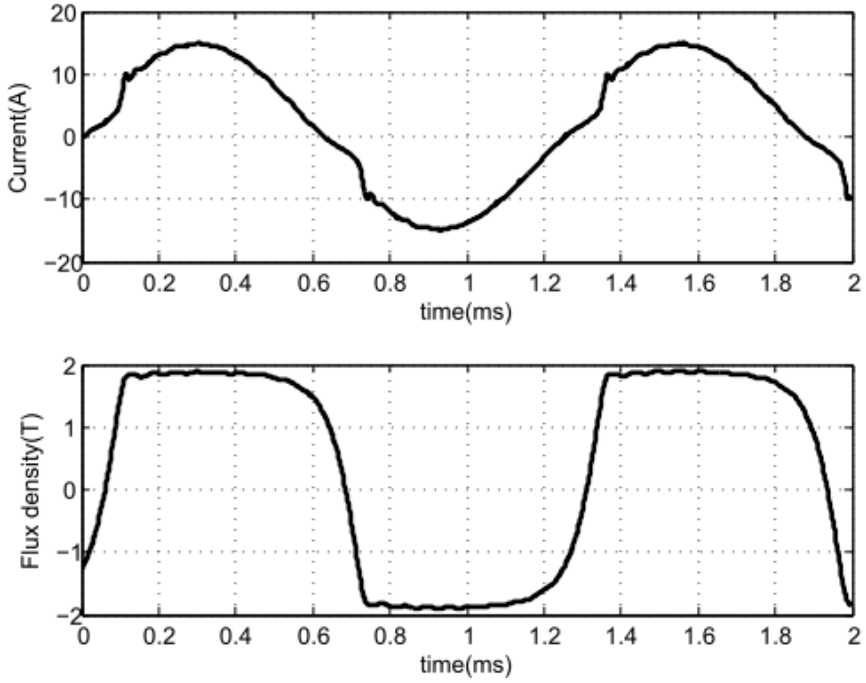

(b)

Figure 4.15: Measured current and induced flux density for a peak sinusoidal demand of 16A at (a) 100Hz (b) 800Hz.

A large number of separate AC core loss measurements were performed, in each case with the current and search coil emf waveforms captured at high sample rate (typically 20 MS/s) at up to 12 bits vertical resolution. A total of 32 measurements were performed with waveforms having measured peak flux densities from ~0.4T to 2T, and fundamental frequencies varying from 100Hz to 4 kHz, although the maximum flux densities achieved at 4 kHz are just above 1.5T due to amplifier stability.

An indication of the coverage of flux density and frequency which is provided by the series of measurements can be obtained from the various Fourier spectrums of the individual measured flux density waveforms. The resulting superposition of all the frequency components is shown in Figure 4.16. It is important to note that the graph is only used as a representation of the region covered by the measurements, and is not used for a frequency domain calculation. The spectrum shows some harmonics as high as 9 kHz. Figure 4.17 shows the average core loss density as a function of peak flux density of the two core samples for the series measured waveforms, noting that the frequencies used to identify each measurement are the fundamental of the current demand to the power amplifier.

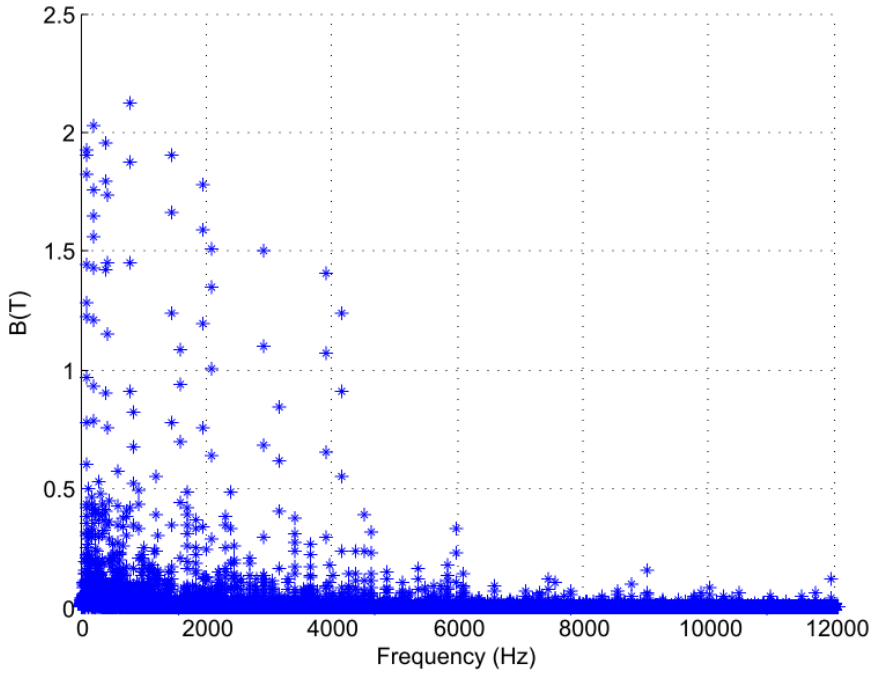

Figure 4.16: Fourier spectrum of the set of the measured flux densities

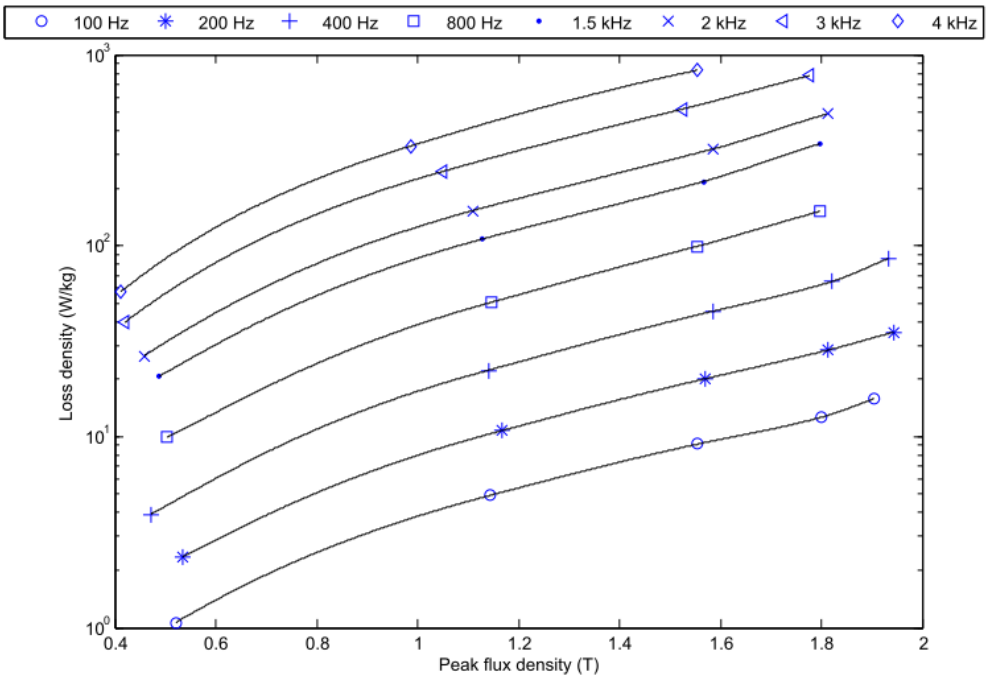

(a)

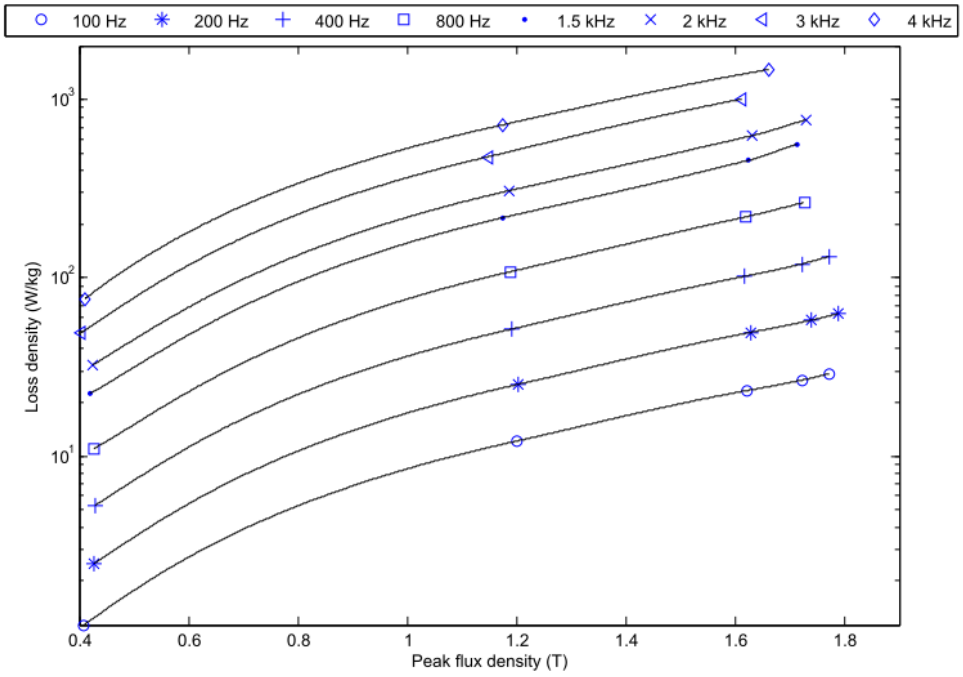

(b)

Figure 4.17: Measured average core loss for the range of frequency demand waveforms for the Vacodur S+ grades: (a) 390MPa, (b) 620MPa.

4.6.1 Extraction of excess loss parameters

For the set of measured search voltage waveforms obtained experimentally, the corresponding flux density waveforms in the core sample can be calculated. The eddy current loss and hysteresis loss were then calculated over one complete cycle using equations 3.9 and 3.16 respectively. The residual loss per cycle calculated by the difference between the measured total and the sum of the calculated hysteresis and classical eddy current loss is assumed to be equal to the excess loss per cycle. Given a particular value of excess loss per cycle, the time domain integration of the instantaneous excess loss predicted by equation 3.10 can be used to establish a value of the constant k_{exc}. By performing this process for each individual combination of excitation magnitude and frequency, a series of estimates of k_{exc} can be obtained. Figure 4.18 shows the resulting values of k_{exc} obtained from the 32 loss measurements, from which it is apparent that there is a significant scatter in the value of k_{exc}. A certain level scatter might reasonably be anticipated since, as noted previously in section 4.2, the excess loss is the only term that requires a fitting parameter which cannot be established from an isolated measure of that loss component alone while also being the smallest term in magnitude. At the lower frequencies, i.e. below 1 kHz or so, the calculated residual loss from which the excess loss constant is predicted was less than 8% of the total measured core loss and even at the higher frequencies was no larger than 15%. As a result, any errors in the hysteresis and eddy current loss, even of a few percent of the total of that component, could cause the value of k_{exc} to vary markedly between measurements.

A more significant factor however may be that the formulation of excess loss by Bertotti in his key paper[6]were based on observations for frequencies up to 400Hz for specific types of lamination grades and thickness. For this range of frequencies a single value of k_{exc} proved adequate, and moreover the 1.5 exponent of the dB/dt term seemed to provide a good description of the observed behaviour. Since then several authors have shown a measured variation in the excess loss parameter with frequency and flux density and consequently several enhancements or variations of the basic Bertotti model have been proposed [17, 18]. In these models the parameters of hysteresis and excess losses are made functions of peak flux density and frequency. Similarly in [19], the model uses hysteresis loss coefficients that vary with frequency and peak flux density, whereas the excess and eddy current losses parameters vary only with flux density. These methods were shown to achieve a better correlation to measurements from 25-400Hz. For higher frequencies, some models suggest splitting the model parameters into different frequency ranges with different

parameters for each range, for example the models described in [20]. However none of the models can unequivocally predict losses over the complete range of frequencies and flux densities considered in this study.

From Figure 4.18 it is evident that employing a single value of k_{exc} for the entire range of frequencies and flux densities considered will lead to significant errors in the prediction of excess loss, although the impact on the overall loss is less pronounced given its modest contribution under most operating conditions. However, the clustering of the data points at a given peak flux density indicates that employing one of several indicators of mean values of the parameter may be a straightforward solution to accommodate with the observed variation in the excess loss parameter.

As the SR machine had peak operating flux densities in the 2T range at frequencies of 4kHz, the value of k_{exc} can be selected such that it gives a better correlation at the higher frequencies and flux densities. Hence the mean of data points in the region of interest marked in Figure 4.18 were used for loss prediction in the SR machine. The measured and predicted losses for the complete data set using this parameter (k_{exc}= 2.34×10^{-4}) are shown in Figure 4.19. It can be seen that the predicted loss at the lower flux densities are higher than the measured loss, however the losses at higher frequencies and flux densities show a good correlation. Since the excess loss forms a relatively small percentage of the total loss, this rather sweeping assumption does not translate into a corresponding significant error in the total loss prediction. The measured and predicted losses for the two samples at room temperature, 200°C and 400°C along with the excess loss parameters employed are included in Appendix B.

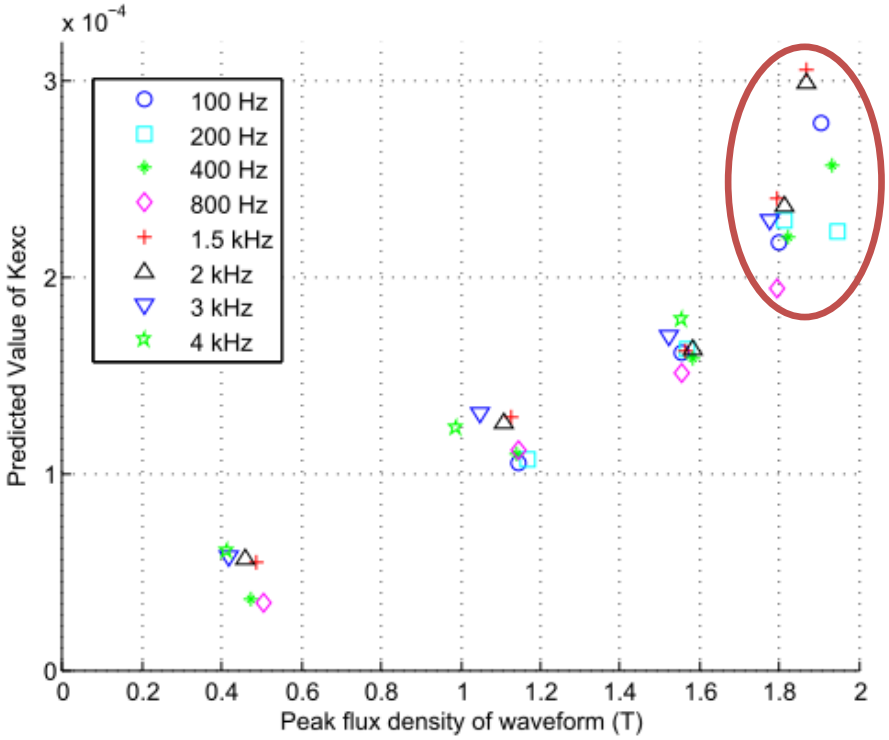

Figure 4.18: Predicted values of k_{exc} from the set of residual loss values.

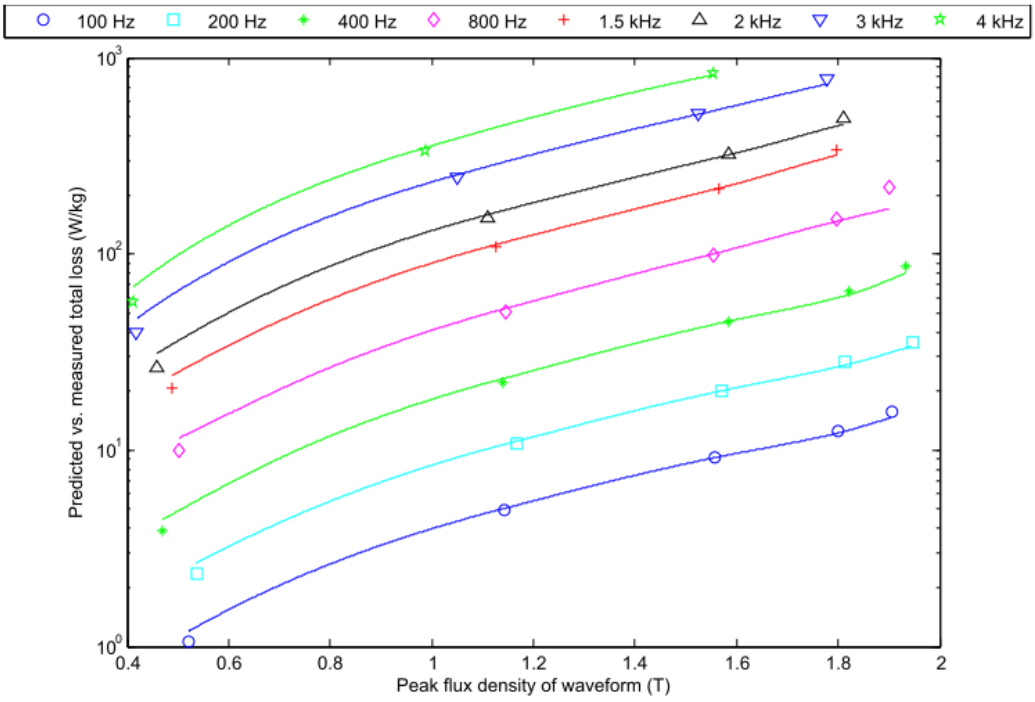

Figure 4.19: Measured (marker) vs. predicted (line) total loss using selected k_{exc}.

4.7 Validation of instantaneous loss model using a toroidal test sample

Although the simulation methodology described in chapter 3 is ultimately aimed at predicting electrical machine performance, in order to experimentally verify its ability to predict instantaneous core loss and accurately reflect this loss in an electrical circuit, the more straightforward case of a ring core sample wound with a toroidal excitation coil was considered. This arrangement provides a reliable means of accounting for the instantaneous power flows as there is no mechanical power to account for, and also provides a very simple magnetic model in terms of geometry. The test arrangement shown in Figure 4.1which was used for material characterisation can be used to undertake the necessary measurements for the model validation.

The measured product of the search coil voltage (appropriately scaled by the turns ratio to give v_{coil}) and the drive coil current provides a measure of the instantaneous power flow into the core. As this measured power consists of core loss and reactive power in unknown proportions at any given instant, it is not possible to directly isolate the instantaneous core loss using the apparatus. Hence, it is necessary to use total instantaneous power flow as a basis to compare measurements with predictions. This said, since the net reactive power over one complete cycle of steady-state excitation is zero, measurements and predictions of core loss can be directly compared in terms of the average loss.

Variations in instantaneous power flow measured for three cases which cover a range of frequencies and flux excitation conditions were selected. The first case consists of a waveform with a peak flux density is ~1.9T and a fundamental frequency of 100Hz, the second a waveform with a fundamental of 4kHz and peak flux density of ~1.5T and a third with a fundamental of 1kHz incorporating several minor loops.

The simplified circuit equivalent of the toroidal sample is shown in Figure 4.20. The measured secondary voltage is scaled to primary turns to obtain the voltage (v_{coil}) across the coil and hence the voltage drop across the resistance and any leakage inductances need not be calculated. This voltage is integrated to calculate the instantaneous flux which is fed to the one dimensional single element ψ, i function (equivalent to material anhysteretic BH curve) to read the anhysteretic current (i_{an}). This is the effective current predicted by a lossless model and the reactive power is calculated as ($v_{coil} \, . \, i_{an}$). The central assumption in the reactive power model is that instantaneous reactive power follows the measured anhysteretic

curve. The core loss current (i_{loss}) is the current that flows parallel to the coil and dissipates the appropriate instantaneous power so that the total power at the terminals is

$$\boldsymbol{v_{coil}} \cdot \boldsymbol{i_{ph}} = \boldsymbol{v_{coil}} \cdot \boldsymbol{i_{loss}} + \boldsymbol{v_{coil}} \cdot \boldsymbol{i_{an}} \quad \textbf{(4.3)}$$

where, ($v_{coil}. i_{loss}$) is the instantaneous core loss and can be calculated from the flux density in the core using the model described in section 3.6. Figure 4.21 shows the measured secondary voltage scaled to primary turns and primary current for two current cycles with a fundamental frequency of 100Hz. The flux density can be calculated from the integrated secondary voltage and is shown in Figure 4.22 along with the applied field strength. The initial transient in the first half cycle is required for the Preisach model to set its initial conditions and only the power for the second cycle is displayed to aid clarity.

Figure 4.23 shows comparisons between measured and predicted instantaneous total power flow. It can be seen that there is a surge in total power as the flux density waveform moves from saturation through the central part of the curve. In regions of saturation the core losses are almost zero and the power flow is mainly reactive. Although the measured and predicted total power in Figure 4.23 shows a very good correlation, it can be seen that there is an over prediction of instantaneous power at both the positive and negative peak section. However, the average measured and predicted power is in good agreement and in this case forms a very small percentage of the total power (as shown by the blue line). The comparisons between measured and predicted values of average power over one complete cycle are summarised in Table 4-2.

Table 4-2: Measured and predicted averages for test case

Average Loss	100Hz test case	4kHz test case	1kHz test case
Measured (W)	1.61	87.5	25.4
Predicted(W)	1.58	88.3	26.3

The measurements were repeated for flux density waveforms with fundamental frequencies varying from 100Hz to 4kHz and were in good agreement. The series of results for the 4 kHz test case are shown in Figure 4.27-Figure 4.31. Figure 4.28 shows the measured flux density for this case which has a peak of just over 1.5T. As mentioned previously, the peak flux density achievable at high frequencies was limited by the power capability of the power amplifier. The predicted and measured instantaneous powers at the source exhibit a much better correlation as compared to the 100 Hz case as can be seen in Figure 4.29. The total power loss constitutes a larger portion of the total power as compared to the 100Hz waveform as is evident in Figure 4.30. Hence the errors in predicting reactive power will have lesser effect on the total power.

Figure 4.24 shows the breakdown of the predicted total power flow into core loss and reactive power, from which it can be observed that the instantaneous losses form a significant fraction of the total power flow at many points in the cycle. It is interesting to note that a standard simulation approach with a lossless FE model would only account for the reactive power component in Figure 4.24, which for this particular test arrangement would yield a significant discrepancy in the overall power flow if core loss was added in as a post-processing operation. Figure 4.25 shows the comparison of the reactive power as predicted using the anhysteretic model to that inferred if the model predicted loss is assumed to be appropriately accounted for. It is evident that the predicted reactive loss has a much larger swing as compared to that required to fit the model, which may suggest that the anhysteretic curve used has limitations in terms of its ability to represent reactive power flow though the circuit.

A possible source of error in which is prominent in this region could be a phase shift introduced in the process of offsetting of the flux density waveform during integration. Figure 4.26 shows the measured BH loop and the corresponding curve traced by the reactive component of power. Almost all the power loss occurs in a small part of the cycle, corresponds to the central region of the loop where the rate of change of flux is at its maximum. There is also a significant shift in the reactive component of the power in this region. Hence a small error in either of the models can give a significant discrepancy in the total predicted power. Nonetheless, the results of the total predicted power demonstrate that a significant improvement can be achieved, in comparison to a lossless model.

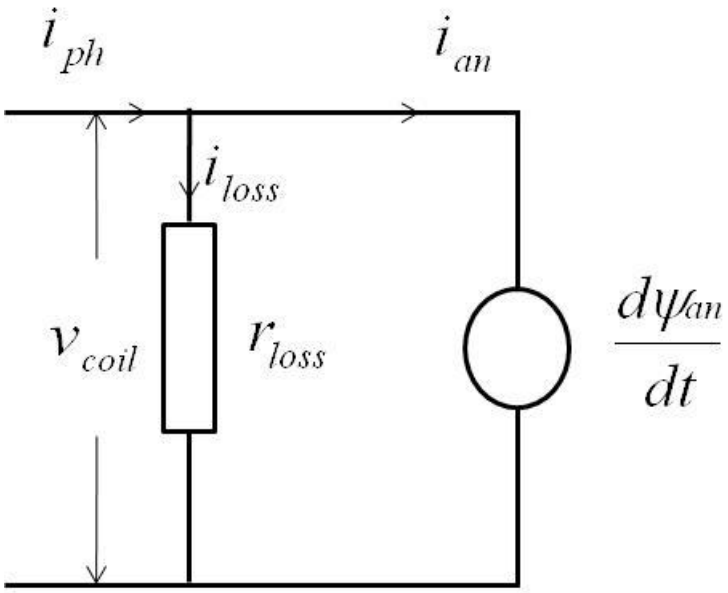

Figure 4.20. Simplified circuit model of a toroidal coil.

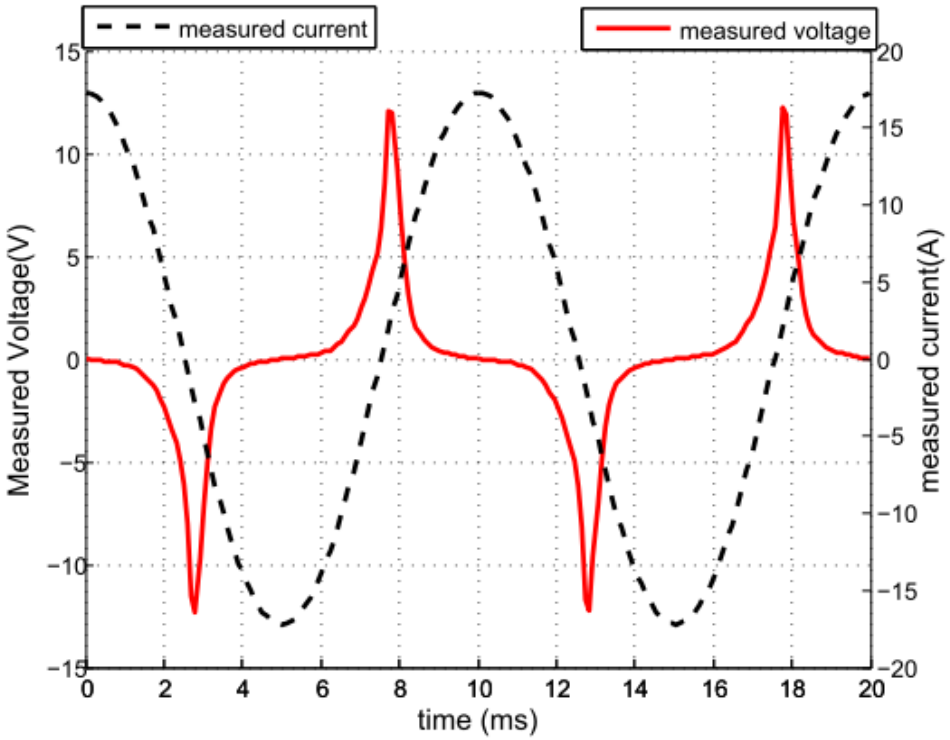

Figure 4.21: Measured voltage and current waveforms for the 100Hz test case.

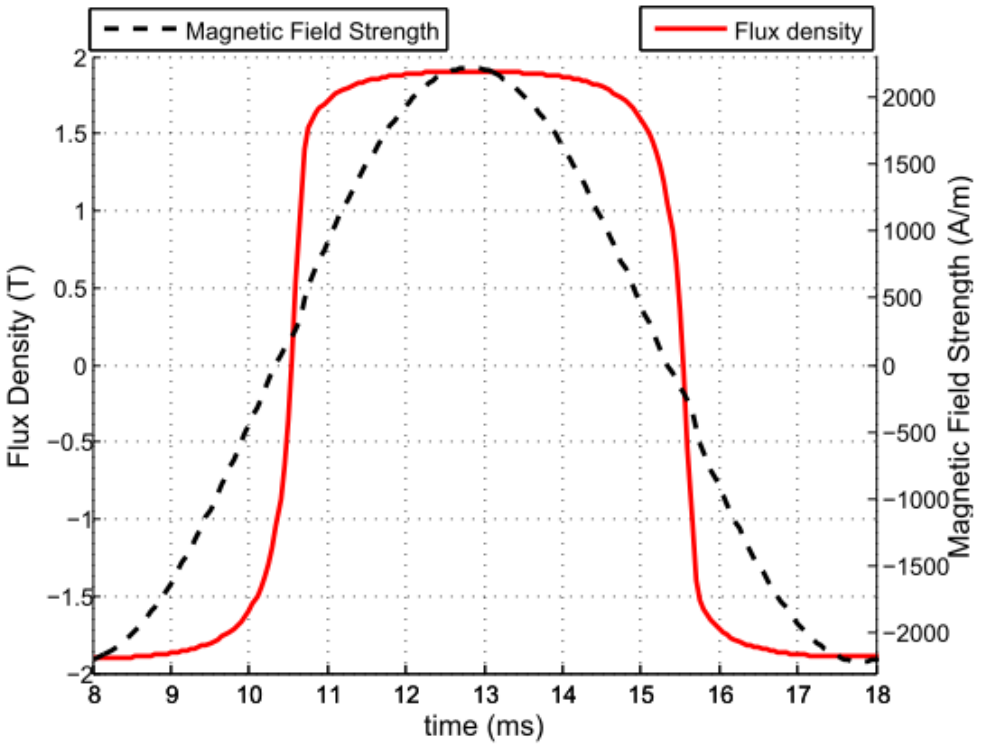

Figure 4.22: Measured flux density for the 100Hz test case.

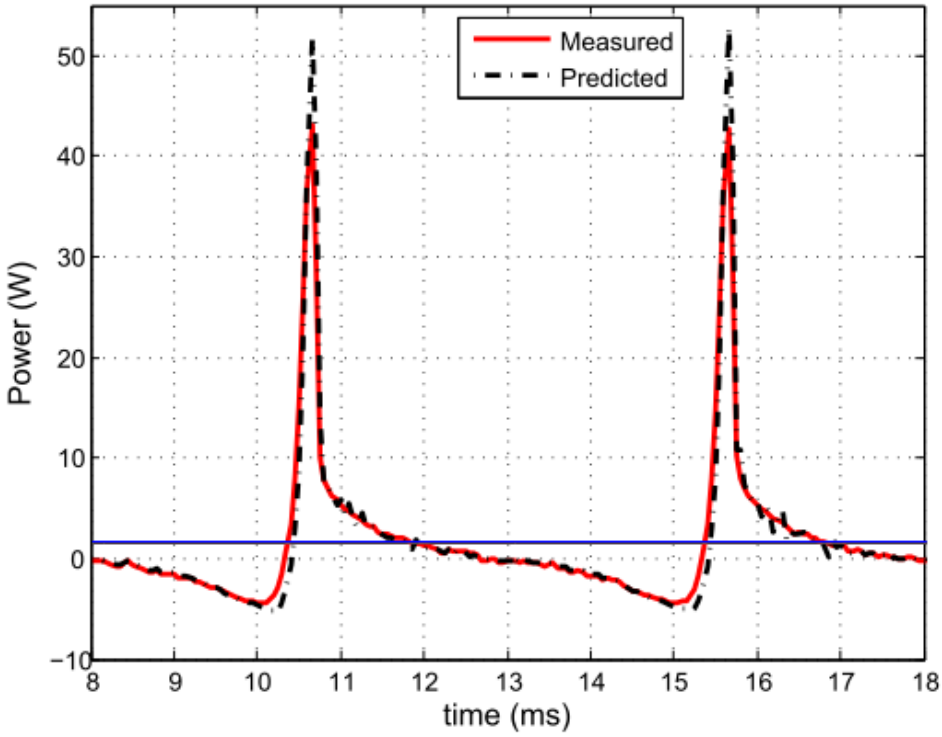

Figure 4.23. Measured and predicted instantaneous power for the 100Hz test case.

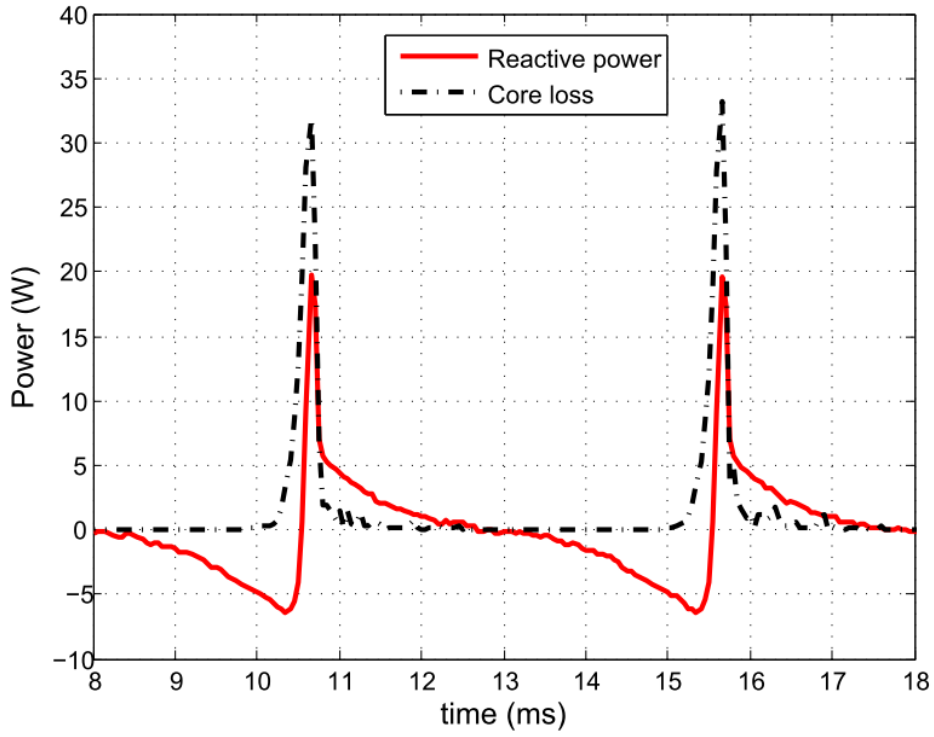

Figure 4.24: Instantaneous core loss and reactive power for the 100Hz test case.

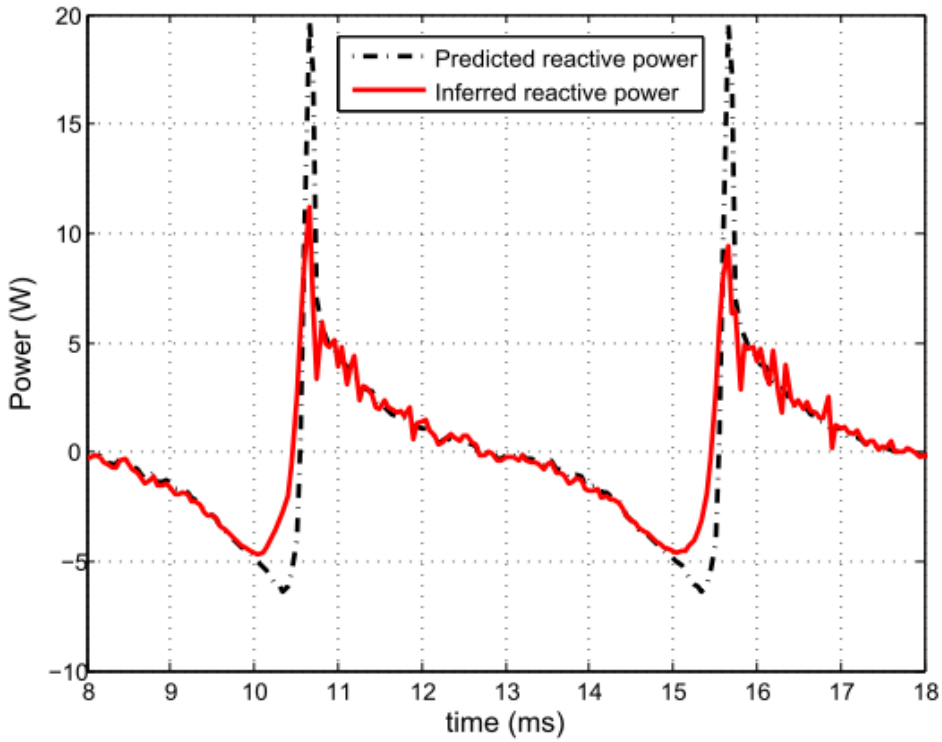

Figure 4.25: Anhysteretic predicted and reactive power inferred from measurements for the 100Hz test case.

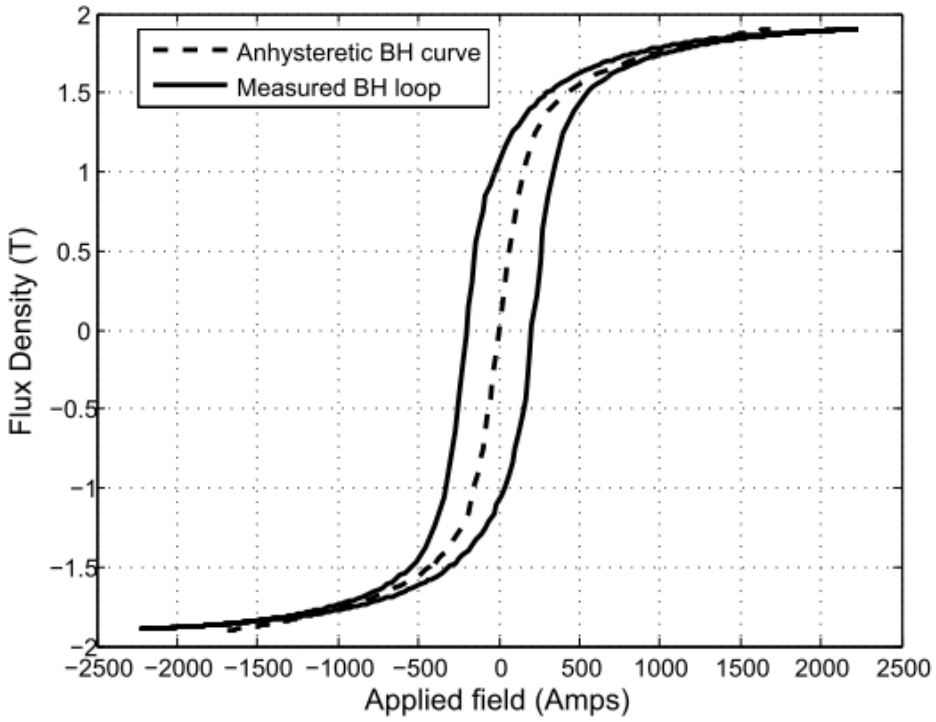

Figure 4.26: Measured BH loop and anhysteretic curve for the 100Hz test case.

The measurements were repeated for flux density waveforms with fundamental frequencies varying from 100Hz to 4kHz and were in good agreement. The series of results for the 4 kHz test case are shown in Figure 4.27-Figure 4.31. Figure 4.28 shows the measured flux density for this case which has a peak of just over 1.5T. As mentioned previously, the peak flux density achievable at high frequencies was limited by the power capability of the power amplifier. The predicted and measured instantaneous powers at the source exhibit a much better correlation as compared to the 100 Hz case as can be seen in Figure 4.29. The total power loss constitutes a larger portion of the total power as compared to the 100Hz waveform as is evident in Figure 4.30. Hence the errors in predicting reactive power will have lesser effect on the total power.

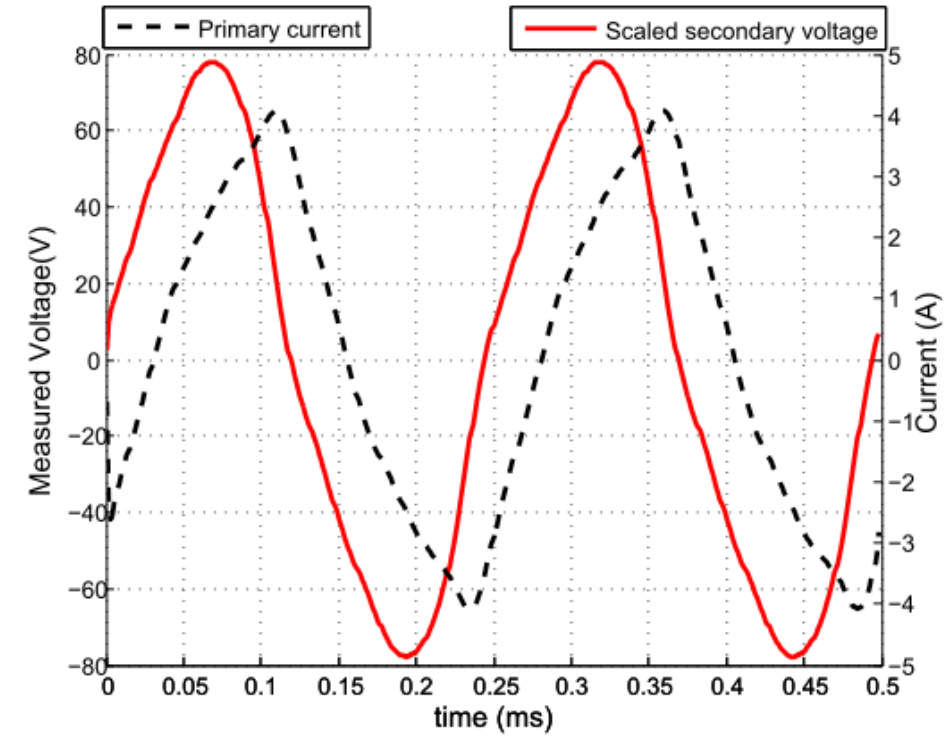

Figure 4.27: Measured voltage and current waveforms for the 4 kHz test case.

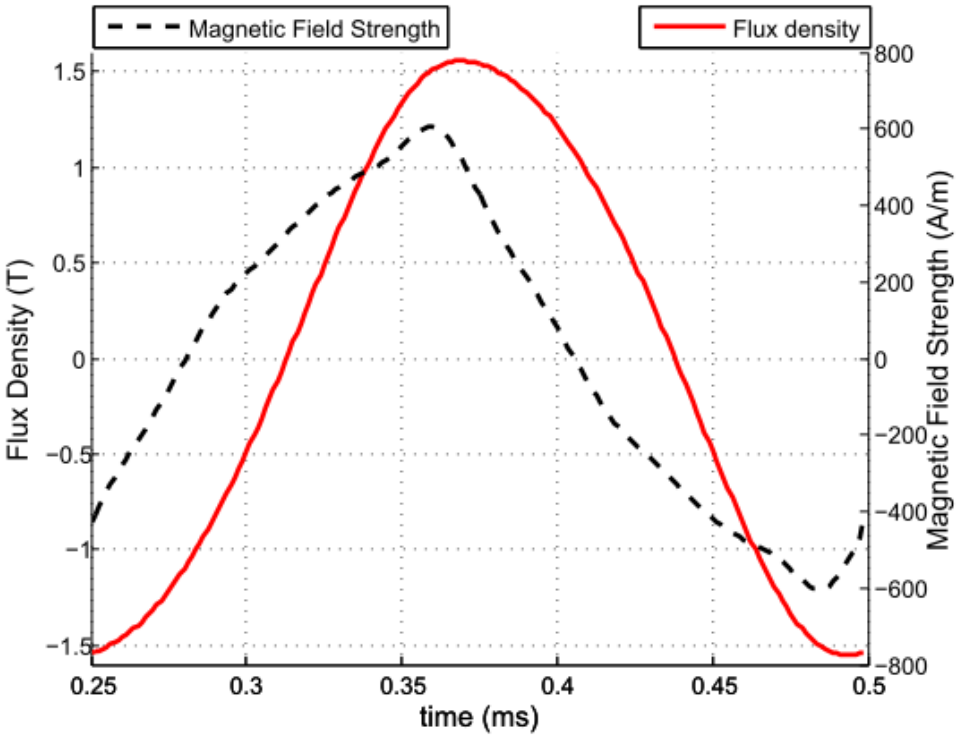

Figure 4.28: Measured flux density for the 4 kHz test case.

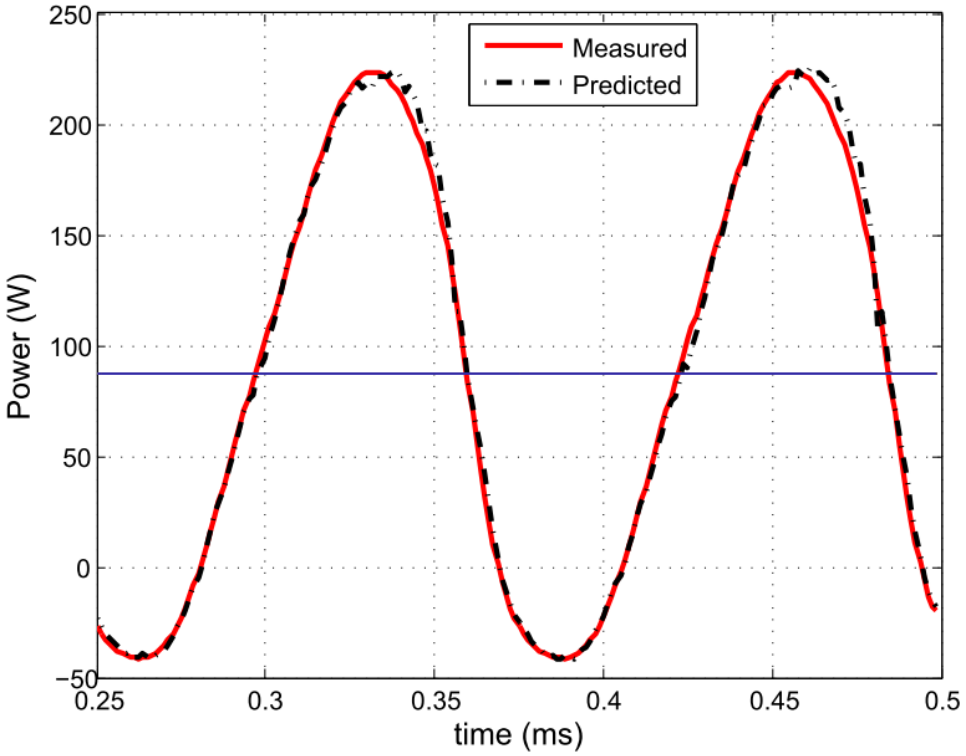

Figure 4.29. Measured and predicted instantaneous power for the 4 kHz test case.

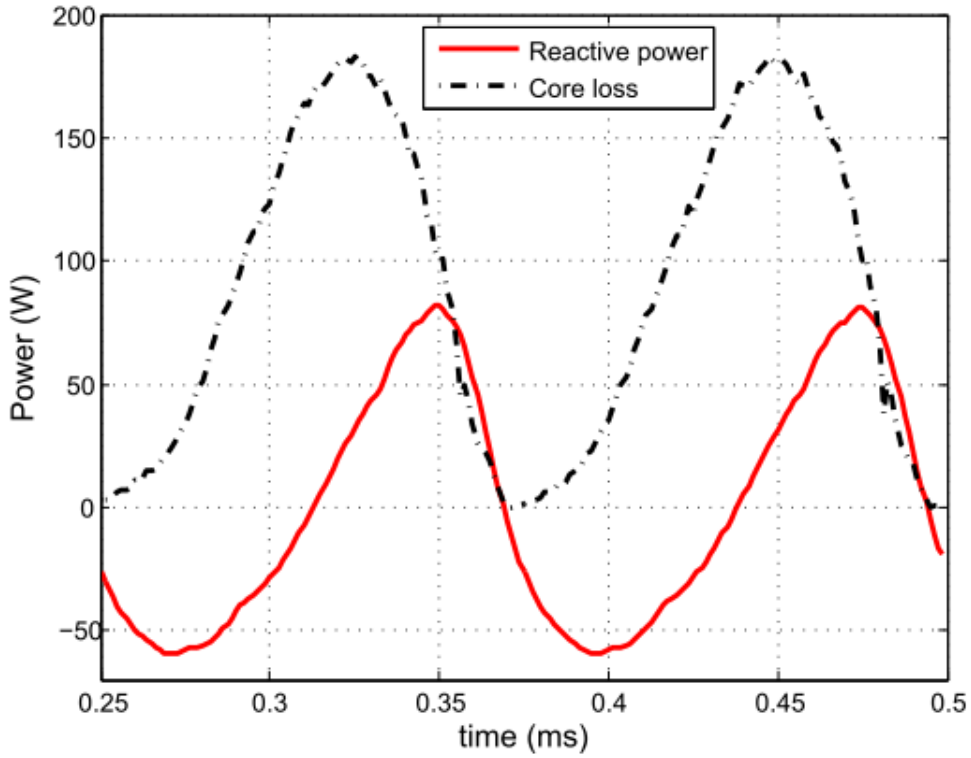

Figure 4.30: Instantaneous core loss and reactive power for the 4 kHz test case.

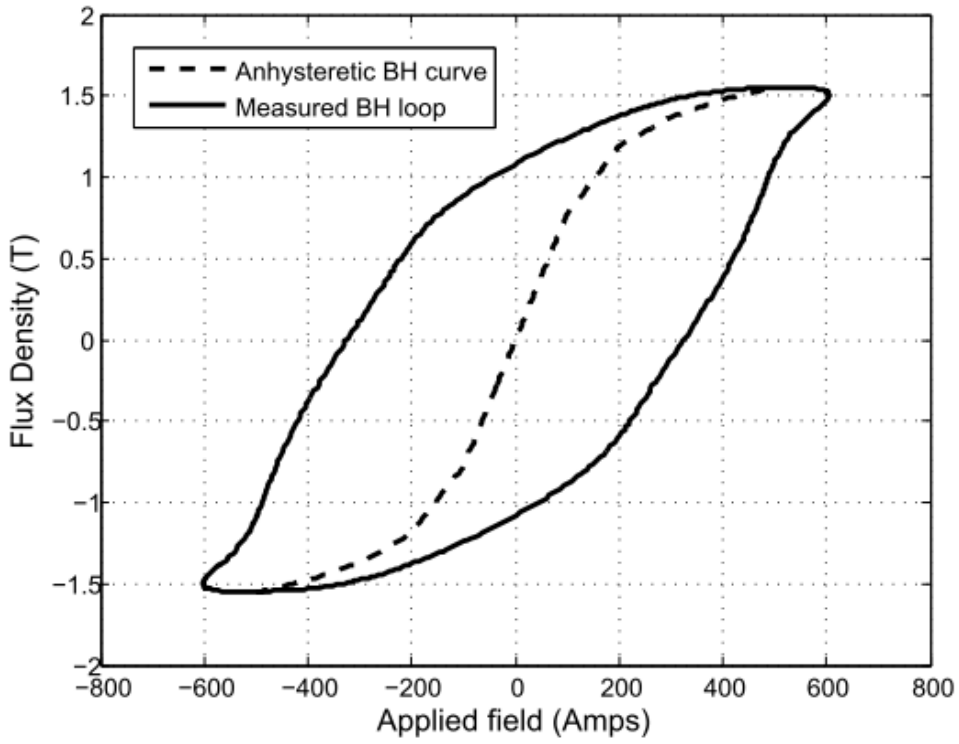

Figure 4.31: Measured BH loop and anhysteretic curve for the 4 kHz test case.

Figure 4.32 and Figure 4.33 shows the breakdown of the total predicted loss into the individual loss components for the 100 Hz and 4 kHz test cases respectively. At 100Hz the hysteresis loss is dominant while the eddy current and excess loss components contribute modestly to the overall loss. At 4 kHz, the eddy current loss is comparable to the hysteresis loss. Table 4-3 shows the average loss of the individual components for the two cases.

Table 4-3: Predicted average values of the individual loss components

Average Loss (W)	100Hz test case	4kHz test case
Hysteresis	1.26	40.2
Classical eddy current loss	0.23	40.0
Excess loss	0.09	8.2

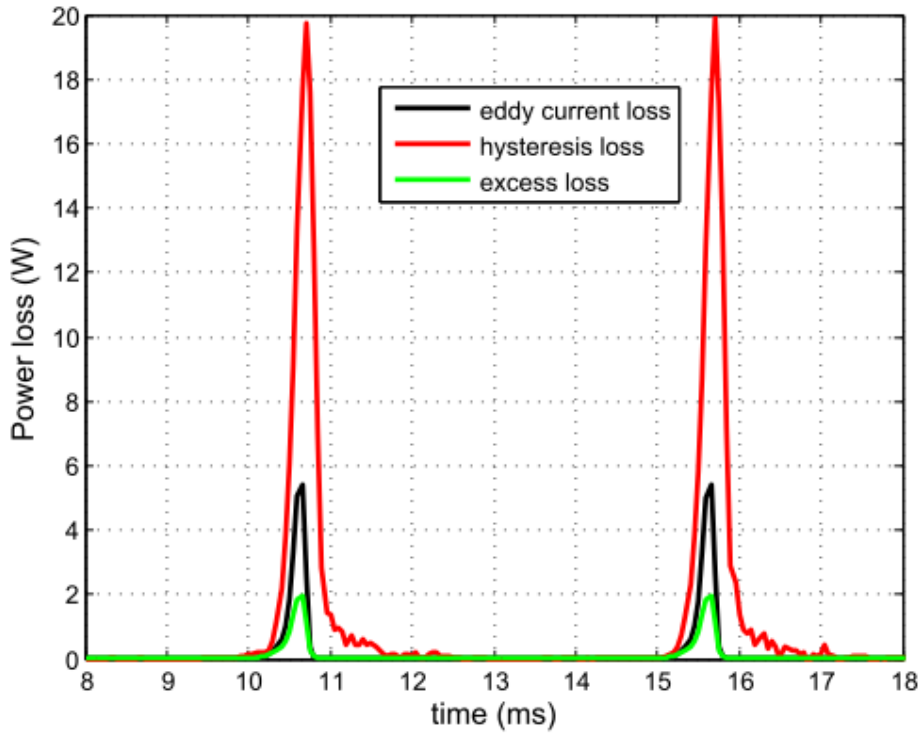

Figure 4.32: Predicted individual loss components for the 100 kHz test case.

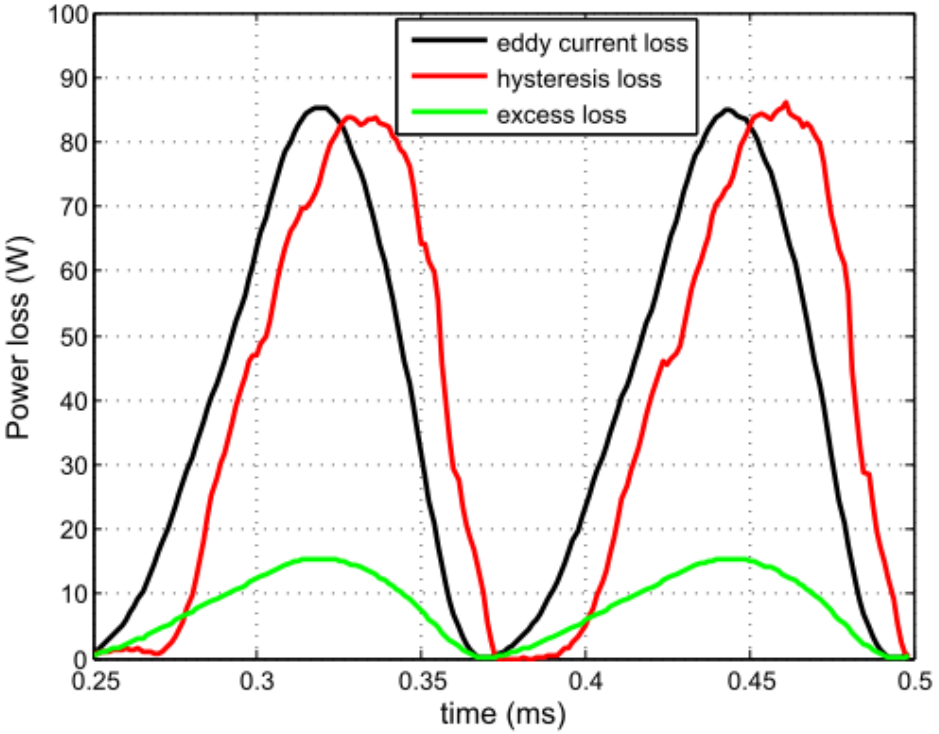

Figure 4.33: Predicted individual loss components for the 4 kHz test case.

The third series of results illustrated in Figure 4.34-Figure 4.37 are for a waveform with a fundamental at 1 kHz incorporating several minor loops. Figure 4.36 shows the comparison of the predicted and measured powers. It can be seen that there are some errors in the model especially around the biased minor loops. Figure 4.38 shows the measured BH loop of the applied test case along with the corresponding anhysteretic curve traced by the model. The shapes and slopes of the minor loops that sit outside the central region are markedly different to the single curve anhysteretic model and hence the larger reactive power flows for these loops cannot be easily modelled by the single curve. Nevertheless the model captures much of the very intricate behaviour and provides a significant improvement in the prediction of instantaneous powers at the source as compared to a lossless model.

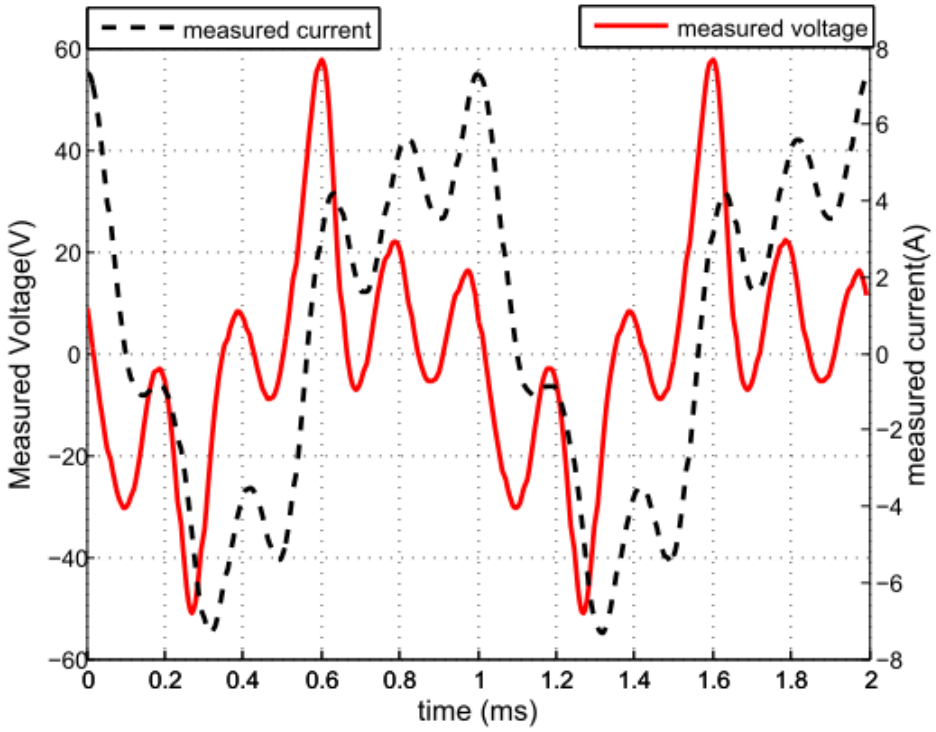

Figure 4.34: Measured voltage and current waveforms for the 1 kHz test case with minor loops.

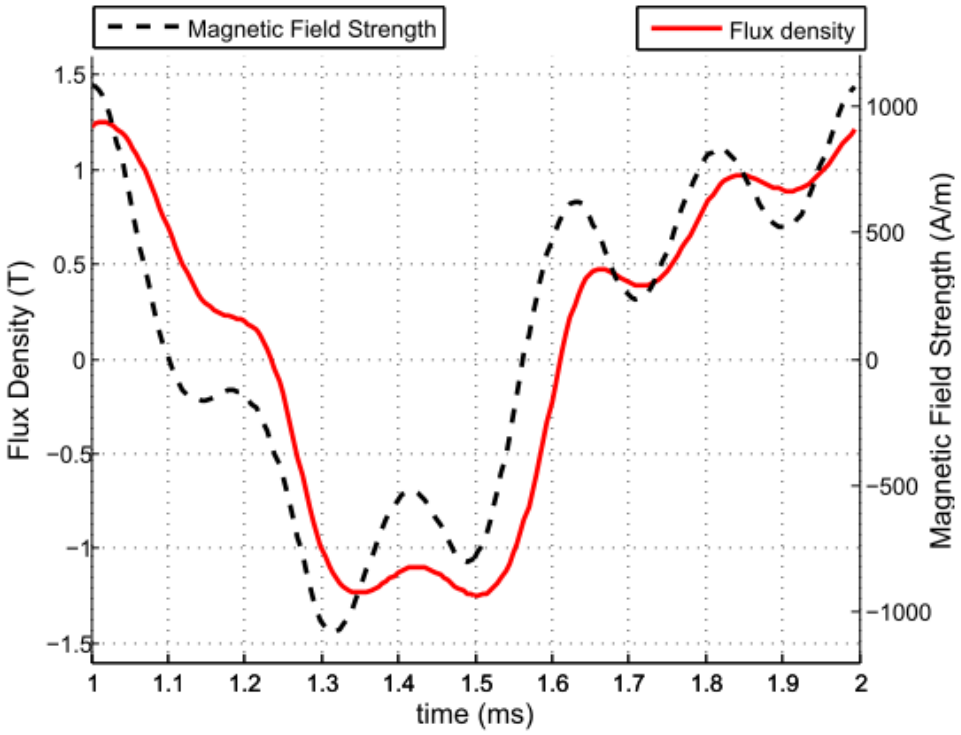

Figure 4.35: Measured flux density for the 1 kHz test case with minor loops.

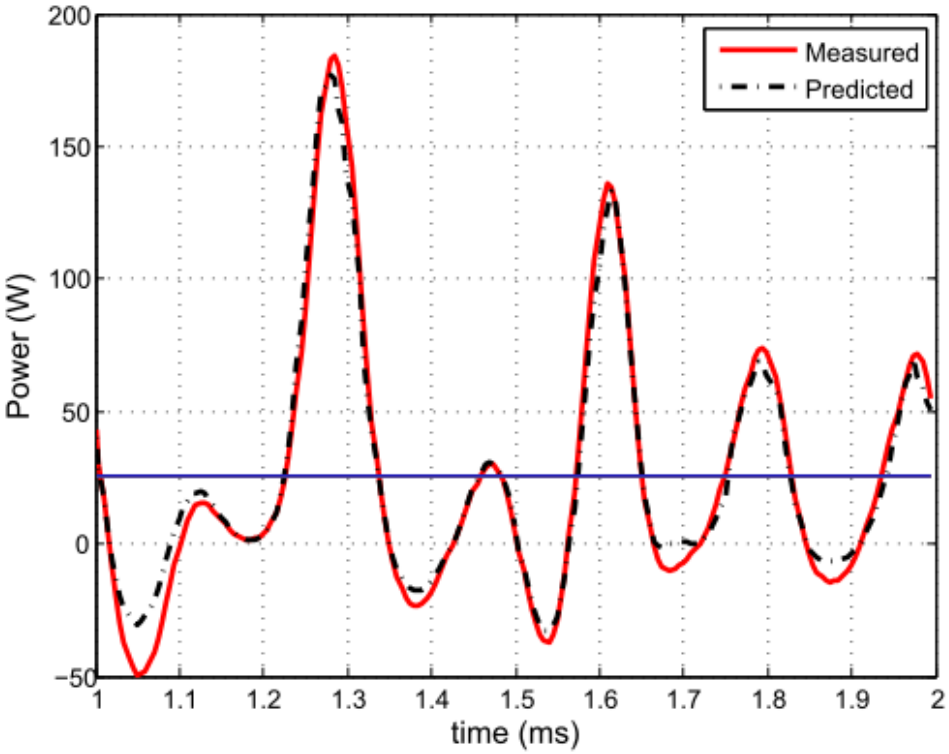

Figure 4.36. Measured and predicted instantaneous power for the 1 kHz test case with minor loops.

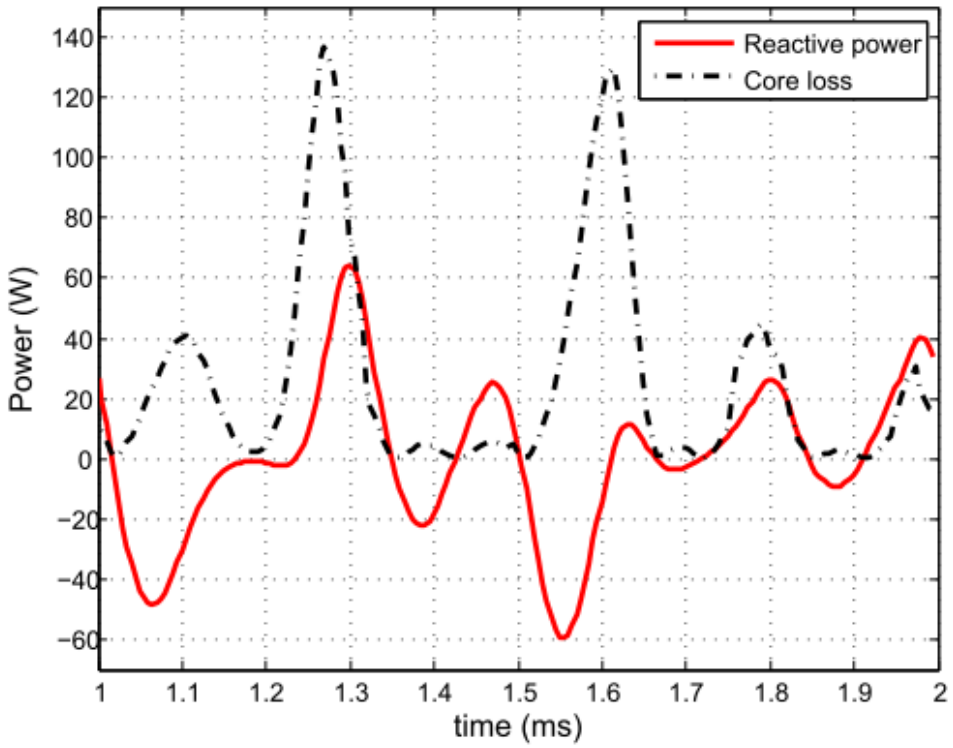

Figure 4.37: Instantaneous core loss and reactive power for the 1 kHz test case with minor loops.

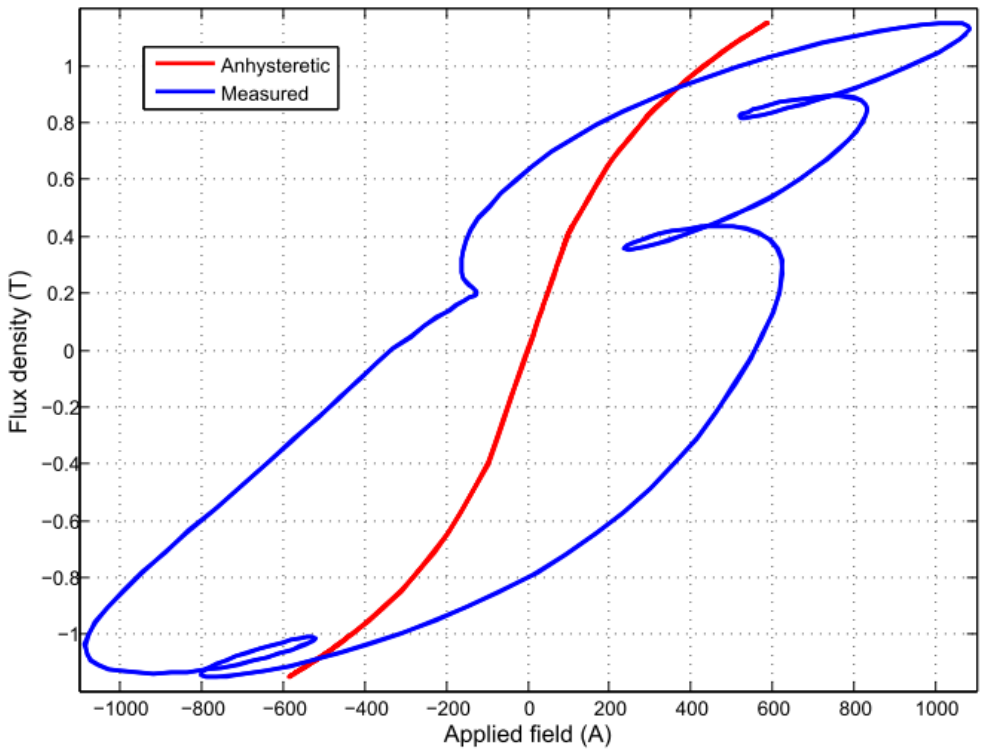

Figure 4.38: Measured BH loop and corresponding curve traced by anhysteretic model.

4.8 High temperature ageing

The literature review in chapter 2 discussed the observation that both the Carpenter 50% Co-Fe grades studied in [1] viz. Hiperco 50 and Hiperco 50-HS exhibited degradation in magnetic properties when aged at temperatures of 500°C, notably in terms of core loss. The data presented in [1] demonstrated that in comparison, the high strength grade Hiperco 50-HS was less affected by elevated temperature ageing, showing a smaller drop in resistivity and lower losses at high frequencies [1]. The VAC grade Vacodur S+ also showed an increase in coercivity on long term exposure to temperatures above 350°C[21]. However very limited data was available to quantify this effect in terms of a direct measure of increase in loss. Due to the absence of magneto-static hysteresis data, it was also not possible to gauge the behaviour of the individual loss mechanisms through the ageing process. Therefore, to gain a better understanding of the behaviour of core loss to long term thermal ageing some additional ageing data was collected. The samples were aged in the high temperature oven at 400°C for a total of 2000 hours. All the measurements described previously in sections 4.5 and 4.6 were repeated at 500, 1000 and 2000 hours. Due to the large set of data collected, a sub-set is described in the following sections. The remaining data is contained in Appendix C for reference. As the two samples composed of the same material grade, but with different heat treatment regimes, very similar trends were observed in both samples.

4.8.1 Effect of thermal ageing on core electrical resistivity

Figure 4.39 shows the measured variation in the electrical resistivity as a function temperature of the two samples taken at the ageing test points. There was a small, but measurable, decrease in the room temperature resistivity with increased ageing of the sample. However the measured resistivity at 400°C for the most aged condition was higher than the corresponding value prior to any ageing. The measurements taken on the Hiperco 50-HS material exhibited similar trends to those reported by Fingers [1]. From a core loss perspective, this should result in comparatively higher eddy current and excess losses at the lower temperatures for the aged conditions whereas the losses at higher temperatures should be lower than those of the un-aged condition. Therefore, the net increase in resistivity due to thermal ageing should be beneficial in terms of reducing higher temperature core loss with time, although the benefits are marginal.

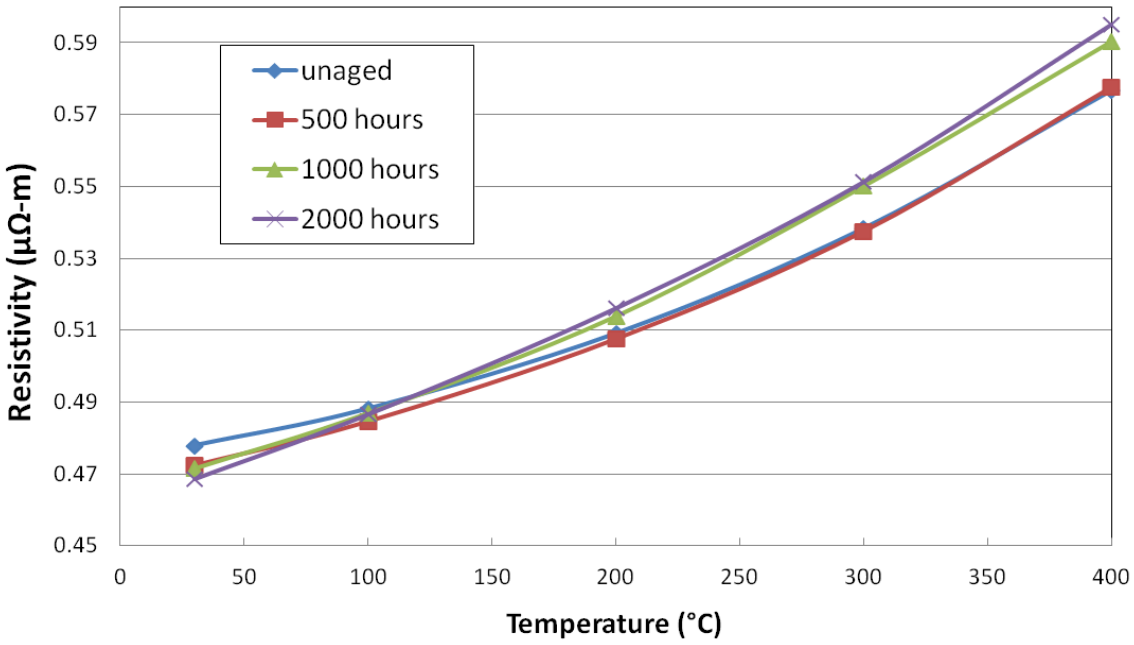

(a)

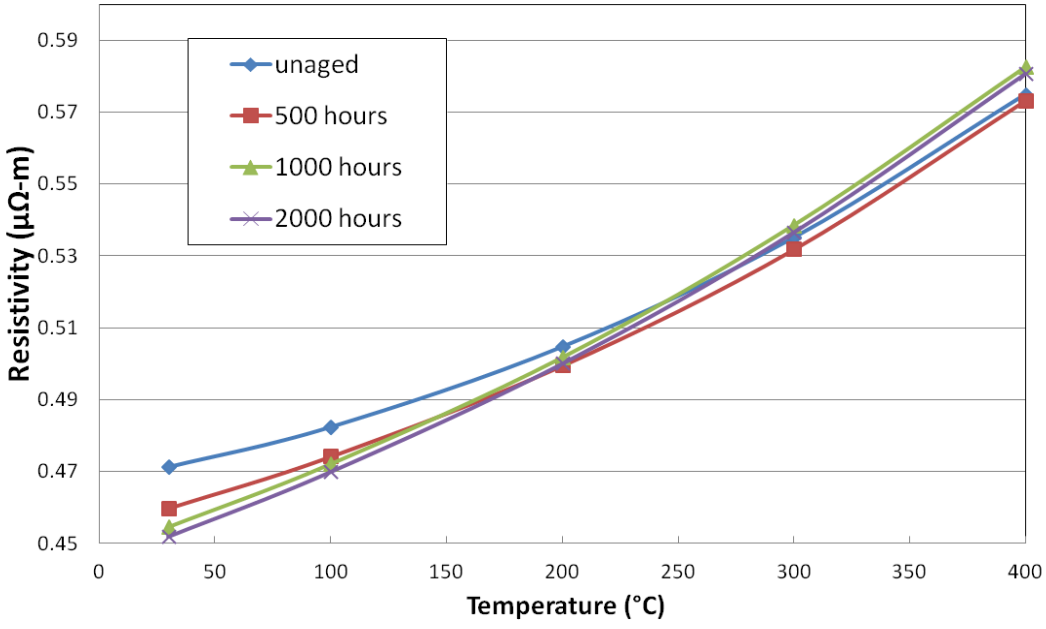

(b)

Figure 4.39: Effect of thermal ageing on resistivity for Vacodur S+: (a) 390MPa, (b) 620MPa.

4.8.2 Effect of thermal ageing on magneto-static behaviour

Figure 4.40 and Figure 4.41 shows the room temperature anhysteretic BH curves for the two samples when aged at 400°C using the horizontal averaging technique described in section 4.5.2. The samples showed a consistent decrease in permeability and saturation flux density with increased exposure to a 400°C environment. Similarly, the energy loss over a cycle under static conditions increased with ageing time. By way of example, as shown by Figure 4.42, there is a ~12% increase in loss at 2T after 2000 hours at 400°C. However, the increase in the measured static loss was lower in comparison to the anticipated values seen in the coefficients obtained using the curve fitting technique described in section 2.7 which suggested ~26% increase in the hysteresis loss for the same ageing time.

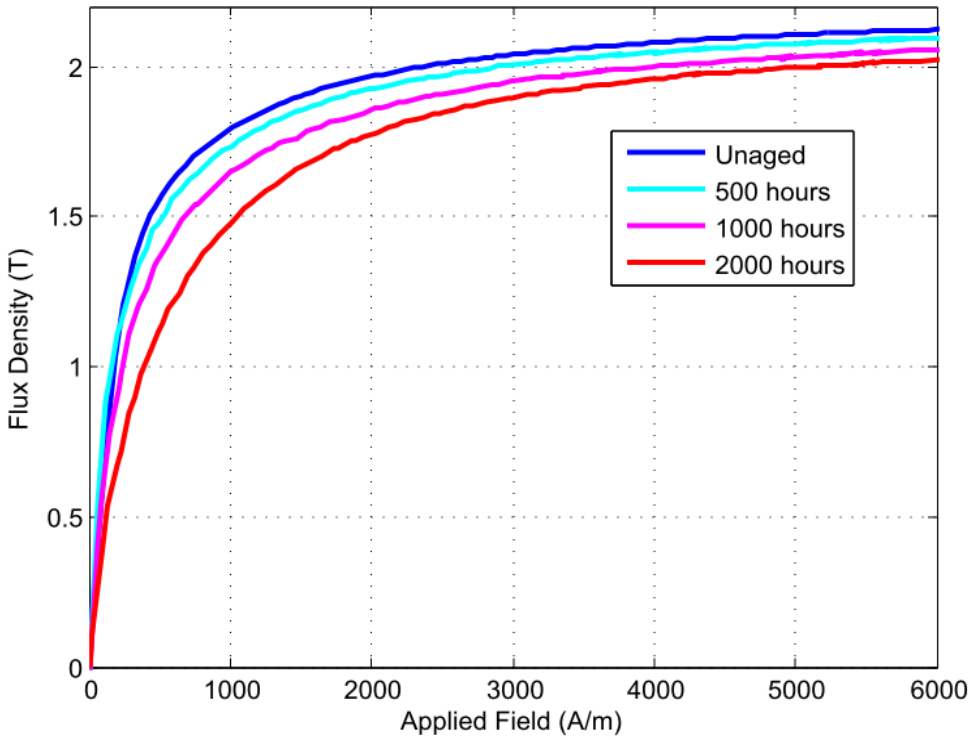

Figure 4.40: Effect of thermal ageing at 400°C on room temperature anhysteretic curves for Vacodur S+ (390MPa)

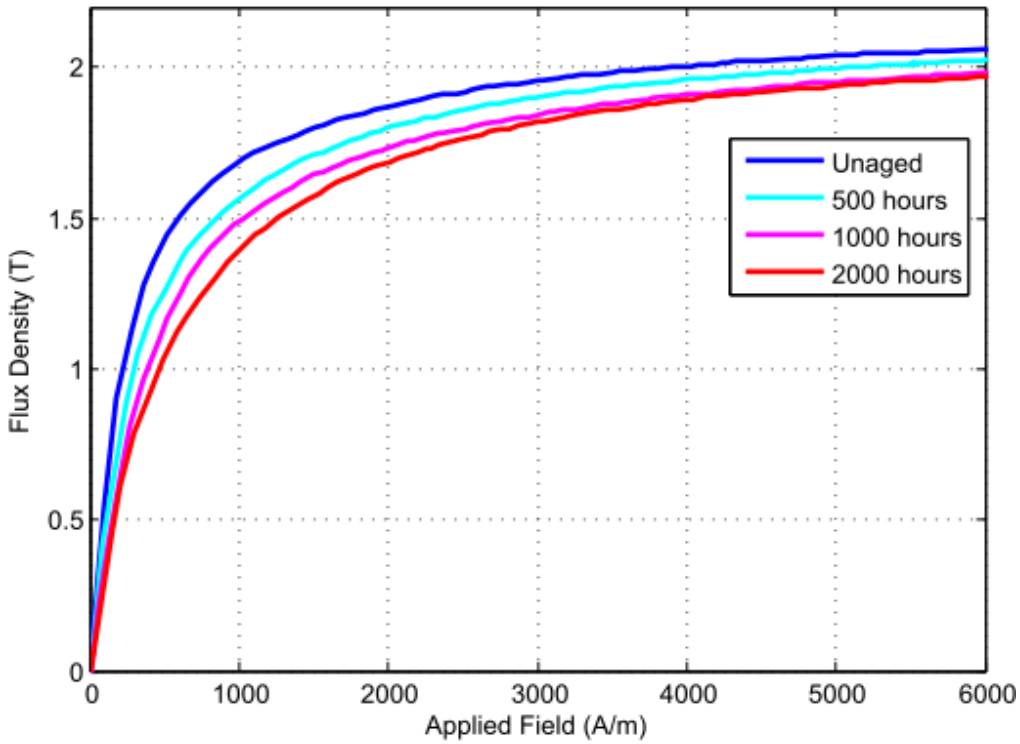

Figure 4.41: Effect of thermal ageing at 400°C on room temperature anhysteretic curves for Vacodur S+ (620MPa).

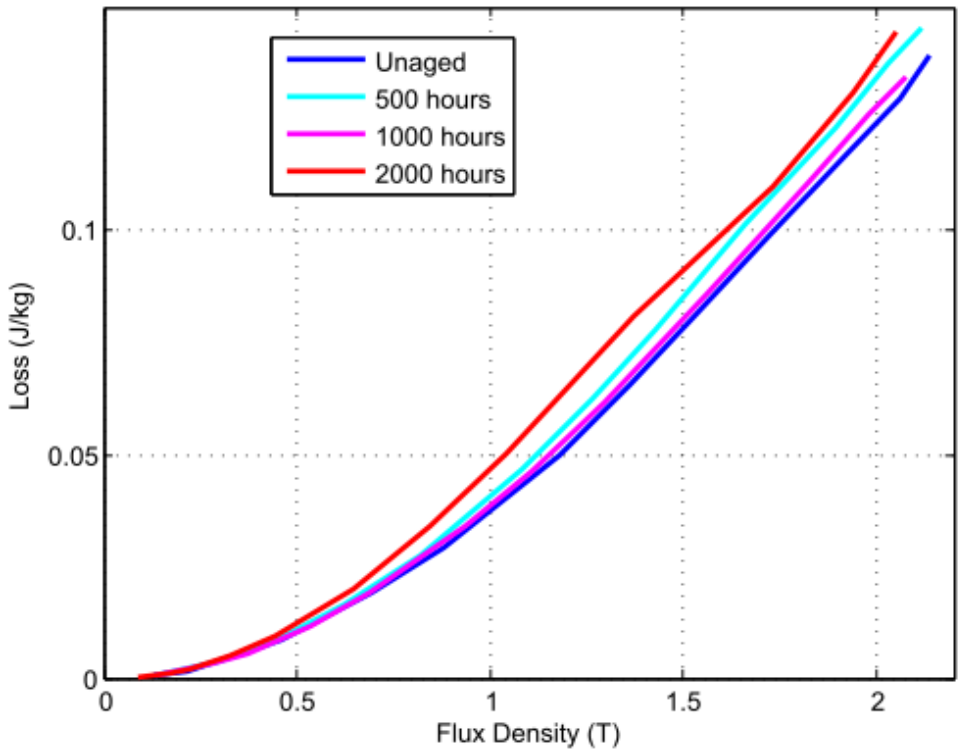

Figure 4.42: Effect of thermal ageing on room temperature static hysteresis losses for Vacodur S+ (390MPa).

4.8.3 Effect of thermal ageing on AC losses

Figure 4.43 shows a sub-set from the many of the measured AC loss measurements taken. In this case, the variation loss is shown as a function of peak flux density for the 390MPa sample for different ageing durations. It can be seen that there is a significant increase in core losses, especially at the higher frequencies (N.B the core loss axis has a logarithmic scale). Similar increases in losses were observed in the Hiperco 50-HS material from the data published in Fingers[1]. Due to the drop in permeability, similar current excitations resulted in lower induced flux densities for the aged samples.

Figure 4.44 shows the predicted vales of k_{exc} for the room temperature measured losses in the 2000 hour aged 390MPa sample. It can be seen that there is a significant increase in the magnitudes of the predicted excess loss constant k_{exc}. The main reason for this increase being that the measured ac losses increased significantly, whereas the measured resistivity and static losses remained relatively stable only changing by small amounts. Hence most of the increase in measured losses has to be absorbed by the excess loss term. The spread in the predicted values of k_{exc} with flux density and frequency also widened. Thus using a single mean value of k_{exc} for the clustered regions described in section 4.6.1 could not be used for the aged samples.

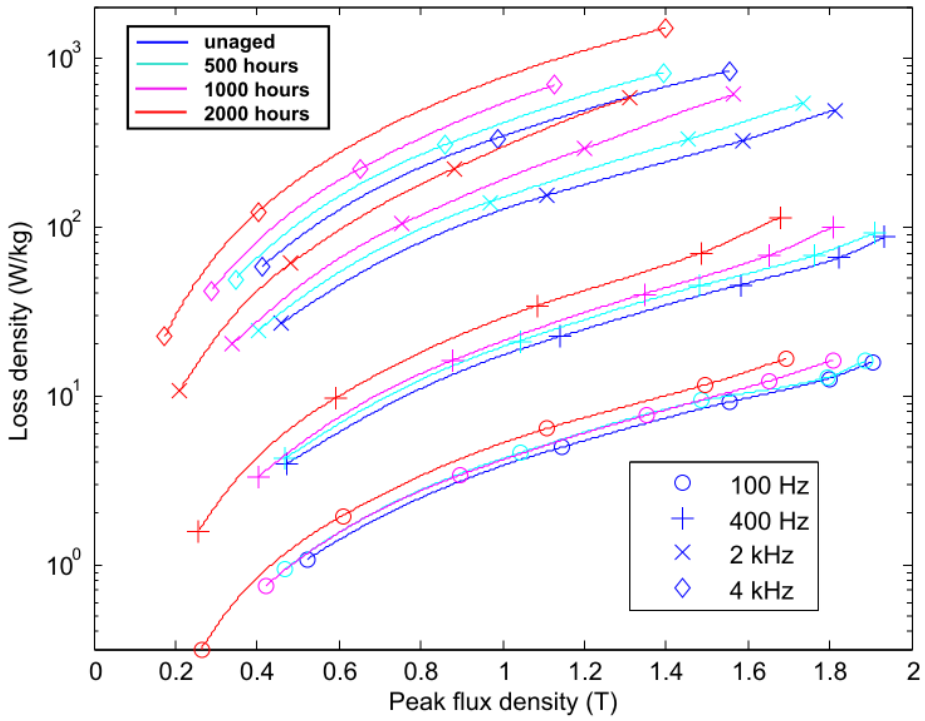

Figure 4.43: Effect of thermal ageing on room temperature ac losses of Vacodur S+ 390MPa.

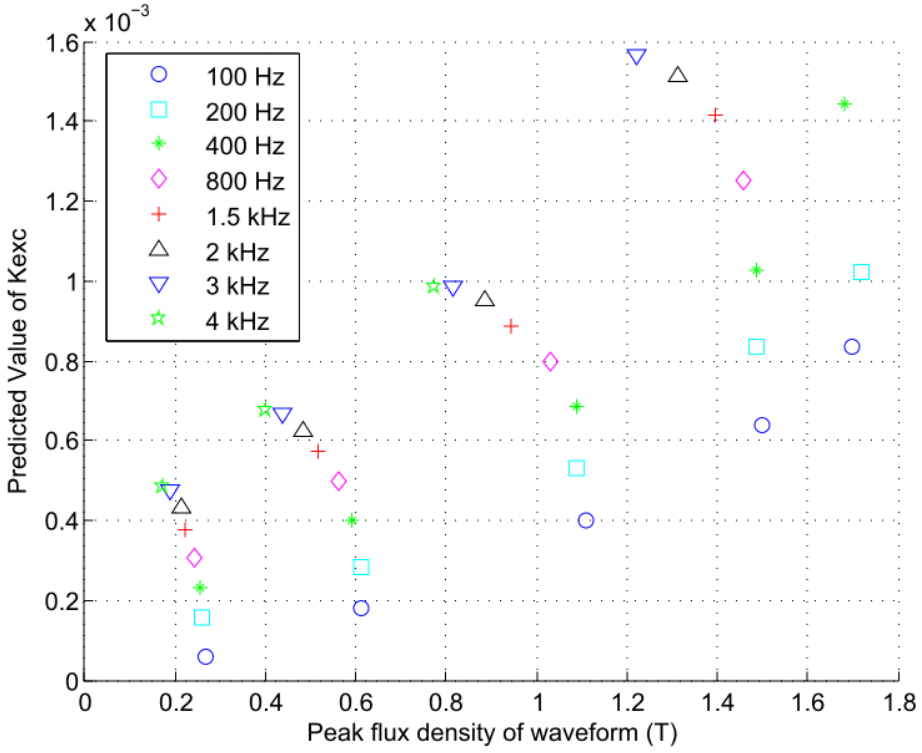

Figure 4.44: Predicted room temperature values of k_{exc} for the 2000 hours aged 390MPa sample.

To account for this increase in predicted excess loss effectively the method for calculating the excess loss and its coefficients had to be modified. As the predicted values of the excess loss coefficient increased with frequency and flux density, an increase in the exponent value which is conventionally set to 1.5 was considered. Rather than using a single term a new excess loss formula was introduced which has the form

$$P_{exc} = k_1 \left(\frac{dB}{dt}\right)^{p_1} + k_2 \left(\frac{dB}{dt}\right)^{p_2} + k_3 \left(\frac{dB}{dt}\right)^{p_3} \quad \textbf{(4.4)}$$

where, the constants k_i and the power terms p_i are fitting parameters which must be calculated from the measured residual loss. Using multiple terms help fit the losses over the complete spectrum using a single set of coefficients rather than using different set of parameters for different regions. Figure 4.45 shows the predicted and measured loss using this technique for the 2000 hour aged 390MPa samples at room temperature. The constants used for this curve fit are shown in Table 4-4. It is worth noting that the exponential terms for the excess loss were as high as 2.7. This model was used to curve fit the measured data for

both samples at all the measured temperatures and ageing times, and showed good correlation for all cases. The parameters calculated and corresponding curve fits are shown in Appendix C.

Table 4-4: Predicted coefficients for the excess loss model

Coefficient / number	1	2	3
p	1.5	1.9	2.7
k	9.56×10^{-5}	1.72×10^{-5}	3.23×10^{-9}

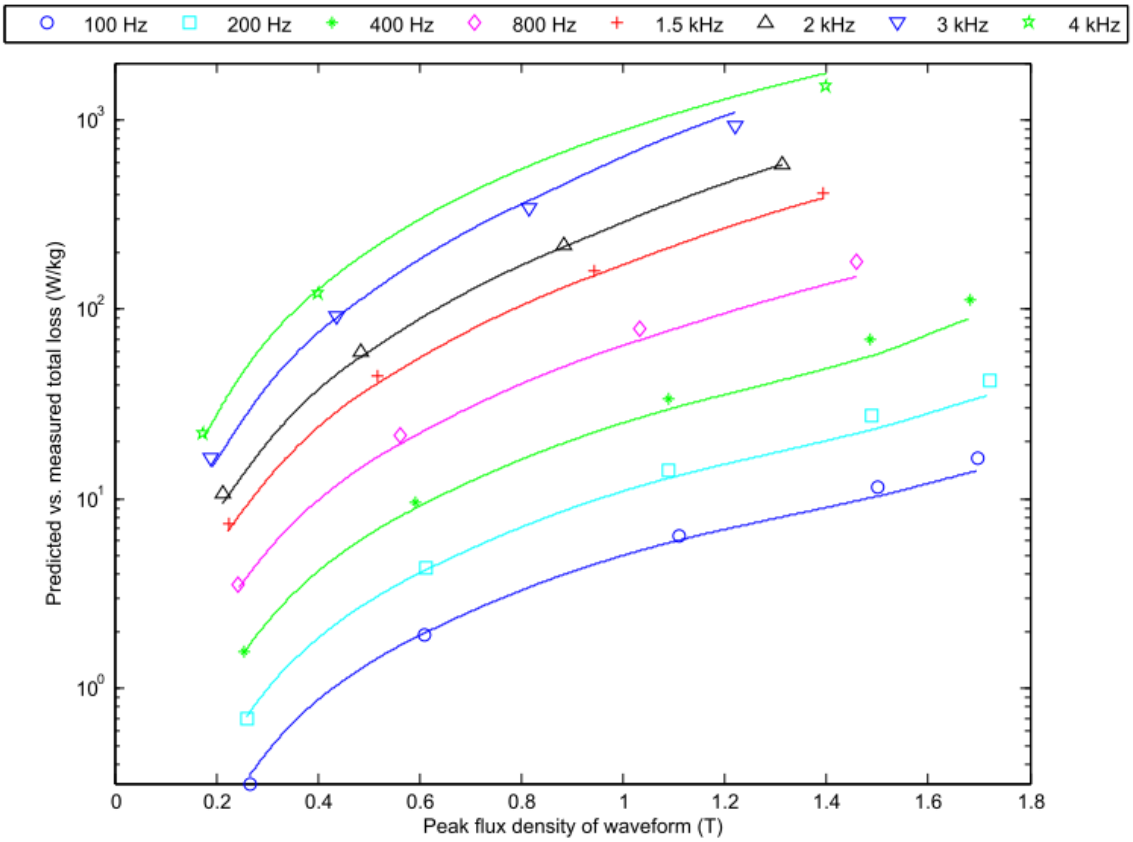

Figure 4.45: Measured (marker) vs. Predicted(line) losses using the modified version of excess loss for the 2000 hour aged 390MPa samples at room temperature.

4.9 Summary

The chapter has described a simplified method to characterise materials for the proposed loss model in chapter 3. The characterisation method takes advantage of the capability of the loss model to predict losses for arbitrary waveforms, and combining these with analytical models and curve fitting techniques generates the required parameters for predicting losses in the specified material. Following on from the literature review in chapter 2, this chapter also supplements the understanding of the behaviour of the high strength 50% Co-Fe materials at high temperatures. The work was directed more towards the effects of the long term thermal ageing on the individual loss mechanisms in the material.

The instantaneous core loss model described in chapter 3 was validated using the available setup required for material characterisation. The results showed very good correlation between the measured and predicted instantaneous powers at the source. However for the test cases considered the anhysteretic or lossless model showed some discrepancies. This illustrated the limitations of using the anhysteretic model for characterising reactive power.

The measurements on the aged showed that the static loop area and resistivity of the material were relatively stable with ageing, and yet there was a significant increase in high frequency core losses. Thus the increase in losses had to be encompassed mainly by the excess loss component. This was contrary to the predictions made using the method described in section 2.7 according to which an increase in both hysteresis and excess losses were predicted.

It was also established that for the aged samples, predicting the dynamic losses over the complete frequency range considered here required modification of the excess loss formula. By dividing the excess loss term into sub-components, an improvement in the loss prediction over the complete range of measured frequencies and flux densities can be observed with a single set of parameters. The parameters obtained using this method showed that values of the exponential power in the excess loss term greater than 2 were required to achieve a good correlation to the measured losses over the entire range.

References

[1] Z. T. Richard Fingers, John Horwath, "High Temperature properties and Aging - Stress related changes of FeCo Materials," Wright-Patterson Air force Base, Ohio AFRL-PR-WP-TR-2006-2176, 2006.

[2] K. Atallah, Z. Q. Zhu, and D. Howe, "An Improved Method for Predicting Iron Losses in Brushless Permanent-Magnet Dc Drives," *Ieee Transactions on Magnetics,* vol. 28, pp. 2997-2999, Sep 1992.

[3] E. Barbisio, F. Fiorillo, and C. Ragusa, "Predicting loss in magnetic steels under arbitrary induction waveform and with minor hysteresis loops," *Ieee Transactions on Magnetics,* vol. 40, pp. 1810-1819, Jul 2004.

[4] S. Zurek, P. Marketos, T. Meydan, and A. J. Moses, "Use of novel adaptive digital feedback for magnetic measurements under controlled magnetizing conditions," *Ieee Transactions on Magnetics,* vol. 41, pp. 4242-4249, Nov 2005.

[5] S. D. Calverley, "Design of a HIgh Speed Switched Reluctance Machine for Automotive Turbo-Generator Applications," PhD, Department of Electronic and Electrical Engineering, University of Sheffield, Sheffield, 2001.

[6] G. Bertotti, *Hysteresis in magnetism : for physicists, materials scientists, and engineers*. San Diego, Calif. ; London: Academic Press, 1998.

[7] A. Standard, "Standard Test Method for Alternating-Current Magnetic Properties of Toroidal Core Specimens Using the Voltmeter-Ammeter-Wattmeter Method 1," ed, 2011

[8] H. Czichos, T. Saito, and L. R. Smith, *Springer handbook of materials measurement methods*. Germany: Springer, 2006.

[9] I. D. Mayergoyz, *Mathematical models of hysteresis*: Springer, 1991.

[10] M. Ruderman and T. Bertram, "Identification of Soft Magnetic B-H Characteristics Using Discrete Dynamic Preisach Model and Single Measured Hysteresis Loop," *Ieee Transactions on Magnetics,* vol. 48, pp. 1281-1284, Apr 2012.

[11] E. Cardelli, E. Della Torre, and G. Ban, "Experimental determination of Preisach distribution functions in magnetic cores," *Physica B-Condensed Matter,* vol. 275, pp. 262-269, Jan 2000.

[12] S. Y. R. Hui and J. Zhu, "Numerical Modeling and Simulation of Hysteresis Effects in Magnetic Cores Using Transmission-Line Modeling and the Preisach Theory," *Iee Proceedings-Electric Power Applications,* vol. 142, pp. 57-62, Jan 1995.

[13] A. Benabou, S. Clenet, and F. Piriou, "Comparison of Preisach and Jiles-Atherton models to take into account hysteresis phenomenon for finite element analysis," *Journal of Magnetism and Magnetic Materials,* vol. 261, pp. 139-160, Apr 2003.

[14] "Datasheet, Soft Magnetic Materials and Semi-Finished Products," vol. Vacuumschmelze, PHT-001 ed, 2002

[15] D. C. Jiles and D. L. Atherton, "Theory of Ferromagnetic Hysteresis," *Journal of Applied Physics,* vol. 55, pp. 2115-2120, 1984.

[16] G. M. Shane and S. D. Sudhoff, "Refinements in Anhysteretic Characterization and Permeability Modeling," *Ieee Transactions on Magnetics*, vol. 46, pp. 3834-3843, Nov 2010.

[17] C. Yicheng and P. Pillay, "An improved formula for lamination core loss calculations in machines operating with high frequency and high flux density excitation," in *Industry Applications Conference, 2002. 37th IAS Annual Meeting. Conference Record of the*, 2002, pp. 759-766 vol.2.

[18] T. L. Mthombeni and P. Pillay, "Physical Basis for the Variation of Lamination Core Loss Coefficients as a Function of Frequency and Flux Density," in *IEEE Industrial Electronics, IECON 2006 - 32nd Annual Conference on*, 2006, pp. 1381-1387.

[19] D. M. Ionel, M. Popescu, S. J. Dellinger, T. J. E. Miller, R. J. Heideman, and M. I. McGilp, "On the variation with flux and frequency of the core loss coefficients in electrical machines," *Ieee Transactions on Industry Applications*, vol. 42, pp. 658-667, May-Jun 2006.

[20] D. M. Ionel, M. Popescu, M. I. McGilp, T. J. E. Miller, S. J. Dellinger, and R. J. Heideman, "Computation of Core Losses in Electrical Machines Using Improved Models for Laminated Steel," *Industry Applications, IEEE Transactions on*, vol. 43, pp. 1554-1564, 2007.

[21] W. Pieper, "Soft Magnetic Cobalt-Iron Alloys at High Temperatures," presented at the High Temperature Magnetic Materials and Components, Oxford, 2009.

Chapter 5 : High temperature switched reluctance machine design

5.1 Introduction

This chapter describes the design optimisation of a switched reluctance (SR) machine for the HP shaft starter/generator application. By way of selecting an appropriate design specification the feasibility of high temperature machine operation is investigated, and an effective design methodology is developed. The key requirement for carrying out a feasibility study of high temperature machines is the knowledge of material behaviour such that its effects on the machine performance can be gauged. The review of the published data on material properties at high temperatures described in chapter 2 illustrated the numerous challenges that must be overcome before a machine can function reliably at high temperatures.

The most noteworthy among these pertain to the long term operation, with material ageing playing a key role in limiting machine performance. The only soft magnetic material capable of continuous operation at temperatures above 350°C viz. the Cobalt-Iron (Co-Fe) grades showed significant degradation with ageing as described in chapters 2 and 4. This will have a knock on effect on the machine temperatures from operating times as low as 500 to 1000 hours. The core loss estimation for the machine in this chapter was carried out using the material characteristics obtained by the methods suggested in chapter 4. However only the material parameters prior to thermal ageing were employed as the ageing data was not collected until after the machine design and build was completed.

Therefore the inevitable increase in losses due to ageing will have to be compensated for by either increasing cooling capability or de-rating machine performance. In order to avoid the latter, selecting an effective cooling strategy is paramount in the design of the machine. Due to the location of the machine on the HP shaft the only easily available method for cooling is via. forced air which is at a temperature of 350°C. Since the maximum hotspot temperature in the coils cannot exceed 450°C there is a margin of 100°C to ambient in which

the losses in the machine must be dissipated. As a result of the increased copper loss at temperatures and relatively higher core loss due to the selected materials, this poses a significant challenge.

5.2 Machine specification

It is envisaged that the initial physical implementation of more electric engines with embedded generation are likely to be for small UAV sized gas turbines. Therefore the specification selected in this case is representative of an embedded HP shaft machine for a UAV sized engine specification. A more conventional gas turbine starter generator specification would require comparatively higher powers and larger size, which can introduce challenges more often related to building and testing of a prototype. A study on rotor mechanical design for a machine specification representative of a larger civil gas turbine, was outlined in [1]. The lower power specification here simplifies the rotor mechanical design allowing for a single piece rotor lamination, and hence the direction of the work is focused more on the challenges related to high temperature operation, laboratory testing at temperature being the ultimate objective.

It should be noted that the HP shaft application would require the machine to be operated as a starter/generator, with the starter specification being different to that of the generating mode. The specification outlined in [2] suggests that in the starting mode, the machine would require similar output power levels at up to a third of the rated speed. However, the temperatures are likely to be relatively lower and the machine would typically operate under motoring mode for a very limited period. Therefore, the machine may be designed solely to the generating mode specification, keeping in mind that some level of compromise in performance/efficiency may result during starting mode operation. As a result the machine specification is described here under generating mode only.

Table 5-1 outlines the main design specification of the machine. The specified rotational speed of 30,000 rpm may be considered to be on the higher side of the HP shaft operating speeds. However this places emphasis on a number of challenges such as the high stresses on the rotor. The rated power is specified at 15kW, which requires an average torque of 4.8N-m. On the drive aspect, the machine is specified to operate from a 270V fixed DC bus, which is the typical rating of the high voltage bus on commercial aircraft gas turbines. For the high speeds considered however, the 270V may be considered to be a relatively low

voltage which necessitates lower inductances to generate sufficient power flow to and from the machine.

The location of the machine on the HP shaft introduces dimensional constraints that have been neglected in this study as the purpose here is to gauge achievable power densities, rather than design a machine to match a specific engine. However some dimensional constraints were selected to represent traits of high pressure shaft such as the inner diameter of the rotor shaft which is constrained by the diameter of the HP shaft. The HP shaft is the outermost of the three shafts and has the largest diameter. The shaft diameter of 60 mm for this machine was selected to be representative of a HP shaft of a small UAV sized engine. The stator outer diameter was not restricted by the specification; although the maximum width of laminations available for the desired material was 220mm for a lamination thickness of 0.15mm.

Table 5-1 : Specification for the HP shaft SR machine.

Quantity	Value
Power (kW)	15
Speed (rpm)	30,000
DC supply voltage (V)	270
Ambient temperature (°C)	350
Peak winding hotspot temperature (°C)	450

5.3 Machine design and sizing

5.3.1 Mechanical aspects in rotor sizing

A useful starting point for sizing an SR machine is to regard the net torque as being proportional to the bore volume[3] using the equation:

$$\mathbf{T = k_t . (BA) . D^2 L} \tag{5.1}$$

The coefficient k_t which takes into account several factors such as the efficiency and saliency ratio which is the ratio of aligned to unaligned inductance. In high speed machines, the maximum outer diameter of the rotor tends to be constrained by the mechanical strength of the rotor material, as it must be capable of withstanding centrifugal loading. A formula for calculating the hoop stress of a SR rotor from its diameter and rotational speed was derived in [4] as

$$\boldsymbol{\sigma_{rot} = k_\sigma \rho_{rot} \omega_{mech}^2 D_{rot}^2} \tag{5.2}$$

Conversely, if the maximum allowable stress levels of the material are known the maximum rotor diameter can be calculated as

$$\boldsymbol{D_{rot} = \sqrt{\frac{\sigma_{max}}{k_\sigma \rho_{rot} \omega_{mech}^2}}} \tag{5.3}$$

The constant k_σ is a dimensionless number estimated from numerous finite element analyses conducted for a range of rotor bore diameter to rotor outer diameter ratios and fillet radius to rotor outer diameter ratios. The value k_σ was shown to vary from 0.206 to 0.222 for rotors with bore diameter to outer diameter ratios ranging from 0.04 to 0.60. It was concluded by the authors of [4] that adopting a single value of k_σ of 0.2 results in an accurate prediction of peak stress for most practical rotor geometries [4].

Although the rotor material possessed a 0.2% yield stress of 620 MPa, the maximum allowable localised stress in the rotor was limited to 175 MPa to ensure sufficient margin to accommodate degradation in the material mechanical properties with ageing as described previously in section 2.5.1. Using equation 5.3, the maximum outer diameter of the rotor was calculated as 100 mm for a rotational speed of 30,000 rpm. The rotor inner diameter was constrained by the diameter of the turbine shaft which was specified to be 60 mm resulting in a rotor design space which comprises of an annulus of radial thickness 20 mm which must contain the rotor teeth and rotor back iron. The net torque produced is a function of the saliency ratio which can be increased if the unaligned inductance is reduced. The unaligned inductance can be reduced if the distance between the stator and rotor tooth tips (d_u) are further away from each other and the rotor tooth height (h_r) is larger as shown in Figure 5.1.

However this relationship is not linear and increasing the ratio of the tooth height to the unaligned distance above values of around 1.5 to 2 results in relatively small further gains in the inductance ratio[5]. Accordingly, an acceptable trade-off in electromechanical performance is obtained with a rotor tooth height of 1.5 times the distance between the teeth at the unaligned position is required. Furthermore, the radial thickness of the rotor core must be at least 1.5 times the width of the rotor teeth to avoid saturation. Therefore, for fixed rotor inner and outer diameters, the number of rotor poles which are likely to produce reasonable electromagnetic performance tend to be limited to some minimum number. Table 5-2 shows the minimum rotor diameter for the different stator and rotor pole combinations given a rotor inner diameter of 60mm. For the 100mm rotor diameter limit imposed by consideration of centrifugal loading, the first feasible stator/rotor pole combination was a 3-phase 12/8 SR machine.

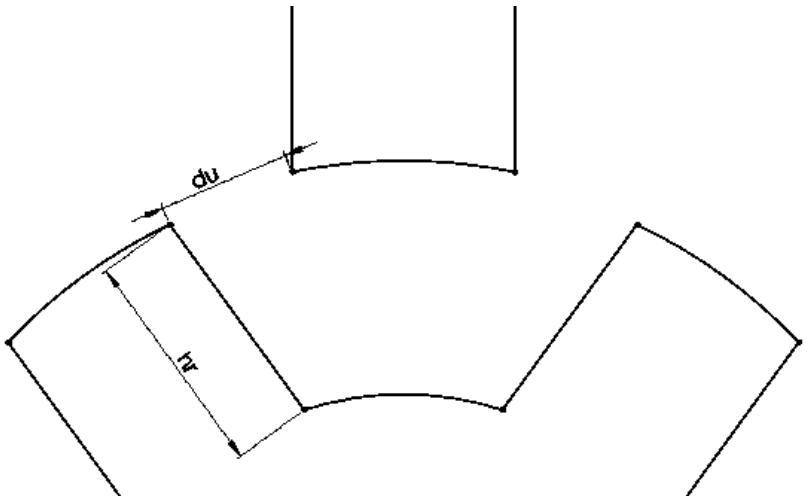

Figure 5.1: SR rotor in the unaligned condition showing tooth height and unaligned distance.

Table 5-2: Minimum rotor diameter for different pole combinations for a fixed inner diameter of 60mm.

Stator and rotor pole combinations	6/4	8/6	12/8
Stroke angle in mechanical degrees	30	15	15
No of phases	3	4	3
Minimum rotor diameter (mm)	193	115	92

5.3.2 Current density and packing factor

The operating current density in the coils is a key factor in the sizing of electrical machines, with higher current densities yielding smaller machines since a reduced slot area is required to accommodate the rated ampere turns. However, the copper loss is proportional to the current density and the resulting temperature in the coils turns out to be a limiting factor. For a small to medium sized machine operating at room temperature, and cooled by either natural convection or modest volumes of forced air, a typical value of the rms current density in the coil tends to be around 6 A/mm^2 rms. In higher power dense machines, current densities as high as 12 to 14 A/mm^2 rms can be adopted, typically in conjunction with forced liquid cooling to manage the increased copper loss.

These starting estimations of current density however cannot be applied to machines operating at 350°C due to the 130% increase in the resistance of the stator coils compared to room temperature. To compensate for the increased resistance at temperature, the current density has to be reduced by at least a factor of the square root of the increase in resistivity. For example a four times increase in Copper resistance may require halving the operating current density. Taking into consideration the limited cooling and relatively small temperature differential between the stator coil hotspot and surrounding ambient a conservative starting estimate of $3A/mm^2$ rms was adopted for the initial design phases. The machine designed using this starting current density is referred to subsequently as the 'baseline design' forms a reference for subsequent designs.

A key factor in the performance of a coil, and in turn the overall machine, is the so-called packing factor which is defined as the proportion of the slot cross-section occupied by the core copper conductor as opposed to insulation, encapsulation voids and gaps. It is useful to consider the net packing factor (i.e. the proportion of the overall slot area occupied by Copper) as being made up by the product of the coil fit factor and the packing factor within the coil cross-section itself. The overall packing factor is a critical feature in the design of machine, and has a first-order impact on the size of a machine to meet a given power rating. From previous experience of manufacturing pre-formed coils using the selected wire and encapsulate, it was found that a reasonable estimate of the achievable coil packing factor was of the order of 0.3. This is low in comparison with machines wound with conventional wire, where packing factors of 0.6 or so can be achieved with pre-formed coils. The combination of low current density and low packing factors is likely to require much deeper slots to accommodate a given mmf. Therefore, the split ratio which is defined as the ratio of the bore

diameter to the stator outer diameter will be lower as compared to conventional machines, resulting in a rather unusual proportion for the machine.

5.3.3 Maximising slot utilization

The constraints of pre-formed coils with low packing factors operating at modest current densities will require comparatively deep slots in the stator. In order to minimize this penalty, an investigation into the geometry of the preformed coils and stator slots was undertaken to maximise the slot fill. The most straightforward embodiment of a pre-formed coil which fits over a parallel sided stator tooth is an essentially rectangular cross-sectioned coil as shown in Figure 5.2. The width of the rectangular coil (labelled as w_c in Figure 5.2) is limited to half the slot opening l_{so} so as to allow adjacent coils to pass each other during assembly of the stator. It can be shown that for the dimensions defined in Figure 5.2(a), the maximum coil fit factor (i.e. the proportion of the slot occupied by the overall coil cross-section) is given by:

$$\mathbf{c_{ff} \approx \frac{2}{\left(1 + \frac{l_{sb}}{l_{so}}\right)}} \tag{5.4}$$

It should be noted that the coil fit factor is influenced by the value of the ratio $\frac{l_{sb}}{l_{so}}$ which is in turn determined by the bore diameter, the slot depth H_s and the number of poles. For most practical machine coil designs, rectangular coils can achieve values of c_{ff} ranging from 0.5-0.7 (tending to be higher in shallower slots).The coil geometry used in this machine is aimed at improving the maximum coil fill factor that can be achieved with coils which can still be pre-formed and then fitted to parallel sided stator teeth. It is based on employing an asymmetrical arrangement of coils in which two different coil cross-sections are used within the machine (as compared to the single rectangular cross-section shown in Figure 5.2a). The proposed arrangement is shown in Figure 5.2b. The individual coil dimensions were selected such that the two coils have equal cross-sectional area. As will be apparent, the coils must be inserted in a specific order, i.e. the rearmost coil must be inserted first.

In establishing suitable coil dimensions for a given slot, it is necessary to meet two constraints, viz.:

- The width of both coils must be less than or equal to the slot opening.
- The coil cross-sectional areas must be equal

For a given slot depth, the only variable in the geometry is the width of the rectangular winding W_c , with the dimensions of the second coil following on as a consequence of W_c . The value of W_c that gives a constant area in both windings is given by the positive root of the equation.

$$\frac{\mathbf{W_c^2}}{\mathbf{2\tan\left(\frac{2\pi}{N_s}\right)}} + \mathbf{H_s W_c - H_s l_{so} = 0} \qquad \textbf{(5.5)}$$

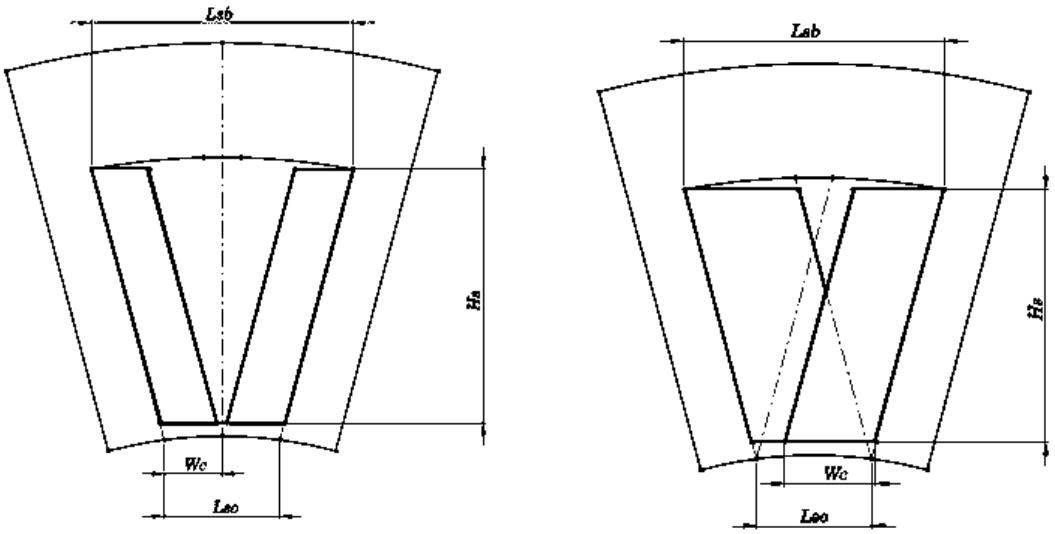

(a) **(b)**

Figure 5.2: a) Simple rectangular cross-sectioned coil. b) Cross section of asymmetrical coil arrangement.

As noted previously, the coil geometry proposed optimises the slot fill factor subject to the constraints that the coils are required to pass each other during insertion of the second coil into the slot and that both are capable of passing through the slot opening. However, implicit in the geometries proposed are additional factors that the coils of adjacent phases which share a slot have equal net cross-sectional area and that only one coil is inserted over

each tooth. It is difficult to envisage a machine where the former condition of equal cross-section would not be desirable or indeed essential for balanced operation. However, the latter condition of a single coil would not have such a fundamental impact on machine performance. Hence, an approach in which the overall coil structure which is inserted onto an individual tooth comprises two or more sub-coil (suitably connected) could be employed. A symmetrical coil arrangement with two sub-coils is shown in the two possible embodiments in Figure 5.3. However, due to similar restrictions in terms of sub-coils needing to pass each other, there are no discernible benefits in terms of fill-factor to warrant incurring the penalty of increased complexity of terminations (with potential consequences for reliability). As will be apparent from Figure 5.3, the constraint that any sub-coil must also slot over a tooth and pass through the slot opening precludes the filling of the all the rear most regions, specifically it cannot fill the triangular shaped wedge which lies behind the dashed limiting line of Figure 5.2b.

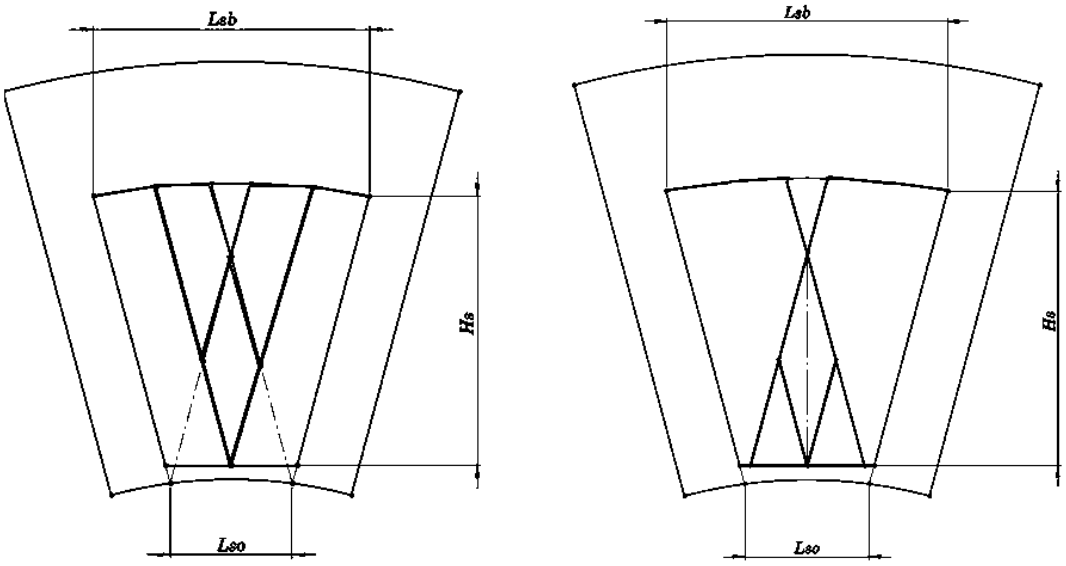

Figure 5.3: Coil arrangements in which each tooth is equipped with two sub-coils.

A 12 slot/8 pole SR machine equipped with this asymmetrical coil arrangement is shown in Figure 5.4. As will be apparent diametrically opposite teeth have the same coil type. It is recognised that the two coil types will have slightly different leakage reactances (the extent of which will vary from machine type to machine type) and potentially marginally different emf constants. However, such differences are likely to be of the order of a few percent at most and unlikely to significantly affect performance. Moreover, it is likely that the

two types of coil can be balanced across the individual phases of the machine. By way of example, in the 12 coil / 3 phase machine shown in Figure 3, phase A would consist of coils at 12, 3, 6 and 9 o'clock, i.e. 2 of each type would make up a series wound phase.

For the stator dimensions shown in Figure 5.4, equipping the machine with straightforward symmetrical rectangular coils would yield a coil fill factor of 57% whereas the asymmetrical arrangement shown in Figure 3 increases this to 83%. The coil arrangement in Figure 5.3 with two sub-coils had a coil fill factor of 84%. Hence either arrangement can be employed, the enhancement from which would have a significant impact on the power density of the machine. On comparison it was found that as the tooth height is increased, the arrangement with two sub-coils produced a marginally higher coil fill factor. This arrangement although designed for high temperature coils, is of equal utility and benefit in all electrical machines irrespective of whether they are required to operate at high temperatures.

5.3.4 Radial air gap between rotor and stator

In singly excited machines, the penalty for utilising a larger air gap in terms of power density can be substantial as the ampere turns required to maintain the air gap flux density increases significantly (broadly in proportion to the air gap up to the point of significant magnetic saturation in the stator and/or core). To accommodate the larger ampere turns, deeper slots are required, which when combined with the constraints on the current density and packing factor described above, results in a relatively large stator outer diameter. The deeper slots may result in increased cross slot leakage which can promote magnetic saturation and the larger stator volume reduces the machines overall power density. In power dense machines, it may be considered preferable to design the machine such that the core material has maximum utilisation by operating it with significant magnetic saturation. However, as the flux density in the core material is driven past saturation, only diminishing returns in flux density are achieved with increasing larger ampere turns which in turn necessitate a larger stator core diameter, increasing the weight significantly. Therefore to keep the required ampere turns low, the operating core flux density can be reduced. The resulting drop in mechanical torque however must be compensated for by increasing the axial length which again has a penalty on weight. In this case the air gap flux density was selected to be 1.8T which is representative of the 'knee point' on the BH curves of the core material.

Conventional SR machine utilise small air gaps of the order of 0.3mm to 0.5mm as is the case with most singly excited machines. In gas turbines applications small air gaps such as 0.3mm may be impractical due to mechanical considerations such as shaft vibrations and uneven thermal expansion. That said, aerospace gas turbines can achieve blade tip clearances in the range of 0.4 to 0.5 mm in the high pressure turbine, by employing active tip clearance control [6] on the turbine casing. This is typically implemented by using a cooling jacket on the casing to shrink the casing size or possibly actively controlled electrical actuators. However it is unlikely that such level of control could be applied to the HP shaft machine air gap and the air gap may have to incorporate the large changes in clearance during the different operating phases of the turbine. Table 5-3 shows the required slot area and split ratio for increasing air gaps, while maintaining the current density at $3A/mm^2$ and air gap flux density at 1.8T. In this instance an air gap of 0.5mm was selected to maintain the stator outer diameter below 220mm which was the maximum width of the stator lamination available from the manufacturer.

Table 5-3: Effect of increasing air gap on the split ratio for a fixed current density of $3A/mm^2$ at a packing factor of 0.3.

Air gap (mm)	Ampere Turns (A)	Slot Area (mm^2)	Split Ratio
0.5	1730	467	0.47
0.8	2637	717	0.40
1.0	3296	900	0.37

5.4 Electromagnetic modelling of the baseline design

The established methods of sizing SR machines [7, 8] were adapted to include the material parameters at high temperatures. The dynamic modelling techniques developed in chapter 3 can be used to achieve improved estimates of core loss and performance. For all the electromagnetic FE simulations the core material was assumed to be at a steady state temperature of 400°C whereas the coils were assumed to be at 450°C. The magnetic material data for the stator and rotor cores at 400°C was measured using the techniques described in chapter 4. The electrical resistivity of the coils at 450°C was calculated using a single-valued

published temperature coefficient of resistance for Copper ($\alpha_c = 0.00393/°C$), which was shown to be constant up to 500°C[6].

A two dimensional cross-section through of the baseline machine design is shown in Figure 5.4 with the key dimensions detailed in Table 5-4. The slot depth required to accommodate the coils was 43mm resulting in a split ratio of 0.47, value which is lower than the typical values of 0.6-0.7 encountered in machines designed to operate at lower temperatures. The total estimated active weight of the machine (i.e. excludes stator casing, rotor hub and shaft) is ~14.2 kg which yields a power density of ~1.1 kW/kg.

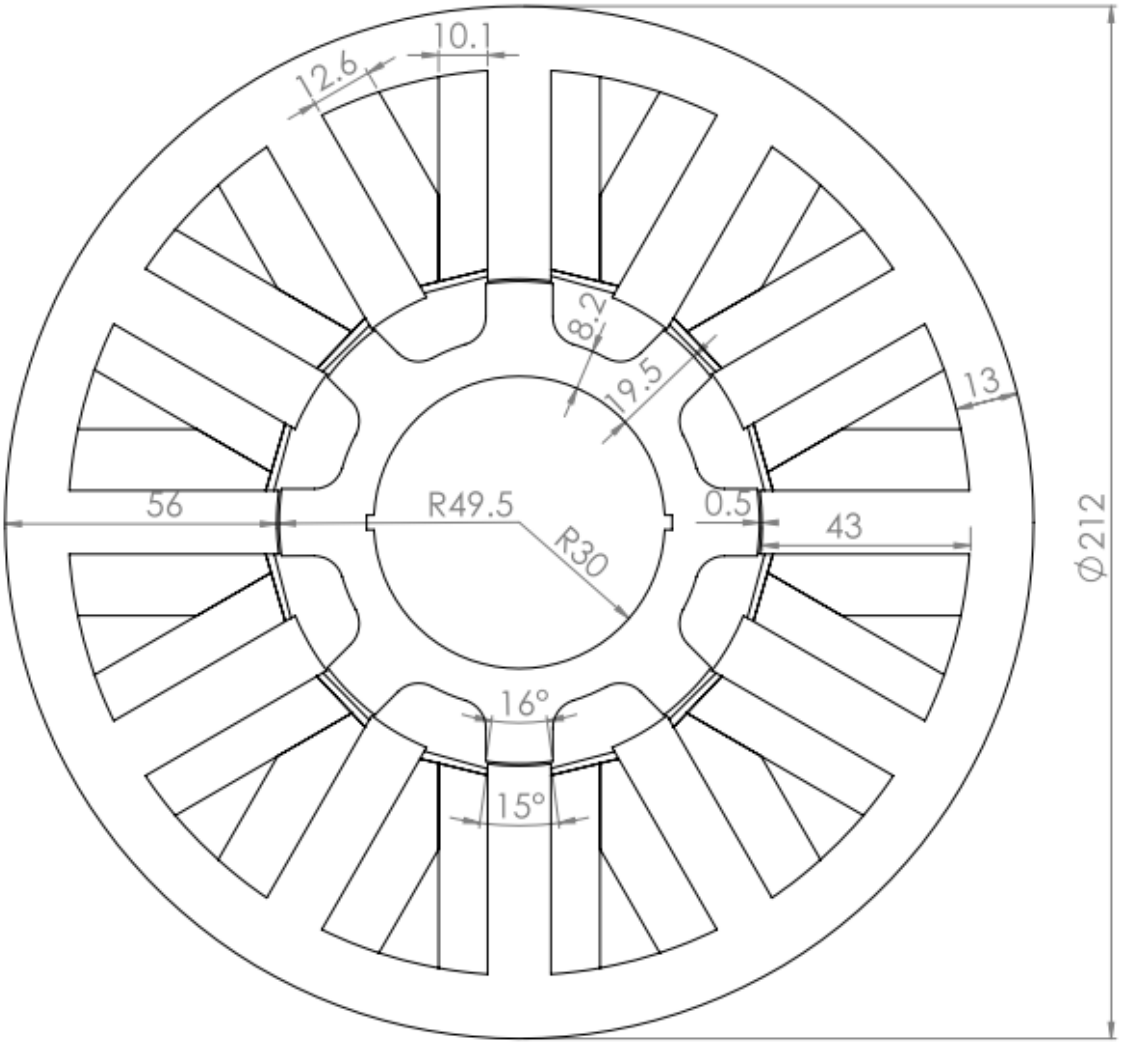

Figure 5.4 : Baseline design drawing with asymmetric coil arrangement (all linear dimensions in mm).

Table 5-4 : Key dimensions for the baseline design

Dimension	Baseline design values	Units
Rotor diameter	100	mm
Air gap flux density	1.8	T
Stator diameter	212	mm
Packing factor	0.3	-
Slot area	432	mm^2
Air gap	0.5	mm
Slot depth	43	mm
Split ratio (rotor outer diameter : stator outer diameter)	0.47	-
Axial length	70	mm
Number of series turns per phase	20	-
Weight of rotor + stator cores	10.2	kg
Weight of Copper + encapsulate	4.0	kg
Total active weight	14.2	kg

The electromagnetic characterisation of the baseline design was performed out using two-dimensional electromagnetic finite element solver, specifically Comsol Multiphysics. The magneto-static field distribution within machine was calculated for a series of increasing ampere turns in each phase from 400 to 6000 A in steps of 400 A at all rotor angular displacements from the unaligned to aligned position in 1° (mechanical) increments. The magnetisation behaviour of the core material was represented by anhysteretic (or lossless) BH curves (one for stator core and a different characteristic for the rotor core).

Figure 5.5 shows the predicted flux linkage for a single phase as a function of stator Ampere turns with the rotor position varying from the unaligned to aligned. The nominal rated current density of 3A/mm^2 corresponds to a phase Ampere turns of 3132A. As shown Figure 5.5, the rated current density corresponds to the onset of saturation in the aligned position. However 3A/mm^2 corresponds to the rms current density, and under dynamic conditions the peak current can be more than two times the rms value. The corresponding variation the static torque per unit length as a function of rotor angle for the phase ampere turns increasing in steps of 400 A is shown in Figure 5.6. The torque at each combination of rotor angle and current was calculated by virtual work method.

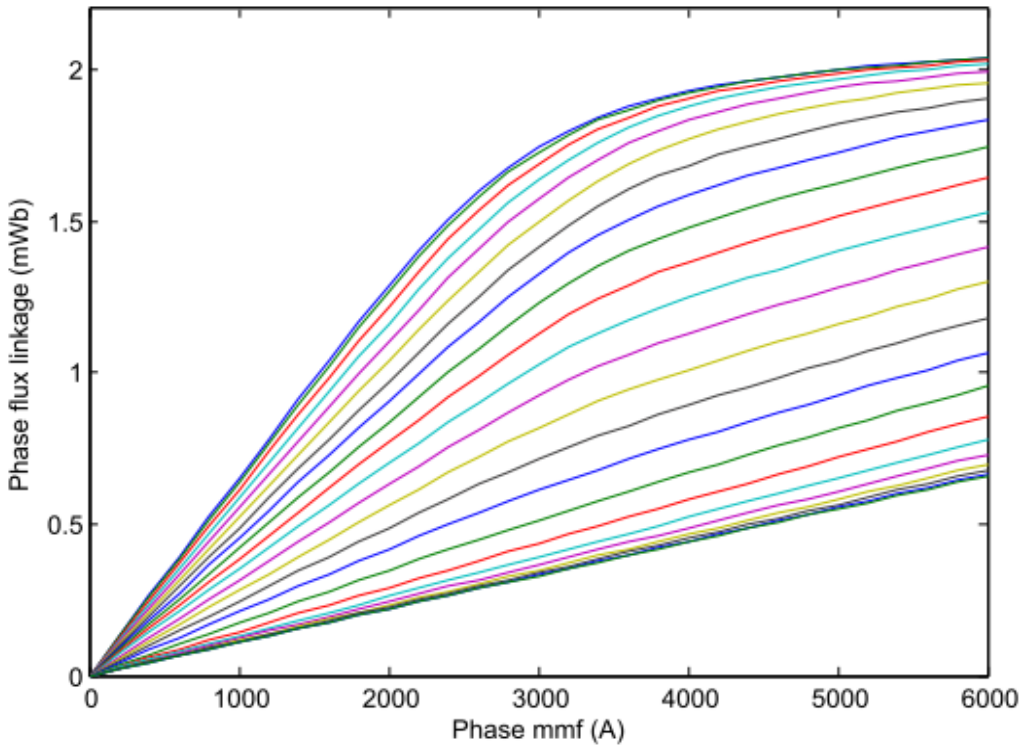

Figure 5.5: Variation in phase flux linkage as function of vs. mmf plot from magneto-static FE solutions for rotor angles varying from unaligned to aligned positions in steps of 1 mech. deg.

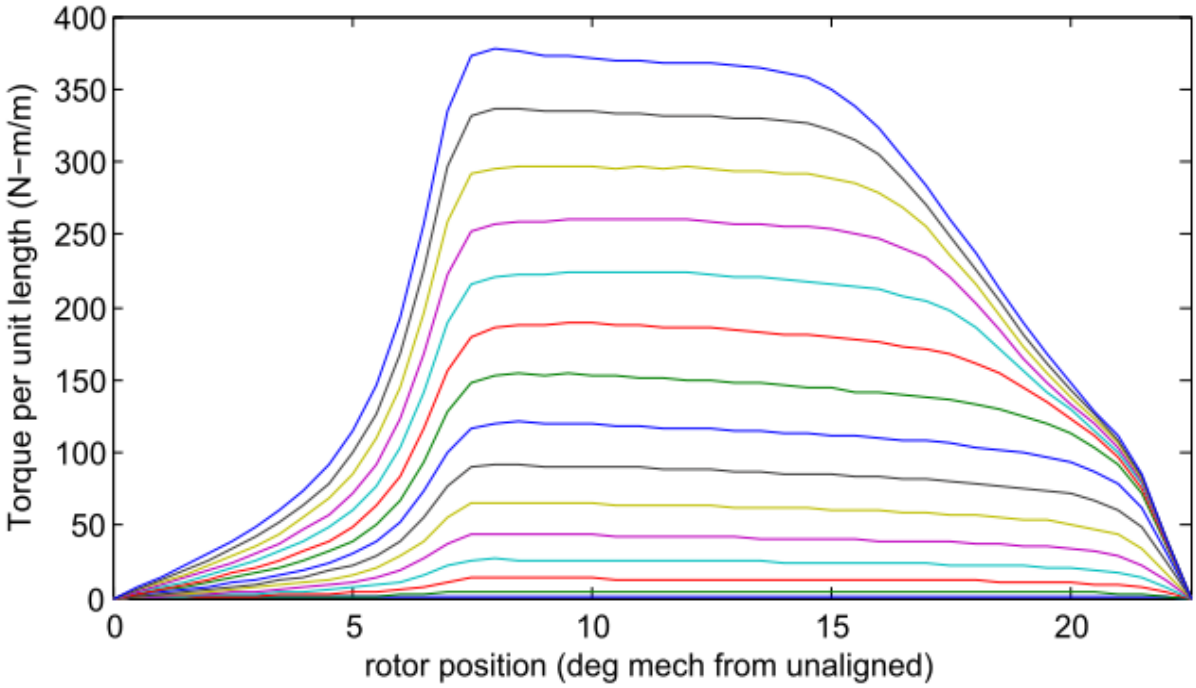

Figure 5.6: Two dimensional magneto-static FE predicted variation in torque as a function rotor position for phase ampere turns varying from 0 to 6000A in steps of 400A.

5.4.1 Inductance and number of turns

The commutation frequency for the 12 slot / 8pole SR machine operating at 30,000rpm is 4kHz. Although some precise shaping of the current may be possible at the lower end of this speed range using PWM, over much of the speed range, single pulse operation or PWM with only a few switching events per commutation interval is likely to be possible. Under these conditions, the form of the current waveform applied to each successive phase will be heavily influenced by the electrical time constant of the winding. For the relatively low rated DC link voltage (270 V) coils with low inductance are likely to be required to achieve competitive torque densities under dynamic conditions, which in turn will require a relatively low number of turns. The phase inductance at any rotor angle can be calculated from the flux linkage characteristics using

$$\mathbf{L_{ph}} = \frac{\boldsymbol{\psi}_{\mathbf{ph}}}{\mathbf{i_{ph}}} \tag{5.6}$$

The net inductance of the machine at any rotor angle and current is proportional to its axial length and square of number of turns in each coil.

Table 5-5 shows the maximum number of turns capable of generating the rated power as a function of specified machine length. Lower inductance can also be achieved by reducing the stack length and utilising higher current densities to generate the rated torque. The stack length of 70 mm produces the rated torque at a current density lower than 3 A/mm^2. The corresponding maximum number of turns is 20 turns per phase. As there are 3 phases and 12 stator poles, each phase has 4 coils which if wound in series requires 5 series turns. The calculated inductance profile from the unaligned to aligned rotor positions for the baseline design is shown in Figure 5.7. The predicted unaligned self inductance for phase A was calculated as 0.044mH, whereas the aligned self inductance is 0.26mH. The maximum mutual inductance to the neighbouring phases was calculated as 8.1μH.

Table 5-5: Required current density and number of turns for different active lengths for the baseline design.

Stator Axial Length (mm)	40	50	60	70	80
No of turns in each coil	26	23	21	20	18
Current density (A-mm^{-2})	3.94	3.50	3.20	2.93	2.78
Average Torque (N-m)	4.85	4.87	4.82	4.77	4.90

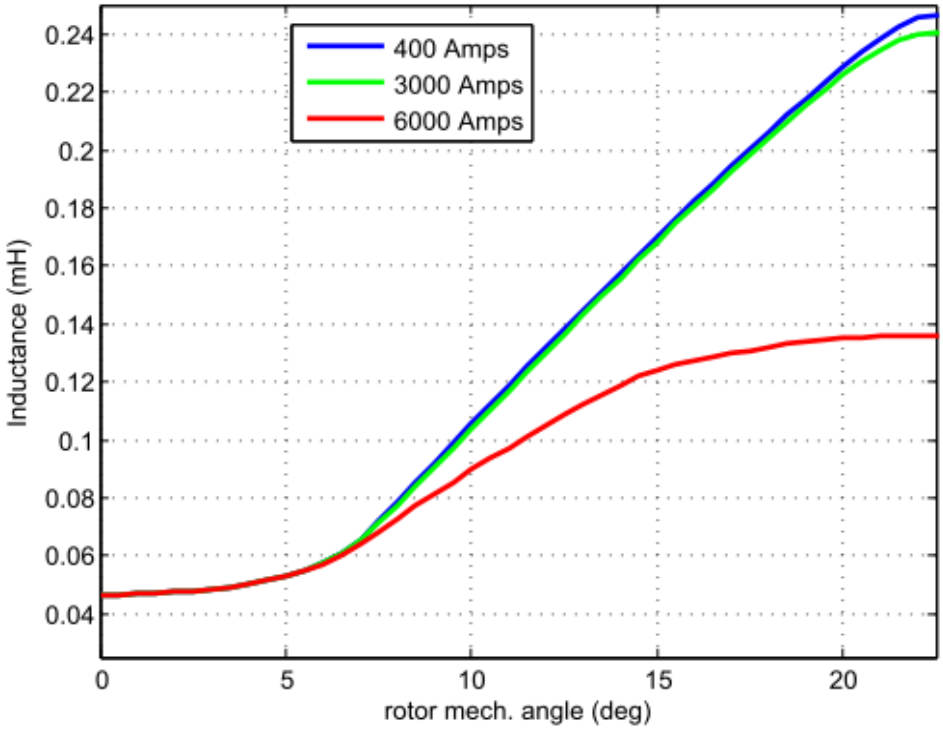

Figure 5.7 : Inductance profile from unaligned to aligned position.

5.4.2 Skin and proximity effects

The low number of turns per coil dictates that the cross-sectional area of each individual turn will be large. By way of example, for 5 series turns per coil the cross-sectional area of each turn is 25.7mm^2, which corresponds to a wire diameter of ~5.7mm for the case of a circular conductor. At high frequencies the current distribution within the conductor can become non-uniform as skin effects force currents towards the surface of the conductor. The consequence is a higher net ac resistance and consequently higher copper loss. The skin depth in a conductor of resistivity ρ_c, with permeability μ, at a frequency ω_e, is given by the formula

$$\delta_p = \sqrt{\frac{2\,\varrho_c}{\omega_e \mu}} \tag{5.7}$$

The skin depth of Copper at 4 kHz is 1.0mm at room temperature, increasing to 1.2mm at 450°C. The selected wire diameter of 0.8mm is below the skin depth and should therefore mitigate against significant problems with AC resistance. However, in order to

make up the conductor cross-section of 25.7mm^2 using this wire, approximately 52 parallel strands are required. There are several physical challenges in manufacturing a high temperature coil with so many multiple parallel strands, as will be described in detail in chapter 6. When multiple strands are employed in parallel, at higher frequencies proximity affects can become more significant which can cause a further increase in copper loss. In a coil, if multiple strands of the same series turn span a large fraction of the slot area, there may be a significant variation in the flux linking of individual strands depending on its location within the slot. This variation in flux linkage across the different strands of a single turn will result in some degree of uneven current flow in the individual strands, leading to potential hotspots in the coil and a net increase in copper loss.

In many electrical machines, proximity effects and uneven current distribution amongst different strands are often compensated for by employing transposition within the bundle of conductors. This serves to provide some degree of, balance in the net flux linkage by spatial averaging [9]. An extreme example of this approach is so-called ‘Litz’ wire which employs a large number of parallel wires with diameters typically less than 0.2mm that are continuously transposed along its length, often with some degree of mechanical rolling to produce a compact and precisely shaped overall conductor. The consequence of this that the process of manufacturing the coils make it comparitively expensive and there is a net reduction in packing factor as the total cross section of Copper within the complete conductor reduces with transposition. The Litz wire however requires the indiviudal strands to be insulated from each other, and typically employ organic varnish type insulations for the purpose. The processes involved in manufacturing Litz wire are not suitable for high temperature insulated wires as the ceramic insulation is prone to abrasion and requires relatively large bend radii to avoid cracking. Therefore, Litz wires were deemed not feasible with high temperautre insulation. In the current protoype machine, the coils were manufactured with multiple parallel conductors of the SK650 wire with transposition of the bundled wires along in the end winding regions. However, as previously suggested it can cause significant complications in the manufacturing process and will be further discussed in chapter 6.

5.5 Dynamic modelling

The methods for modelling machines under dynamic conditions were described in detail in Chapter 3. The method proposed includes the effects of core loss in the circuit simulation in order to achieve improved representations of power flow and currents at the terminals of the machine. This model was partly verified on a toroidal sample, as described in section 4.7. A comparison between the simulated and measured results showed a marked improvement in the prediction of instantaneous power flow at the terminals of the toroidal sample when compared to a post-processing approach to core loss calculation.

However, although the toroidal sample was useful for model validation, it does present a rather simplified example for modelling power within a circuit. Since the power flowing into the device is either stored as reactive power or dissipated as loss. In the SR machines by contrast, there is the added feature of mechanical power flow. In many well designed SR machines operating with high performance core materials, the sum of the reactive power and mechanical power at any instant tend to be significantly larger than the core loss. Hence, the accuracy of the core loss model has less direct impact on the SR machine performance when compared to the test case of the toroidal sample.

5.5.1 Circuit implementation

The methodology and algorithm described in section 3.5 was implemented without the performing iterations within each time step to achieve convergence of coil voltage and phase current. Even with the higher resistivity of copper at elevated temperatures, the voltage drop due to coil resistance remains very small in relation to the DC link (e.g. 0.6V at rated current of 80A). The circuit model was implemented in Simulink, and the machine FE model was solved at each time-step using Comsol Multiphysics via the Comsol Matlab interface module.

Figure 5.8 shows the top-level block diagram of the Simulink model for the circuit simulations. The contents of the individual Simulink blocks are included in Appendix D. The Power-Sim toolbox was used to generate the voltage waveforms from a three phase H-bridge converter operating from a 270V fixed DC supply. The gate signals were generated using preselected turn-on and turn-off angles and fed to the converter model. The resulting phase voltages at the converter output are shown in Figure 5.9.

The voltage waveforms are applied to the circuit model to calculate the anhysteretic current waveforms from the ψ-ί look up tables. The predicted anhysteretic current is then fed into the electromagnetic finite element model via a *Matlab S- function*. The FE model calculates the flux density in individual elements and the total core loss is calculated using the instantaneous core loss model described in section 3.6. The core loss model was implemented in Matlab code as part of the S-function. The core losses in all the individual elements are aggregated to calculate the total instantaneous core loss. As discussed in section 3.4, the core loss calculated for entire machine must be assigned into the loss corresponding to each conducting phase. This was implemented by multiplying the ratio of the flux linkages of the conducting phases to the total core loss as described previously in section 3.4. The individual phase core loss can be subsequently used to calculate the core loss current i_{loss}. This current is then added to the anhysteretic current in the current time step to predict the currents and coil voltages for the next step. The predicted phase currents, voltages and torque are read into Matlab workspace for processing and plotting.

Figure 5.9 shows the applied phase voltages and predicted phase currents, torque and instantaneous loss for baseline design of the SR machine. Due to the high speed and frequencies involved, the machine was driven under single pulse operation, and hence no direct control is exercised while the current is flowing. This said, the 'turn on' and 'turn off' angles provide a means of controlling average power, although not via a straightforward relationship. The core loss model shows that the peaks of core loss tend to coincide with the peak mechanical power. The periodicity in the total instantaneous core loss depends on the arrangement of the coils, specifically how successive coils are connected in terms of polarity. If an alternate north-south (NSNSNS) arrangement is used then the periodicity in core loss is the same as the torque, i.e. one stroke angle. The flux waveforms in the rotor and stator however show longer cycle periods equivalent to three stroke angular durations. The total loss averages out amongst the different phases of the machine. However, in this arrangement the average losses are higher compared to the grouped NNNSSS pole arrangement. This arrangement has a periodicity of 3 strokes, but shows a lower loss during the third stroke as illustrated in Figure 5.10.

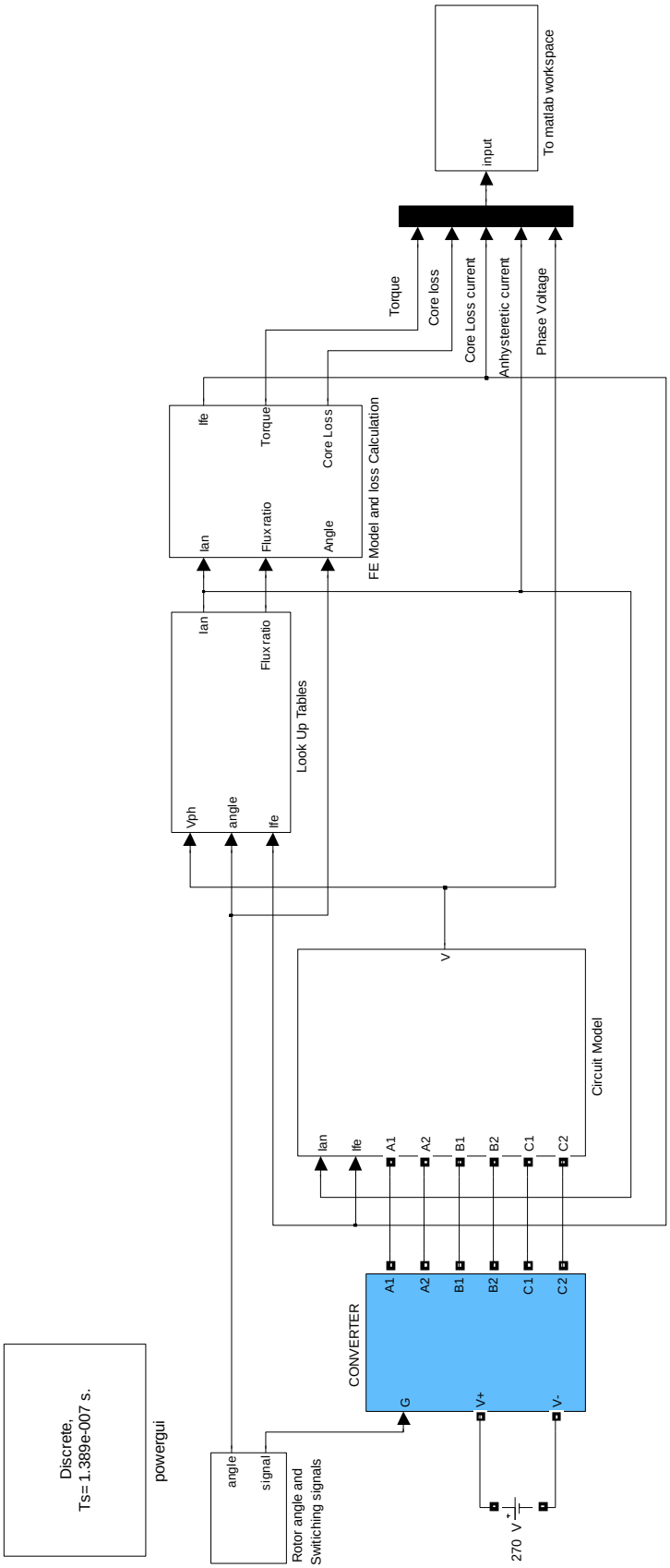

Figure 5.8: Simulink block-diagram of circuit coupled FE simulation.

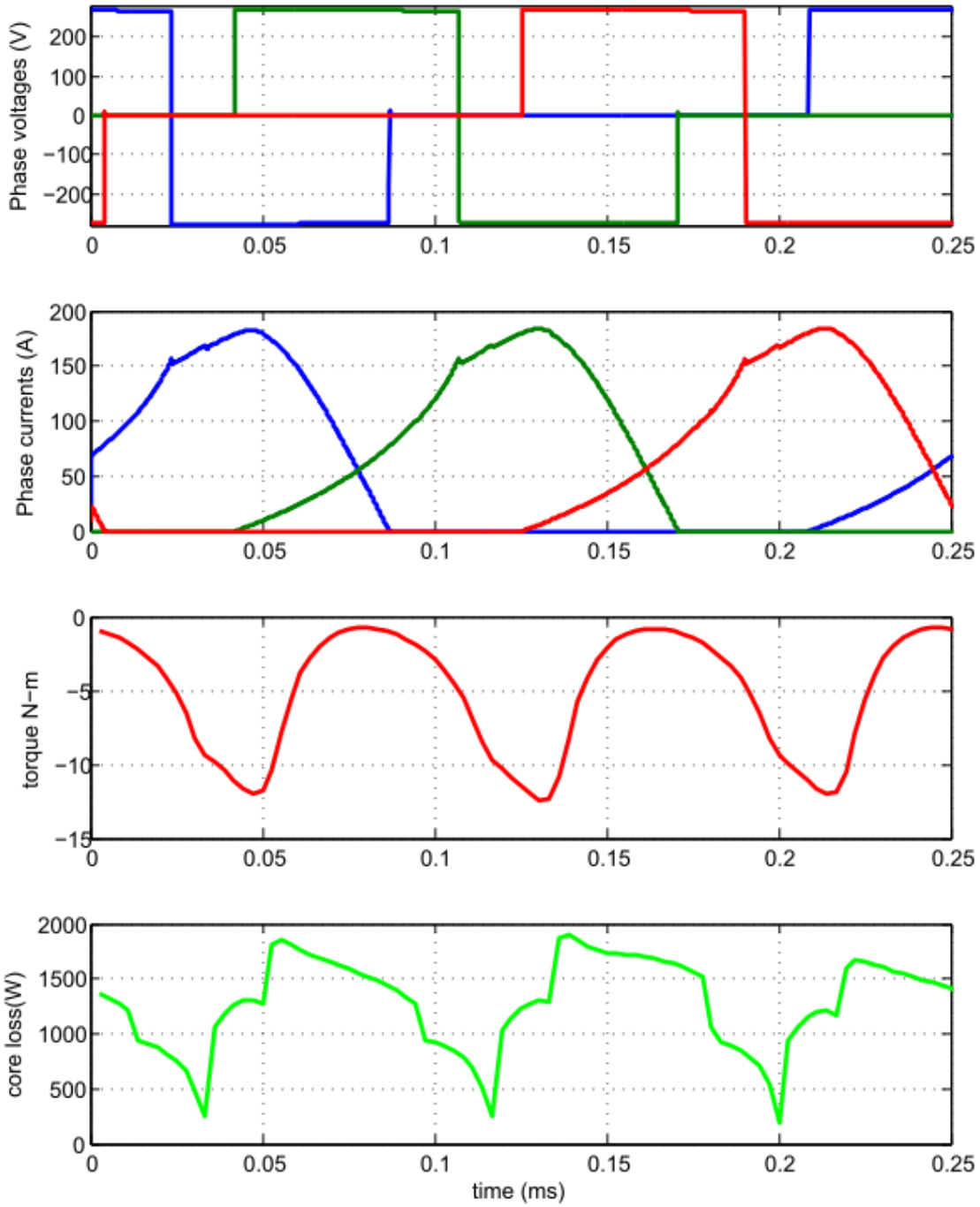

Figure 5.9 : Phase voltages, currents, torque and instantaneous loss for a 15kW 30,000rpm (270Vdc pulse from an independent H-bridge between rotor angles 22.50 and 32.16).

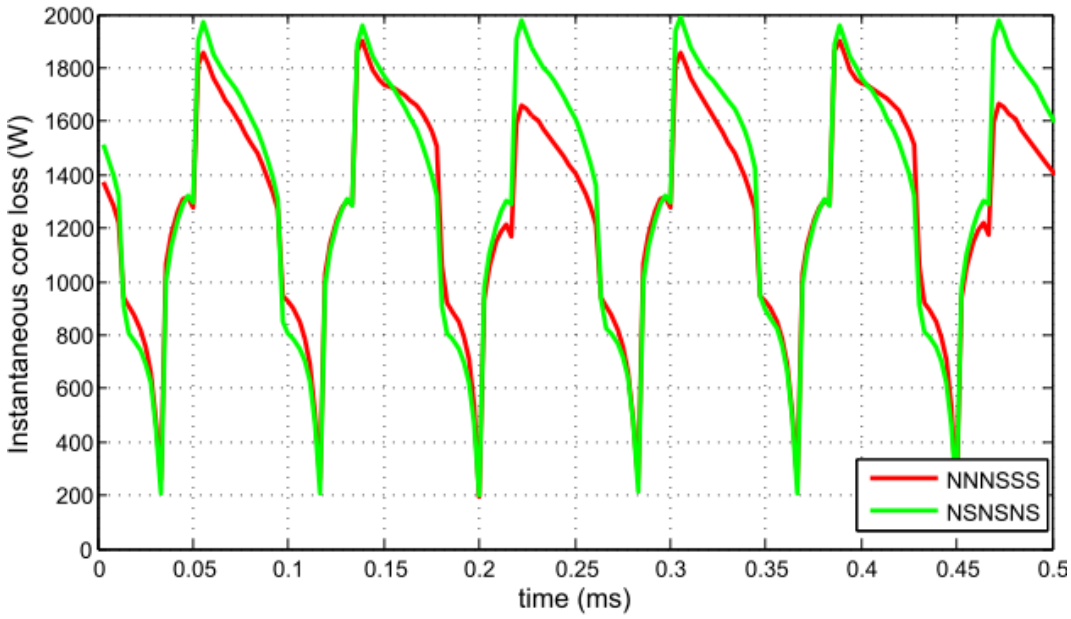

Figure 5.10: Predicted instantaneous core loss for the baseline design using different pole arrangements.

In order to illustrate the benefits of incorporating the core losses into this simulation methodology, further simulations were performed without feeding back the core loss current into the electric circuit. The current waveforms for the SR machine with and without core losses represented in the circuit are compared in Figure 5.11 in generating mode at a rotational speed of 30,000 rpm. In both cases, the excitation consists of a 270V voltage pulse applied between rotor angles of 22.50 and 32.16 deg. (0 deg. corresponds to the unaligned condition, 22.5 deg. the aligned condition and 45 deg. the subsequent unaligned condition).

In the first part of the current cycle, power is drawn from the source as the coils are energised, i.e. the core is ‘fluxed’. It can be seen that, as expected, a larger current is drawn from the source when the core loss is included as compared to the lossless model. As discussed previously, the higher current will increase the voltage drop across the coil resistance and hence the effective voltage across the electromagnetic model and hence the flux predictions. However, the voltage drop across the resistor only constitutes a small fraction of the applied voltage, and hence will only have a minor effect on flux predictions. Hence, during this fluxing period, the core loss predicted by both models is very similar.

In the second half of the conduction cycle, the polarity of the voltage is reversed, and power is delivered back into the supply. In this phase of the cycle, the current drawn into the source predicted with the inclusion of core losses is lower than that predicted by the lossless

model, and hence less power is delivered to the source. As the predicted current is higher in flux interval and lower in the de-fluxing interval, the net rms current is only reduced by a modest amount. The average power delivered to the source is however much lower than that predicted by the lossless model, with a reduction of 8%. As would be expected, in order to produce the required electrical output power, a higher mechanical power must be drawn from the prime-mover to overcome the core loss than is predicted with the lossless model.

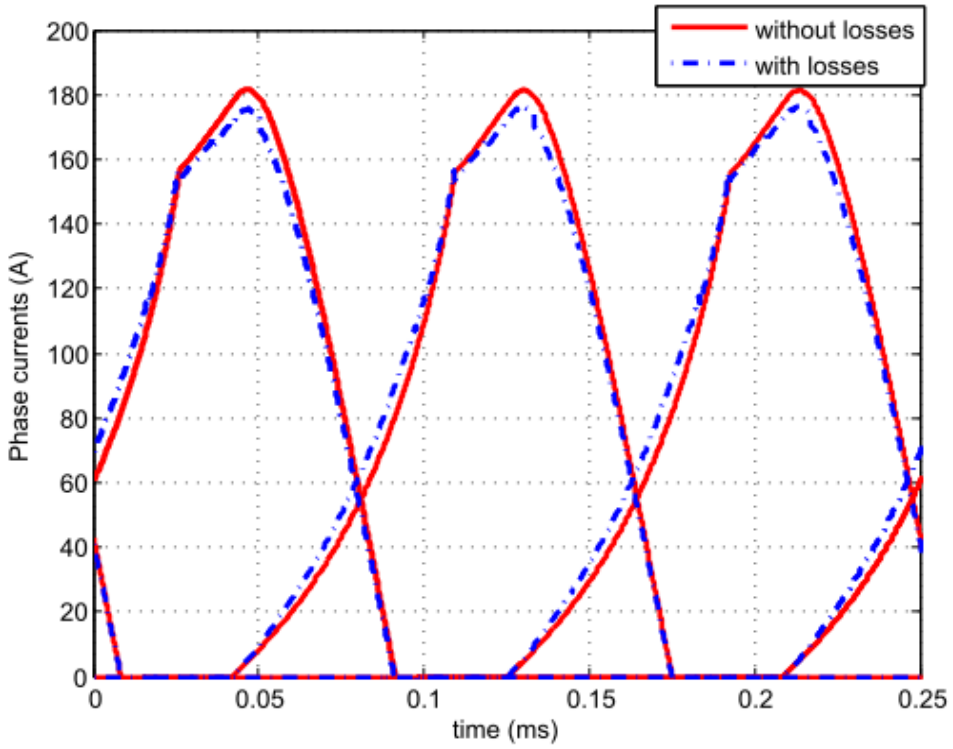

Figure 5.11: Effect of the inclusion of core loss on predicted current waveforms for the three phases.

5.5.2 Power balance

The effects of representing the core loss on the predicted average power values of the SR machine are illustrated in Table 5-6. The first case shows the predicted powers for the circuit simulations without core loss represented in the circuit simulations. The negative sign on the power indicates flow of power is into the circuit as the machine is operated in generating mode. The second column shows the machine with core losses included in the model. The power delivered to the load for the same conditions drops to 13.88kW which matches the sum of the mechanical power and losses. Hence the total power in the circuit

simulation is balanced. The third column shows the case for the machine model with losses included, and updated such that it delivers 15kW to the converter. The average mechanical power required is now 16.52kW resulting in an average torque of 5.25Nm. In this case a larger conduction angle is required which increases the mechanical torque and phase currents. The result shows a 13% increase in predicted copper loss, whereas the core loss is less affected.

Table 5-6: Average powers predicted with and without losses represented in circuit simulations.

Predicted components of power	Core losses not included	With losses	Generating rated power
Mechanical power (kW)	-15.18	-15.16	-16.52
Core Loss (kW)	1.16	1.16	1.16
Copper Loss (W)	133	130	148
Power into converter (kW)	**-15.04**	**-13.87**	**-15.21**
Mechanical Power +Losses (kW)	**-13.88**	**-13.87**	**-15.21**

5.5.3 Copper losses

Since copper loss is directly proportional to the resistance of the coil, which itself is a function of temperature, a reasonable estimate of coil temperature is a prerequisite for calculating copper losses in the dynamic circuit simulation model. In this case, for the circuit simulations it was assumed that the steady state temperature in the coils is 450°C and uniform throughout the coil volume. This value was selected as it corresponds to the maximum allowable temperature in the coils. At this temperature, the resistivity of Copper is 4.65×10^{4} Ω-m as compared to 1.68×10^{4} Ω-m at 20°C.

For a given fixed value of rms current, the thermal model employs an iterative loop which updates the resistivity of copper with temperature and recalculates the copper loss and the resulting temperatures for until convergence is achieved. It is important to recognise that

the thermal model was used separately from the dynamic simulation model described in section 5.5. Hence, the model considers the effect of the temperature coefficient of resistivity solely in terms copper loss and resultant temperatures, but does not account for this temperature dependency in the electrical circuit. In the electrical circuit model, the resistance remains fixed at the value calculated for a wire temperature of 450°C.

Under dynamic conditions, the skin and proximity effects may cause copper losses to increase with frequency as discussed earlier in section 5.4.2. Although the diameter of the wire selected was below the skin depth at the fundamental operating frequency, due to the pulsed nature of the voltages, there may be significant harmonic currents present whose classically skin depths are smaller than the wire diameter. Furthermore, due to the number of parallel strands used to form one series conductor, proximity effects may start to play a role at the frequencies of interest at the high-speed operating point. As explained in section 2.2, Nickel migration during the course of high temperatue ageing can cause an increase in copper loss. As these effects can add significant complication to the machine design, their effects were investigated by means of a sensitivity study described in section 5.9.

5.5.4 Core losses

The total instantaneous core loss was calculated using the dynamic model described in chapter 3. The predicted individual loss components in each element were averaged over a cycle and the sum total of the elements were used to calculate the contribution of the individual loss terms. Table 5-7 lists the breakdown of the total losses in the stator and rotor into their individual constituent loss components. It can be seen that even at the high frequencies, hysteresis loss forms a significant proportion of the total loss in the stator and rotor. As the un-aged material parameters were employed in the simulations, the excess losses were a relatively small percentage of the total losses. The total core loss was 1.16kW which forms 8% of the total power. Although the high core losses results in a modest efficiency, since power density and ability to operate at 350°C are the overriding design considerations, in this application the modest efficiencies, although undesirable, will need to be accommodated.

Table 5-7 : Predicted losses for baseline design at 15kW and 30krpm

Type of Loss	Stator (W)	Rotor(W)	Total(W)
Hysteresis	289	215	504
Eddy current	327	103	430
Excess	176	53	229
Total core losses	792	371	1164
Copper loss			148
Total loss			1312

The spatial distribution of the average total core losses in the stator and rotor are shown in Figure 5.13 and Figure 5.13 respectively. As would be expected, the loss density in the tooth tips is extremely high in due to concentration of flux during the partial alignment of the rotor and stator teeth. Employing an auto-ranging linear colour scale to the produce a graphical representation of the loss with such localised extreme values of loss causes a large fraction of the stator core to appear towards the lower end of the colour range. The majority of the stator cross section showed loss densities of below a 100W/kg. The loss densities in the rotor are relatively higher due to the material characteristics, i.e. the emphasis on mechanical as opposed to magnetic properties in terms of its heat treatment, were typically below the 200W/kg mark.

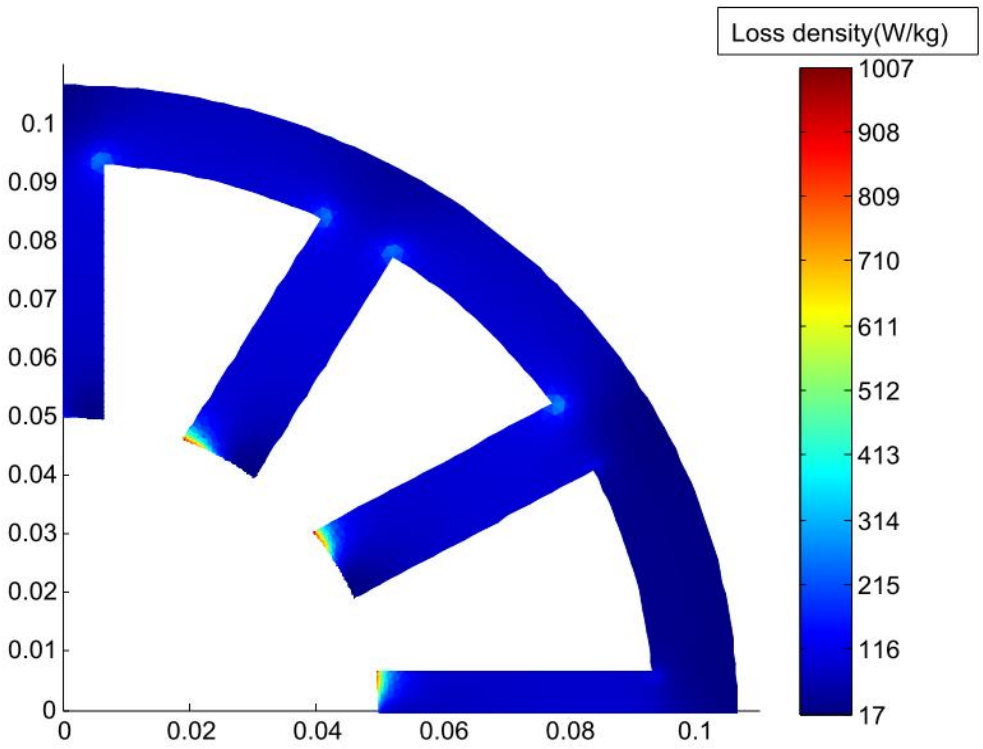

Figure 5.12: Core loss density distribution for baseline machine operating at 15kW and 30,000rpm in the stator.

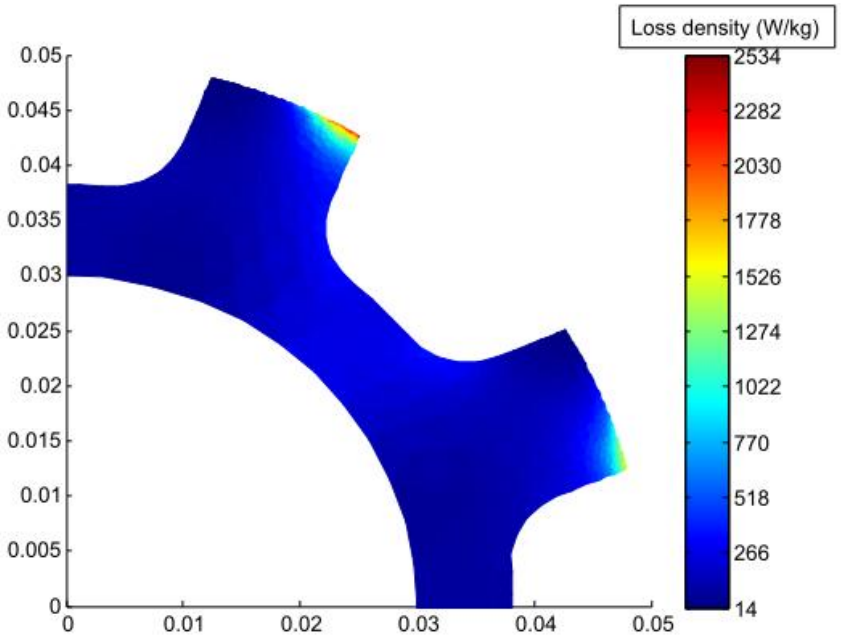

Figure 5.13: Core loss density distribution for baseline machine operating at 15kW and 30,000rpm in the rotor.

5.6 Thermal modelling

5.6.1 Introduction to thermal modelling

Having developed methods for predicted the various components of loss, it is necessary to use these in conjunction with a thermal model of HP shaft machine and its immediate surrounding environs. A thermal model is of particular importance because of the high temperatures involved and the small operating temperature margin from the ambient of 350°C to a maximum hot-spot of 450°C. The thermal model is critical in determining the power densities that can be achieved. There are a number of methods to model the thermal behaviour of electrical machines, the most common techniques being the lumped parameter thermal networks, often in combination with parameters derived from thermal FE models, or full FE models. Recent versions of commercial electromagnetic FE packages such as Flux[10] and JMAG[11] now include add-ons for thermal modelling, although this is generally limited to conduction within the machine geometry with external cooling from surfaces being represented by boundary conditions and/or heat transfer coefficients.

An important factor in the accurate thermal modelling of machines is reliable and quantitative understanding knowledge of the cooling techniques employed and the resulting heat transfer coefficients. In order to calculate the heat transfer coefficients, the temperature distribution of the cooling medium must be known, which in turn depends on the flow rates of the medium. In the last decade or so, there has been a significant interest in using computational fluid dynamics (CFD) to model air flows around machine elements and estimate the convection coefficients as a function of the airflow. However the complex geometries involved necessitates enormous computing power, and can be prohibitively time consuming. A comprehensive review of these techniques can be found in [12].

A more realistic approach is to apply convective heat transfer coefficients to external surfaces. Some commercial FE solvers are increasingly providing features to include a variety of different cooling techniques which can be used as a basis for comparison. The convection coefficients are calculated from a set of correlation formulae, which can be found in standard heat transfer text books such as [13-15]. The heat transfer coefficients of fluids vary significantly with pressure and, to a lesser extent, temperature and hence the correlation formulae can be used only under the specified range of conditions. These are typically specified by means of a range of Reynolds number which represents fluid flow rates, and Prandtl numbers which represent fluid properties. For air or liquid cooled machines,

representative heat transfer coefficients may be calculated using such correlation formulae, using known physical properties of the coolant at the representative temperatures and pressures. In many cases, such as the HP shaft machine, there is little in the way of detailed or reliable information on the air pressures and cooling techniques that will be eventually employed. Therefore, some assumptions would need to be made with regard to the fluid properties and flow rates that are likely to be encountered. However, since the value of the resulting heat transfer coefficients employed are sensitive to these assumed conditions, it proved necessary to adopt a different approach to bounding the thermal model.

5.6.2 Finite element thermal model of baseline design

The rotor core losses are expected to be dissipated almost entirely through the shaft of the HP shaft with a likely further contribution from forced cooling over the rotor surfaces. Hence, it was deemed a reasonable assumption, that only losses generated in the stator need to be dissipated via the stator core into the casing which is fitted directly onto the stator core back. However it is recognised that should a substantial temperature differential exist between the rotor and stator, there may be significant heat transfer across the air gap via. radiation. This allows the rotor and stator to be thermally decoupled from the point of thermal modelling. It was assumed that the cooling air available has a mean inlet temperature of 350°C.

The thermal model for the rotor relies on the heat sinking ability of the main HP shaft and requires details of the rotor location on the turbine shaft and the capability of the turbine shaft to draw heat from the rotor. Due to the early stages of this research, in terms of the overall concept of a HP embedded machine, such detailed information was not available. Hence it proved necessary to resort to approximate surface heat transfer coefficients.

As the stator carries a significant fraction of the total loss (core and copper loss components) and contains the most temperature sensitive elements, viz. the coils which have to be maintained at temperatures within 450°C, it is arguable that the entire viability of high temperature operation largely depends on the stator steady state temperatures. Hence, focus was given to modelling the stator region, recognising that ultimately, some mechanical design effort may be required in terms of ensuing that that the rotor arrangement can provide the heat dissipation required. The FE thermal model for the stator was implemented using the Comsol Multi-physics 3D solver. Due to both axial and circumferential symmetry, a region

which corresponds to one quarter of the tooth geometry was modelled as shown in Figure 5.14.

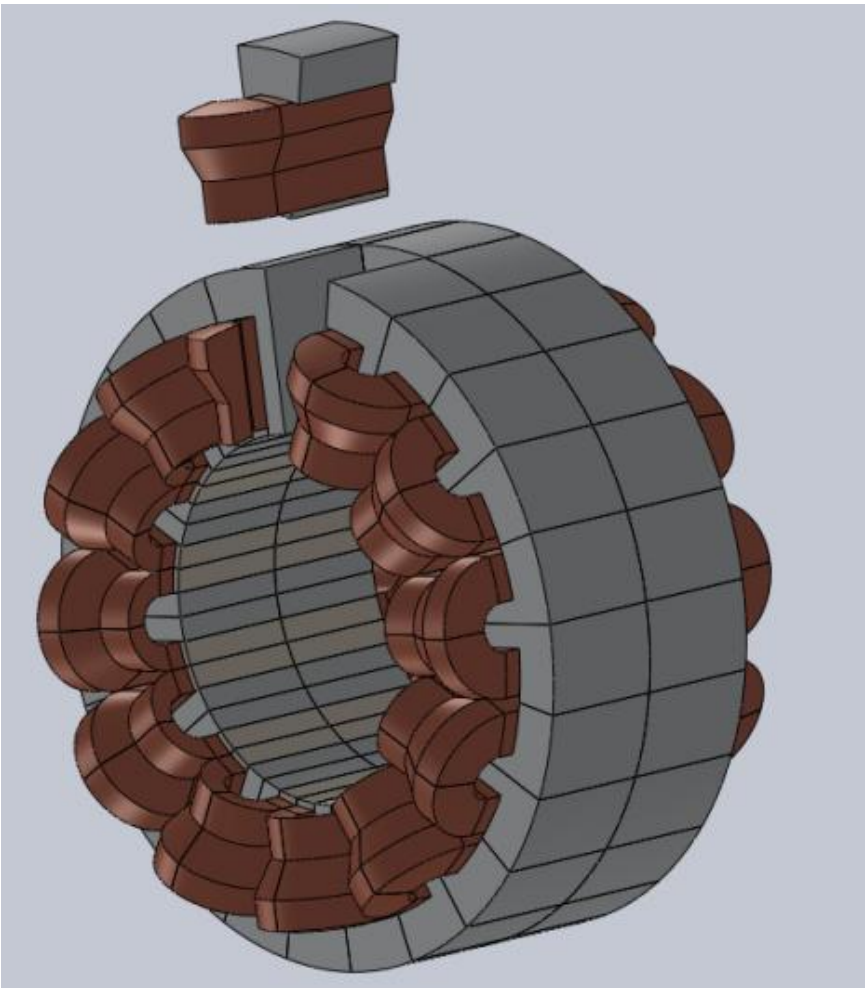

Figure 5.14: Exploded view of stator geometry showing quarter tooth symmetry.

5.6.3 Stator thermal model

The thermal properties of the materials employed in the thermal model are listed in Table 5-8. The slot liner was modelled as a thin thermally resistive layer on the surface boundary between the coil and stator. The coils are modelled as a homogenous composite material which is a combination of the wire and encapsulate properties in the appropriate proportions which reflect the coil packing factors achieved. The thermal conductivity of the coil across its cross section is low and depends largely on the conductivity of the encapsulant material. In the axial direction however, the conductivity is relatively higher due to the continuity of Copper in that direction. The end windings have to take into consideration the

rotation of the conductors and hence the anisotropic thermal conductivities in these regions were defined in cylindrical co-ordinates. A method to estimate and measure the net thermal conductivity across a coil cross section is described in [2]. In measurements conducted in [16] on the particular wire and encapsulant combination used in this design study, the net cross sectional thermal conductivity was measured to be 2.5 W/mK.

Table 5-8: Heat transfer parameters of materials employed in thermal model.

Material	Thermal conductivity ($W\text{-}m^{-1}.K^{-1}$)	Density ($kg\text{-}m^{-3}$)	Specific Heat ($J\text{-}kg^{-1}.K^{-1}$)	Source
Vacodur S+	30	8120	427	[17]
Titanium 6-4	6.7	4430	523	[18]
Copper	385	8910	385	[19]
Encapsulate	1.4	2340	880	[20]
Slot Liner	0.1	900	1000	[21]
Slot wedge	4.6	4000	350	[22]

The conductivity of the core in the axial direction is a function of the lamination and insulating varnish employed to manufacture the stack and can be calculated using

$$\frac{\mathbf{1}}{\mathbf{k_{stack}}} = \boldsymbol{\alpha_{sf}} \frac{\mathbf{1}}{\mathbf{k_{lam}}} + (\mathbf{1} - \boldsymbol{\alpha_{sf}}) \frac{\mathbf{1}}{\mathbf{k_{var}}} \quad \textbf{(5.8)}$$

The stacking factor α_{sf} is typically in the range of 0.9-0.95 and is usually a function of the manufacturing processes employed in assembling and fixing the core and the individual lamination thickness. The laminations are insulated by an oxide layer as the more usually adopted varnishes (which largely tend to be based on organic solvents) cannot be employed at high temperatures. A stacking factor of 0.95 was assumed in this case and an approximate varnish thermal conductivity of 1W/mK was assumed.

The sources of heat in the stator are the copper loss in the coils and stator core loss. The copper loss source is assumed to be evenly distributed throughout the coil volume. The loss in the stator core is divided spatially into three sections, the tooth tip, the tooth body and the back iron, and can be seen by the separating lines in the thermal model diagram shown in Figure 5.15. The breakdown of the average core losses in the rotor and stator regions are shown in Table 5-9. An element-by-element level coupling of core loss from the electromagnetic loss model to the heat transfer model can be implemented if the two-dimensional mesh in the loss model is extruded in three-dimensions in the thermal model. However, this adds a significant level of complexity and element number to the thermal model, which is not required since the high thermal conductivity within the plane of the Co-Fe laminations (at least relative to other thermal conductivities in the model) dictates that the temperature gradient within each lamination is small.

Table 5-9: Distribution of the total core losses in the different rotor and stator regions.

Region	Stator(W)	Rotor(W)
Tooth Tip	75	87
Tooth Body	347	103
Back-iron	371	181

The first pass thermal model shown in Figure 5.15 was implemented along with a 10 mm thick Titanium casing cooled directly on its outer surface. The heat transfer coefficient as a function of the Nusselt number over a flat surface with forced air cooling can be calculated using the correlation formula[13]:

$$\mathbf{N_u} = \frac{\mathbf{0.928 P_r^{1/3} R_e^{1/2}}}{(\mathbf{1} + (\mathbf{0.0207/P_r})^{\mathbf{2/3}})^{\mathbf{1/4}}} \tag{5.9}$$

$$\mathbf{N_u} = \frac{\mathbf{h_s L_c}}{\mathbf{k_f}} \tag{5.10}$$

This equation is specified for fluids with $P_r \geq 0.5$ and $R_e < 5 \times 10^5$. For air at 350°C at standard atmospheric pressure over the length of the axial machine (70mm) the heat transfer coefficient vs. air velocity is plotted in Figure 5.16. However at higher atmospheric pressures, the heat transfer coefficient for the same air velocity is relatively higher as the density of air is higher, resulting in a larger Reynolds number.

As the specific pressure and air velocities remain to a large degree unknown, the first iteration of the thermal model was based on specifying a surface heat transfer coefficient of 100 W/m^{2}K on the casing outer surface with an ambient temperature of 350°C. At standard atmospheric pressure, this would require an air velocity of ~27 m/s which may be considered to be high for a typical test set-up. However in the high pressure compressor region of a jet engine, the air velocities can be as high as 200m/s and hence, providing provision could be made to duct high velocity air to the casing, a heat transfer coefficient of 100 W/m^{2}K could be realised.

Titanium was selected as the casing material since its coefficient of thermal expansion is well matched to that of the Co-Fe stator lamination stack. It also offers a significant advantage in terms of weight reduction compared to a stainless steel or other high temperature aerospace alloys. The cooling air in the high pressure compressor may contain some level of abrasive debris, and exposing the coils surface directly to such debris may cause long-term damage. Hence, it is likely that only very modest cooling may be available for the coil end windings, either through some level or air re-circulating inside a fully enclosed stator, or possibly a conductive path though a fully encapsulated stator. A maximum heat transfer coefficient of 30 W/m^{2}K was envisaged using such techniques and was applied to the exposed surfaces of the coils in the end-winding regions. For the similar case of a flat surface with the cooling air at 350°C, would require an air velocity of less than 3m/s to produce a convection coefficient of 30 W/m^{2}K.

The resulting temperature distribution from the FE simulation of the stator section is shown in Figure 5.15. The FE simulation showed a maximum localised temperature of ~515°C at the tooth tips of the core under steady-state conditions. Although the cross-slot thermal conductivity of the coil is modest, the most significant thermal drop in the model was observed to be across the Titanium casing. Indeed, rather surprisingly, the hot-spot was not in the coil but rather in the core. This is a consequence of the relatively poor thermal conductivity of Titanium which is only ~ 6.7W/mK at 400°C and the large contribution of the

core loss to the overall loss. Alternative lightweight casing materials with higher thermal conductivities, notably Aluminium, tend to have high thermal expansion coefficients and as a result, cannot be used in direct contact with the stator core.

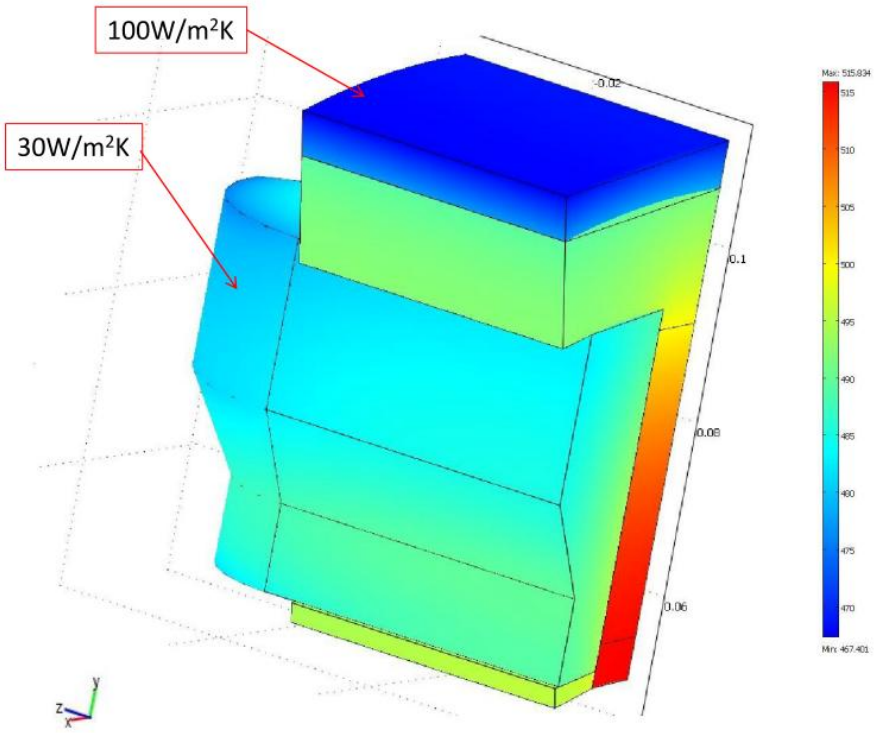

Figure 5.15: Thermal model of baseline design using Titanium casing.

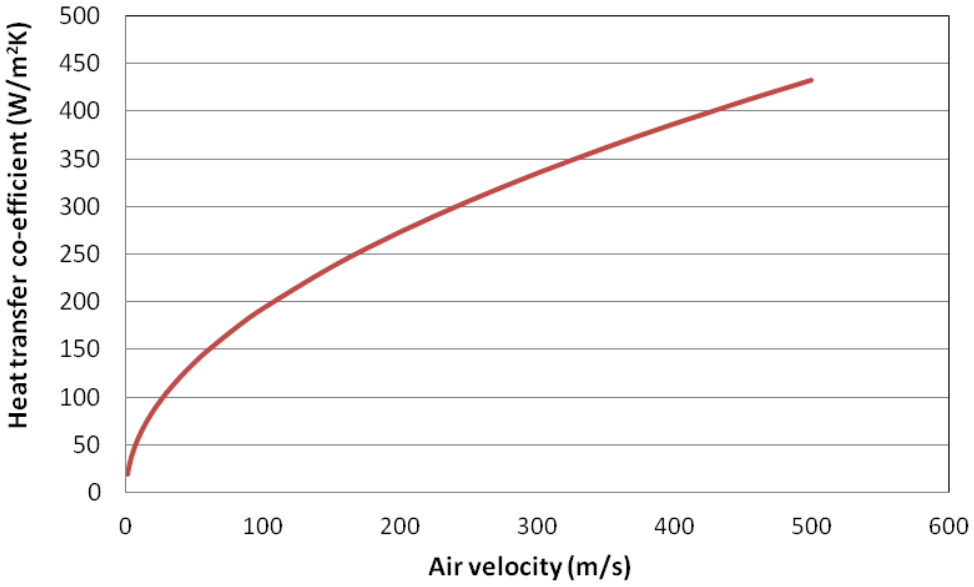

Figure 5.16: Surface heat transfer coefficient as a function of air velocity for air at 350°C with a 70mm long flat plate.

The results from these FE simulations were hence considered misrepresentative and a means to obtain a bounded thermal problem without having to define any of the cooling requirements or casing structures was essential to move forward. Given all the uncertainties involved in the cooling that can be applied, rather than specifying heat transfer coefficients for the external cooling surfaces, an alternative method was employed in which the boundary condition imposed on the outer surface of the stator core was a fixed temperature. This approach assumes that in due course, a casing and cooling arrangement can be put in place which is capable of maintaining this specified core temperature with the predicted losses. This approach was adopted with an assumption that the back of the stator core would be maintained at 400°C by the cooling system irrespective of the losses within the machine. The consequence of this set-point was that there was some 50°C of temperature drop between the back of the core and the surrounding cooling air at 350°C. Moreover, it provides scope for a temperature difference of 50°C within the machine from the back of the stator core to the stator hot-spot (which might be in either the core or the coils).

It was also assumed that all the losses would be dissipated via the back of the core into the casing, with no cooling provided directly to the end windings. On the basis of these assumptions and boundary conditions, the maximum hot-spot temperature in the coil could then be calculated using the FE thermal model. The thermal performance of each design can be quantified by two figures of merit

- The temperature difference between the hotspot in the stator and the surface of the core back iron.
- The heat flux through the surface of the back iron which would need to be dissipated in order to maintain its temperature at 400°C.

The temperature distribution in the stator calculated using this revised thermal FE model for the baseline design is shown in Figure 5.17. The hotspot temperature of the machine is ~453°C with a heat flux of 20kW/m^2 to be drawn through the back of the stator core. Although the hotspot temperature is higher than the coil maximum of 450°C, this is by a mere 3°C and can be reduced if some cooling is applied to the coil surfaces.

However, the heat flux which passes through the back of the stator core under this condition is 20kW/m^2, a value which requires aggressive cooling given that there is only a 50°C margin to the 350°C ambient. On the basis of a directly cooled stator back iron with a

70mm length, the average heat transfer coefficient required on the core back iron is ~400W/m^{2}K, which is 4 times higher than the previously selected value. The predicted temperature distribution of Figure 5.15 demonstrates that such aggressive cooling requirements cannot be achieved by employing a Titanium casing given its modest thermal conductivity. Moreover, the casing would need to achieve a high degree of heat spreading, since the surface area on the core back iron occupies a fraction of the overall casing surface area (the remainder being the overhang to accommodate the end-windings).

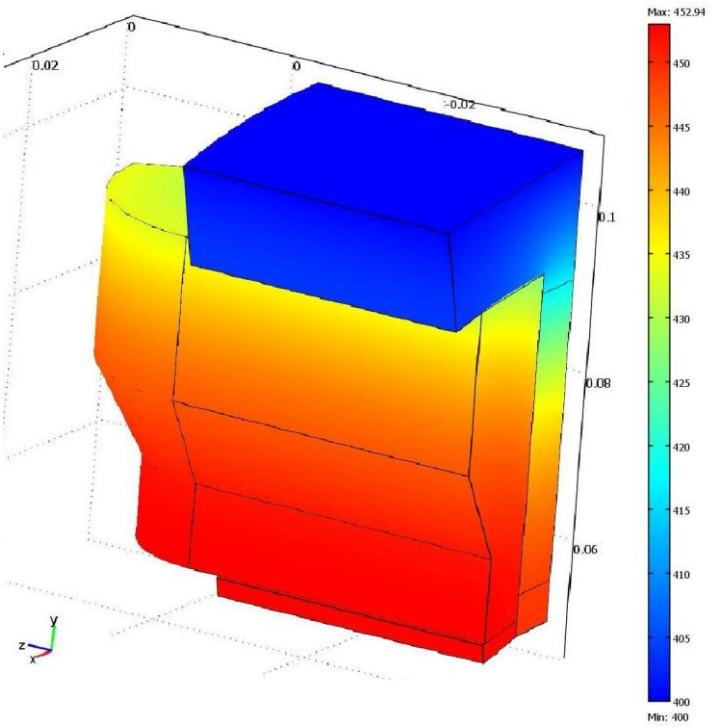

Figure 5.17: Updated thermal model without casing and imposed temperature of 400°C on back of the stator core

5.6.4 Rotor thermal model

The dominant source of heat generated in the rotor is the core loss in the rotor laminations (other contributions being aerodynamic drag and bearing friction). As previously explained, due to the heat treatment selected for the rotor material to achieve superior mechanical properties, the core loss densities were higher than the stator. It was initially assumed that the absence of coils in the rotor (which limit the peak temperatures of the stator

to 450°C) may allow higher temperatures to be accepted in the rotor. However, the deterioration in the rotor material mechanical and magnetic properties due to thermal ageing at temperatures above 350°C suggests that the temperatures in the rotor must also be kept in check.

The main path for heat dissipation in the rotor is assumed to be through the main engine shaft. Additional cooling can also be generated over the rotor surfaces via. forced air cooling. However, increasing the forced air cooling may result in an increased aerodynamic loss and a careful balance would need to be struck. Figure 5.18 shows the thermal model of a quarter of the rotor tooth section. A fixed heat transfer coefficient (h_s) of 10 W/m^{2}K on the rotor exposed surfaces is assumed and the heat transfer coefficient on the rotor shaft is progressively increased while noting the maximum rotor temperatures. This allows an estimate to be made of the cooling capability required from the engine shaft to maintain a specific rotor temperature. A summary of the findings from this sensitivity analysis is shown in Figure 5.19. These simulations were repeated with increased cooling on the exposed rotor surfaces of 30 and 50 W/m^{2}K. To restrict the rotor temperatures to the ~400°C requires a very challenging heat transfer coefficient from the inner bore of the rotor to the shaft in the region of 500 W/m^{2}K. The results also demonstrate that achieving peak rotor temperatures below 400°C may not be possible irrespective of any amount of cooling for the specific conditions. The temperatures in the rotor are more likely to be in the range of 450-500°C, which can be achieved with arguably more realistic heat transfer coefficients of 100-150 W/m^{2}K at the shaft/core interface.

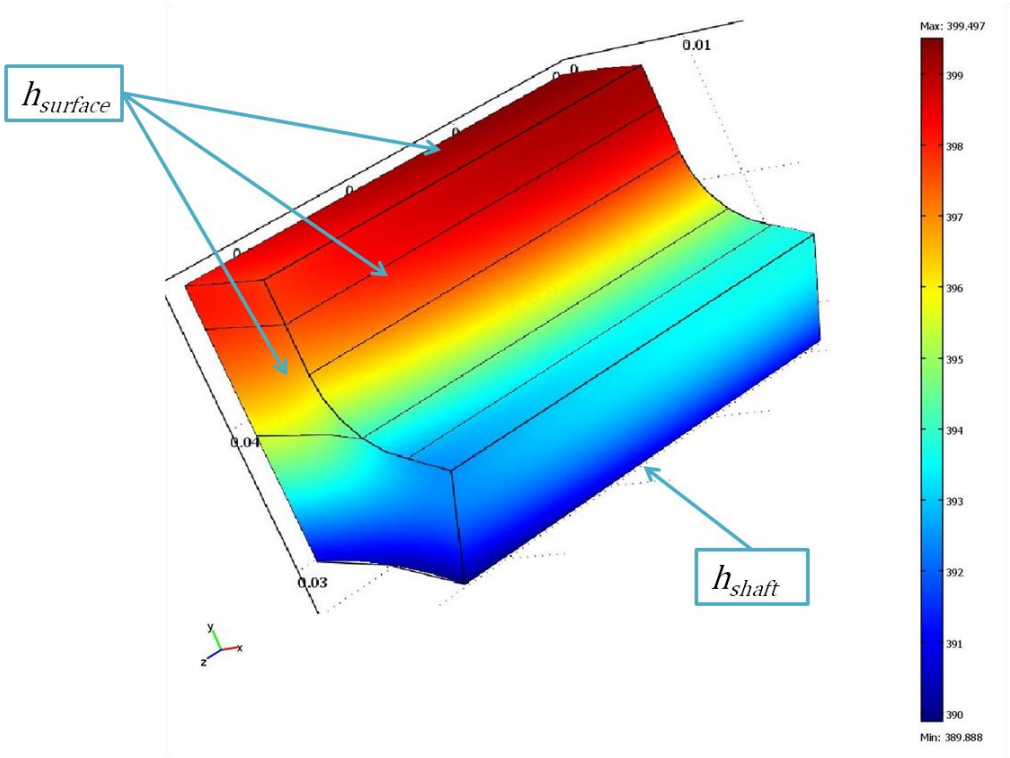

Figure 5.18: Rotor thermal model for a quarter tooth section of baseline SR machine.

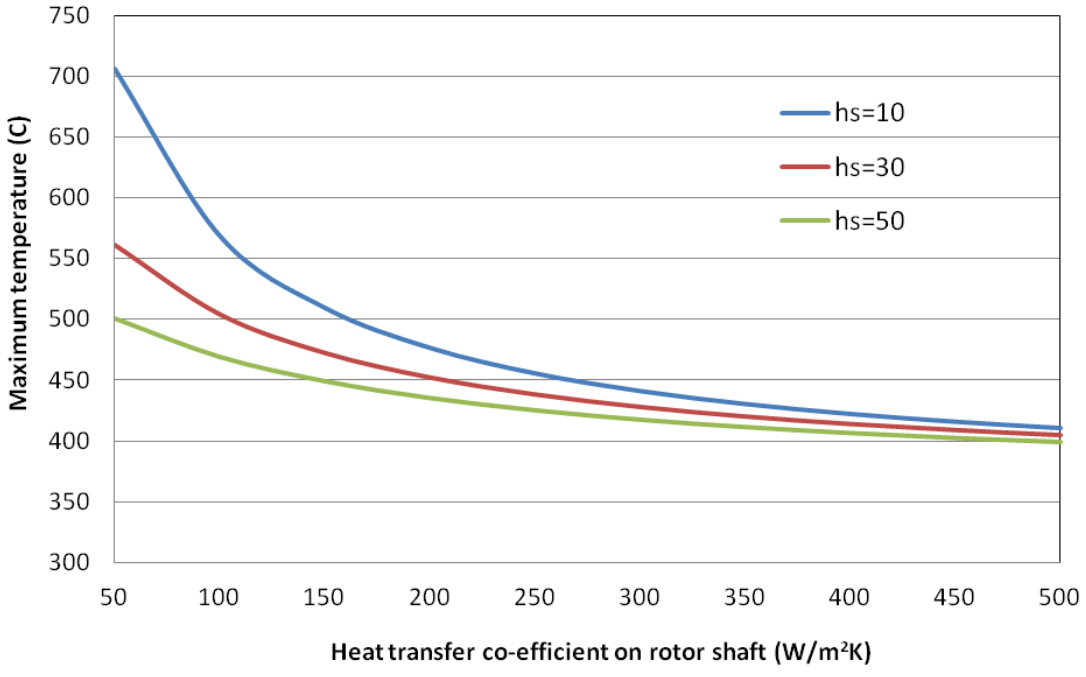

Figure 5.19: Maximum localised rotor temperatures for varying heat transfer coefficients on the rotor shaft and exposed surfaces.

5.7 Baseline design results

As noted previously, the initial baseline design was based on a simplistic specification of a current density and hence slot areas. The analysis of this baseline design proved to be an invaluable exercise in terms of gaining various insights into the key design issues in high temperature machines. Although the initial concern at the outset of the analysis was that the higher resistivity of copper would lead to excessive copper loss, it transpired that it was a relatively low contributor to the overall loss due to the low current density employed in the stator. Conversely, the core loss proved to be the dominant loss mechanism in the stator from an efficiency and, somewhat surprisingly, thermal standpoint as well. As explained previously the main reason for the high core loss was a combination of the material grade and the high speed and pole number of the machine. The estimated core loss was ~8% of the total power. This has a significant effect on the efficiency of the machine, although it may prove to be an acceptable trade-off as the cost of achieving higher power density in this specific application.

The hotspot temperature was 3°C higher than the 450°C limit which demonstrates that the baseline design was not far from meeting the requirements. However, the dissipation of losses from the stator to the surrounding cooling air is arguably the greater challenge. To attain a 20 kW/m^2 heat flux through the back iron requires a very aggressive cooling mechanism in combination with an effective heat spreader. The limitations of Titanium as a thermal conductor, and the lack of alternative lightweight structural casing materials with suitable thermal expansion coefficients and high temperature corrosion resistance, dictated that an alternative approach to cooling the stator through the casing was required.

It is worth noting that the active power density of 1.16kW/kg can be considered relatively low for mainstream aerospace applications. However given the multitude of compromises and material challenges in operating at such high temperature, the power density achieved may prove to be competitive. Table 5-10 shows the results from the electromagnetic and thermal modelling for the baseline design.

Table 5-10 : Predicted electromagnetic and thermal performance of the baseline design (15kW, 30,000 rpm).

Parameter	Baseline design values	Units
Rms current density	2.9	$A.mm^{-2}$
Slot area x rms current density	1253	A
Copper loss @ 450°C	148	W
Stator core loss	792	W
Rotor core loss	371	W
% Copper loss in stator	15.7	-
Mechanical power	16.5	kW
Power delivered to converter	15.2	kW
Power density	1.1	kW/kg
Total power loss	1312	kW
Core loss density	93.7	W/kg
Copper loss density	75.7	W/kg
Overall loss density	92.5	W/kg
Temperature differential between the hotspot and the core back iron at 400°C	52.7	°C
Average heat flux to maintain stator at 400°C [does not include rotor loss]	20.0	kW/m^2

5.8 Selection of turn on and dwell angles

There are several combinations of turn on and dwell angles that can be utilised to generate a rated power and speed when the machine is operating in a single-pulsed mode at high speeds. Each combination will give rise to different current waveform and consequently different copper and core losses. A method to analyse the effects of the operating angles with respect to power and copper loss was described in [23], which solves the basic circuit simulation described in section 3.2 for all the possible combinations of turn on and dwell angles. The power and copper loss contours are displayed as shown in Figure 5.20 for the SR machines baseline design rotating at 30,000rpm. This enables selecting appropriate turn on and dwell angles to minimise copper loss for a particular power contour.

Recreating this plot using the dynamic model with core loss included is not feasible due to the higher simulation times. However, of the possible turn on and dwell angle combinations that generate 15kW at 30,000rpm, three operating points of interest are considered as shown in Figure 5.20. Table 5-11lists the simulation results for the three selected operating points. There are several alternative criteria that could be set to establish the optimal combination, e.g. minimum copper loss, minimum torque ripple, maximum torque per unit copper loss etc. In this study, the optimum turn-on and dwell angles were selected such that the temperature differential (ΔT) from the coil to the back of the core is minimised.

In the case of the baseline design, the highest efficiencies were achieved when operating at point B, which has the lowest core losses, and highest copper losses. However the high copper losses results in a larger ΔT across the stator geometry. Conversely, operating point A has the lowest copper loss but higher core losses and hence a larger ΔT across the stator geometry. It was found that operating point C resulted in minimum ΔT across the stator and hence was employed for all the subsequent machine design studies.

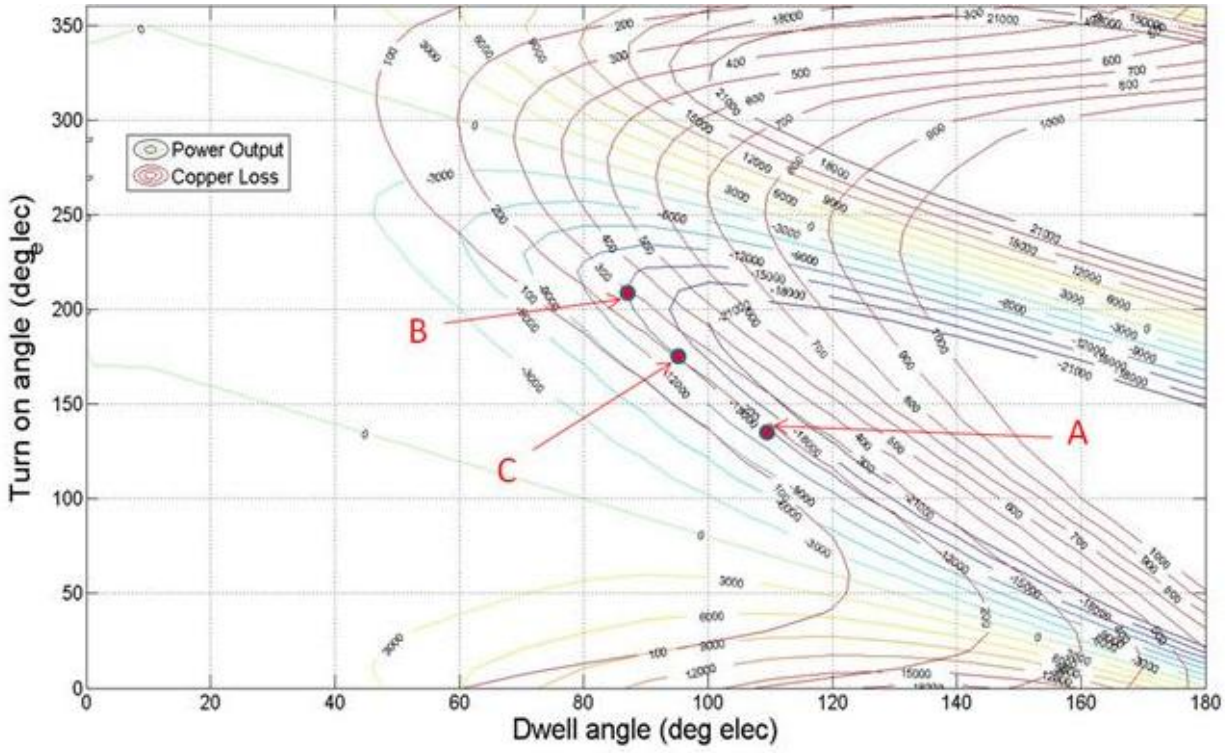

Figure 5.20: Contours plots for equal power and copper loss as a function of turn-on and dwell angles for baseline SR machine.

Table 5-11: Effect of operating points on the baseline SR machine.

Parameter	Operating point A	Operating point B	Operating point C
Turn on angle (deg electrical)	132.0	212.0	180.0
Dwell angle (deg electrical)	112.2	86.2	93.3
Rms current density ($A.mm^{-2}$)	2.7	3.5	2.9
Slot area × rms current density (A)	1166.4	1524.3	1252.8
Copper loss (W) @450°C	130	222	148
Stator core loss (W)	979	719	792
Rotor core loss (W)	505	252	371
Total power loss (W)	1614	1193	1312
Mechanical power (kW)	16.8	16.5	16.5
Power delivered to converter (kW)	15.2	15.3	15.2
Efficiency	89.4	92.2	91.4
Overall loss density (W/kg)	113.9	84.2	92.5
ΔT to the hotspot with the back of core at 400°C (°C)	59.4	58.5	52.7
Average heat flux to maintain back of stator core at 400°C (kW/m2)	23.5	20.0	20.0

5.9 Machine optimisation

As mentioned previously, the baseline design has a thermal hot-spot higher than the 450°C limit albeit by only 3°C. It was evident from the thermal model that the core loss was the dominant loss mechanism from the thermal standpoint, and the high loss densities in the tooth body and tooth tips were the key drivers of the temperature difference between the

localised hot-spot and the back of the stator core. These observations suggests the baseline design was based on an overly cautious choice of deep stator slots (to allow low levels of current density to be used) which led to a penalty in core loss in the long stator teeth. If shallower slots are employed, the core loss in the stator teeth will be reduced and the thermal resistance between the tooth tips and end windings to the back of the core can be reduced. This may well result in a lower temperature hot-spot in the coil despite the increased current density in the coil required to maintain the rated mmf in a shallower slot. There is therefore likely to be some optimal slot depth which yields the lowest temperature difference between the coil hot-spot and the back of the core (which is fixed at 400°C in this analysis). It is also worth noting that optimum in terms of this criterion is unlikely to coincide in a minimum overall loss, since the one Watt of core loss is more readily dissipated than one Watt of copper loss.

In order to establish the optimum slot depth, an optimisation study was performed. During this study, the following key dimensions and parameters were kept fixed: rotor outer diameter, core axial length and air gap flux density. As the slot depth was varied, the overall stator outer diameter was correspondingly modified. Hence a reduction in slot depth yields savings in overall volume and mass. A summary of the key performance attributes of a series of design updates with reducing slot depths is shown in Table 5-12. The updated designs showed that the optimum slot depth was ~32mm, and the resulting average current density 4.1A/mm^2. For shallower slots, the copper loss started to dictate the hot-spot temperature. The stator for the 32mm slot depth case had a temperature difference of 48.8°C to the back of the core.

Although the temperature gradient is only reduced by ~4°C, the optimised design is 2.87 kg lighter with a 11% reduction in the overall stator loss. However, the heat flux density at the back iron remained largely unchanged at ~20kW/m^2, since the net surface area at the back of the core reduces with the smaller stator outer diameter. Therefore, despite the reduced loss, a heat transfer coefficient of 400 W/m^{2}K to the 350°C ambient was still required from the back of the core. It should be noted however that as no cooling was applied to the stator coils in the thermal model, and that some heat dissipation from the end windings may be possible which would in turn reduce the cooling requirements on the stator back iron. The reduction in stator size as compared to the baseline design, improves the power density to 1.35kW/kg.

Table 5-12: Optimisation of stator slot depths

Parameter	Baseline design	Update 1	Update 2	Update 3	Update 4	Update 5
Stator outer diameter(mm)	212	196	190	185	182	179
Slot area (mm^2)	432	324	285	253	234	215
Slot depth(mm)	**43.4**	**35.0**	**32.0**	**29.5**	**28.0**	**26.5**
Rotor : stator split ratio	0.47	0.51	0.53	0.54	0.55	0.56
Number of series turns per phase	20	20	20	20	20	20
Rms current density ($A.mm^{-2}$)	**2.9**	**3.7**	**4.1**	**4.5**	**4.7**	**5**
Slot area x rms current density (A)	1253	1186	1157	1126	1107	1075
Mass of Cobalt Iron(kg)	10.2	9.1	8.7	8.3	8.2	6.2
Weight of Copper (kg)	1.9	1.4	1.3	1.2	1.1	7.9
Total Weight (kg)	14.2	12.0	11.3	10.7	10.3	9.9
Copper Loss (W) at 450degC	**148**	**186**	**204**	**229**	**235**	**246**
Stator Core Loss (W)	**792**	**685**	**632**	**595**	**566**	**541**
Rotor Core Loss (W)	**371**	**386**	**382**	**381**	**378**	**377**
Mechanical Power (kW)	16.50	16.53	16.47	16.49	16.39	16.30
Power delivered to converter (kW)	15.20	15.27	15.24	15.28	15.20	15.12
Power density (kW/kg)	1.07	1.25	1.35	1.43	1.48	1.52
Total Power loss (W)	1312	1257	1218	1205	1173	1164
Delta T to the HS with the back of core at 400C(C)	**52.7**	**49.7**	**48.8**	**50.1**	**51.4**	**53.8**
Average Heat Flux to maintain stator at 400C (kW/m^2)	**20.0**	**20.0**	**19.9**	**19.9**	**19.9**	**20.0**
Copper loss adjusted by thermal model (W)	144	181	199	218	230	248

5.10 Sensitivity of optimum

The machine optimisation described above demonstrated that thermal hotspot temperature below the 450°C limit can be achieved by employing a current density of ~4A/mm^2 in 32mm deep slots However, the analysis which underpinned this optimisation included several assumption (e.g. the limitation of the core loss model in terms of predicting excess losses over the entire frequency spectrum), while several factors could not be readily incorporated in the machine models such as high frequency copper losses, ageing effects in the Co-Fe core and Nickel diffusion in the conductor. All these factors could influence the outcome of the optimisation in terms of identifying the most appropriate slot depth. Hence, a sensitivity study was performed which involved varying systemically the copper loss and core loss values from their as-predicted values to gauge the sensitivity of the optimum slot depth to the precision of the loss predictions..

The copper loss (P_{cu}) in the thermal model was increased from its originally calculated values in steps of 10% up to 140% of the original loss in order to assess the potential impact of factors such as Nickel diffusion and AC losses. Figure 5.21 shows the change in the maximum temperature in all the designs for increasing copper loss. As expected, progressively increasing the losses increase the maximum stator temperatures over the 450°C limit and the optimum moves towards the larger slot depths, however only by small amounts. Next, the core losses (P_{core}) in all the stator sections of the thermal model were increased in steps of 25% to 200% of the originally predicted loss in an attempt to replicate material ageing and any inaccuracies in the loss model. Figure 5.22 shows the increase in stator temperatures for this systematically increased core loss. As would be expected, the optimum slot depth tends to move towards shallower slots. However, the optimum slot depths did not move significantly away from 32mm value identified previously.

As the core losses can be expected to double at ageing times of around 5000 hours, it is evident that maximum stator temperatures under 450°C will not be sustainable using the existing designs, and the machine output power may have to be reduced as the operating time increases. A key assumption in the thermal model was that all the losses in the stator must be dissipated through the back iron alone. Figure 5.23 shows that if some cooling provision were to be made on the coil end windings, this would reduce the hotspot temperature. The values of surface heat transfer coefficient (h_s) in Figure 5.23 range from 5 W/m^{2}K (typical for natural convection) through to 15 W/m^{2}K (representative of some forced-air cooling). The

optimum slot depths however remained relatively unchanged. This sensitivity study has demonstrated that the optimum dimensions only change by relatively small amounts and are robust to changes in material properties and the specific assumptions employed in the designs.

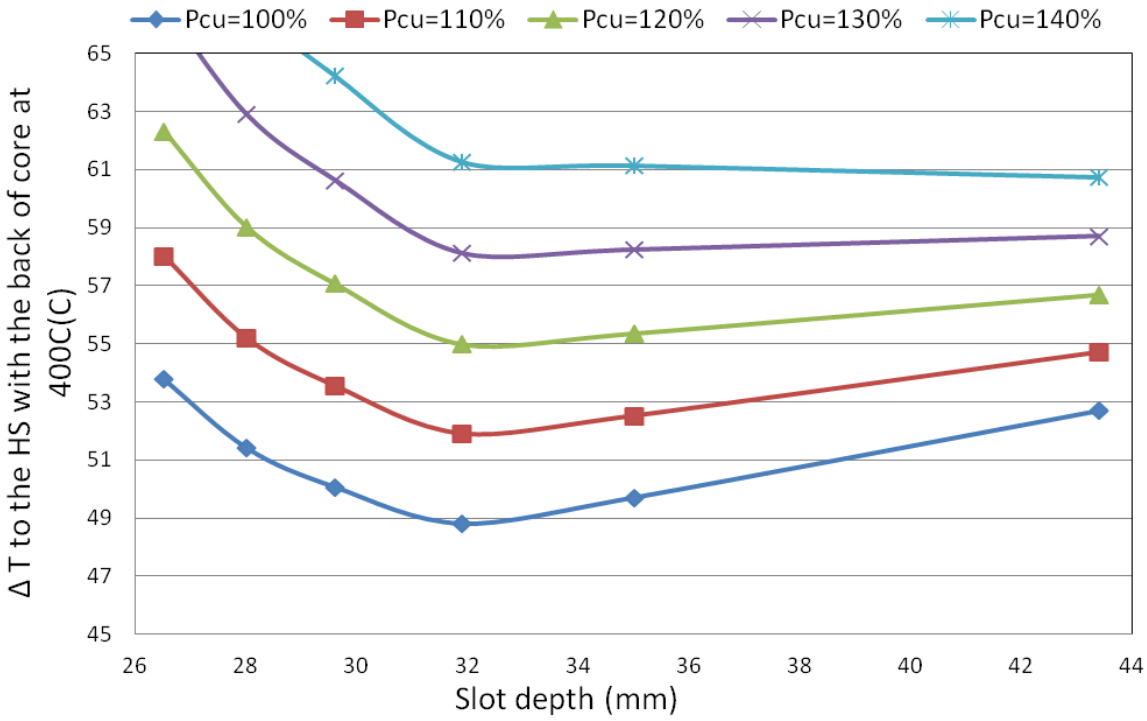

Figure 5.21: Sensitivity of design to increased copper losses.

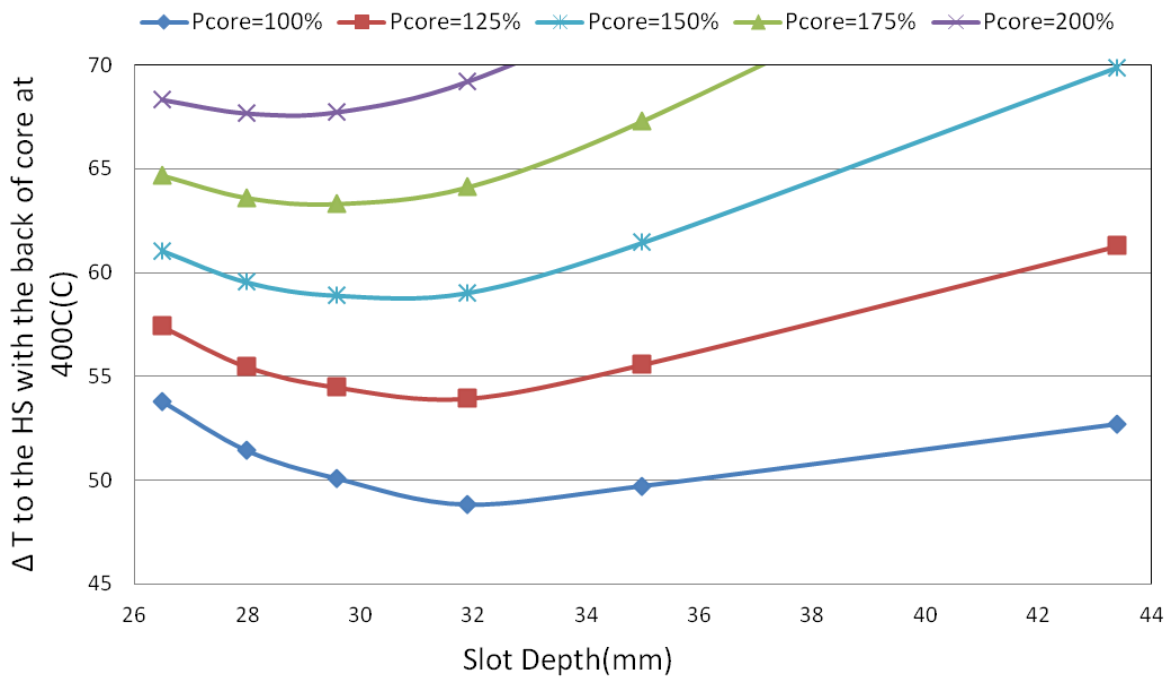

Figure 5.22: Sensitivity of designs to increased core loss.

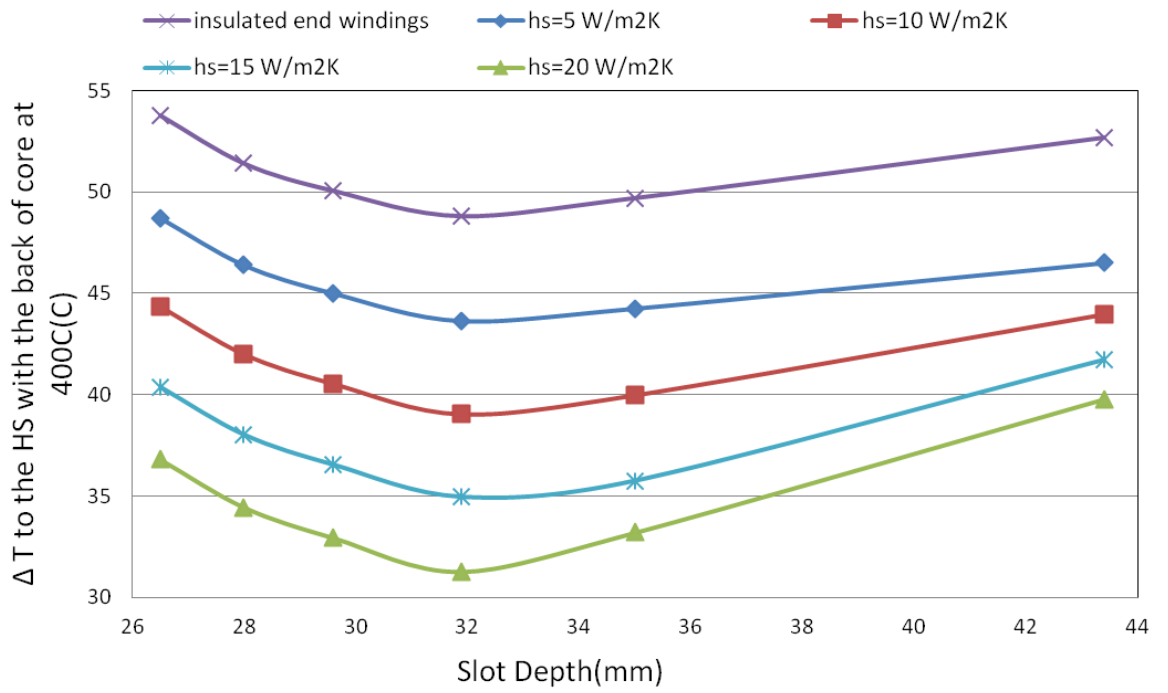

Figure 5.23: Sensitivity of optimum to additional cooling provisions.

5.11 Summary

The chapter has highlighted the key challenges in designing SR machines for HP shaft applications, particularly the influence of elevated temperatures. As there is little existing knowledge or established guidelines for designing machines at elevated temperatures and employing the appropriate materials, a design methodology has been outlined which incorporates all the material properties at the specified temperatures. However more complicated phenomena such as ageing were more difficult to incorporate into the initial design stage. These were therefore modelled by means of a sensitivity study. The design outcome showed that only modest power densities can be achieved for steady state operation at 350°C (order of 1.35kW/kg) and even this is contingent on being able to handle very high heat flux densities at the back of the core. However, once ageing affects manifest itself the machine performance might have to be de-rated to avoid further temperature rise and material degradation.

The inclusion of the core loss model in the circuit simulations for the SR machine resulted in a very complex implementation in comparison to the toroidal sample described in chapter 4. Due to the combination of the reactive and mechanical power at any instant being much larger than the core loss, the effect of the loss on the predicted current waveform was much smaller than observed in chapter 4. However, the circuit simulations demonstrated that the net power delivered to the load reduces as the circuit simulations are power balanced. The circuit simulations with 15kW delivered to the load showed a 13% increase in predicted copper loss, which in the case of the HP shaft machine can lead to a significant temperature rise in the coils. The solution times required and overall complexity of the model increased significantly using the proposed method. The loss model also required a larger data set for characterisation of materials. This said a somewhat simpler technique to characterise materials for the loss models described in chapter 4 can be employed.

The thermal modelling techniques were based on decoupling the cooling mechanism from the active machine thermal model. The model reserved a 50°C temperature differential to the 350°C ambient across which the ~20kW/m^2 of heat flux would have to be drawn. This may seem like a significant task for a conventional heat sink but given the high air velocities in the HP shaft region, this can be realised using several possible solutions, one of which is described in chapter 6. The final design highlighted in the optimisation table showed robustness to changes in losses and modelling techniques only moving by small amounts in

either direction for rather large changes in model parameters. Therefore it was selected as the preferred design option for the machine build and test described in the next chapter.

References

[1] D. J. Powell, G. W. Jewell, D. Howe, and K. Atallah, "Rotor topologies for a switched-reluctance machine for the 'more-electric' aircraft engine," *Iee Proceedings-Electric Power Applications,* vol. 150, pp. 311-318, May 2003.

[2] D. J. Powell, "Modeling of High Power Density Electrical Machines for Aerospace," PhD, Electrical and Electrical Engineering, University of Sheffield, Sheffield, 2003.

[3] R. Arumugam, D. A. Lowther, R. Krishnan, and J. F. Lindsay, "Magnetic-Field Analysis of a Switched Reluctance Motor Using a Two-Dimensional Finite-Element Model," *Ieee Transactions on Magnetics,* vol. 21, pp. 1883-1885, 1985.

[4] S. D. Calverley, Jewell, G.W., Saunders, R.J., "The Calculation of Centrifugal Stress in Four Pole Switched Reluctance Rotors," *IEE Proceedings - Electric Power Applications,* vol. 150(1), pp. 97-105, 2003.

[5] A. V. Radun, "Design Considerations for the Switched Reluctance Motor," *IEEE Transactions on Industry Application,* vol. 31, pp. 1079-1084, 1995.

[6] S. United States. National Bureau of, *Copper wire tables*. Washington, D.C.: National Bureau of Standards, 1966.

[7] P. Vijayraghavan, "Design of Switched Reluctance Motors and Development of a Universal Controller for Switched Reluctance and Permanent Magnet Brushless DC Motor Drives," PhD, ELECTRICAL ENGINEERING, Virginia Polytechnic Institute and State University, Blacksburg, Virginia, 2001.

[8] A. V. Radun, "Design Considerations for the Switched Reluctance Motor," *Ieee Transactions on Industry Applications,* vol. 31, pp. 1079-1087, Sep-Oct 1995.

[9] P. B. Reddy and T. M. Jahns, "Analysis of bundle losses in high speed machines," in *Power Electronics Conference (IPEC), 2010 International*, 2010, pp. 2181-2188.

[10] Cedrat. *Flux*. Available:

[11] JMAG. *Simulation technology for electromechanical design*. Available:

[12] A. Boglietti, A. Cavagnino, D. Staton, M. Shanel, M. Mueller, and C. Mejuto, "Evolution and Modern Approaches for Thermal Analysis of Electrical Machines," *Ieee Transactions on Industrial Electronics,* vol. 56, pp. 871-882, Mar 2009.

[13] A. Bejan, *Heat transfer*. New York ; Chichester: John Wiley & Sons, Inc, 1993.

[14] J. M. Coulson and J. F. Richardson, *Chemical Engineering. Vol 1 : fluid flow, heat transfer and mass Transfer*, 3rd Ed. ed. [S.l.]: Pergamon, 1977.

[15] J. P. Holman, *Heat transfer*, 9th ed., International ed. ed. Boston [Mass.] ; London: McGraw-Hill, 2002.

[16] S. Gibson and D.Powell, "Phase 1: Down-selection of commercial high temperature wires," Rolls-Royce University Technology Centre in Advanced Electrical Machines and Drives RR/HEAT/TR/2008/03, 2008.

[17] Datasheet, "Soft Magnetic Materials and Semi-Finished Products," vol. Vacuumschmelze, 2002

[18] *Metals Handbook, Properties and Selection: Nonferrous Alloys and Special-Purpose Materials*, 10 ed.: ASM International 1990.

[19] "High conductivity Coppers; For Electriacl Engineering." Copper Development Association, 1998

[20] S. Gibson, "Commercial high temperature encapsulation/potting material and coil testing," University of Sheffield, Sheffield2008.

[21] "3000F Ceramic paper." Cotronics Corp. http://www.cotronics.com/vo/cotr/fc_papers .htm

[22] "960 Machinable Alumina." Cotronics Corp. http://www.cotronics.com/vo/cotr/pdf/ 55960.pdf

[23] M. Michon, S. D. Calverley, D. J. Powell, R. E. Clark, and D. Howe, "Dynamic model of a switched reluctance machine for use in a SABER based vehicular system simulation," *Conference Record of the 2005 IEEE Industry Applications Conference, Vols 1-4*, pp. 2280-2287, 2005.

Chapter 6 : High temperature machine demonstrator and testing

6.1 Introduction

This chapter addresses the manufacture of the high temperature demonstrator SR machine, the associated test-rig and the testing. The final dimensions of the machine cross-section which were established in Chapter 5 are shown in Figure 6.1. A full set of engineering drawings for all the machine and test-rig components are contained in Appendix E.

There are two factors which must be taken into account in selecting the materials for manufacturing a high temperature machine casing and test rig. Firstly, any structural materials should have a thermal coefficient of expansion which is reasonably well-matched to the core and active materials. Secondly, the materials should be resistant to corrosion at elevated temperatures while providing required mechanical properties. The material selected for all the structural components in this case was a Titanium 6-4 alloy. This material provides the closest thermal match to Co-Fe ($10.7x10^{-6}$ per°C for Co-Fe as compared to $9.7x10^{-6}$ per°C for Titanium 6-4), has high mechanical strength, low weight and is also commonly used within the gas turbines. However, Titanium has a fairly low thermal conductivity (6.7 W/mK) as mentioned in chapter 5, which means that it is not particularly effective at dissipating heat through the casing. In addition to many structural elements within a machine, there is also a need to identify insulating materials for slot liners, slot wedges and end-plates for the core stack. At these elevated temperatures, the many polymer insulators cannot be used, and recourse to ceramic materials, such as Alumina, Macor, etc. is necessary.

The bearings prove to be the biggest challenge in terms of producing a demonstrator machine. Almost all industrial bearings are not capable of operating at high temperatures and hence the complete machine cannot be placed in an environment chamber. This also entails that the bearings have to be relatively distant from the active machine which is at temperature and cooled separately. The cooling air for the machine itself has to be at a temperature of 350°C and requires specialist fans and heaters. In the machine design described in chapter 5, it was found that although the 450°C temperature limit could be maintained within the coils it

required a substantial amount of heat to be dissipated through a small surface area of the core back iron. In order to supplement the cooling at the back iron some cooling could be applied on the coil end windings. The rotor cooling scheme described in chapter 5 was based on the turbine shaft providing a significant proportion of the heat sink. In the demonstrator machine however a Titanium shaft has to be employed, which as mentioned has a good thermal expansion match to the rotor laminations, but has a low thermal conductivity. Therefore the cooling on the rotor surfaces may have to be increased. In order to raise the machine temperatures and provide the high temperature airflows, a method employing a coil heater and fan arrangement with a closed loop is proposed.

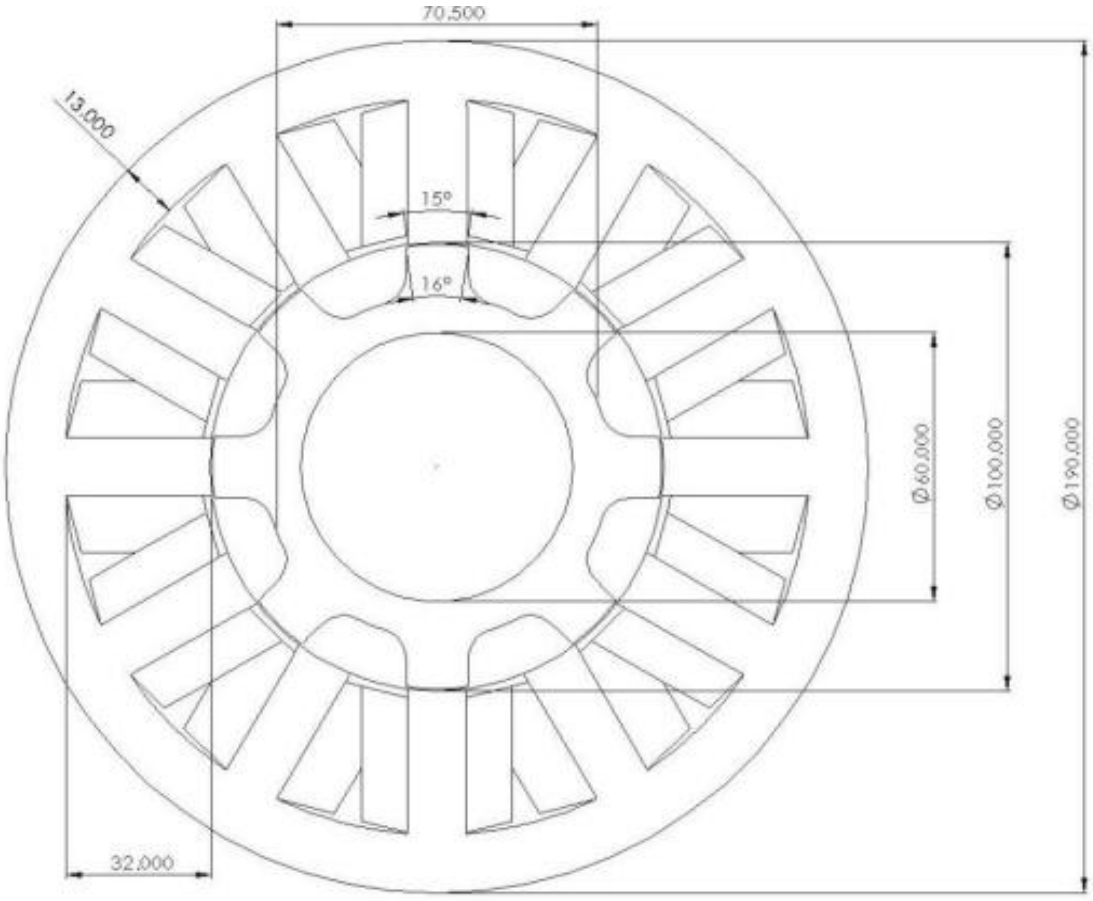

Figure 6.1 : Cross-section of the final machine design with leading dimensions.

6.2 Cooling techniques for stator core

The initial study on the baseline design highlighted the high fluxes which need to pass from the back of the core to the Titanium casing and that this was unlikely to be achievable with a plain cylindrical core-back mated into a Titanium casing, which would then be externally cooled. In order to overcome this limitation, direct cooling of the stator core may prove to be the only way to dissipate the heat from the back of the stator core. This was employed in a manner that still provides separation between the coolant air and the stator void, recalling that the stator void may need to be completely enclosed as the purity of the cooling air cannot be guaranteed. This section describes one particular approach developed to realise direct cooling.

Direct cooling of machine core laminations is by no means a new concept, and has been used on several types of machines in several different embodiments. These include placing cooling ducts in strategic locations on the stator [1], extending stator laminations by fining [2], or combinations of such techniques [3] which provide enhanced cooling. Large high power generators tend to have complex cooling systems which incorporate radial and axial coolant flow within the core [4-6].

One representation which has been reported for low to medium power machines consists of channelling the coolant (whether this is simply air or a liquid) in laminations containing one or more recessed sections [7]. The laminations have the same shape but are arranged in such a way as to form a labyrinthine path along the outer surface of the stator core. The general method consists of channelling the coolant through the labyrinth, directly cooling the exposed surfaces of the stator. The coolant path is generally a combination of axial and circumferential paths, often with right-angle changes of path direction. This method provides a considerable increase in the surface area available for cooling as compared to a plain cylindrical outer surface, which in turn improves heat transfer from the stator core. However, the effect of forcing high velocity coolant around such a tortuous path, particularly impinging normal to a surface in the vicinity of right-angle turn, may give rise to problems in terms of back-pressure and possibly aerodynamically induced heating.

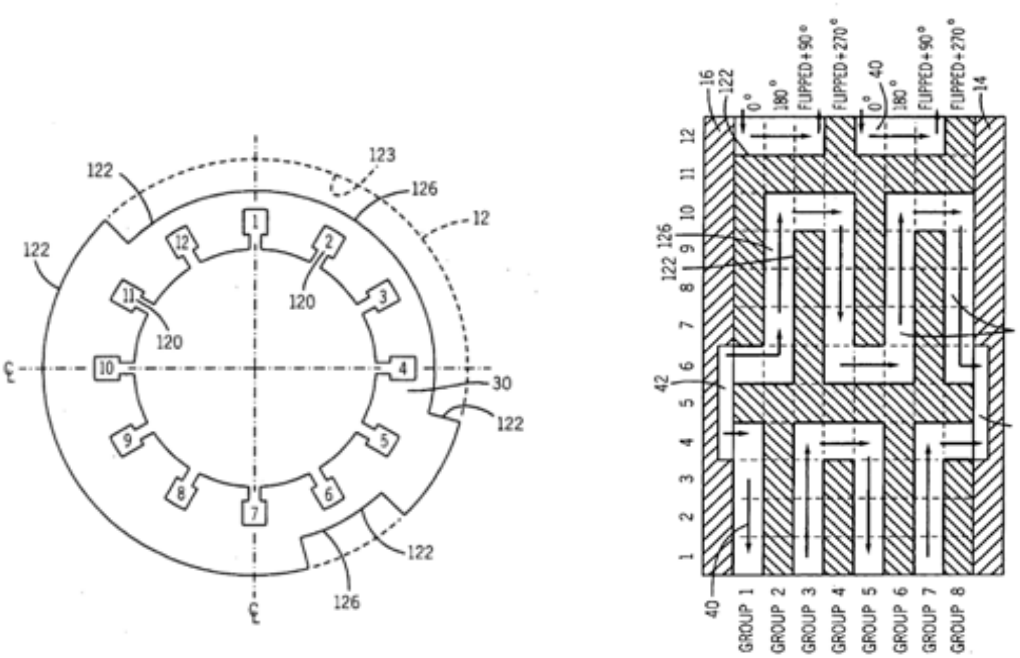

Figure 6.2: Cooling arrangement proposed in [7].

An alternative to a labyrinthine flow channel is to employ circumferential flow around the rear of the stator core with radial orientated ‘fins’. On implementation of this approach was initially described in a paper by [8]. The method proposed in [8] is based the single lamination profile shown in Figure 6.3, in which rotational indexing (by 90°) allows a group of laminations in turn to have exposure to the circumferentially flowing coolant. The essence of the arrangement is best appreciated by inspection of Figure 6.3. The principles developed in [8] were taken on by different authors in [9] which reports on further analysis of magnetic and thermal aspects of circumferentially cooled machines. This follow-on paper addresses the need to optimize the ratio of the back iron to fin height to reduce cogging and saturation at the edge of the fin.

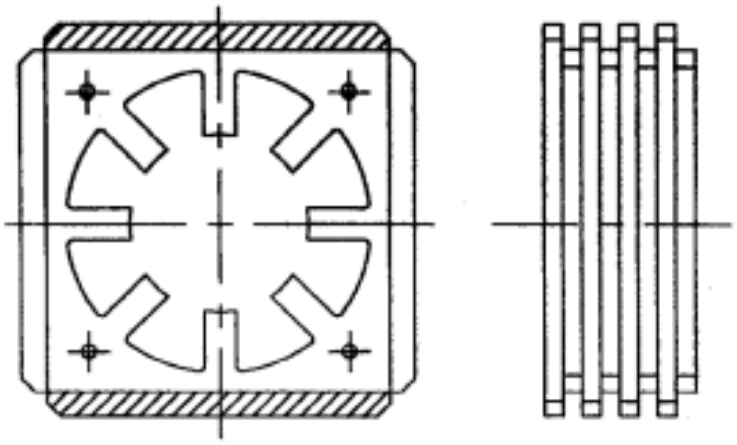

Figure 6.3: Lamination profile for circumferential flow as proposed in [8].

In the case of the HP shaft machine considered in this thesis, there is a requirement for a large increase in exposed surface area, with minimum weight penalty. The surface area gain i.e. the ratio of the heat exchange surface area with and without fins, depends on the number of laminations in a sub-lamination group which act as one external fin. Allowing each lamination to form a fin on itself (i.e. in essence a grouping of one) would yield maximum surface area gain, but with thin laminations (0.15-0.2mm) the channel width may be too narrow for high velocity airflow, and depending on the height of fin, may give concerns for rigidity noting that these fins may well be the sole mechanism to centrally aligning the stator core within the case. Moreover, the equalisation of air-flow between channels, which in essence form an array of parallel paths from a single entry manifold may prove problematic if small tolerance variations give rise to significant changes in individual channel widths. Grouping laminations together will increase the channel width but reduce surface area for cooling. More critically, laminations in the centre of the group will be hotter than those with exposed surface area, since the heat flow must cross one or more interfaces between adjacent laminations before reaching a surface which is exposed to the forced-air. Against this significant background of published patent and research papers, the scope to enhance this basic principle to achieve higher levels of performance, i.e. improved cooling, was investigated.

6.2.1 Proposed method of circumferential cooling

The new method, adopts many of the same principles of previously published concepts based on circumferential flow, but takes a new approach to addressing several limitations. It is based on a combination of a modified individual lamination profile and the means by which they are subsequently arranged to form a stator core. Three possible embodiments of the proposed concept for a 12/8 switched reluctance machine stator are shown in Figure 6.4.

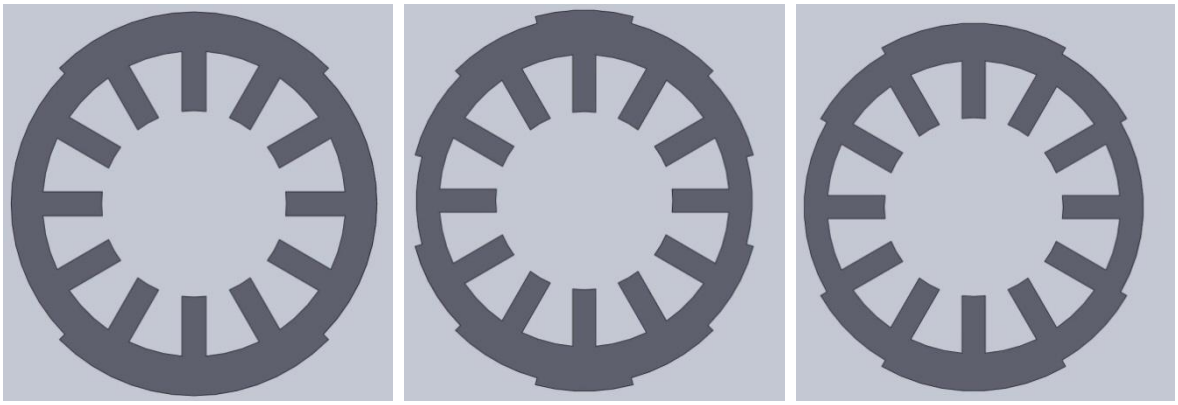

Design 1 **Design 2** **Design 3**

Figure 6.4: Alternative stator core lamination profiles.

These three designs share common features, and would be arranged in a similar manner to form a complete stack. Improvements in performance are obtained with increasing elaboration of the profile. The key factors which drive the adoption of these designs of lamination are:

i) Each lamination should have exposed surface area for cooling for at least a proportion of the periphery, in order to exploit the high in-plane thermal conductivity.

ii) It is desirable with such thin laminations to group them such that the resulting channel width (which has implications on pressure drop and equalising flow from a single input manifold) is as wide as possible – the conflict with requirement (i) is a key driver.

iii) The stator should have a single symmetrical lamination profile, rather than requiring a complex and costly set of tooling to stamp out several different profiles for use in combination.

The key differences between the three lamination profiles of Figure 6.4 are the number of radial steps and the angle subtended by these steps. The three profiles provide varying degrees of exposed surface area and channel widths. Taking each profile in turn:

Design 1 – This lamination design is based on two stepped regions around the periphery, which can be offset in a rotational sense by an integer number of tooth widths to expose each lamination in turn to impinging air. The exposed surface will be the full height of the fin and hence the resulting coolant channel has a rectangular cross-sectional area.

Design 2 – The three steps on the lamination profile and the symmetry of the 12/8 machine dictates that successive laminations are transposed by 30° relative to each other. The resulting stator core has stepped fins which result a V-shaped spiral channel around its circumference which is the equivalent of 5 lamination thicknesses wide at the outermost diameter. Figure 6.5 shows an assembled stack for design 2 in which the lamination thickness has been greatly exaggerated to aid clarity. The staggered nature of the exposed fins at any point around the periphery are such that neighbouring laminations provide a degree of structural support to the central, and tallest fin at that point. This may prove to be an important feature given the aspect ratio of the fins. Furthermore, it is conjectured that the steps at regular intervals around the periphery will increase turbulence in the flow which could enhance heat transfer. This stator core would be fitted into a plain cylindrical casing which picks up on the outermost diameter. This arrangement only requires a single intake and a single outlet which are arranged diametrically opposite each other.

Design 3 – This has a reduced number of steps as compared to design 2. In this case, the angle subtended by the outermost step is twice that of design 3, which could provide some benefits in terms or location in the casing (not that this is unduly a concern for design 2). It results in the same exposed area as design 2, but the channel width is reduced by one lamination thickness.

When considering variant for SR machines with a number of teeth that is not the 12 of this example, it important to note that the number of transpositions is limited by the number of teeth. Furthermore, it is important to maintain at least half symmetry in order to retain the lamination concentrically within a plain cylindrical casing. Machines with higher numbers of stator teeth could adopt more step levels to suit the geometry.

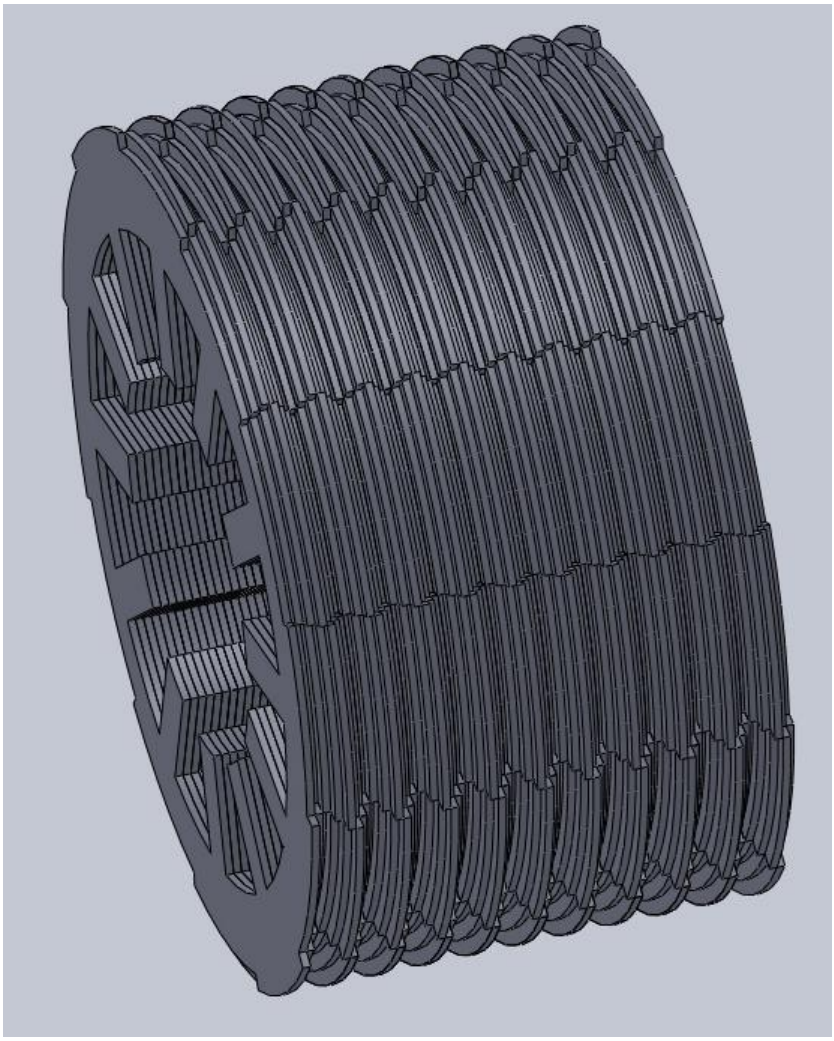

Figure 6.5: Stator core assembled from a series of 'Design 2' laminations (lamination thickness increased to 2mm to aid clarity).

Figure 6.6 shows representative outer casings for the lamination designs in Figure 6.4. The two features presented in the casing are,

i) The entry and exit slots for the coolant flow.

ii) The key-ways required for locating the laminations.

In design 1, the channel formed between successive laminations only traces 90 deg of the machine circumference. This requires 2 sets of inlet and outlets for coolant. Designs 2 and 3 have the exact same casing structure, as in both designs successive lamination's are transposed by 30 deg and hence require 12 key-ways. The channels formed have spiral paths that trace the whole circumference of the machine. Thus, only one inlet and one outlet are

required. The casing design shows a split path for the lower and upper regions of the machine. It should be noted that there may not be equal flow in both paths due to unequal pressure drops caused by tolerances of the build. If this imbalance is significant, some degree of adjustment of the cross-section of the aperture at the inlet could be made to equalise flow-rate. In all three cases, the inlets and outlets must span the whole axial length of the core to ensure coolant flow in all channels.

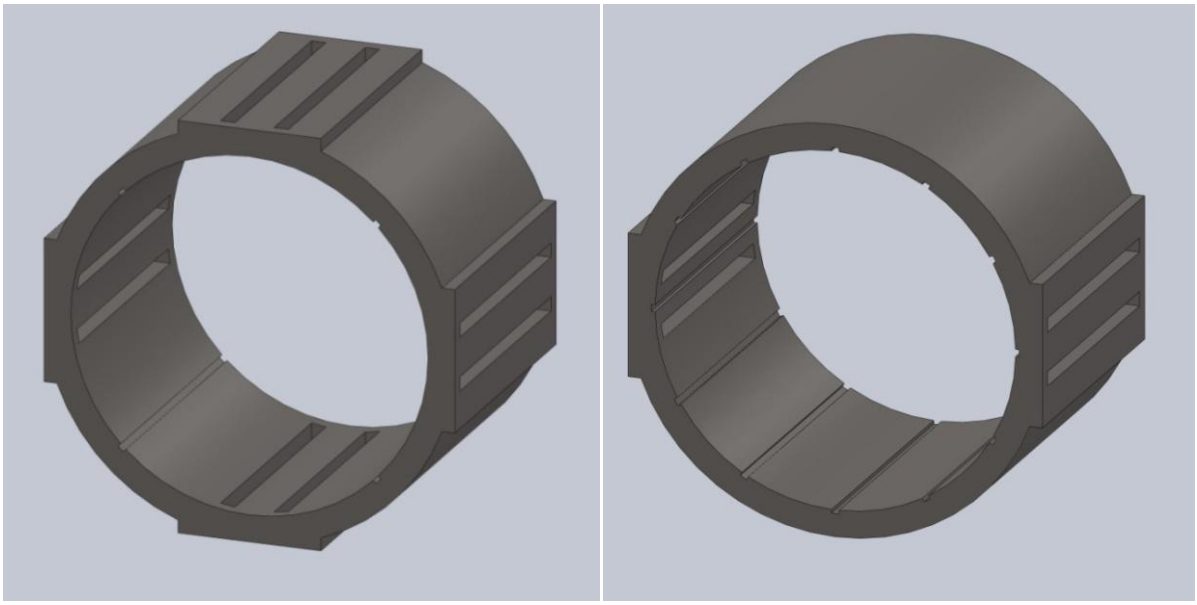

Design 1 **Design 2 and 3**

Figure 6.6: Stator casing designs for lamination designs in Figure 6.4.

Table 6-1 shows a comparison of the three laminations for the specific case of the 12/8 baseline SR machine design. All three lamination profiled designs are based on adding fins to the final machine design which has a cylindrical outer stator diameter 190mm. In order to provide a fair basis for comparison, the fin dimensions were set such that the additional weight in each of the 3 cases is the same.

The figures of merit quoted for lamination profile 1 is based on a grouping of 5 laminations in order to yield the same channel width as profile 2. All three profiles inevitably add weight when compared to a plain cylindrical stator core. However for the same added weight laminations 2 and 3 provide a better surface area gain. Lamination 3 however provides a slightly lower channel width as compared to lamination 2.

Table 6-1: Comparison of lamination designs for same fin height.

Parameter	Design 1	Design 2	Design 3
Stator outer diameter for cylindrical profile (mm)	190	190	190
Core overall axial length (mm)	70	70	70
Lamination thickness (mm)	0.15	0.15	0.15
Number of laminations	467	467	467
Original surface area of plain cylindrical stator core (m^2)	0.042	0.042	0.042
Fin height (mm)	12	12	12
Number of steps	1	3	2
Height of step (mm)	12	4	6
Angle of transposition (deg)	90	30	30
Area added per fin (mm^2)	3695	1232	1232
Total surface area (m^2)	0.34	0.57	0.57
Surface area gain compared to plain cylindrical stator core	8.25	13.75	13.75
Width of channel (mm)	0.75	0.75	0.6
Added weight (kg) based on density of 8120 kg/m^3	1.05	1.04	1.04

This section has described the development of a new method of enhancing the exposed surface area at the rear of the stator core to enhance cooling, albeit at the expense of some increase in core volume and weight. It provides a means of customising the lamination profile to balance the surface area increase versus channel width and offers scope for significantly increasing the mechanical rigidity of fins of a given height. Of the 3 designs considered, design 2 was deemed to offer the most favourable combination of thermal and mechanical properties and was hence adopted in the demonstrator machine.

6.3 Bearings for high temperatures

The switched reluctance machine under study is nominally rated for 15kW at 30,000rpm (air gap=0.5mm). The ambient temperature of the test chamber into which the machine is fitted needs to be maintained at 350°C for testing. Commercial bearings with grease or oil lubrication tend to have maximum temperature ratings of 120-150°C, this being a limit of the lubrication rather than the bearing structure itself. As the temperatures increase the tolerances in the bearings reduce and as a result wear rates increase. Manufacturers advise that, at rated speed, each 10°C rise in temperature over 70°C will tend to reduce the lifetime of the bearing by a factor of two. Therefore, even at modest temperatures of 120-150°C, conventional the bearings have limited lifetimes which are of the order of a few tens of hours with a significant risk of bearing seizure.

Commercially available bearings from the manufacturer NSK known as SPACEA bearings were identified as being capable of running in extreme conditions, including temperatures up to 450°C. These bearings employ solid lubrication which allows such high temperature but unfortunately are only available for relatively low rated speeds, e.g. for a shaft diameter of 30mm maximum speeds are of the order of ~650 rpm. Although the rated speeds are low compared to the speed of the SR machine they would be of interest for low speed proof of concept type test demonstrator purposes. However these highly specialised bearings were only made to order with prohibitive lead times of at least 12 to 18 months. As a result, standard readily available angular contact bearings had to be used for the current test demonstrator.

Standard bearings need to be suitably insulated from the high temperature environment around the machine active components. In addition, measures must be taken to keep a low temperature differential between the inner and outer races of the bearing. A difference in temperature leads to uneven thermal expansion which reduces the internal clearance of the bearings leading to thermal seizure. Bearings are typically rated by the product of the maximum speed (N) and average bearing diameter (D_m). The high precision angular contact bearings procured have a D_m*N rating of 1000000 and hence can employ a maximum inner diameter of ~30 mm at 30,000 rpm. The advantage of the higher precision bearings is that the wear rates are lower which can increase lifetimes at the higher operating temperatures.

Two test rig architectures were identified as potentials for bearing insulation. The first shown in Figure 6.7 is based on having the bearings mounted externally and remotely in bearing stands on a base plate. The stator and machine internals will be heated to 350°C while the bearings will be outside at a certain distance and decoupled from the machine internal. The advantage of this topology is the bearings are in a benign environment. However the major drawback is that the shaft has to be much longer than the active rotor length. This has implications on the maximum rotor speed in terms of rotor dynamics in terms of factor such as bending moments at high speeds. As the stator is mounted on a base plate there is an uneven thermal expansion between the cool bearing stands and the stator and rotor which are at high temperatures. Due to the small operating air gap, this difference in centre heights as the temperature is increased will be problematic. Hence, it is necessary to incorporate some means of adjusting the centre height of each bearing to compensate for the thermal expansion.

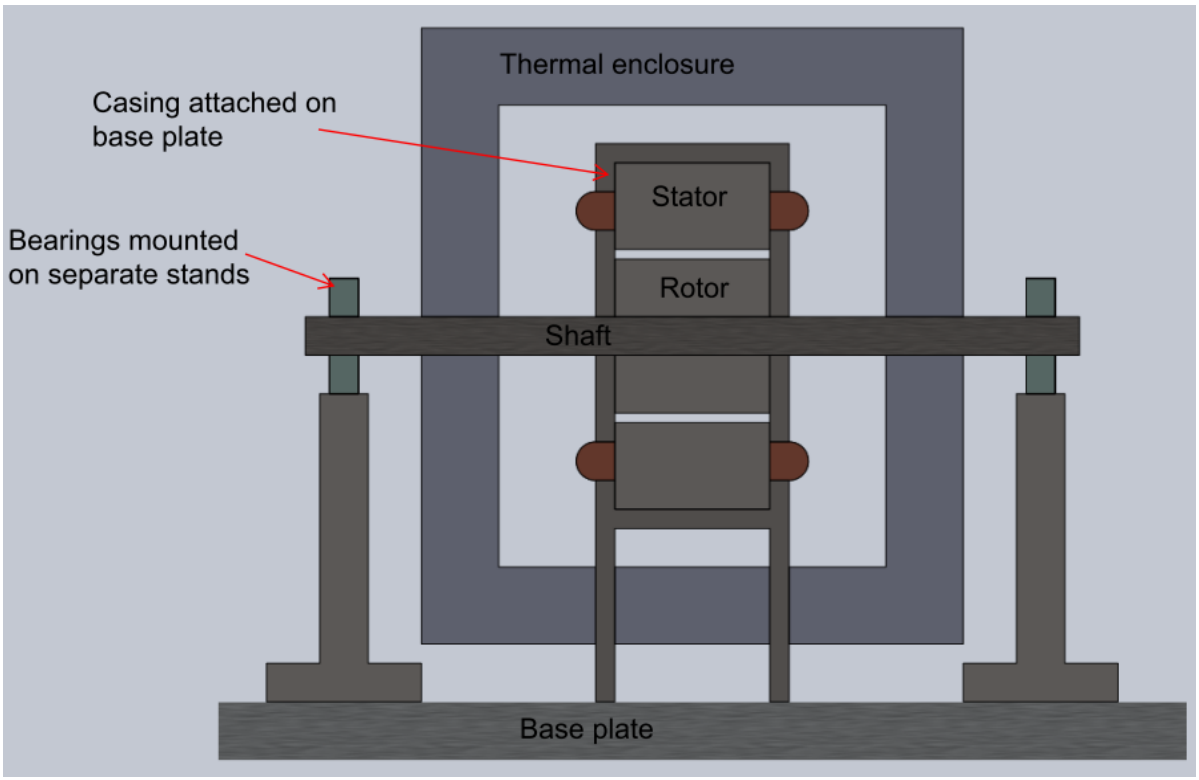

Figure 6.7: Cross section view of test-rig schematic with bearings located on separate end stands.

The second rig architecture of Figure 6.8 avoids some of the more complex thermal expansion by locating the bearings within highly modified end-caps which are connected to the main stator. This would still require that the bearings have to be somehow insulated from the internal 350°C ambient and then cooled to temperatures less than 150°C. The advantage of this topology is that the distribution of temperature is symmetric about the rotor/stator axis giving rise to more even thermal expansion. However, it necessitates complex cooling arrangements for the bearings which at 350°C pose a significant challenge. By providing aggressive cooling on the bearing the length of the shaft may be reduced allowing for higher rotational speeds. However the rotor shaft itself would act as a short thermal path to the bearings and a method would be required to insulate the bearings from the shaft since differential thermal expansion between the races could cause the bearing to seize. As a result, the first option of mounting the bearings on separate stands which can be thermally insulated was preferred, although it was recognised that there would be little prospect of reaching the 30,000rpm rated speed.

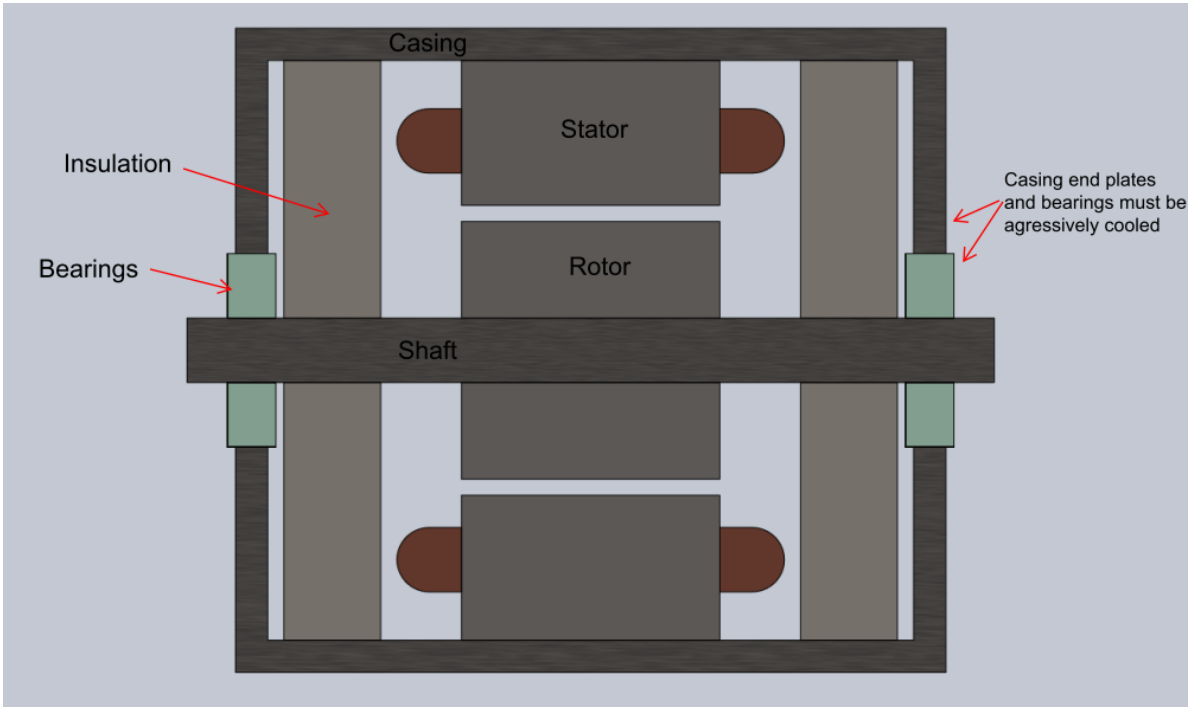

Figure 6.8: Cross section view of test-rig schematic with bearings located on casing endplates.

6.4 Test-rig manufacture

The design and subsequent manufacture of the test-rig posed many challenges in terms of bearings, rotor dynamics and thermal management. A full set of engineering drawings for the various components is included in Appendix E. In addition, a series of photographs of the manufactured components during the build process are contained in Appendix F. A key driver in the design of the test-rig was the need to locate the bearings in an environment with a maximum temperature of some 120°C. This necessarily required significant extension of the shaft so that the bearing could be located outside the 350°C environment with scope to force cool the exposed section of the shaft and bearing stands. Furthermore, it was deemed necessary to include provision for adjustment of the centre height of the rotor relative to the stator. This was achieved by means of adjustable bearing stands which could be set when the machine was at its operating temperature. The general arrangement of the test-rig is shown in Figure 6.9.

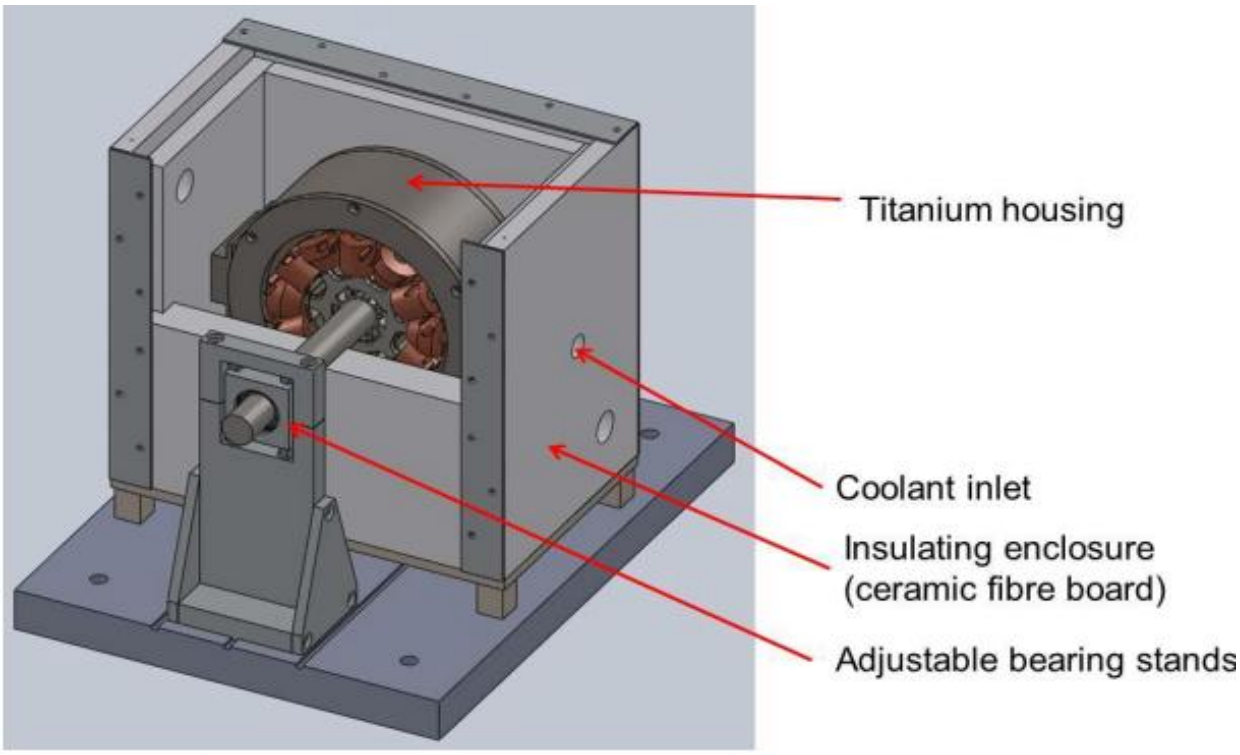

Figure 6.9: General arrangement of the high temperature test-rig.

6.4.1 Manufacture of stator components

The stator core was manufactured by wire erosion from a total of 470 laminations of Vacodur S+ Co-Fe, each lamination being 0.15mm thick. The stator laminations were pre heat-treated at 820°C for 4 hours to achieve optimum magnetic properties. The stator lamination profile includes a series of stepped projections around the outer periphery which enhance heat transfer from the core as described in section 6.2.1. The laminations require a casing containing a series of keyways on the inner bore to provide circumferential location of the indexed stator core laminations and two rectangular bosses with apertures which interface with the externally provisioned cooling.

The tubular section of the machine casing was manufactured from a cylindrical bar of Titanium, principally by wire-erosion. The stator core laminations were inserted into the stator casing, with each successive lamination being indexed by one keyway pitch. The tubular section of casing is attached to two Titanium end-caps which serve to axially constrain stator core and include integral legs to connect the casing to the test-rig base-plate via. a set of Titanium feet. The two end-caps, which were manufactured by a combination of milling and wire-erosion, are identical and connect to the tubular section of the casing with M6 Titanium bolts.

The ceramic slot-wedges, which serve to retain the windings within the slots were externally manufactured by laser cutting 1mm thick Alumina sheets. The rectangular slot wedges span the full axial length of the core in one-piece and are retained by specific slots near the leading edges of the stator teeth. Due to the technique used in stacking the stator and the transposition of the stator laminations the tolerances on small features in the laminations such as the keyways in the laminations for the slot wedges require much larger tolerances.

To provide secondary coil insulation and prevent abrasion of the wire insulation by the core, the stator slots were lined with Rescor 390 ceramic paper. This paper is compressible (nominal starting thickness of 0.8mm thick) and has a modest thermal conductivity of 0.05 W/mK. After some initial trials of this paper at temperature it was found that the binder used in the manufacture of the paper burns off at around 200°C after which the paper becomes very fragile and crumbles to pieces fairly easily. Once in the slot and in position this should not cause significant issues in terms of insulation failure. Alternatives

with better strengths such as silica woven cloth can be considered. However these would have a relatively lower dielectric strength.

As with all cores manufactured from thin laminations, it is desirable to apply a degree of axial compression to the core by some form of clamping to overcome the natural tendency for the core to spring apart. Whereas the core can be readily clamped around the outer regions of the stator core, the individual teeth cannot be so readily clamped and some means must be accommodated to prevent the teeth from flaring out axially. Given that any clamping structures must pass through the semi-circular void at the end of each stator coil, it is desirable, if not essential, that they are made from non-electrically conducting material. The first attempt at realising appropriate clamping was based on incorporating a series of Alumina sheets at each end of the core (specifically two 1mm thick sheets and a 0.5mm thick to make a total thickness of 2.5mm. The Alumina sheets were laser cut to the same profile on the inner edge as the core laminations. However, because of the limitations of available sheet size, the Alumina parts only spanned an angle of 90°. The outer edge did not include the same stepped projections at the outer edge, but rather has a circular profile with an outer diameter corresponding to the bore of the tubular section of the Titanium casing.

Unfortunately, the Alumina clamping plates achieved little in the way of drawing together the tooth regions of the core at clamping force levels which they themselves could withstand. Attempts to apply sufficient force to draw in the toothed regions resulted in failure of the Alumina sheet, in most cases at root of the tooth sections. Following a review of the requirement of the clamping plates and the failure of the Alumina parts, a modified clamping-plate arrangement was adopted based on a 3mm thick Titanium sheet which was profiled by wire-erosion to provide continuous support at the rear of the core and finger-like projections along the stator teeth of the core. In order to minimise the losses that would be induced in these Titanium end-plates, the support limbs which pass through the semi-circular voids in the stator cores were narrowed considerably in comparison with the width of the tooth being clamped. Figure 6.10 shows the assembled stator using Titanium clamping plates.

Figure 6.10: Assembled stator casing, core and Titanium clamping plates.

6.4.2 Stator coils

The manufacture of the stator coils provided the greatest challenges in terms of developing new techniques of manufacture and in ensuring the requisite degree of dimensional tolerance. Several iterations of the winding design, jigs and coil forming methods were trialled, including a re-manufacture of a full new set of 12 coils to replace an earlier set. The wire selected was Von-Roll SK650 which is based on a copper core conductor with Nickel plating which is lap wound with a phlogopite mica tape. The coils were encapsulated with Sauerisen No.10 encapsulant. This coil and encapsulant combination was down-selected during a previous systematic study [10] on a wide range of commercially produced high temperature wires and encapsulant.

The machine stator winding is a 3-phase, 12 slot winding with 20 series turns per phase. Hence, if the coils which make up are phase to be connected in series, then each phase would be made up of 4 coils of 5 series turns each. Of the two coil geometries proposed in section 5.3.3, the asymmetric coil arrangement was preferred over the two sub-coil geometry

for ease of manufacture. The required equivalent wire diameter for each series turn if a single conductor was used is ~4.8mm. Wires with such large diameters tend to have limited formability and as such can be very difficult to shape them into the required racetrack shaped coils in small to medium machines. Therefore, a parallel bundle of thinner wires with diameters in the range of 0.3mm to 1.2mm are typically used to manufacture coils which require a large cross-sectional area per turn. Additionally, the parallel wires require some form of transposition due to proximity effects as described in section 5.4.2.

However, the SK650, in common with all commercially available high temperature wires is only available in a very limited number of diameters, with 1mm overall diameter (0.8mm diameter core conductor) being the only diameter available at the time of winding design. As the selected conductor core diameter was 0.8mm, ~36 strands would be required per turn to make up the required cross-sectional area of one turn. In addition, the 4 coils would have to be terminated in the machine which requires high temperature terminations or else the individual coils would have to be brought out of the machine and terminated. Alternatively, the 4 coils of one phase could be wound in one continuous pass eliminating the need for coil to coil terminations.

In general, it is preferred in electrical machines to have the coils of a given phase connected in series to avoid issues such as unequal current distribution between coils. The use of asymmetric windings also derive benefit from employing series coils as it evens out any imbalance from the coils with different shapes having slightly different flux inductances. On the other hand, manufacturing high temperature coils for series connection this machine with the large number of multiple parallel strands required to achieve 5 series turns per coil is procedure very difficult process in terms of achieving a competitive packing factor, especially as these coils would be wound by hand in the demonstrator. In addition, the very large cross-sectional area of the region covered by one series turn will results in some degree of variation in flux linkages across this region, causing uneven current distribution which may lead to localised hotspots.

By making up one phase from a parallel connection of 4 coils, the number of turns in each individual coil can be increased. This makes the coils easier to manufacture. The terminations in this case can be made outside the machine, but most importantly coils with lower number of strands are easier to wind. Therefore, for the demonstrator machine a parallel connection of coils were employed, with each individual coils comprising 20 series turns, each of which comprises 9 parallel strands on 1mm overall wire diameter. It is

recognised that parallel connection of the coils is not ideal in terms of ensuring equal currents, and ultimately means of dealing with the uneven current sharing between coils may have to be included on the converter side.

The winding is based on employing two different coil cross-sections with the consequence that the arrangement of coils sharing a given slot is asymmetric as discussed previously in section 5.3.3. This arrangement was developed to enhance the slot fill while still maintaining the ability of adjacent coils to pass each other during the sequential insertion of coils. The coils are ex-situ wound on two different Aluminium jigs (to produce the two different cross-sections required). One of the jigs, prior to winding, is shown in Figure 6.11. The central limb around which the coil is wound is insulated with Kapton tape to prevent damage to the mica insulation. The coil is wound by rotating the jig using a chuck of a conventional lathe, albeit by hand at a very slow rate.

Figure 6.11: Aluminium coil winding jig.

As part of the coil forming process, the encapsulant was applied to each successive layer as the coil is built up by manual spreading in order to produce a rigid coil assembly. In an attempt to ensure that the cured coil retains its shape and dimensions when released from the jig, the process adopted for the first series of coils used clamping plates to precisely clamp the coil in shape during the initial drying of the coil encapsulant. Figure 6.12 shows a wound coil clamped into the jig (N.B. jig shown being that with the different cross-section to that shown previously in Figure 6.11).

Figure 6.12: Wound coil clamped in jig during curing of the encapsulant.

Many iterations and variants of the coil winding process were trialled during the manufacture of coil set for the demonstrator machine. There were several key modifications made to the coil design and the process as these trials progressed. The initial coil winding technique that was trialled was based on winding all 9 parallel strands simultaneously. The wire bunch also had to be periodically transposed to reduce proximity effects as described in section 5.4.2. These transpositions were restricted to the end turns in order to maximise packing factor in the slot area. However, winding with all 9 strands at once gave rise to significant difficulties in terms of controlling the lay-up of individual conductors, with tendency for conductors to cross-over. Such deviations from a precisely laid-up arrangement of individual wires diminish the achievable packing factor within the coil (i.e. the proportion of the overall coil cross-section which is occupied by copper as opposed to gaps and insulation). The difficulties of handling 9 wires in parallel, and the problems of maintaining precise location of each wire is illustrated by Figure 6.13, which shows the second layer of the coil being wound.

Figure 6.13: Initial winding trials with 9 parallel wires wound simultaneously.

In order to overcome these difficulties, which would have led to unacceptable reductions in packing factor, the coil winding technique was modified to employing 8 strands and winding 4 parallel strands at a time in an alternate fashion. Thus the coil includes some degree of imbalance as any form of bundle transposition would cause a significant decrease in packing factor. The loss of parallel strand compared to the original 9 stand design will lead to a higher current density and copper loss. However, on the basis of repeated unsuccessful attempts to employ 9 strands, this was considered essential in order to manufacture representative coils. This revised approach allowed far greater control over the disposition of individual wires as shown in Figure 6.14 which shows the 8 parallel conductors nearing completion, with the entry conductors of the 8 parallel conductors (which are shrouded within a braided fibre sheath) being evident in the background.

Figure 6.14: Coil part-way through manufacture based on winding with two sets of 4 parallel strands.

Using the revised method of winding two sets of 4 parallel stranded bundles wound alternatively, a full set of 12 coils was manufactured, i.e. 6 of each cross-section, in order to populate the stator core. As noted previously these were left clamped in the jigs overnight to allow the encapsulant to dry. On release from the jig, these were tested for dimensional clearance over the stator tooth and that they passed a coil of the different type during insertion. The coils were assessed one by one as the coils were manufactured and then set aside pending assembly of the full stator coil. However, although a full set of coils was manufactured in this way, when it came to final assembly of the stator winding, the majority of the coils would not fit into the slots, and by virtue of being essentially rigid could not be deformed to fit.

Some further trials indicated that this was due to the protracted nature of the full cure process of the encapsulant and that whereas a dry surface was achieved within a matter of hours, full curing to a rigid state was only achieved over period of 72 hours or so. This is consistent with the behaviour observed when insulation testing the coils, specifically a 1000V

insulation test between parallel strands. Tests of coils showed that the insulation withstand was achieved progressively over several days as the water based encapsulant fully dried out. To accommodate this ‘relaxing’ of the coil dimensions during cure, the process was modified to clamp the coil in the jig for an extended period of at least 72 hours. Although this slowed the rate of manufacture, it did result in more dimensionally stable coils. On removal from the clamp, the coils were inserted into the lined stator slots, with the remaining half of each slot being occupied either by a previously inserted coil or a PTFE wedge with the same cross-section as the coil that would be subsequently inserted into that region. This prevented invasion of the remaining half of the slot during any subsequent ‘relaxation’ of the coil. A part-populated stator core in which the PTFE wedges are visible is shown in Figure 6.15.

In addition to this change in process, the coil design was modified to reflect the difficulties encountered in fitting of the first set of manufactured coil. In order to provide a greater margin on the coil, particularly the tendency for the last few conductors to spring through the thin outer layer of encapsulant, the number of series turns in each coil was reduced from 20 to 19. The net packing factor of the coils produced was under the previously achieved 0.3, mainly due to the complications added by manufacturing coils with 8 parallel strands. Although this will have some impact on performance, i.e. an increase of some 5% in the operating current density, this design modification yielded significant dividends in terms of coil fit to the slot and hence additional margin on insulation reliability. Having identified these process and design modifications, a second full set of 12 coils were manufactured and inserted into the stator assembly. The stator fully populated with coils with slot wedges is shown in Figure 6.16.

Figure 6.15: Part populated stator core illustrating the PTFE wedges employed to retain coil geometry during final cure.

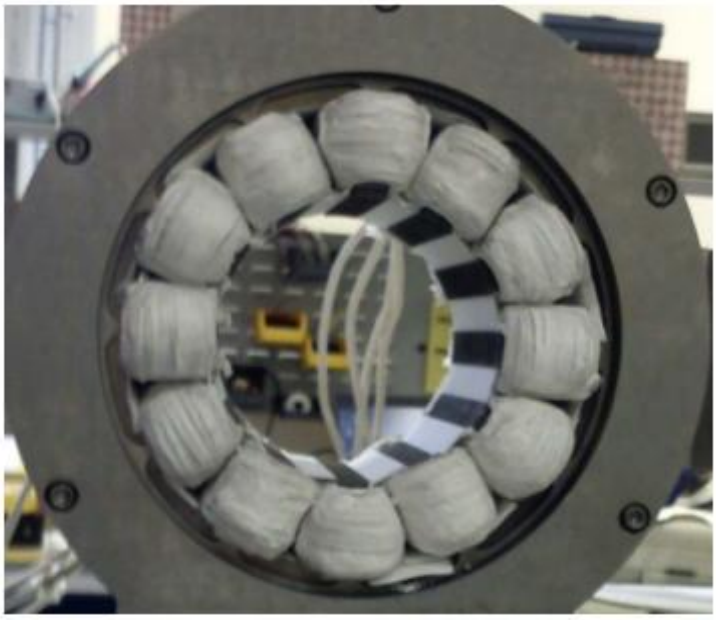

Figure 6.16: Fully wound stator assembly.

6.4.3 Rotor manufacture

The rotor core was manufactured from the same Vacodur S+ grade of Co-Fe as the stator core, but was subjected to a different heat treatment regime to achieve high mechanical strength at the expense of increased core losses. The rotor laminations were pre heat treated at 720°C for 2 hours to achieve a 0.2% yield strength of 620 MPa. The rotor core laminations were also produced by wire-erosion.

The rotor core is connected to the main shaft by means of a Titanium hub which was manufactured by wire-erosion. As mentioned previously, Titanium was selected as this is well matched in terms of thermal expansion with the Co-Fe core. Two notable design features, are the integral keys which locate into keyways on the inner bore of the rotor core and the axial skew in the 6 apertures from one end to the other. This skew was incorporated to provide some axial pumping of air to aid cooling of the rotor, although the extent of this benefit was not quantitatively assessed at the design stage.

The rotor core is retained axially and clamped by a pair of Titanium clamping-plates which are profiled to provide support to the sides of the rotor teeth. They are recessed away for the working air gap in order to reduce the magnitude of the eddy current induced losses. The main shaft which runs through the rotor core and the bearing stands was manufactured from Titanium (in order to provide a good thermal expansion match to the hub and Co-Fe core). Figure 6.17 shows the completed rotor assembly clamped using a set of Titanium bolts.

Figure 6.17: Completed rotor assembly.

6.4.4 Ancillary components

As discussed previously, in order to accommodate various potential differential thermal expansions between the hot and cold elements of the test-rig, it was deemed prudent to incorporate a mechanism which allowed the centre height of the rotor shaft to be adjusted. This was realised using adjustable bearing stands. The bearing vertical position can be allowed to float during the warm-up phase of the test rig with the rotor core resting on the bore of the stator core. Once the rig is up to temperature, the vertical position can be centralised and the bearings locked in place.

The entire test-rig is built up on an Aluminium base-plate into which are incorporated various slots and locating holes as detailed in the engineering drawings in Appendix E. A series of 4 Titanium feet were manufactured to connect the legs of the stator casing end-caps to the base-plate. The machine with the exception of the bearing stands is located within a thermal enclosure in order to achieve the desired ambient temperature of 350°C. This chamber was manufactured from layers of ceramic fibre board with Aluminium external framing. It incorporates a series of holes and to accommodate various structural, electrical

and cooling air elements. A pair of ports was also manufactured in Titanium to interface the bosses on the side of the tubular section of casing to cooling ducts through which 350°C air is passed to effect cooling to the rear of the stator core.

6.5 Procedure for raising the test-rig temperature

As described above, the HP shaft machine requires 350°C air flowing through the back of the stator core in order to draw heat from the stator. In the case of the demonstrator machine this cooling air can be initially used to raise the temperature of the machine and ambient to 350°C. The cooling air must then maintain this temperature and dissipate the losses in the stator. The 50mm thick thermal enclosure insulates the bearings and externals from the machine.

Raising air temperature from room temperature of 20°C to a temperature of 350°C requires a significant amount of power especially at higher flow rates if the system is a non-re circulated system, i.e. the hot air is exhausted on exit and the incoming air is draw in at 20°C. Figure 6.18 shows the calculated outlet temperatures for different flow rates and the power required to raise the temperature of standard pressure air at 20°C for such a non-recirculating system [11]. It can be seen that with a 9kW heater a flow rate of 50 ft^3/min (85 m^3/hr) must be maintained to gain an outlet temperature of 350°C. If the volume flow is increased, the heater outlet temperature drops sharply and the required heater rating increases. Therefore a closed loop or recirculating heater and fan arrangement has been proposed. As the hot air from the machine is fed back to the heater, the required increase in temperature from the heater and higher flow rates can be utilised. However this requires the fan to have a high inlet temperature capability.

A higher fan inlet temperature will necessitate smaller powers to raise the air temperature to the rated 350°C. The highest inlet temperature of a commercially available fan that could be sourced for this project was ~300°C. Therefore in the closed loop form the heater would only require to raise the temperature by some 50°C. A 9kW heater could raise the temperature by 50°C at flow rates of above 400 cubic ft/min (680m^3/hr).

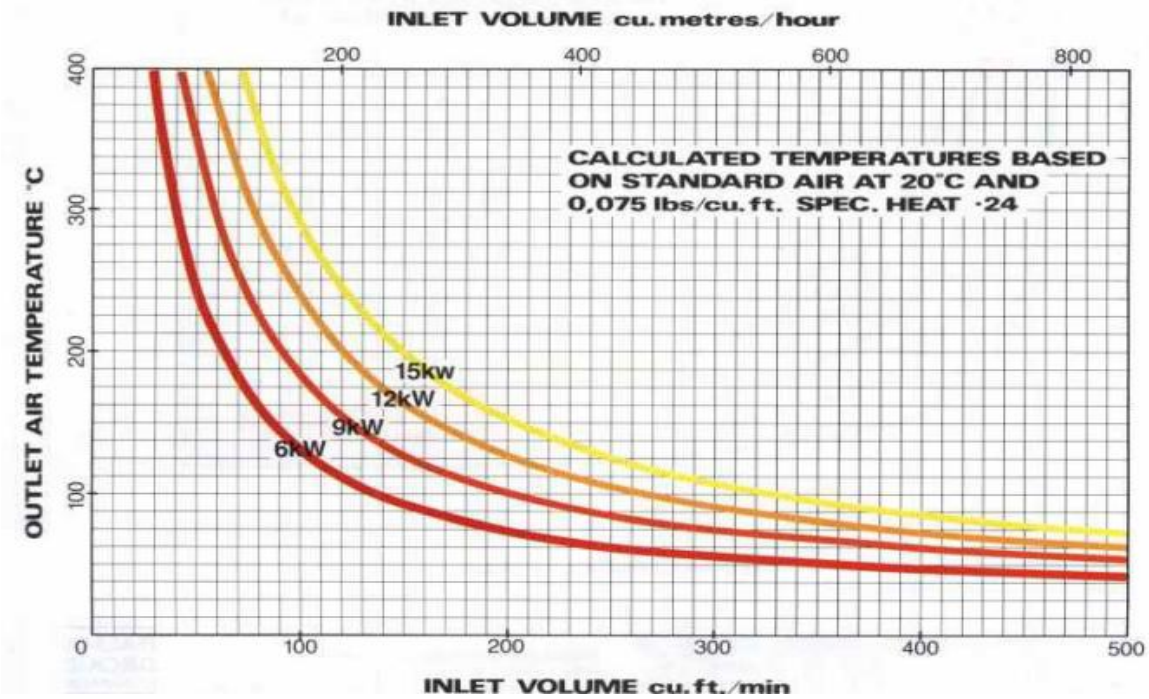

Figure 6.18: Outlet temperatures vs. flow rates for specific heater power ratings [11].

A schematic of the overall test-rig is shown in Figure 6.19. The fan which circulates the hot air is a high temperature centrifugal fan (Secomak 669SO) which is capable of long-term operating with an inlet temperature of 300^0C. This is a medium pressure fan with a static pressure of 1.7 kPa and a rated maximum flow rate of 750 m^3/hr, albeit at a much reduced pressure of 1.1 kPa. The heater is a 3 phase 9kW Secomak model 632. It consist of a stainless steel tube (containing resistive heating elements) covered with an insulated jacket to maintain low external surface temperatures. The fan outlet is connected directly to the heater inlet. The heater coils are switched on/off using relays controlled by a PID controller and a standard V/f control is implemented to adjust the fan speed. The demonstrator SR machine if operating on full load would produce ~1.2kW of loss, a significant percentage of which is dissipated through the back of the core and into the re-circulating air raising the exit air temperature to ~400°C. It is therefore necessary to effect some cooling of the return leg if the fan inlet is to be maintained at 300°C. This may have to be managed by partially exhausting some high temperature air and mixing with some room temperature air.

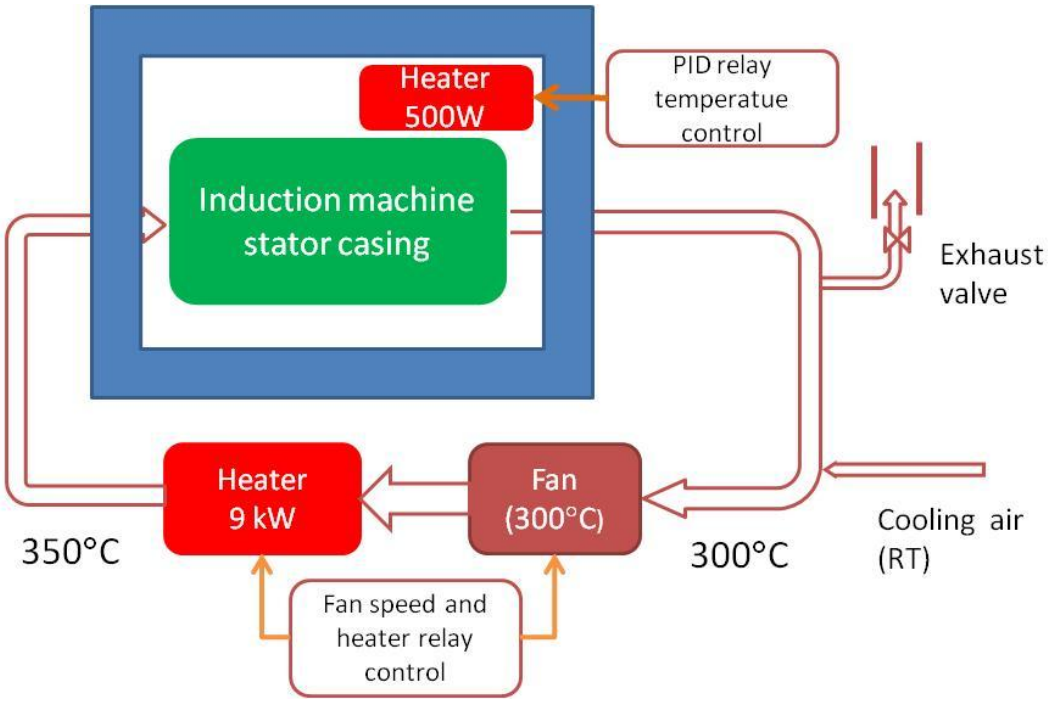

Figure 6.19: Schematic of the test-rig used for high temperature testing.

The outlet of the heater was connected to the SR machine casing by means of a flexible, high temperature ducting which is shown in Figure 6.20a prior to the application of additional insulation. However, the temperature drop between the heater outlet and the machine inlet proved excessive in terms of achieving the desired steady-state temperatures and a single layer of some 10 mm thick of loose Rescor ceramic fibre blanket (akin in form to 'cotton wool') which was kept in place by an overwrap of a Silica woven cloth was used to insulate the duct as shown in Figure 6.20b. An additional layer of the loose ceramic fibre insulation was then added, which was maintained in place with Rescor 390 ceramic paper and Aluminium foil as this proved more suitable for tight wrapping of the loose insulation. The final duct arrangement used for the tests is shown in Figure 6.20c.

(a) Flexible duct with no insulation

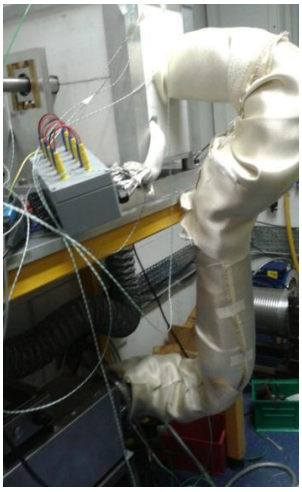

(b) Single layer of additional insulation with Silica cloth over-wrap

(c) Second layer of insulation with Aluminium foil over-wrap

Figure 6.20: Heater to machine ducting at various levels of insulation.

However, the limited pressure capability of the fan and the apparently large flow rate restriction presented by the complex series of narrow channels in the back of the core through which air flows resulted in rather modest air flow rates. This low flow rate resulted in problems with ensuring sufficient power flow into the system, since for reasons of safety, the heater power was regulated by the heater output temperature rather than by a down-stream sensor. The low flow rates resulted in rather rapid heating of the regulating temperature for the controller which in turn gave rise to significant modulation of the heater power despite the fact that the machine components were lagging significantly in terms of temperature rise.

Although improving the insulation between the heater output and the machine inlet allowed some improvements in steady-state temperature capability, ultimately it became necessary to include a supplementary 500W, 230V ceramic heating element in the enclosure itself. This heater, which is rated for a continuous operating temperature of up to 700°C, is shown in Figure 6.21. This was independently controlled by a dedicated PID controller using a thermocouple mounted in the heater block itself. This reduced the time taken to heat up the rig components, and more particularly allowed a steady-state machine temperature of 350°C to be reached before testing the machine. In order to maximise the heating rate of the entire rig, the set-point temperature for the main air circulating heater was initially set at a

temperature substantially higher than the final target temperature and stepped down as the remainder of the rig heated up.

For the purposes of measuring representative coil temperatures, thermocouples were attached to the surfaces in the end-winding regions of selected coils using an Idenden 10-02 ceramic adhesive. It is recognised that this is a localised temperature and that there will be some degree of temperature gradient within the coil, particularly but not exclusively, when the machine is excited and there is appreciable copper loss generated in the stator coils themselves. Due to the location of the air inlet and outlet, a temperature variation across the machine will be expected especially under unexcited conditions. The thermocouple measurements were taken from coils numbered A1, B1 and C4 shown in Figure 6.22, as these were deemed to provide a representative set of coil locations and temperatures. It was observed that during initial ramping up of the test-rig temperature, the coil B1 would always have higher temperatures than coil A1, followed by C4. The average coil temperature quoted in the figures below is based on the average of the 3 measured coil temperatures and was considered to be the overall machine average.

In addition to thermocouples attached to the machine coils, the temperature at other key points in the test rig were measured using thermocouples. The locations of these thermocouples are:

1. Inlet temperature - measured by a thermocouple mounted in the air-flow in the conical section of the ducting at the inlet to the insulated enclosure.

2. Outlet temperature - measured by a thermocouple mounted in the air-flow in the conical section of the ducting at the outlet to the insulated enclosure.

3. Ambient temperature - measured by a thermocouple in the main cavity of the enclosure

4. Room temperature - measured by a thermocouple in the main test cell in which the entire test-rig was located. This temperature is not regulated per-se, but a powerful extract system can be used to avoid any significant drift in the room temperature.

Figure 6.21: Supplementary ceramic heater used in 350°C tests.

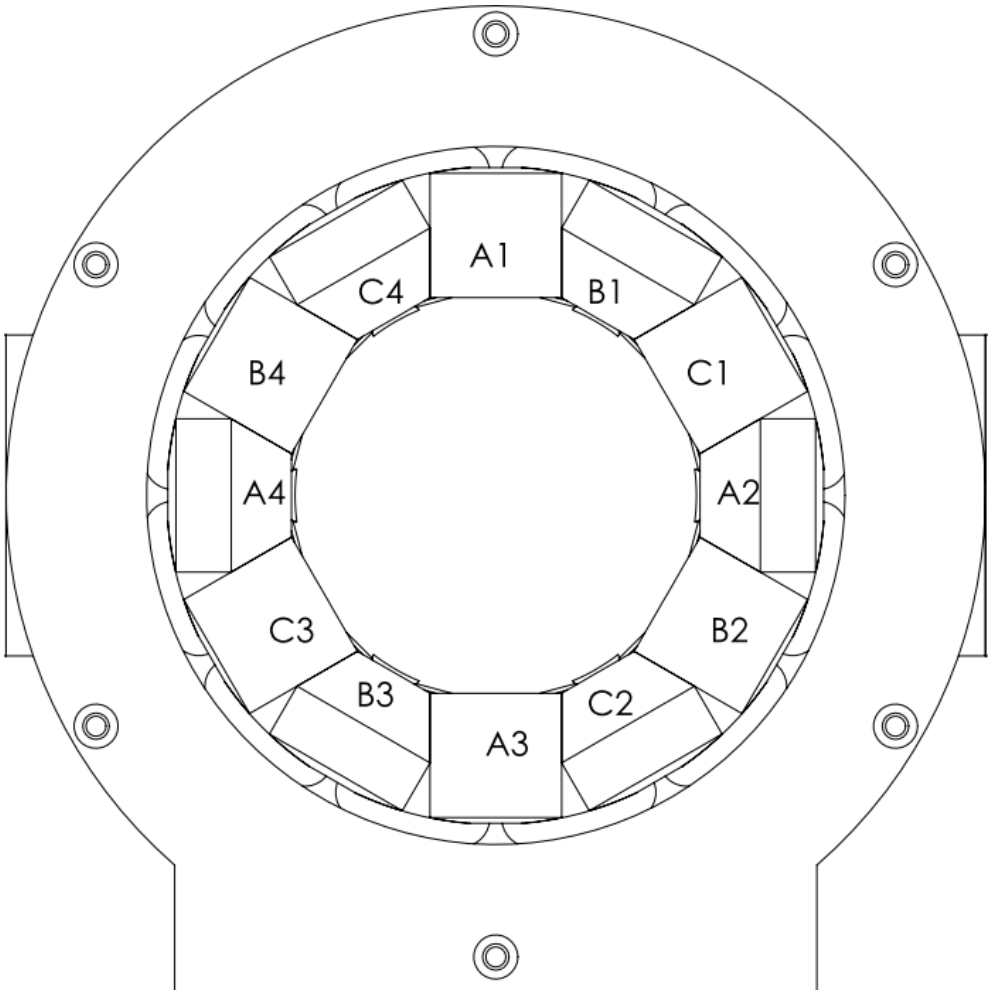

Figure 6.22: Numbering of coils as positioned in the stator.

The variations in temperatures at key points around the test-rig up the point at which the testing was conducted are shown in Figure 6.23 for the 200°C test case. The initial set point on the heater outlet was set to 350°C. The downward steps in the inlet temperature show the effect of the manual adjustment of the system regulating temperature at the heater outlet which was dropped to 275°C at steady state. The set temperature of the ceramic heater was reduced from the initial set maximum of 700°C to 500°C at steady state.

As noted previously, a significant temperature variation was observed across the stator. The average temperature of the three coils was adopted as being representative of the average temperatures across the entire stator. For this temperature set-point of 200°C, the system takes ~2.5 hours to come to a reasonable steady-state. Figure 6.24 shows the variation in the measured temperatures for the 350°C test case. The heater outlet temperature for this case had to be increased from 450°C to 500°C in order to achieve the 350°C (average of the three measured coil temperatures). For the 350°C test case the system took ~5 hours for the average temperature in the coils to reach a steady state.

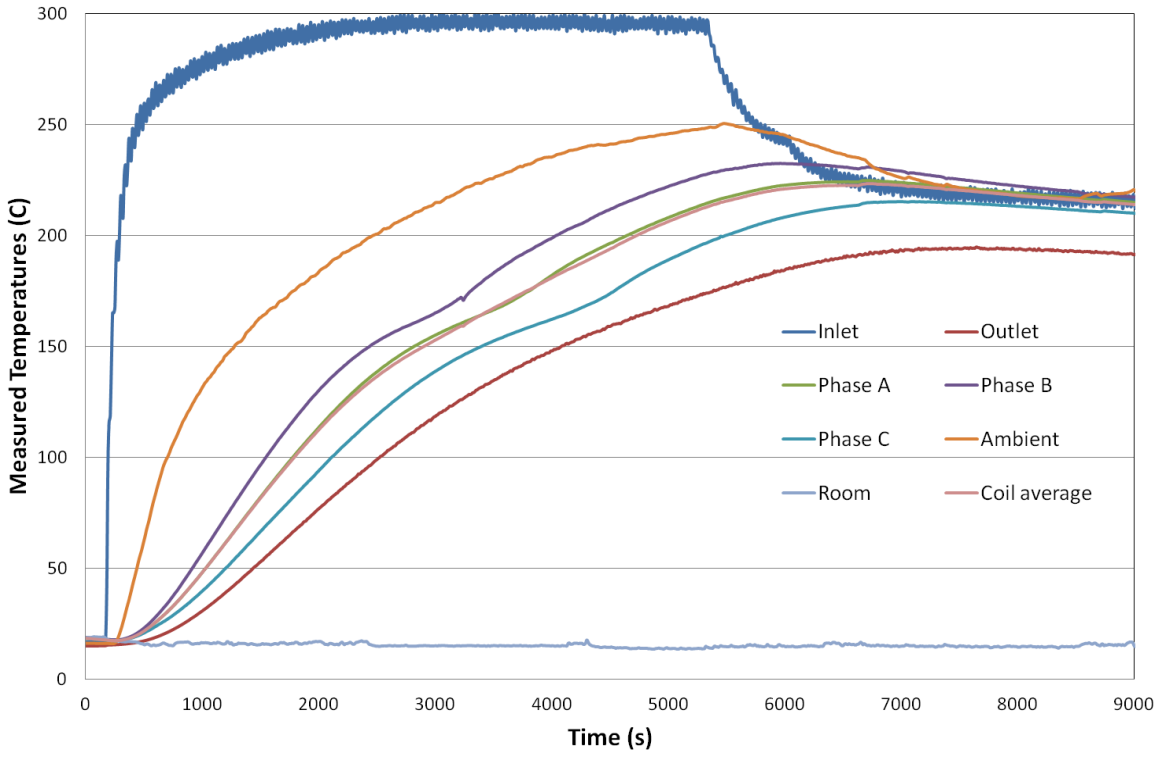

Figure 6.23: Measured temperatures during heat-up procedure for 200°C test.

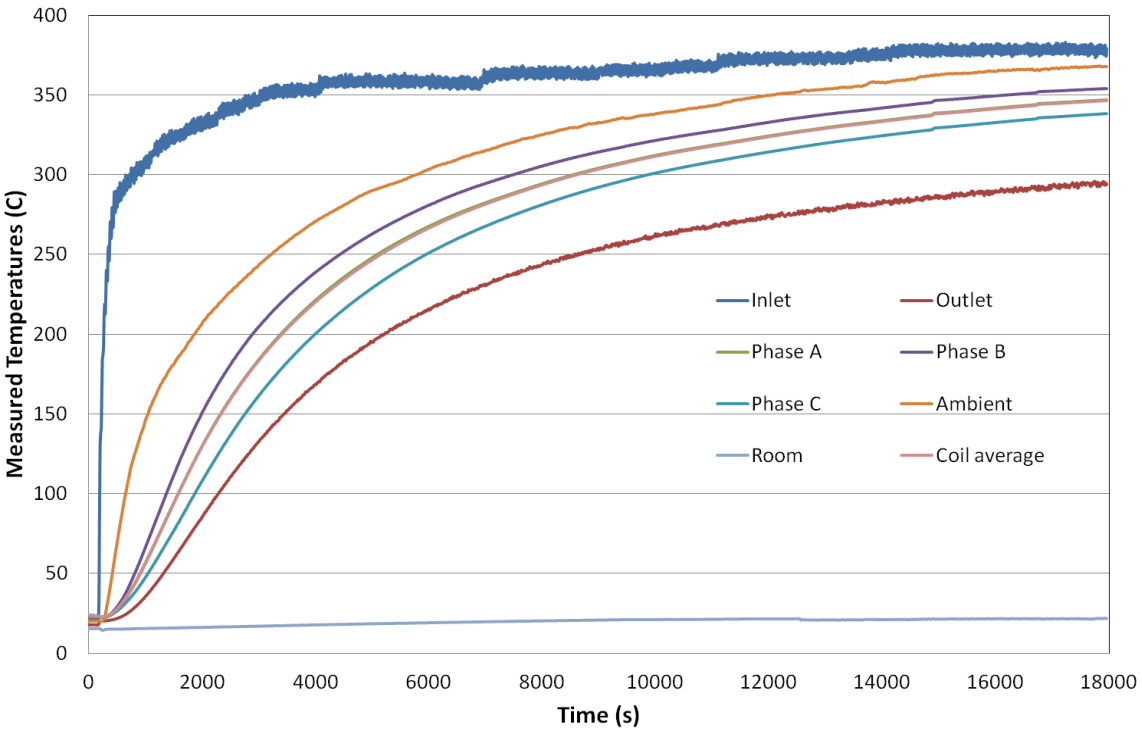

Figure 6.24: Measured temperatures during heat up to 350°C.

6.6 Testing schedule

Ultimately, in order to fully validate all the findings from the design study reported in chapter 5, it would be necessary to run the machine at the rated power and speed in a well controlled 350°C which prescribed air flow conditions in the cooling path. It was planned to perform some level of machine running at elevated temperatures in the test-rig by using a three-phase SR drive developed during a previous research project [3], and further developed as reported in [12]. Unfortunately, static testing of the SR machine and initial attempts to achieve some degree of rotation highlighted several practical problems which hindered the full commission of the test-rig.

The setting up of the bearing stands at elevated temperatures and the limited overall stiffness of the overall drive-train gave rise to significant problems with unbalanced magnetic pull, to the extent that for currents in excess of 15A, it proved difficult to prevent the rotor from being drawn into contact with the stator bore. This may in part have been the result of the difficulty of reliably setting a symmetrical air gap, when trying to do this remotely with one degree of freedom at each end at elevated temperatures. Despite many endeavours to produce a system of sufficient stiffness and precision to run at elevated temperatures,

ultimately it was concluded that a fundamental re-appraisal of the test-rig, specifically in terms of the bearing arrangements would be required as detailed in section 6.7 at the end of this chapter. The level of rig re-design required in terms of structural and thermal issues around the bearings, was deemed to be prohibitive in terms of the outcomes of this research. Hence, testing of the demonstrator machine was limited to static considerations of many important aspects of behaviour, including extensive testing at the rated temperature of 350°C.

6.6.1 As-manufactured coil resistance and inductance

Prior to raising the machine temperatures, the resistance and inductance of the individual coils were measured. Due to the inherent saliency of the SR machine the inductance of the coils are functions of the rotor position. Therefore the minimum and maximum inductance was recorded by keeping the rotor at the aligned and unaligned positions. The coil resistances were measured using a Cropico DS5000 micro-ohmmeter, and the inductance was measured on a Hioki LCR meter at 1 kHz. As might be expected given the manual procedures involved in manufacturing coils, there was some variation in measured resistance and inductance. Normalising the mean values to 100%, gives resistance and inductance variations of ±7% and ±10% respectively.

Table 6-2: Measured as-manufactured resistance and inductances of the individual coils.

Coil	Resistance (mΩ)	$L_{unaligned}$ (μH) @1kHz	$L_{aligned}$ (μH) @1kHz
A1	25.0	178	695
A2	23.9	164	771
A3	24.2	178	704
A4	24.1	164	613
B1	25.0	163	720
B2	26.4	176	760
B3	25.2	161	648
B4	24.9	177	632
C1	27.4	184	750
C2	27.8	176	723
C3	25.9	190	698
C4	25.3	167	642

6.6.2 Measuring flux linkage vs. current curves

The measured variations in flux linkage as a function of current and rotor angular position provides significant information regarding the torque capability using simple test equipment. The procedure involves driving a set of DC currents at a fixed rotor position and measuring the flux linkage in the coil. This would require a separate drive coil for carrying the current and sense coil to measure the flux-linkage of each phase. Since the SR machine coils consisted of 8 parallel strands insulated from each other, one strand was separated and used as a sense coil, and the remaining 7 strands were bunched and used as the drive coil. The rotor position was kept fixed at known angular positions using a locking mechanism shown in Figure 6.25. The measurements were taken by connecting all the coils in phase A in series. The flux linkage was measured using the Magnet Physik EF14 integrating flux meter, and a

20V, 100A Tektronix DC power supply with a current limit was used to drive the phase currents.

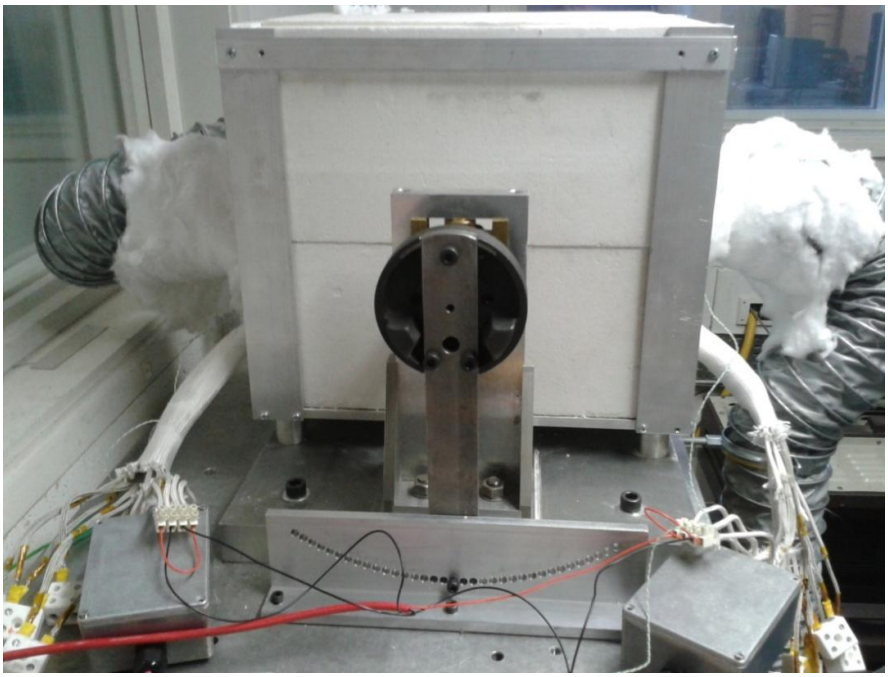

Figure 6.25: Arrangement for measuring flux-linkage versus current curves at temperature.

In measuring successive curves it is necessary to recognise that there may be some residual magnetisation remaining from previous excitation. These effects will be more pronounced around the fully aligned position. In order to minimise the effects of residual magnetisation, the current schedule was selected to be representative of a demagnetisation curve. The highest current was selected first, after which, the direction was reversed with the same magnitude. The current was then reduced in steps and consequently reversed to represent what may look like a step-wise demagnetisation curve. The procedure was also repeated with an increasing current profile and alternatively by selecting individual currents without switching polarities. In all the cases, the difference in the flux measurements was marginal and hence either scheme can be employed.

Figure 6.26 shows a comparison of the predicted variation in the flux linkage as a function of current for a series of discrete rotor positions at room temperature. Although the flux linkage curve broadly matches the predicted curves, there is a small reduction in flux linkage at the aligned positions, which will correspond to a reduction in torque capability.

Figure 6.27 shows the measured flux linkage curves at room temperature, 200°C and 350°C. As expected there was a reduction in flux linkage close to the aligned conditions due to the reduction of permeability of the core.

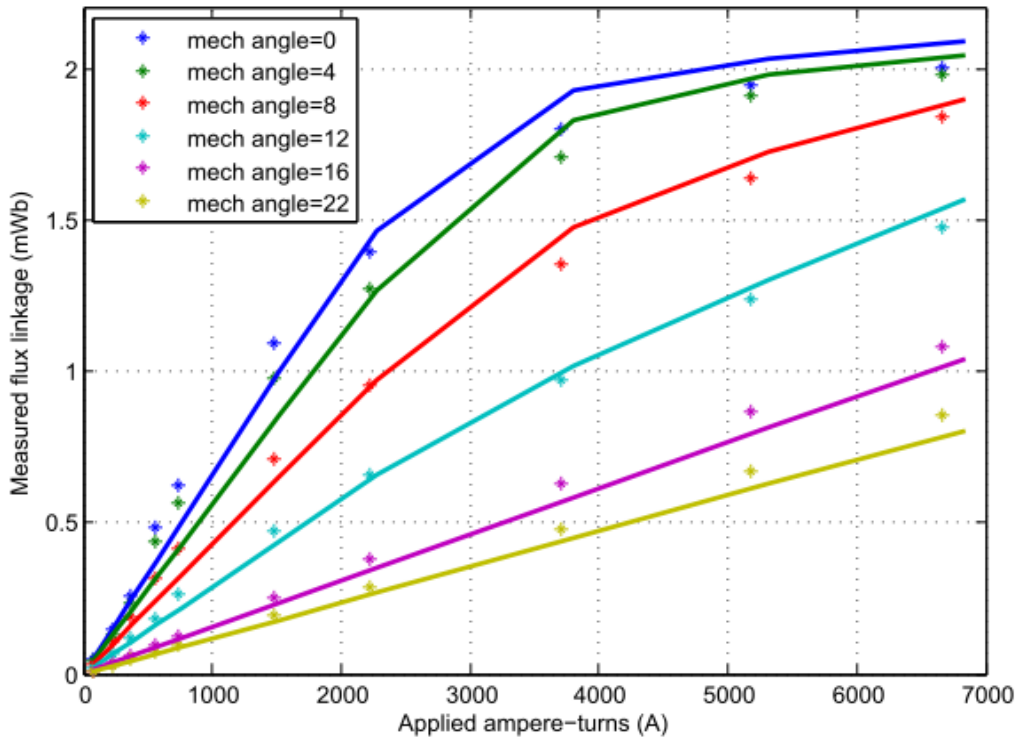

Figure 6.26: Comparison of measured (markers) and predicted (lines) flux linkage vs. current characteristics at various rotor angular positions (Mechanical angle of 0 corresponds to fully aligned position).

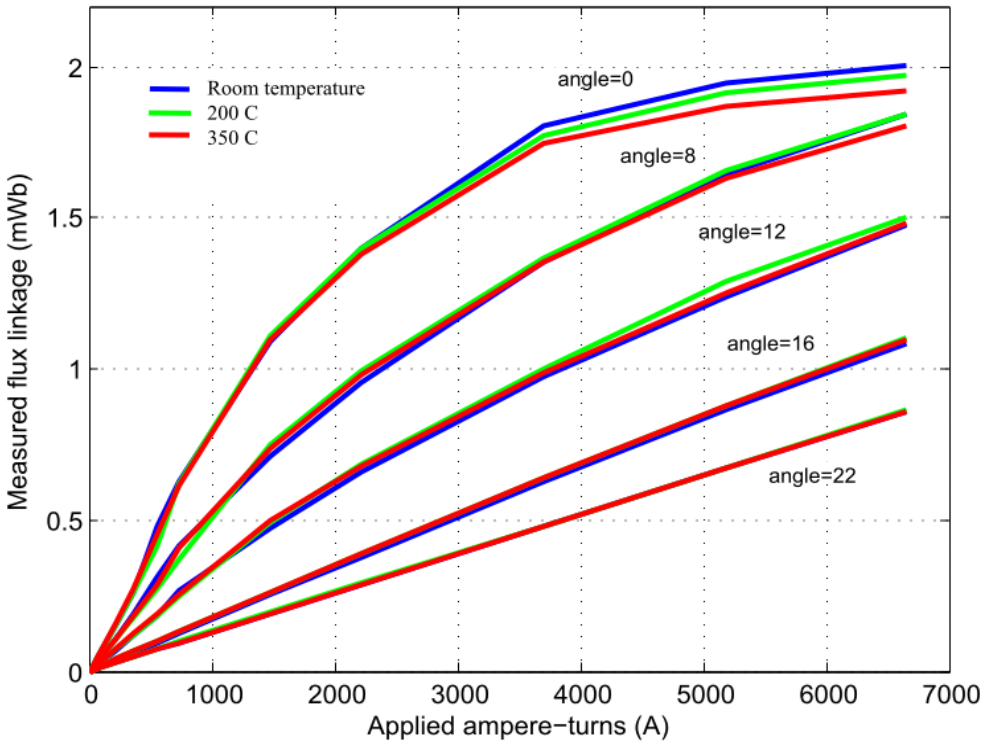

Figure 6.27: Comparison of measured flux linkage vs. current characteristics at various rotor angular positions at room temperature, 200°C and 350°C.

6.6.3 Steady state coil temperatures

As mentioned previously, due to issues with bearing and rotor alignment, the SR machine could not be tested under rotating conditions. Therefore, after reaching the test temperatures and conducting the ψ, i measurements at elevated temperatures, further test were performed to establish representative thermal conditions within the coils (recognising that the absence of core loss means that the temperature distribution within the machine will be markedly different from rated operating conditions of 15kW at 30,000rpm).

The DC power supply was used to drive the rated current through all the coils. As the predicted rms phase current was 78A for an arrangement with 4 coils connected in parallel, each coil has an rms current of ~20A assuming equal current sharing. In this case, all 12 coils were series connected to the power supply (operating in constant current mode). The rated current of 20A was driven through the coils with ambient chamber temperatures of 200°C and 350°C for a period of 2 hours during which steady-state temperatures were achieved. The DC current and voltage across the series connection of 12 coils were measured in order to calculate the increased resistance and hence estimate a mean coil temperature from the

manufacturer's published temperature coefficient of resistance for the actual wire (0.004041 per °C as compared to 0.00393 per °C for pure copper).

The measured variation in temperatures from the thermocouples is shown in Figure 6.28 for the 200°C test case. The mean coil temperature estimated from the current and voltage measurements is shown in Figure 6.29. For the 200°C case the bulk coil temperature increased by ~65°C which may be higher than expected considering the core losses were not present in the stator. The measured average coil temperatures at the end windings increased by 75°C above the nominal 200°C ambient. The ambient temperatures within the enclosure also crept up as it was not directly controlled (recalling that the control temperature is the heater outlet). Figure 6.30 shows the measured localised coil temperatures for the 350°C test case with rated current in the coils. Figure 6.31 shows a 75°C rise in bulk coil temperature as estimated from the increase in total coil resistance. The measured average coil temperatures at the end windings increased by 80°C above the nominal 350°C ambient in this case.

The higher than expected coil temperatures were due to the low flow rates achieved by the fan and heater arrangement, restricting the level of cooling provided at the back of the stator core. The major drawback of the lower flow rates however was that a significant temperature differential existed across the stator from the air inlet to the outlet of ~80°C at the 350°C temperature set-point. This meant that the coils closer to the inlet had temperature a higher than 350°C (up to 380°C) and those at the outlet lower. Therefore a means to more uniformly heat up the demonstrator machine would need to be employed for future test rigs and a higher flow rate cooling air must be applied to reduce the large temperature differential across the stator.

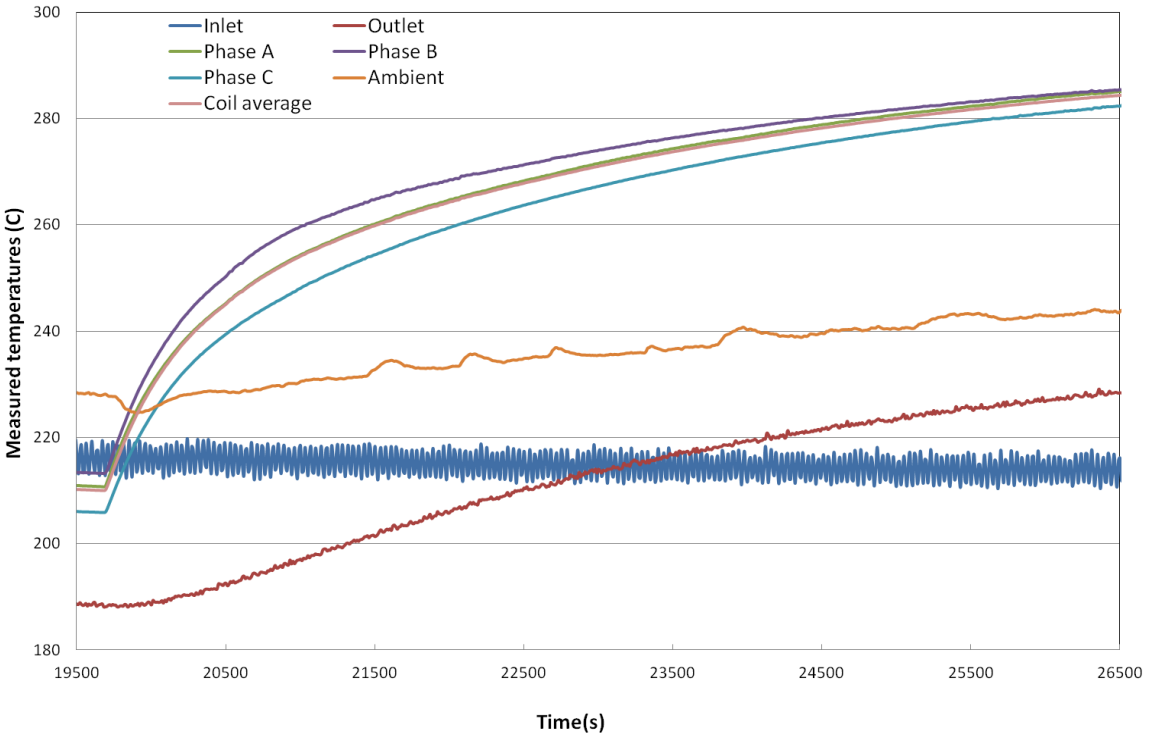

Figure 6.28: Measured temperatures with rated current in coils at 200°C.

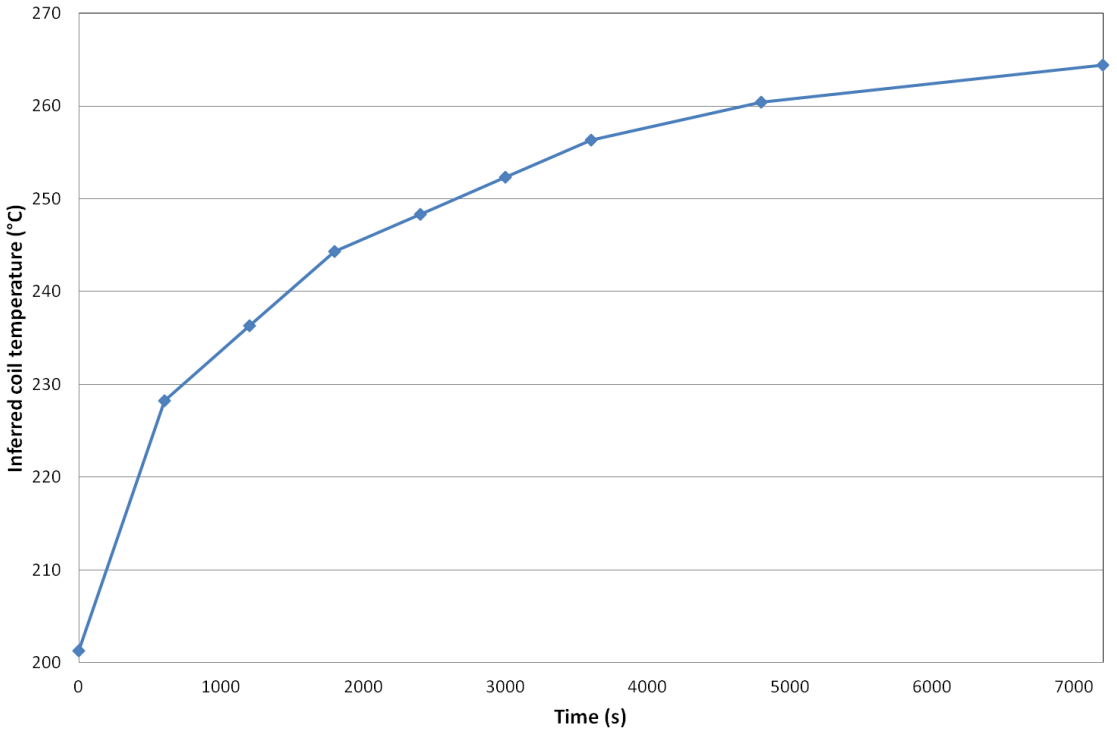

Figure 6.29: Average coil temperature inferred from resistance measurements at 200°C.

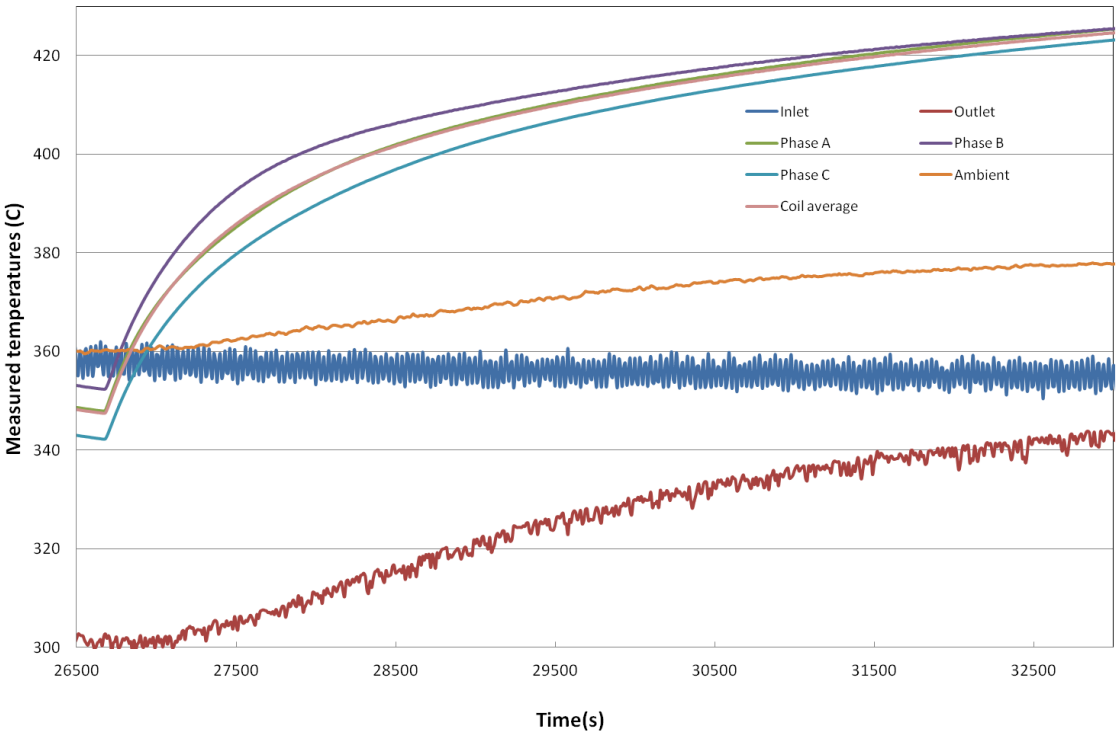

Figure 6.30: Measured temperatures with rated current in coils at 350°C.

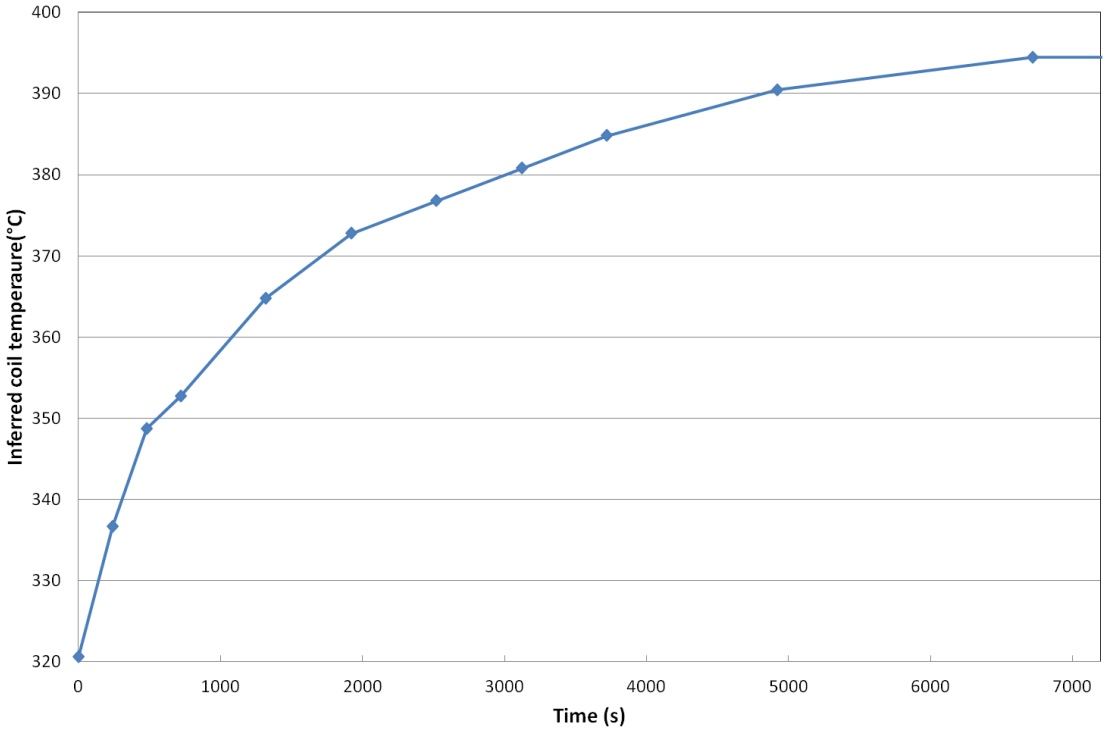

Figure 6.31: Average coil temperature inferred from resistance measurements at 350°C.

6.7 Proposed upgrades to demonstrator machine and test rig

As mentioned in section 6.3 the unavailability of bearings at operating temperatures imposed a number of compromises on the rotational machine test-rig at high temperatures, which turned out to be very restricting in terms of demonstrating viable rotation of the demonstrator. The test-rig architecture of having the bearings situated remotely from the machine on separate end stands was successful at keeping bearings insulated and below its rated temperatures. However, the method employed to adjust the rotor centre height at both ends could not align the rotor accurately enough at elevated temperature, resulting in excessive unbalanced radial forces when the coils are excited. Therefore, an essential upgrade would be to modify bearing stands and include necessary systems to measure the rotor position with respect to the stator, when the machine is at temperature and largely inaccessible. Recourse to a more conventional integrated machine end-cap with highly localised cooling of the bearings might be another option, i.e. something akin to Figure 6.8. The dynamometer machine used to drive/load the demonstrator machine would also need to be mounted on adjustable endplates such that the two shafts can be aligned at temperature.

The second major shortcoming of the test-rig was the inability to sustain sufficiently high air flow rates due to the large pressure drop across the cooling fins on the stator back iron and the modest pressure capability of the fan employed. Overcoming this problem either requires procuring a high pressure/high temperature fan, or reconsidering the cooling strategy altogether, the first option being the preferred. The search for commercially available high pressure/temperature fans however proved fraught, and it may be necessary to employ a bespoke fan design to more closely replicate the kind of high pressure, high temperature air flow that would be available in an engine.

Managing the rotor losses in the machine has been largely over-looked in this study, but is a significant factor if rotor temperatures are to be contained. Another issue faced was the need to employ Titanium end plates due to the mechanical failure of the preferred Alumina counterparts. A simple method to overcome this would be to employ a relatively lower core stacking factor, in order to reduce the stresses on the end plates.

6.8 Summary

This chapter has described the manufacture of a high temperature electrical machine demonstrator together with an associated test-rig. Of the various elements of the machine, by far the most challenging in terms of the need for several iterations of the process has been the manufacture of the stator coils. The final set of coils had a lower than expected packing factor, however the initial prediction of packing factor of 0.3 was based from relatively simple single stranded circular coils. The larger number of parallel wires makes manufacturing high temperature coils much more problematic, and methods of increasing packing factors are vital for such machines.

The limitations on bearings also proved to be a significant factor in constructing a demonstrator for high rotational speeds. The need to accurately centre the rotor axis and cancel out unbalanced forces required significant modification to the built test rig and hence limited the possibilities of testing the SR machine. The cooling strategy proposed for the stator although provides a large surface area gain required high pressure air which could not be achieved from the high temperature fan. However as mentioned in section 6.7, with extensive structural modifications to the bearing arrangement (most likely a radical re-design) and modifications to the heating arrangement dynamometer, the testing of the machine is considered as future work.

References

[1] W. E. Rippel and D. M. Kobayashi, "Lamination Cooling System Formation Method," United States Patent, 2009.

[2] S. T. Evon and W. E. Martin, "Enhanced Electrical Cooling," United States Patent, 2006.

[3] S. D. Calverley, "Design of a HIgh Speed Switched Reluctance Machine for Automotive Turbo-Generator Applications," PhD, Department of Electronic and Electrical Engineering, University of Sheffield, Sheffield, 2001.

[4] A. Mulach, "Stator Core Cooling for Dynamoelectric Machines," 1980.

[5] G. L. Flem, "Cooling arrangements for rotating electrical machines," 1999.

[6] P. L. Andrew and F. J. Rink, "Direct cooled dynamoelectric machine stator core with enhanced heat transfer capability," 1999.

[7] Rich Schiferl, Michael J Melfi, and Q. J. Dong, "Lamination Stack Cooling Path," 2007.

[8] Y. G. Dessouky, B. W. Williams, and J. E. Fletcher, "Cooling enhancement of electric motors," *Iee Proceedings-Electric Power Applications*, vol. 145, pp. 57-60, Jan 1998.

[9] M. Festa, H. D. Eberhardt, and W. Hofmann, "Design Aspects of Circumferentially Cooled Frameless Machines," *2009 International Conference on Electrical Machines and Systems, Vols 1-3*, pp. 1284-1289, 2009.

[10] S. Gibson, "Commercial high temperature encapsulation/potting material and coil testing," University of Sheffield, Sheffield2008.

[11] Cedrat. *Flux*. Available:

[12] M. Michon, "Switched reluctance turbo-generator exhaust gas energy recovery system for ice vehicles. ," Ph.D., Department of Electronic and Electrical Engineering, University of Sheffield, Sheffield, 2008.

Chapter 7 : Conclusions

7.1 Introduction

This thesis has described research contributions in the field of electrical machines for operation in high temperatures, which culminated in the design, construction and preliminary testing of an SR machine for operation in a 350°C ambient. The thesis has described methods to overcome many of the challenges of high temperature machine operation, particularly in terms of the modelling and understanding of the impact of temperature on key material properties and aspects of machine performance. Some of the key outcomes and resulting suggestions for future work in this area are outlined in this chapter.

7.2 Material properties

The research has demonstrated material properties for operation at such temperatures are critical feature, both in terms of material selection and the effect of temperature and ageing on performance. Key findings are

i. The magnetic properties of high temperature grades of permanent magnet materials are so dilute at 350-400°C (e.g. 50% of room temperature remanence of conventional grades) that they are unlikely to be suitable for use in high temperature machines, without a step change in magnetic performance from new materials.
ii. There is evidence that thermal ageing rates increase at temperatures above 300°C and begin to accelerate above 350°C. Hence, thermal ageing of core materials is an important issue to factor in during material grade selection and predictions of machine performance when operating at these temperatures.

7.3 Electromagnetic modelling of machines

In order to more reliably predict the performance of machines at elevated temperatures, several new modelling methods were developed and used during the course of this research:

i. A method to calculate instantaneous core loss was introduced, which was formulated such that it could be used in circuit simulations to ensure power balance.

ii. The Preisach model was shown to predict instantaneous hysteresis loss effectively for complex excitations.

iii. The method employed to represent losses in the circuit simulation had some drawbacks, notably the requirement to divide the total loss among different phases.

iv. The instantaneous core loss model showed good correlation when validated against experimental measurement on a toroidal sample. However for the test cases considered, the anhysteretic or lossless model showed some discrepancies. This illustrated the limitations of using a single anhysteretic curve for characterising reactive power.

v. The effects of including core loss in the system predictions for the SR machine model were not as pronounced as expected in terms of the effect on the machine current and torque. Nevertheless, the model provides a rigorous power balanced approach to dynamic circuit coupled FE modelling.

7.4 Material characterisation for loss models

The relative lack of published data on high temperature magnetic properties for use in the proposed model made it necessary to undertake a substantial programme of material characterisation, the key outcome of which are:

i. By taking advantage of the ability of the model to predict loss for arbitrary flux waveforms, simple open loop measurements methods such as those proposed in chapter 4 can be employed.

ii. Prediction of losses over a large frequency range up to 4 kHz has been shown to have limitations. The model based on using the residual loss to calculate excess loss coefficients showed a significant spread of the predicted excess loss coefficients. Therefore it was not possible to specify a single value of the co-efficient to cover such a wide range of frequency and flux density.

iii. The measurements on the aged samples demonstrated that the static loop area and electrical resistivity of the Co-Fe core material were relatively stable with ageing at high temperatures, and yet there was a significant increase in high frequency core

losses. Thus, there is reasonable evidence base to suggest that excess loss is a significant contributor to the increase in loss with temperature.

iv. The spread of values of excess loss coefficients was much larger in the case of the aged samples. Therefore, a modified dynamic model was proposed which employs a larger number of parameters in order to better fit the measured loss data. However this model, which is based on fitting parameters to observations, does not have a rigorous theoretical basis and, was used as a means to an end.

7.5 Design of a high temperature SR machine

The design optimisation of a 15kW 30,000rpm SR machine for 350°C ambient operation was described in detail. Key issues which arose in the design are:

i. The design illustrated the effects of the material properties on the machine sizing and operation.

ii. Although the initial concern at the outset of the analysis was that the higher resistivity of copper would lead to excessive copper loss, it transpired that it was a relatively small contributor to the overall loss was the high core loss.

iii. The high core loss, which is largely a consequence of the material grade selection and the high frequency nature of the machine, proved to be the dominant loss mechanism in the stator from an efficiency and, somewhat surprisingly, thermal standpoint.

iv. The final design showed that moderate power densities (order of ~1.35 kW/kg) can be achieved for the rated specification at an ambient temperature of 350°C. However the machine required a significant amount of heat dissipation from the core back iron.

v. Several practical factors were not incorporated in the machine models, such as high frequency copper losses, ageing effects in the Co-Fe core and Nickel diffusion in the conductor. All these factors could influence the outcome of the optimisation in terms of identifying the most appropriate slot depth. This was mitigated to some degree by a sensitivity study.

vi. The rotor would require a significant degree of cooling on its exposed surfaces to maintain temperatures below 450°C.

7.6 Construction and testing of the high temperature demonstrator machine

The many challenges faced in the manufacture of a machine prototype and test-rig for high temperatures has been discussed at length in chapter 6. Key outcomes include:

i. The manufacture of reliable high temperature coils was the most challenging aspect of the machine build. Typically high speed machines require coils with multiple parallel strands, employing methods such as bundle transposition to reduce AC copper losses.

ii. The bearings were the main limitation to testing machines at temperature. The non-availability of high temperature bearings required the use of bearing stands that were insulated from the high temperatures. This lead to several complications such as uneven thermal expansion, which required adjustment of the bearing heights.

iii. A method to cool the stator core directly by employing a large number of parallel cooling channels was proposed as a solution to dissipating the large heat flux at the stator core. This method takes advantage of the high velocity and high pressure air present in the HP compressor of the gas turbine. However the method used to generate the high temperature air in the lab had severe limitations due to the low pressure of the high temperature fan.

iv. The practical demonstration of a reliable, high-speed, power-dense electrical machine operating in a 350°C ambient still remains a somewhat distant prospect at the culmination of this research. However, this is now largely an issue of mechanical arrangements and bearing rather than one of limited electromagnetic understanding.

Appendix A: Curve fits of core loss model to published data for Hiperco50-HS.

This appendix illustrates results of employing the curve-fitting technique described in section 2.7, on the published data of thermally aged Hiperco 50-HS samples. The published core loss data at temperatures up to 400°C at ageing times of 1000, 2000 and 5000 hours were fitted to the standard core loss model described in section 2.7.

Table A.1: Variation in parameters of loss model with temperature for 1000 hours aged Hiperco 50-HS.

Temperature (°C)	Room Temperature	200	400
Resistivity ($\mu\Omega$-m^{-1})	38	43	51
k_{exc}	0.8x10^{-4}	1.0x10^{-4}	1.5 x10^{-4}
k_h	0.12	0.11	0.10
a	1.9	2.0	2.0
b	-0.15	-0.15	-0.15

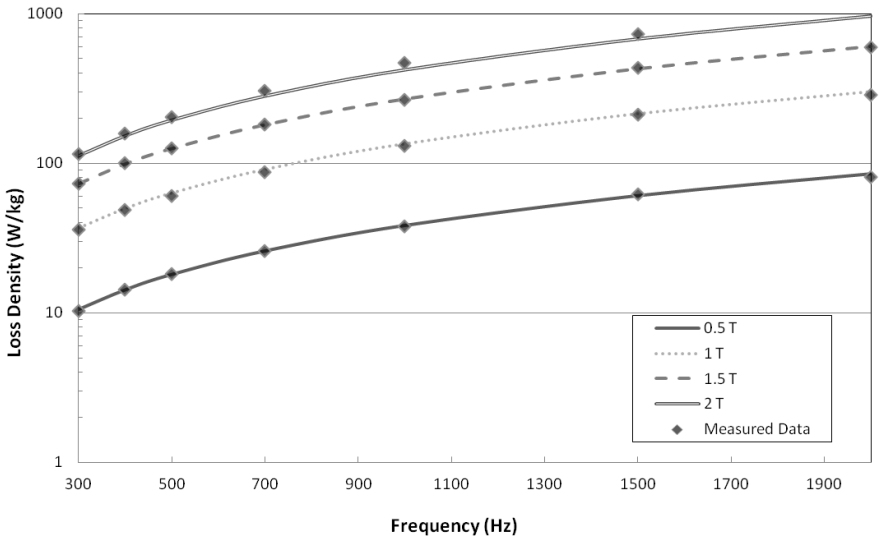

Room temperature

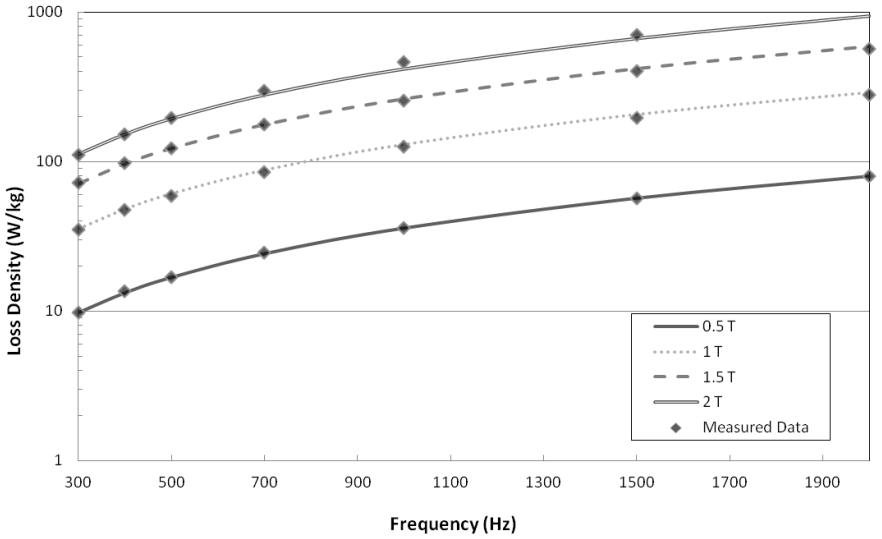

200°C

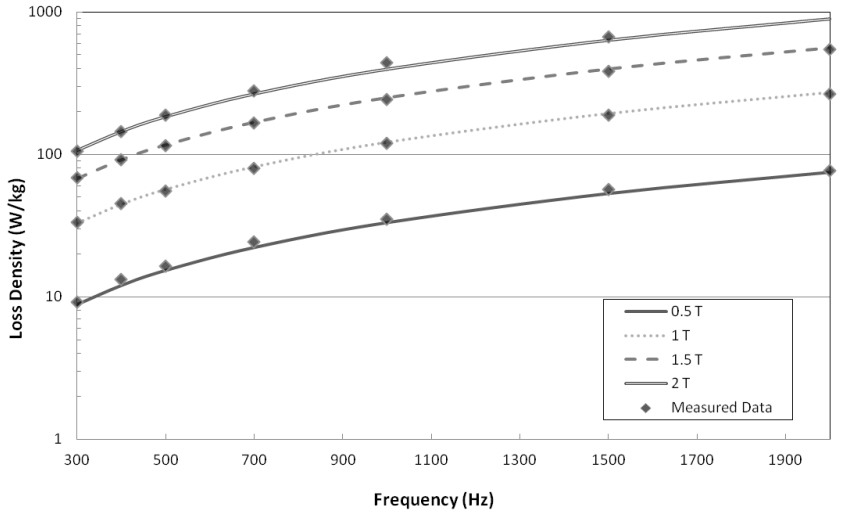

400°C

Figure A.1: Curve fit of loss model to 1000hrs aged Hiperco50-HS.

Table A.2: Variation in parameters of loss model with temperature for 2000 hours aged Hiperco 50-HS.

Temperature (°C)	Room Temperature	200	400
Resistivity ($\mu\Omega$-m^{-1})	36	40	49
k_{exc}	0.8x10^{-4}	1.2x10^{-4}	1.4 x10^{-4}
k_h	0.12	0.12	0.11
a	1.9	1.9	1.9
b	-0.15	-0.15	-0.15

Table A.3: Variation in parameters of loss model with temperature for 5000 hours aged Hiperco 50-HS.

Temperature (°C)	Room Temperature	200	400
Resistivity ($\mu\Omega$-m^{-1})	31	35	41
k_{exc}	1.0x10^{-4}	1.6x10^{-4}	2.0 x10^{-4}
k_h	0.14	0.13	0.125
a	2.0	1.9	1.8
b	-0.15	-0.15	-0.15

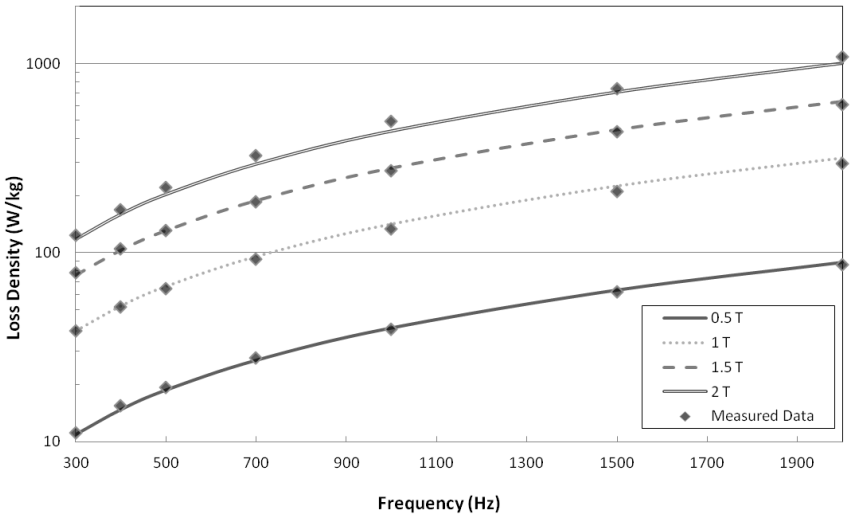

Room temperature

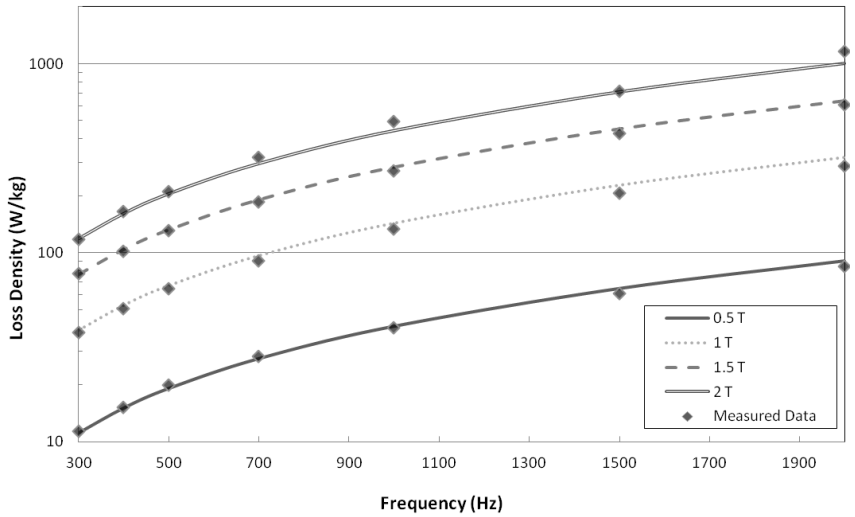

200°C

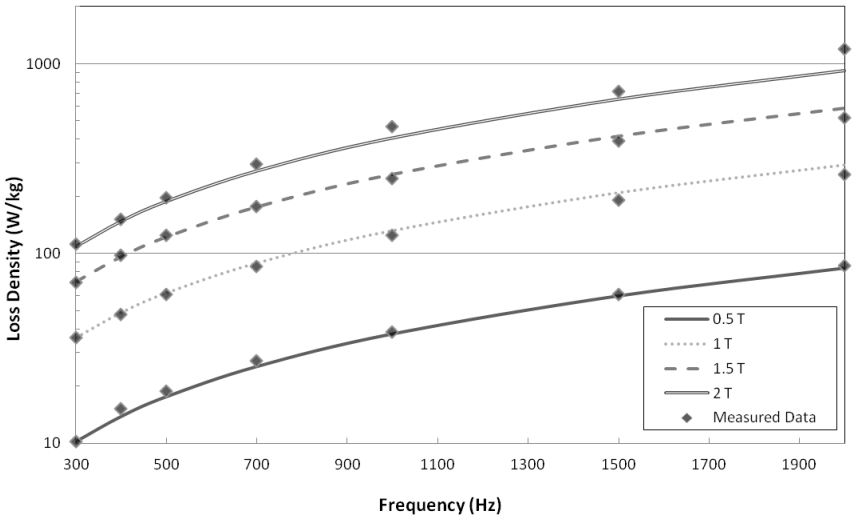

400°C

Figure A.2: Curve fit of loss model to 2000 hours aged Hiperco50-HS.

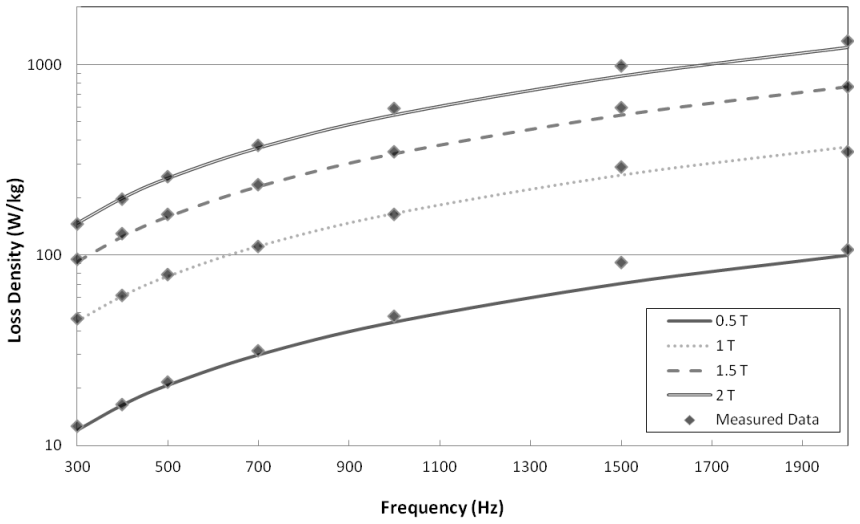

Room temperature

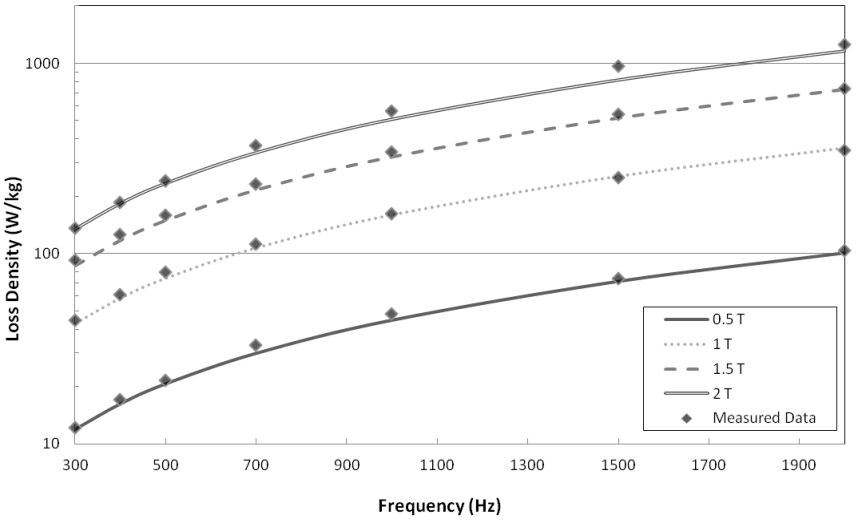

200°C

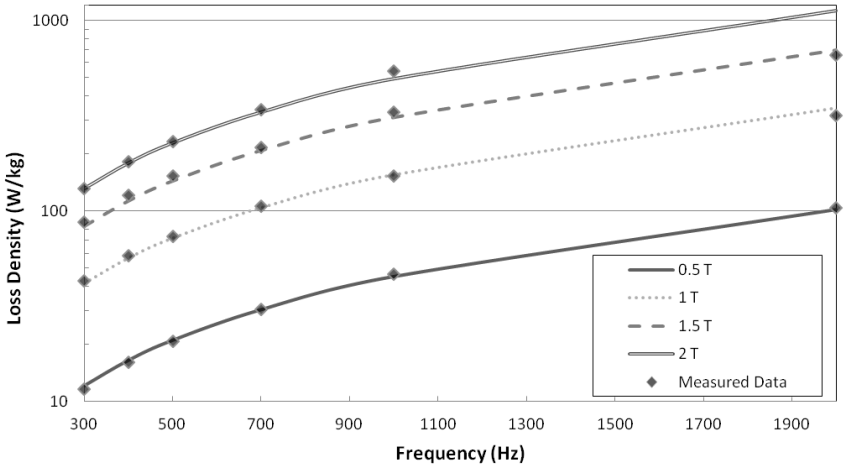

400°C

Figure A.3: Curve fit of loss model to 5000 hours aged Hiperco50-HS.

Appendix B: Measured and predicted core loss in un-aged Vacodur S+ samples

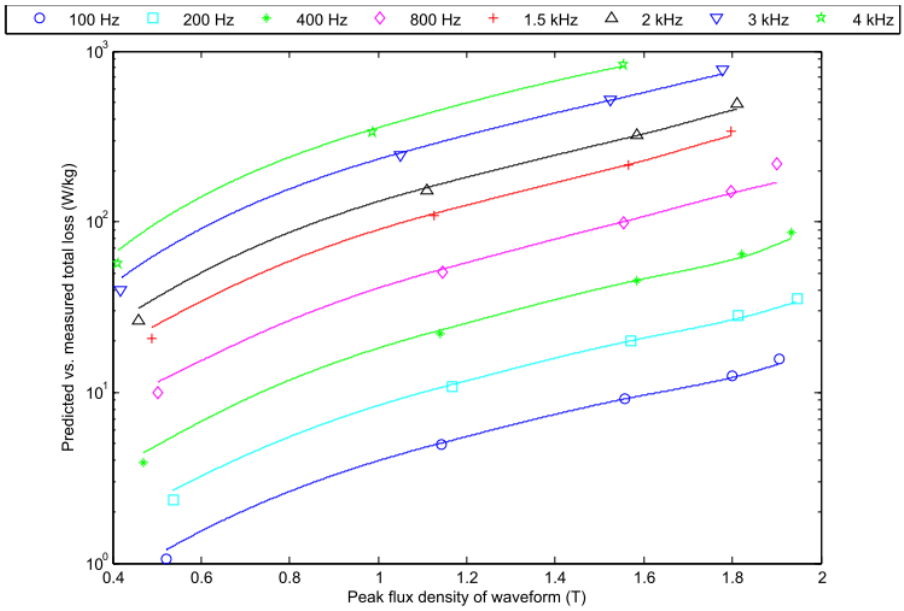

Figure B.1: Measured (marker) vs. predicted (line) total loss at room temperature using $k_{exc}=2.3x10^{-4}$ for Vacodur S+ (390MPa).

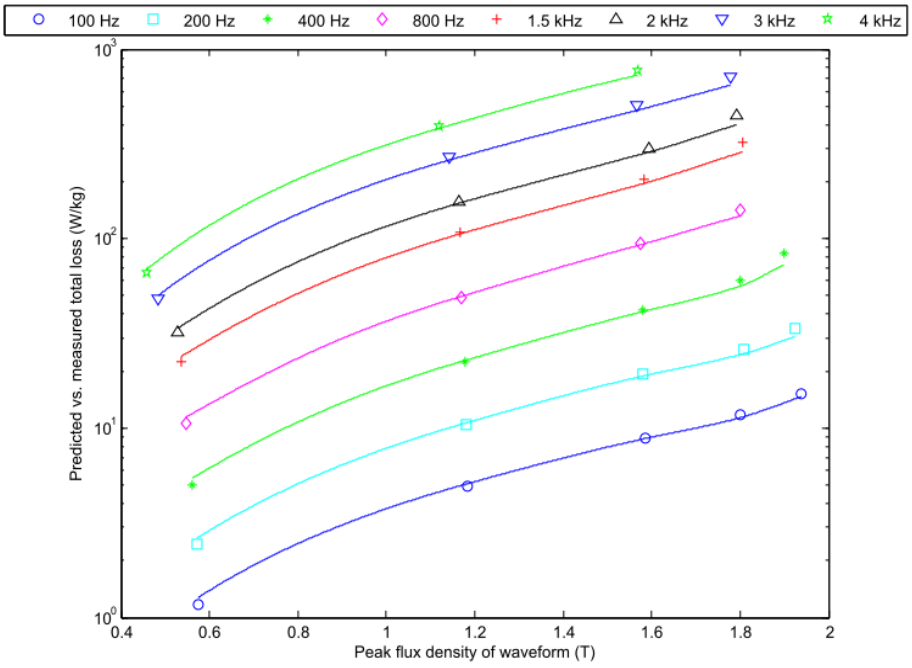

Figure B.2: Measured (marker) vs. predicted (line) total loss at 200°C using $k_{exc}=2.1x10^{-4}$ for Vacodur S+ (390MPa).

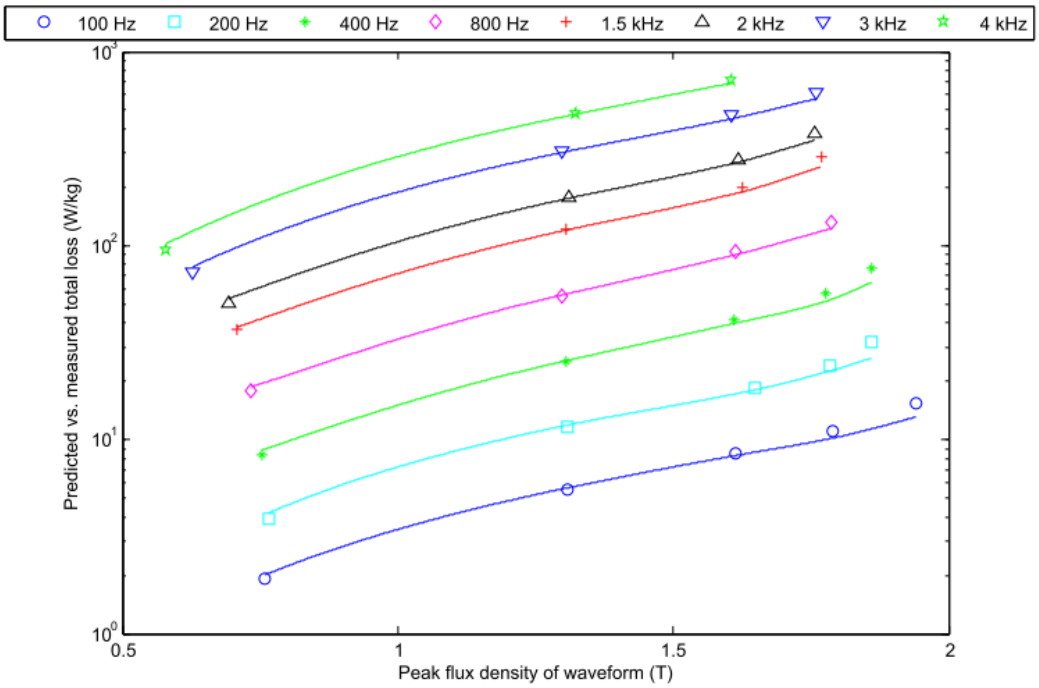

Figure B.3: Measured (marker) vs. predicted (line) total loss at 400°C using $k_{exc}=1.5x10^{-4}$ for Vacodur S+ (390MPa).

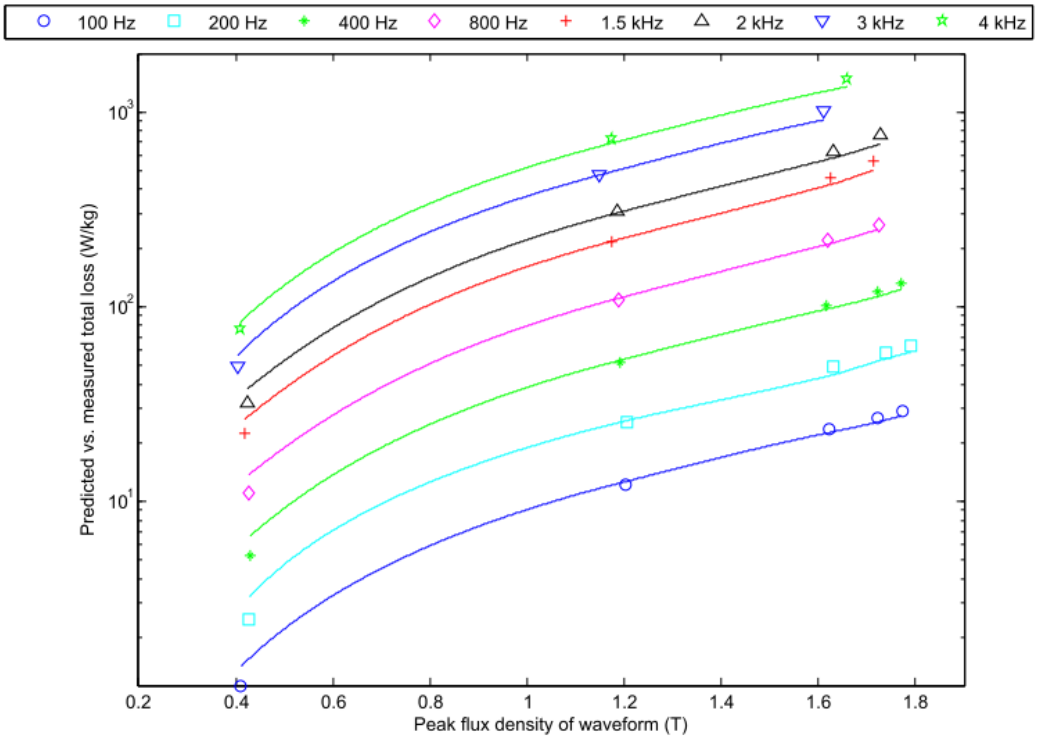

Figure B.4: Measured (marker) vs. predicted (line) total loss at room temperature using $k_{exc}=4.4x10^{-5}$ for Vacodur S+ (620MPa).

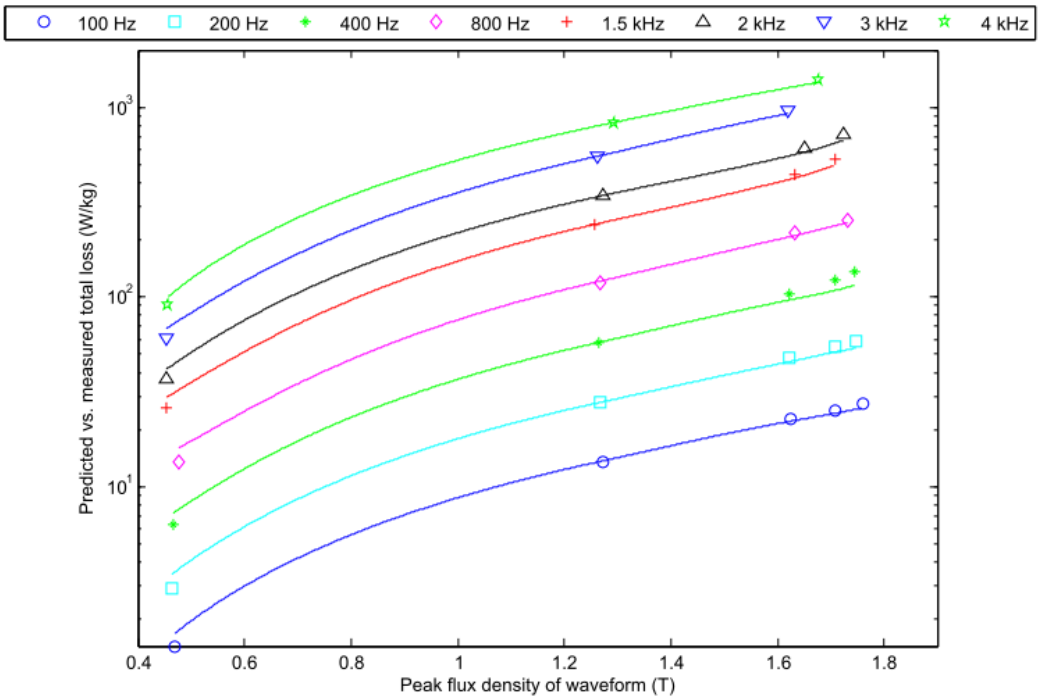

Figure B.5: Measured (marker) vs. predicted (line) total loss at 200°C using $k_{exc}=6.2x10^{-5}$ for Vacodur S+ (620MPa).

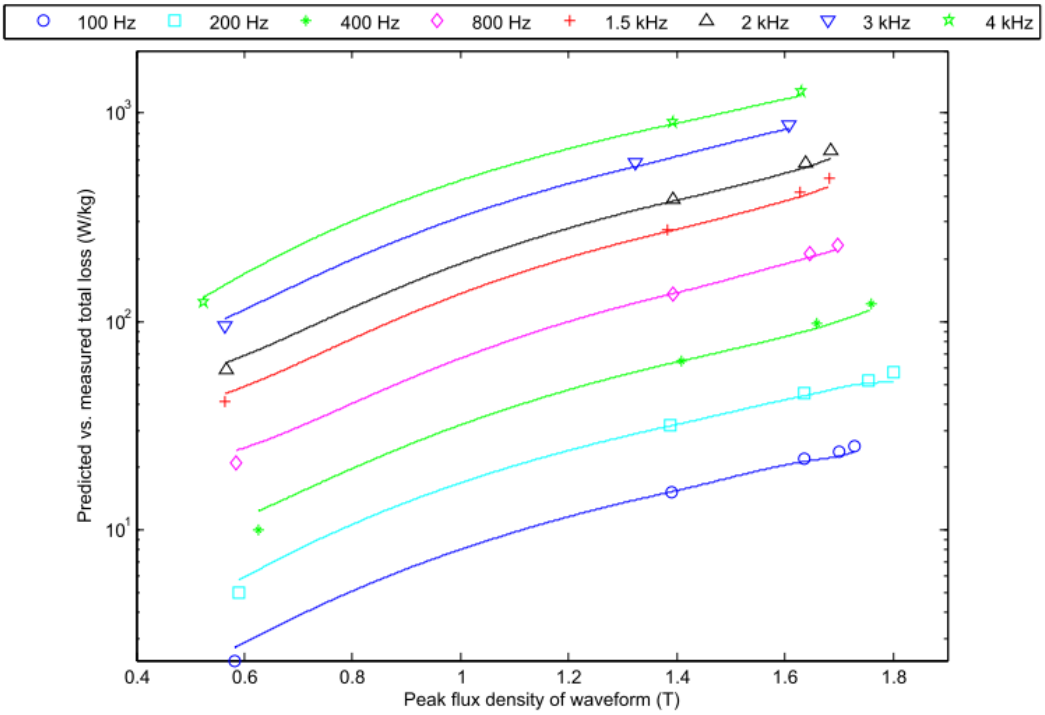

Figure B.6: Measured (marker) vs. predicted (line) total loss at 400°C using $k_{exc}=5.3x10^{-5}$ for Vacodur S+ (620MPa).

Appendix C: Measured and predicted core loss in the aged Vacodur S+ samples

Table C.1: Predicted excess loss coefficients for 500 hours aged Vacodur S+ (390Mpa).

Sample	Co-efficient / number	1	2	3
500 hours aged Vacodur S+ (390Mpa) at room temperature	p	1.5	1.8	2.2
	k	3.53×10^{-5}	6.08×10^{-6}	2.04×10^{-7}
500 hours aged Vacodur S+ (390Mpa) at 200°C	p	1.5	1.8	2.2
	k	2.67×10^{-5}	6.87×10^{-6}	1.64×10^{-7}
500 hours aged Vacodur S+ (390Mpa) at 400°C	p	1.5	1.8	2.2
	k	3.87×10^{-5}	5.63×10^{-6}	2.42×10^{-7}

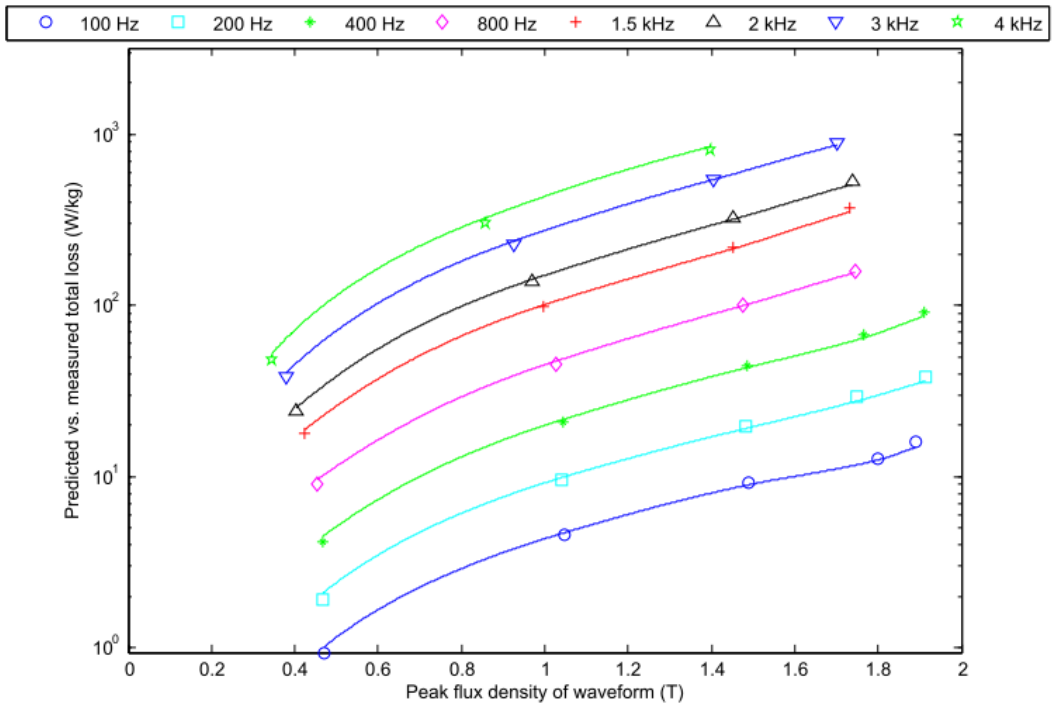

Figure C.1: Measured (marker) vs. predicted (line) total loss for 500 hour aged Vacodur S+ (390MPa) at room temperature.

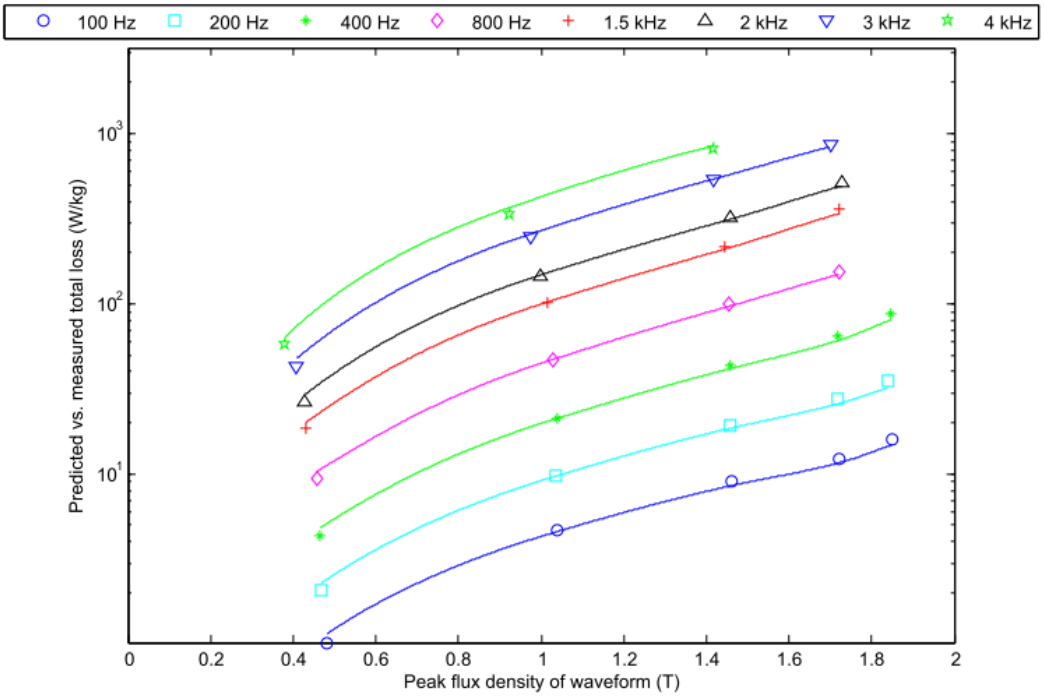

Figure C.2: Measured (marker) vs. predicted (line) total loss for 500 hour aged Vacodur S+ (390MPa) at 200°C.

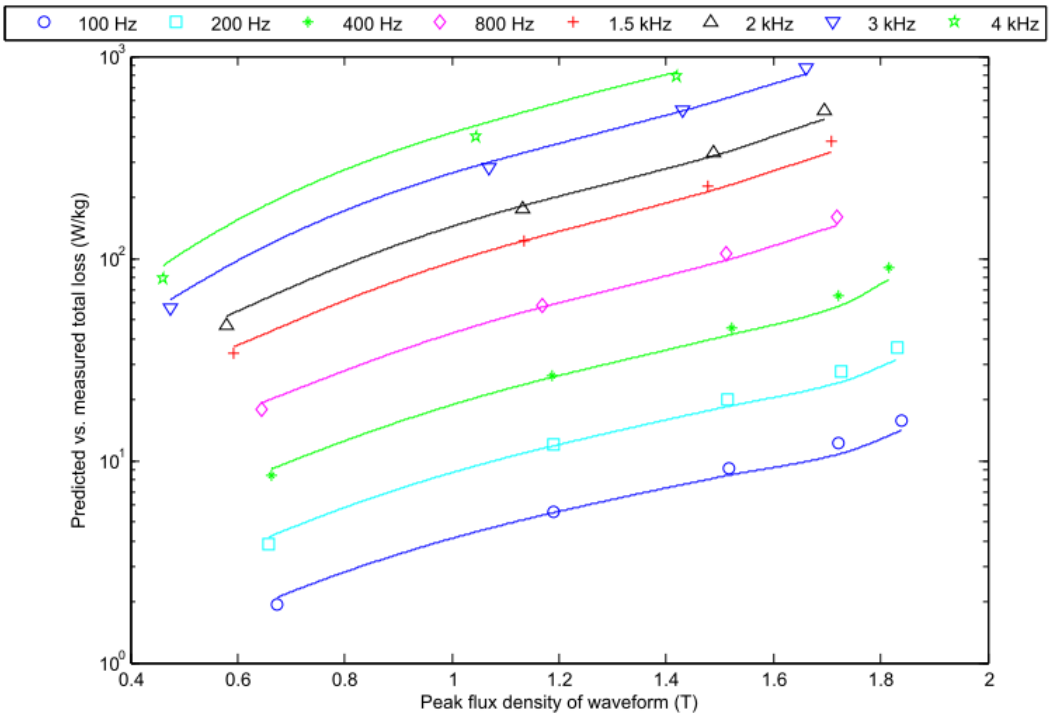

Figure C.3: Measured (marker) vs. predicted (line) total loss for 500 hour aged Vacodur S+ (390MPa) at 400°C.

Table C.2: Predicted excess loss coefficients for 500 hours aged Vacodur S+ (620Mpa).

Sample	Co-efficient / number	1	2	3
500 hours aged Vacodur S+ (620Mpa) at room temperature	p	1.5	2.1	2.5
	k	6.88×10^{-5}	1.90×10^{-6}	2.71×10^{-8}
500 hours aged Vacodur S+ (620Mpa) at 200°C	p	1.5	2.1	2.5
	k	6.96×10^{-5}	1.68×10^{-6}	1.06×10^{-8}
500 hours aged Vacodur S+ (620Mpa) at 400°C	p	1.5	2.1	2.5
	k	1.54×10^{-5}	1.20×10^{-6}	1.79×10^{-8}

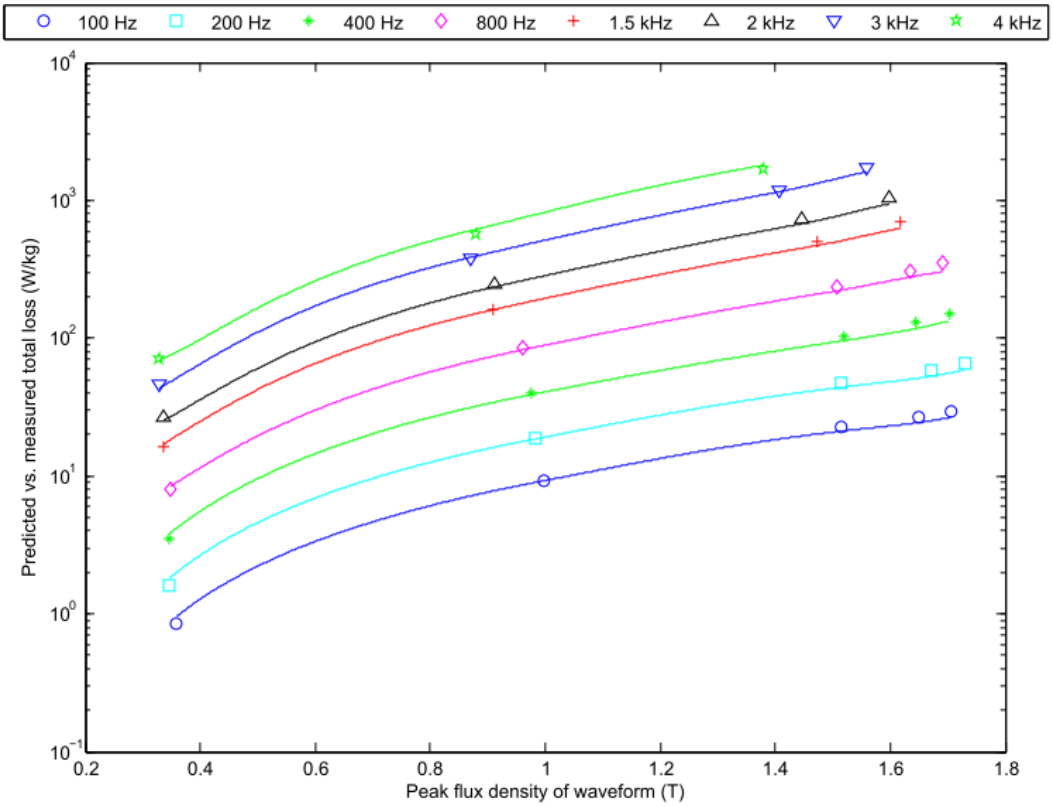

Figure C.4: Measured (marker) vs. predicted (line) total loss for 500 hour aged Vacodur S+ (620MPa) at room temperature.

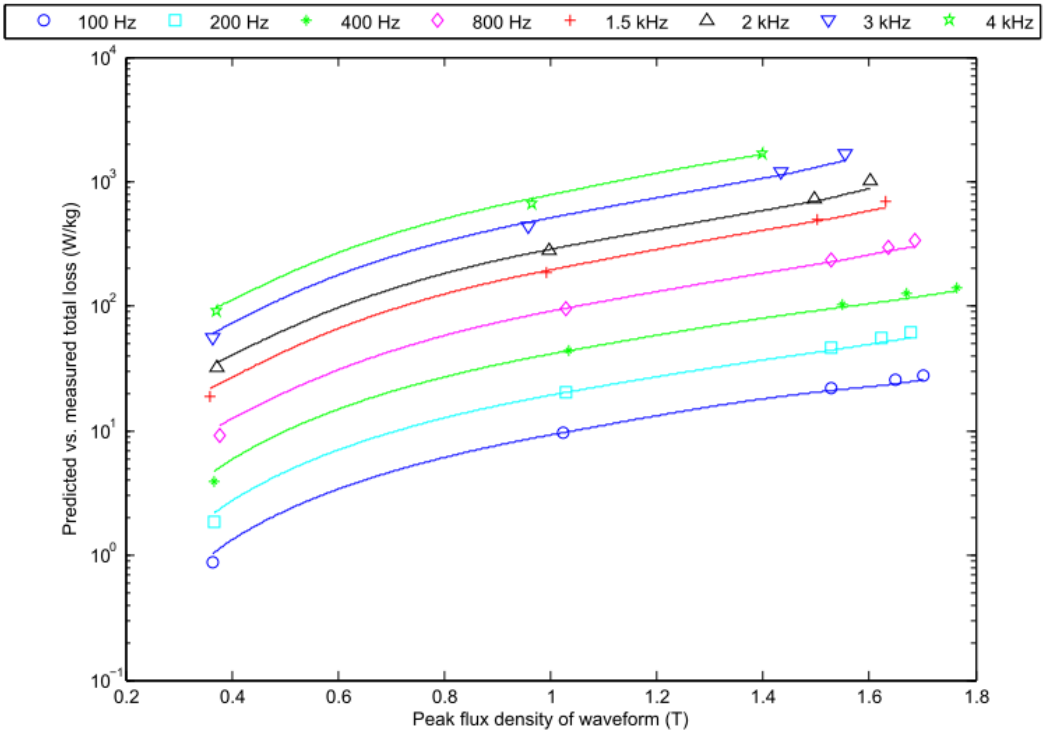

Figure C.5: Measured (marker) vs. predicted (line) total loss for 500 hour aged Vacodur S+ (620MPa) at 200°C.

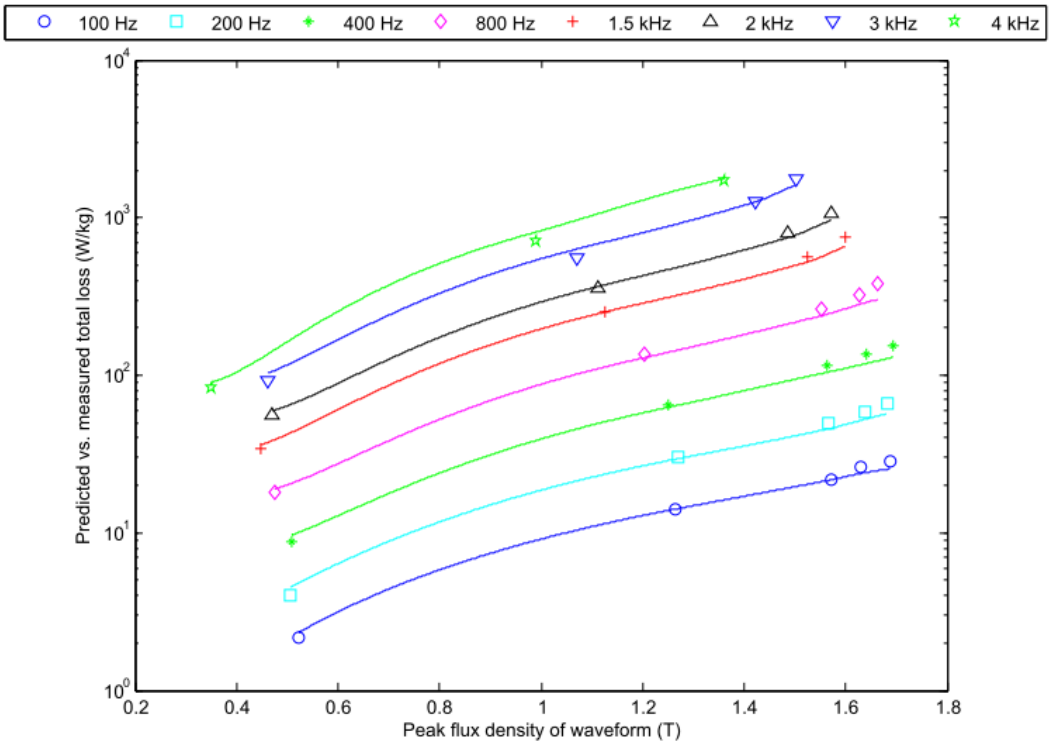

Figure C.6: Measured (marker) vs. predicted (line) total loss for 500 hour aged Vacodur S+ (620MPa) at 400°C.

Table C.3: Predicted coefficients for the excess loss model for 1000 hours aged Vacodur S+ (390Mpa).

Sample	Co-efficient / number	1	2	3
1000 hours aged Vacodur S+ (390Mpa) at room temperature	p	1.5	1.9	2.7
	k	1.11×10^{-4}	3.68×10^{-6}	2.64×10^{-9}
1000 hours aged Vacodur S+ (390Mpa) at 200°C	p	1.5	1.9	2.7
	k	6.61×10^{-5}	4.02×10^{-6}	3.55×10^{-9}
1000 hours aged Vacodur S+ (390Mpa) at 400°C	p	1.5	1.9	2.7
	k	8.56×10^{-5}	3.69×10^{-6}	3.22×10^{-9}

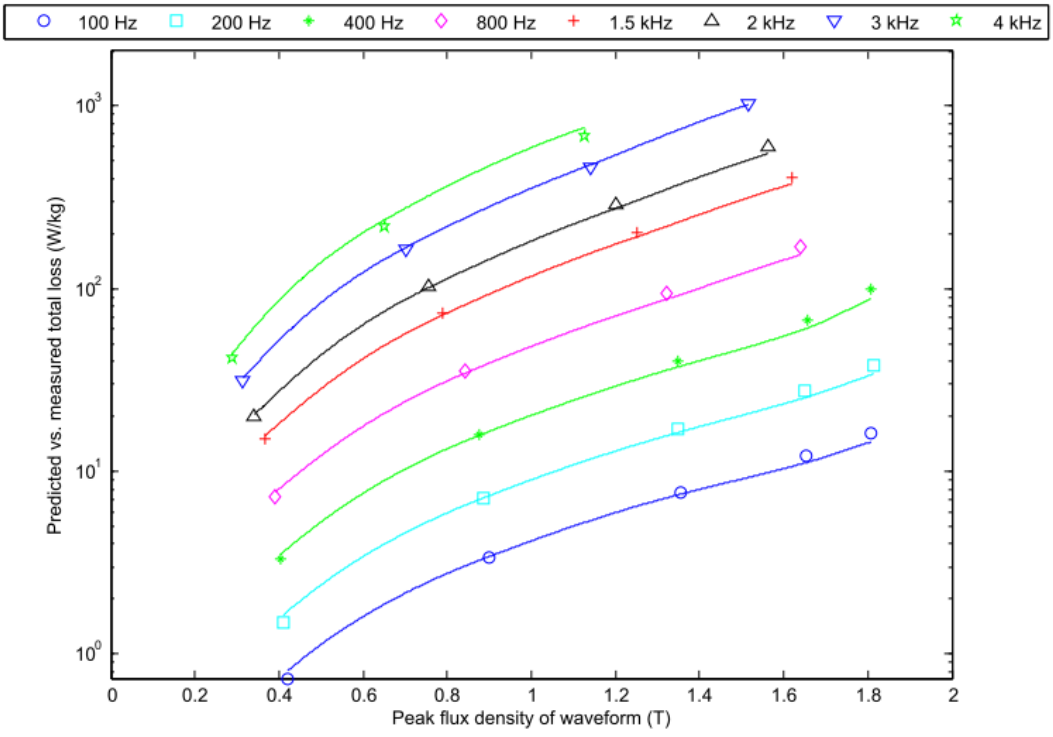

Figure C.7: Measured (marker) vs. predicted (line) total loss for 1000 hour aged Vacodur S+ (390MPa) at room temperature.

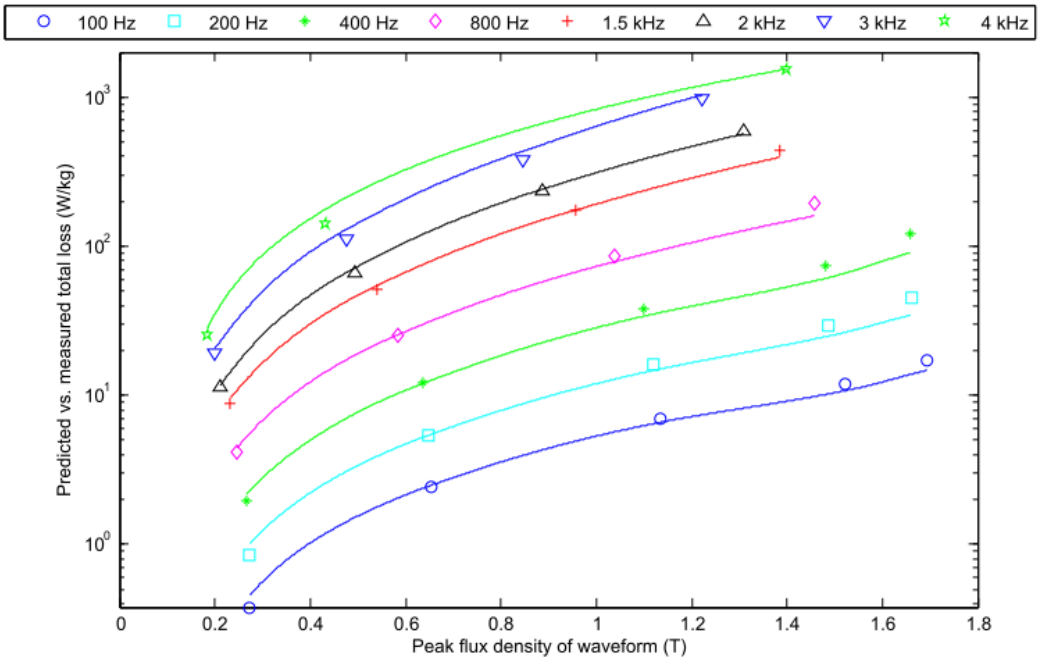

Figure C.8: Measured (marker) vs. predicted (line) total loss for 1000 hour aged Vacodur S+ (390MPa) at 200°C.

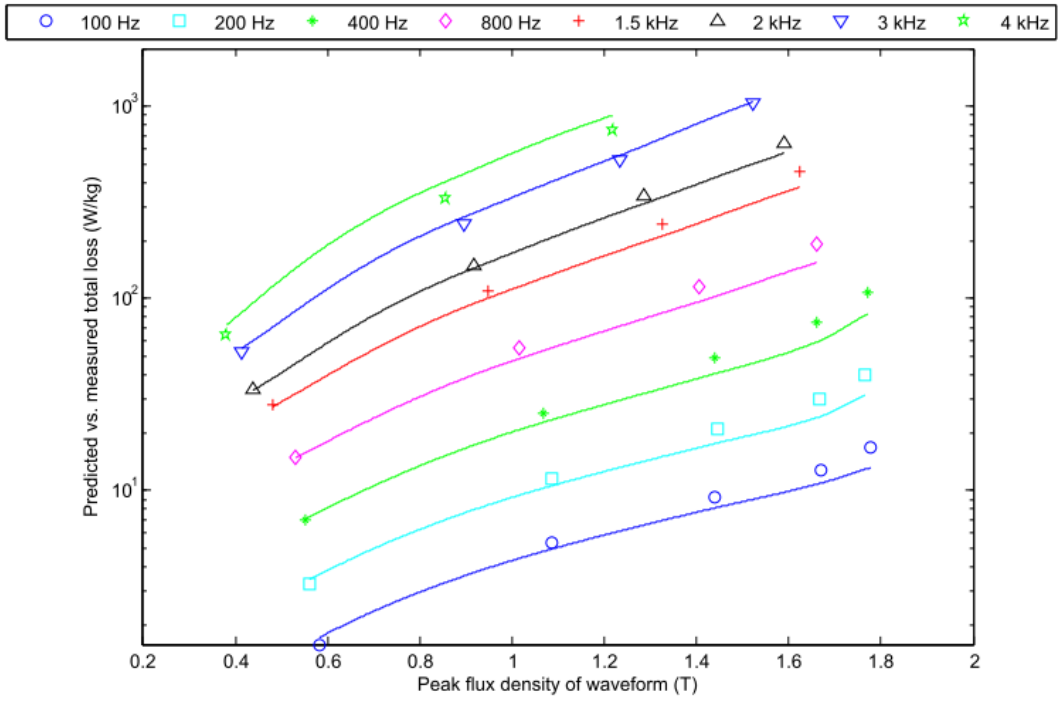

Figure C.9: Measured (marker) vs. predicted (line) total loss for 1000 hour aged Vacodur S+ (390MPa) at 400°C.

Table C.4: Predicted coefficients for the excess loss model for 1000 hours aged Vacodur S+ (620Mpa)

Sample	Co-efficient / number	1	2	3
1000 hours aged Vacodur S+ (620Mpa) at room temperature	p	1.5	1.9	2.6
	k	1.48 x10^{-4}	1.12 x10^{-6}	1.90 x10^{-8}
1000 hours aged Vacodur S+ (620Mpa) at 200°C	p	1.5	1.9	2.6
	k	1.74 x10^{-4}	3.70 x10^{-6}	2.02 x10^{-8}
1000 hours aged Vacodur S+ (620Mpa) at 400°C	p	1.5	1.9	2.6
	k	3.52 x10^{-4}	1.24 x10^{-5}	1.16 x10^{-8}

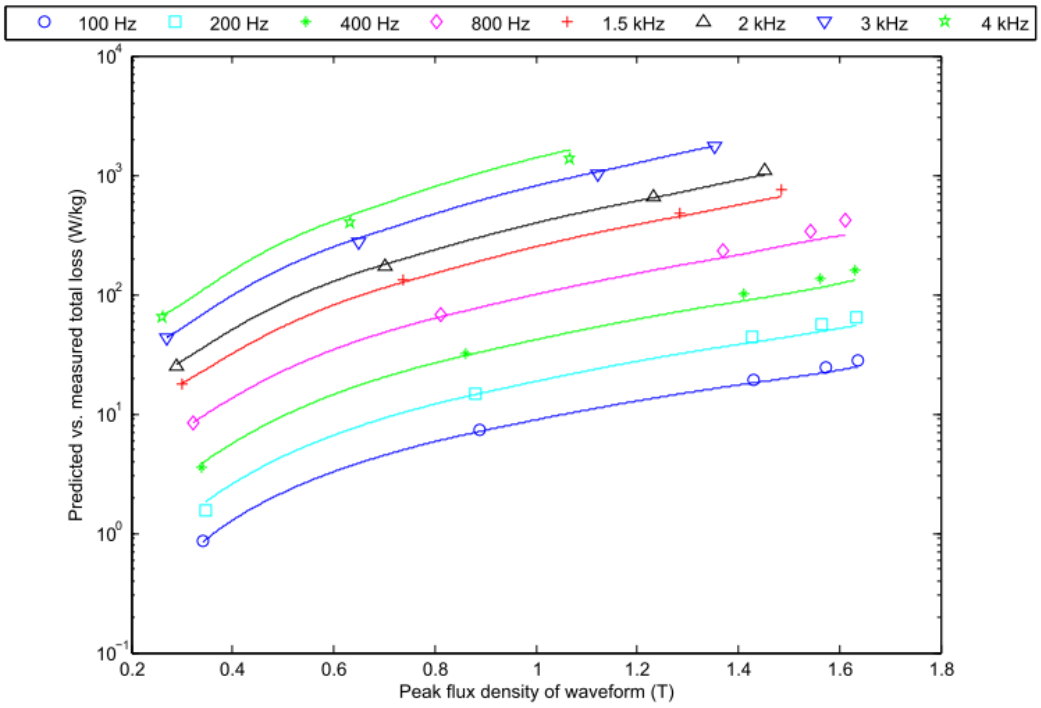

Figure C.10: Measured (marker) vs. predicted (line) total loss for 1000 hour aged Vacodur S+ (620MPa) at room temperature.

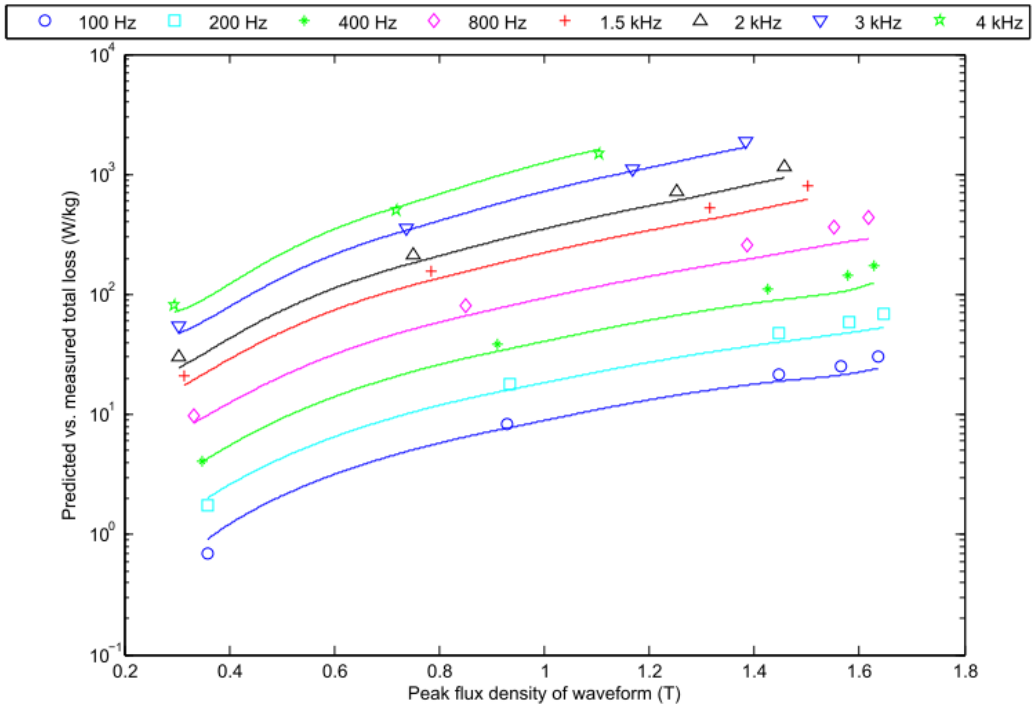

Figure C.11: Measured (marker) vs. predicted (line) total loss for 1000 hour aged Vacodur S+ (620MPa) at 200°C.

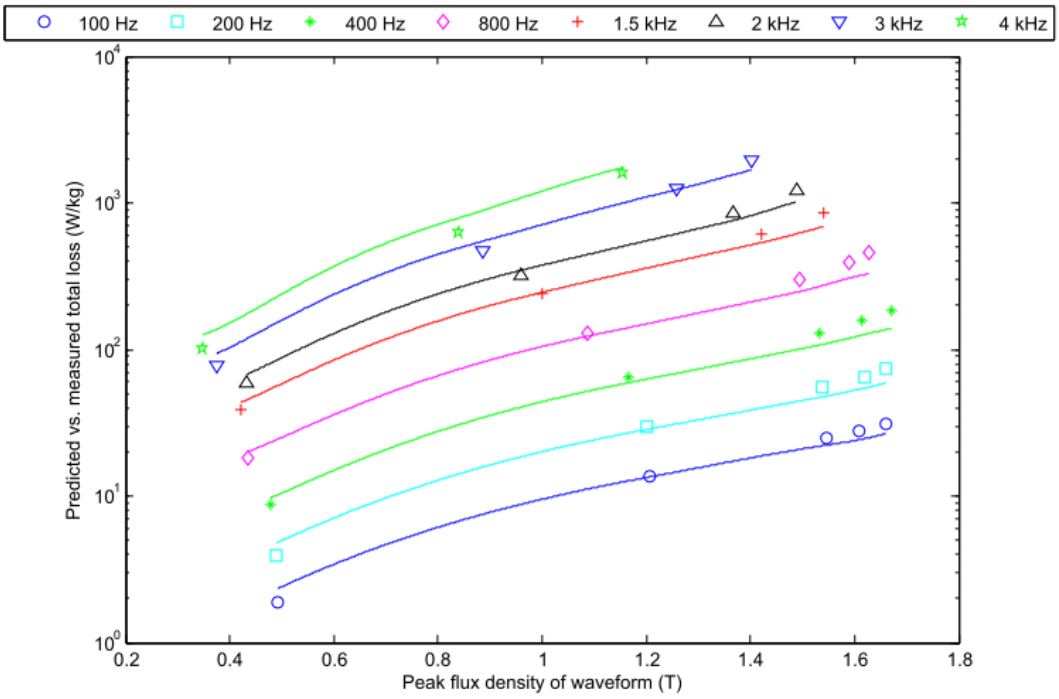

Figure C.12: Measured (marker) vs. predicted (line) total loss for 1000 hour aged Vacodur S+ (620MPa) at 400°C.

Table C.5: Predicted coefficients for the excess loss model for 2000 hours aged Vacodur S+ (390Mpa)

Sample	Co-efficient / number	1	2	3
2000 hours aged Vacodur S+ (390Mpa) at room temperature	p	1.5	1.9	2.7
	k	9.56×10^{-5}	1.72×10^{-5}	3.23×10^{-9}
2000 hours aged Vacodur S+ (390Mpa) at 200°C	p	1.5	1.9	2.7
	k	1.30×10^{-4}	1.72×10^{-5}	4.42×10^{-9}
2000 hours aged Vacodur S+ (390Mpa) at 400°C	p	1.5	1.9	2.7
	k	3.15×10^{-4}	7.38×10^{-6}	7.77×10^{-9}

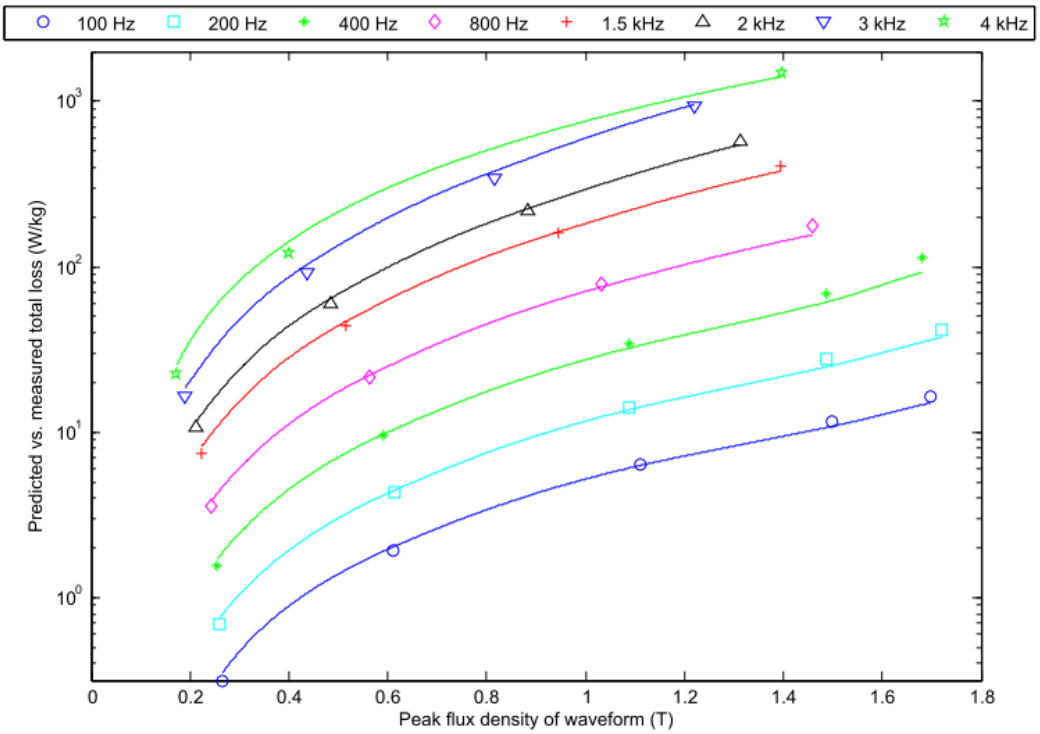

Figure C.13: Measured (marker) vs. predicted (line) total loss for 2000 hour aged Vacodur S+ (390MPa) at room temperature.

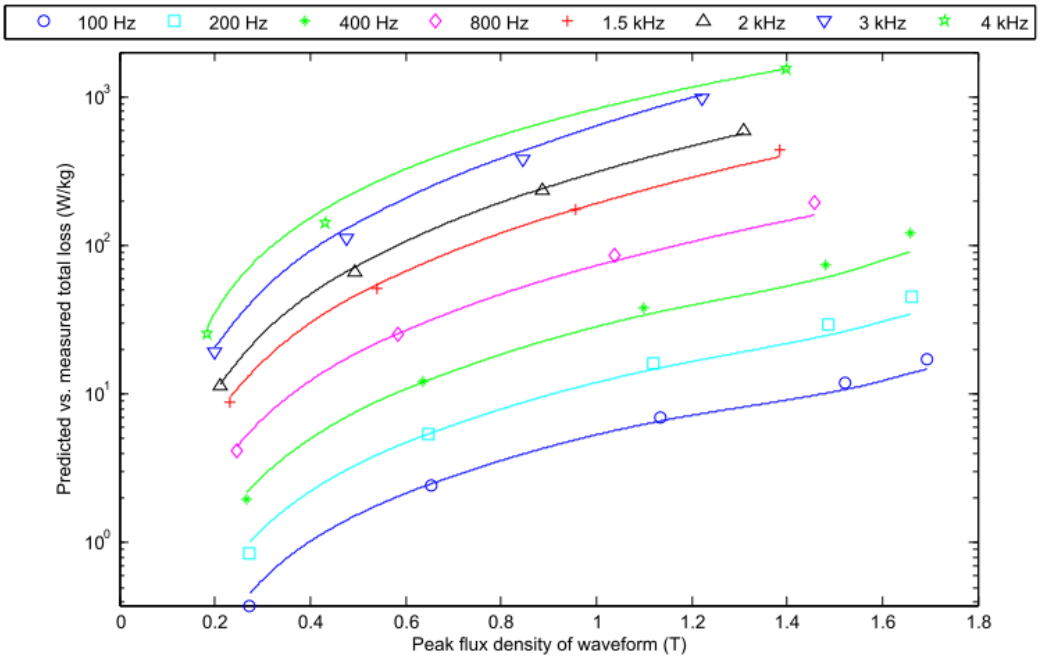

Figure C.14: Measured (marker) vs. predicted (line) total loss for 2000 hour aged Vacodur S+ (390MPa) at 200°C.

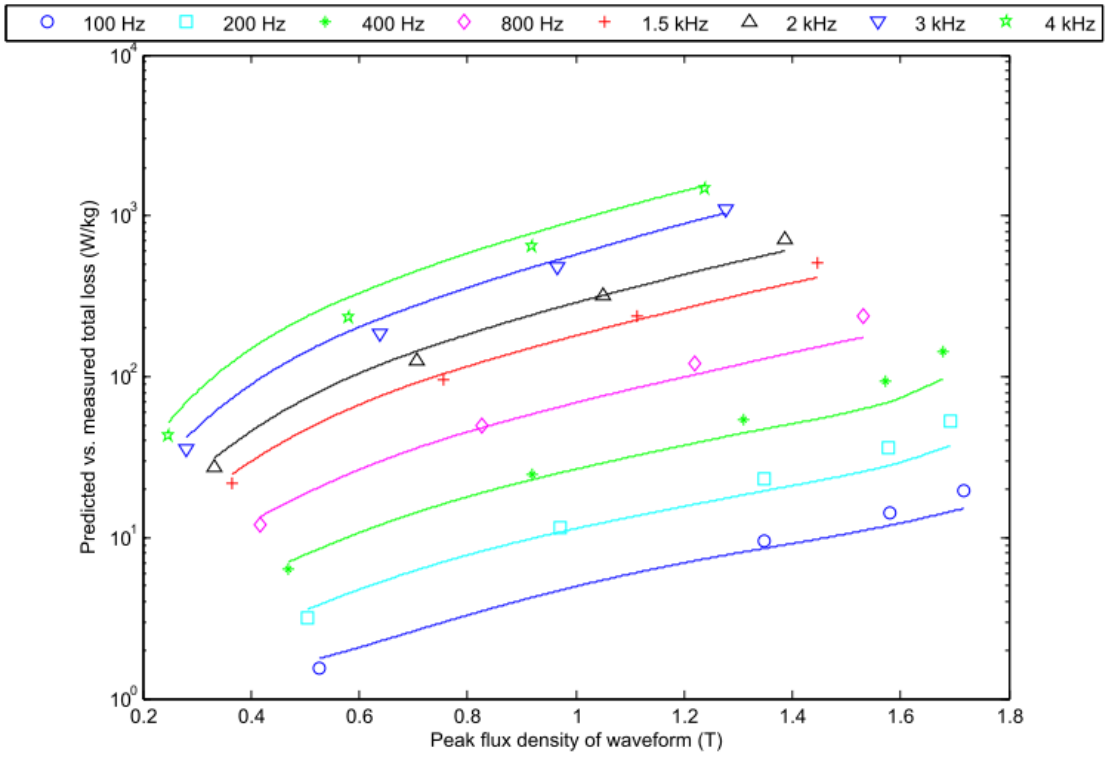

Figure C.15: Measured (marker) vs. predicted (line) total loss for 2000 hour aged Vacodur S+ (390MPa) at 400°C.

Table C.6: Predicted coefficients for the excess loss model for 2000 hours aged Vacodur S+ (620Mpa)

Sample	Co-efficient / number	1	2	3
2000 hours aged Vacodur S+ (620Mpa) at room temperature	p	1.5	1.8	2.2
	k	2.22×10^{-4}	2.18×10^{-5}	2.07×10^{-6}
2000 hours aged Vacodur S+ (620Mpa) at 200°C	p	1.5	1.8	2.2
	k	2.49×10^{-4}	1.52×10^{-5}	2.25×10^{-6}
2000 hours aged Vacodur S+ (620Mpa) at 400°C	p	1.5	1.8	2.2
	k	4.76×10^{-4}	3.06×10^{-5}	1.83×10^{-6}

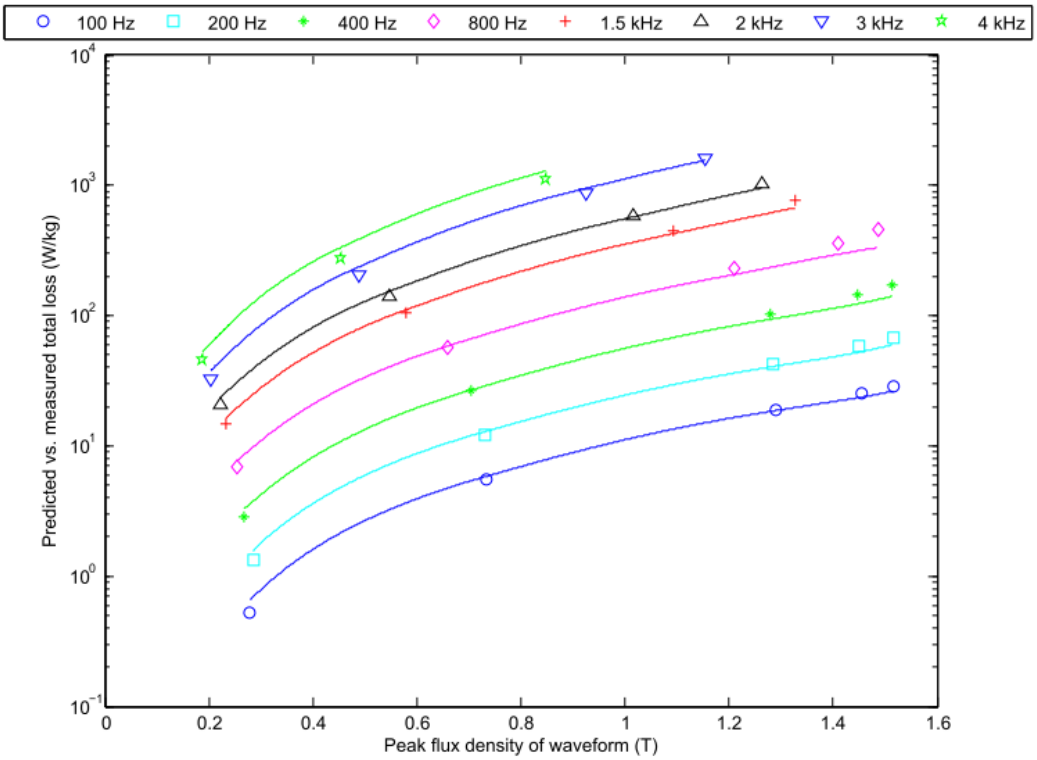

Figure C.16: Measured (marker) vs. predicted (line) total loss for 2000 hour aged Vacodur S+ (620MPa) at room temperature.

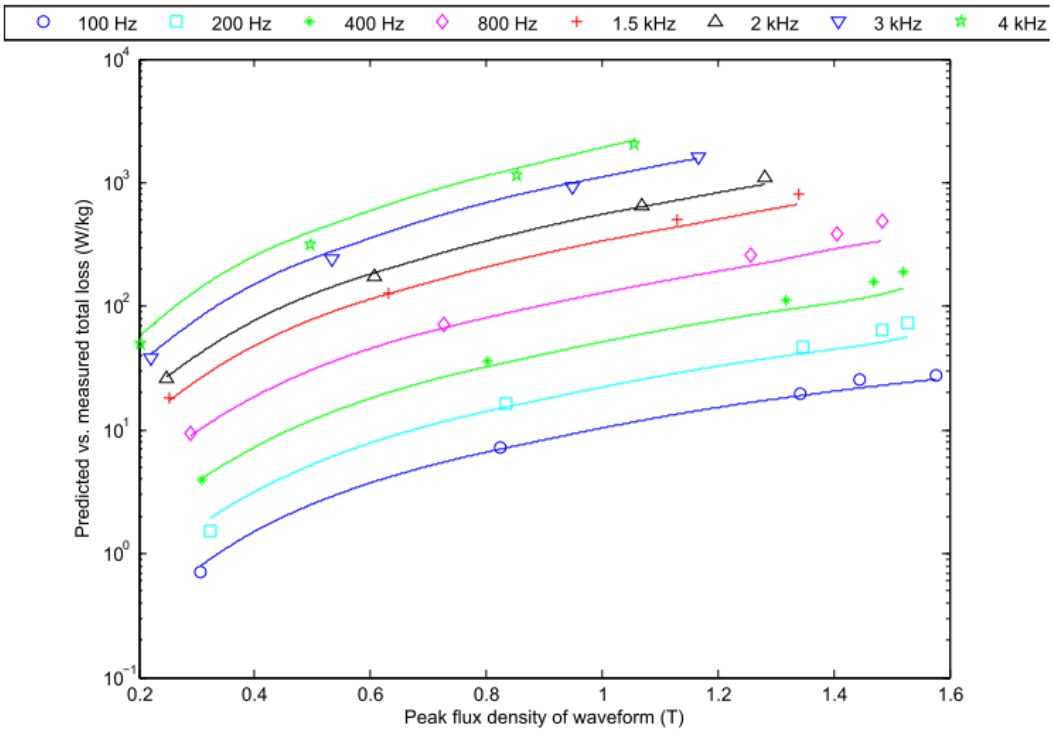

Figure C.17: Measured (marker) vs. predicted (line) total loss for 2000 hour aged Vacodur S+ (620MPa) at 200°C.

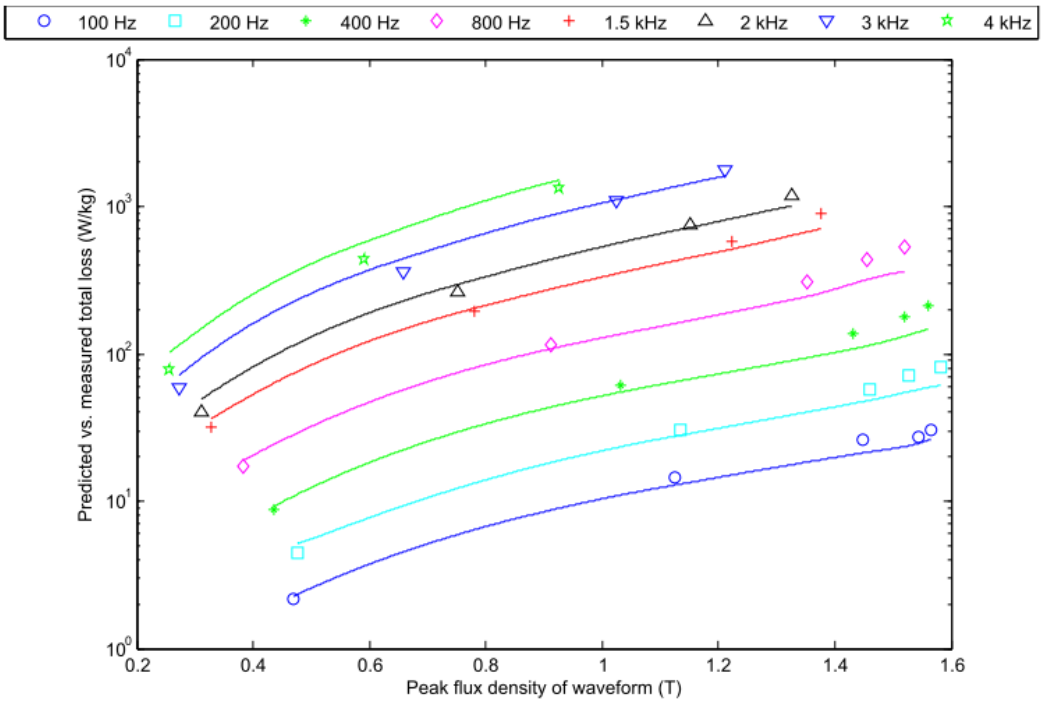

Figure C.18: Measured (marker) vs. predicted (line) total loss for 2000 hour aged Vacodur S+ (620MPa) at 400°C.

Appendix D: Simulink models

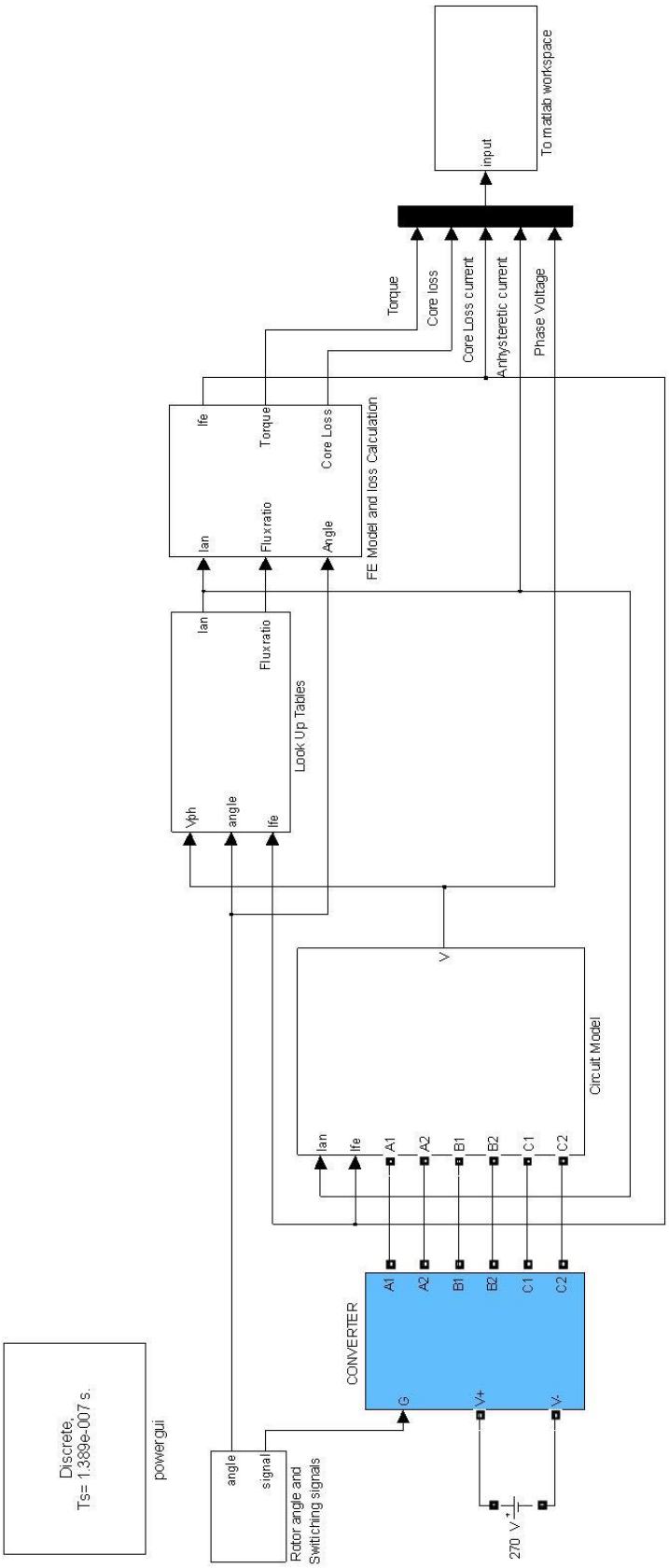

Figure D.1: Main Simulink model for the SR machine.

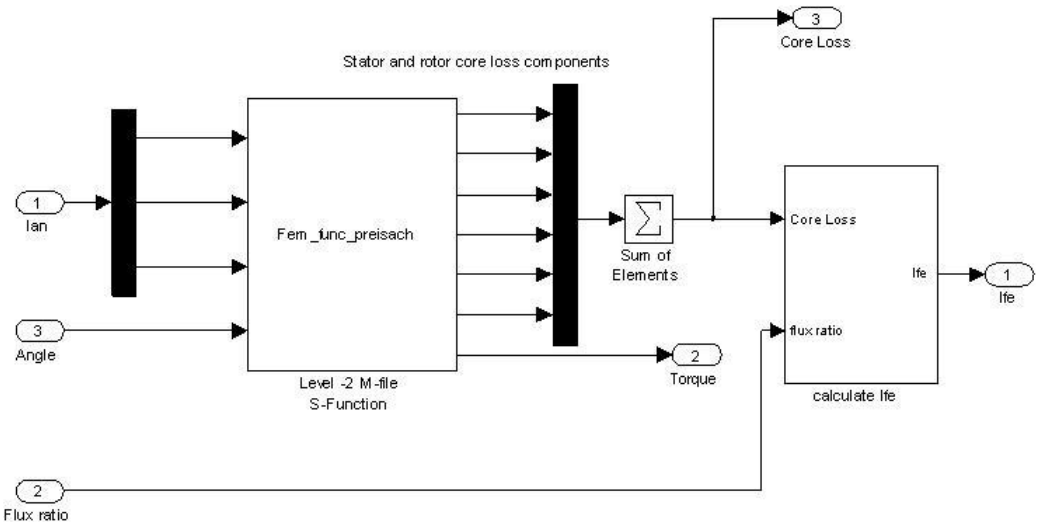

Figure D.2: Core loss model.

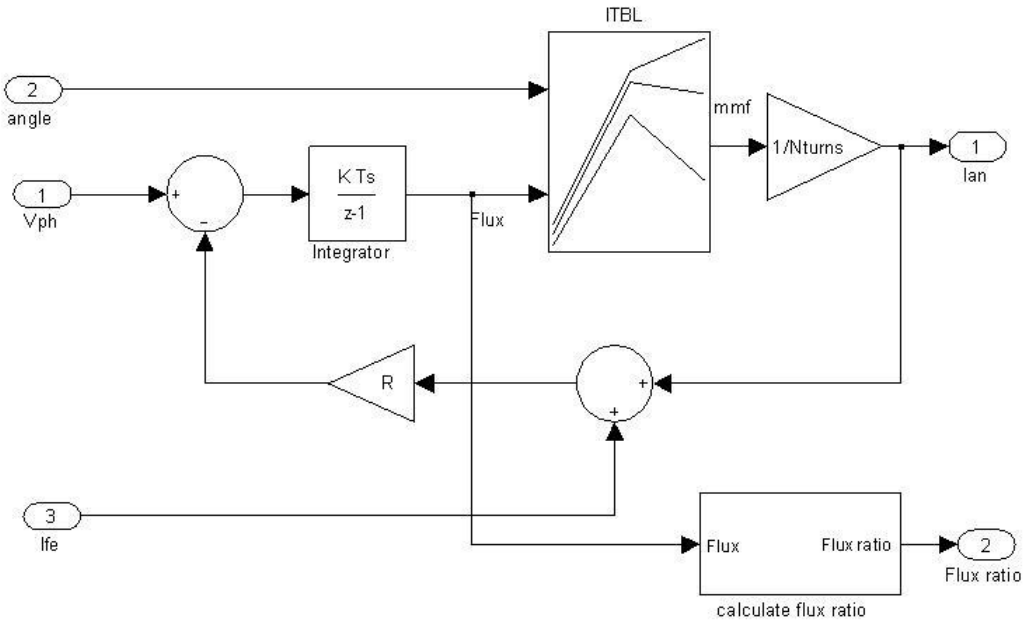

Figure D.3: Machine model from look up tables.

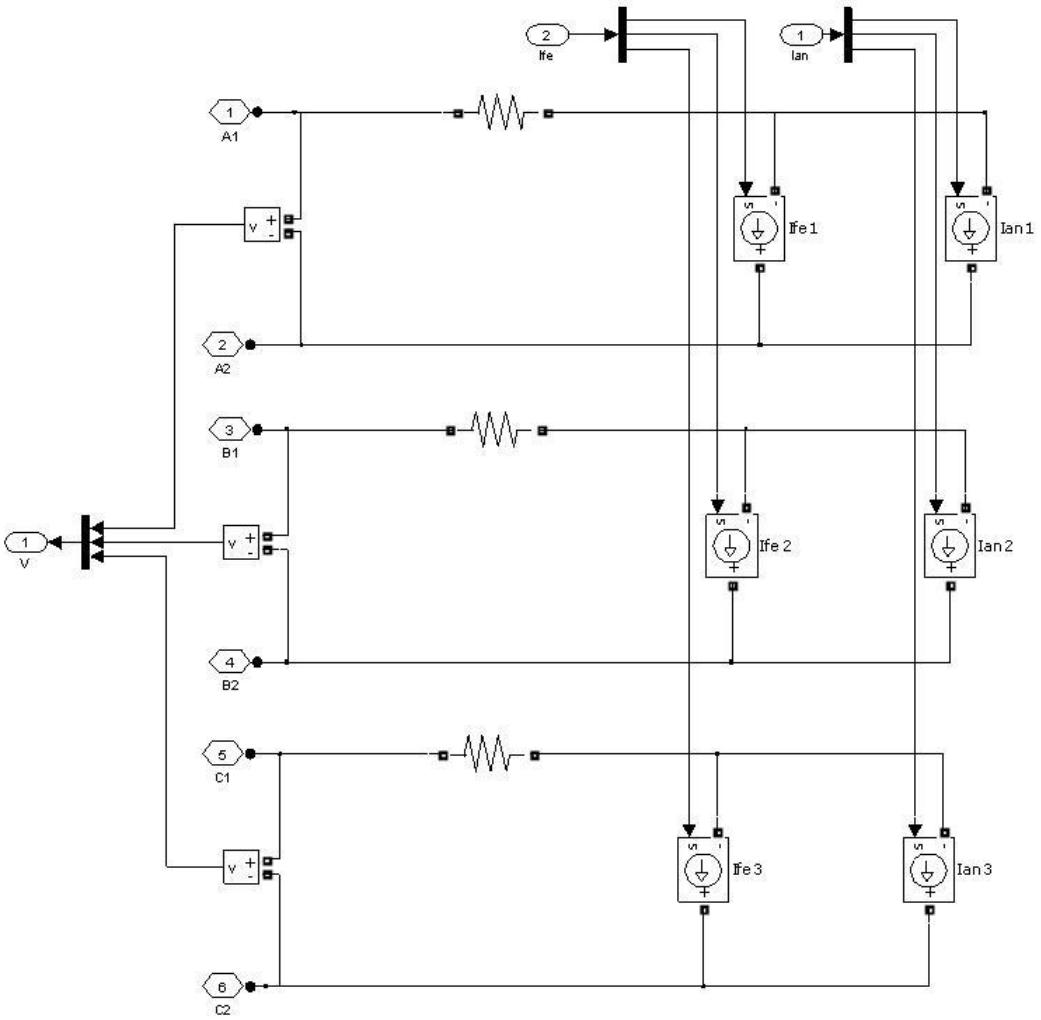

Figure D.4: Circuit model

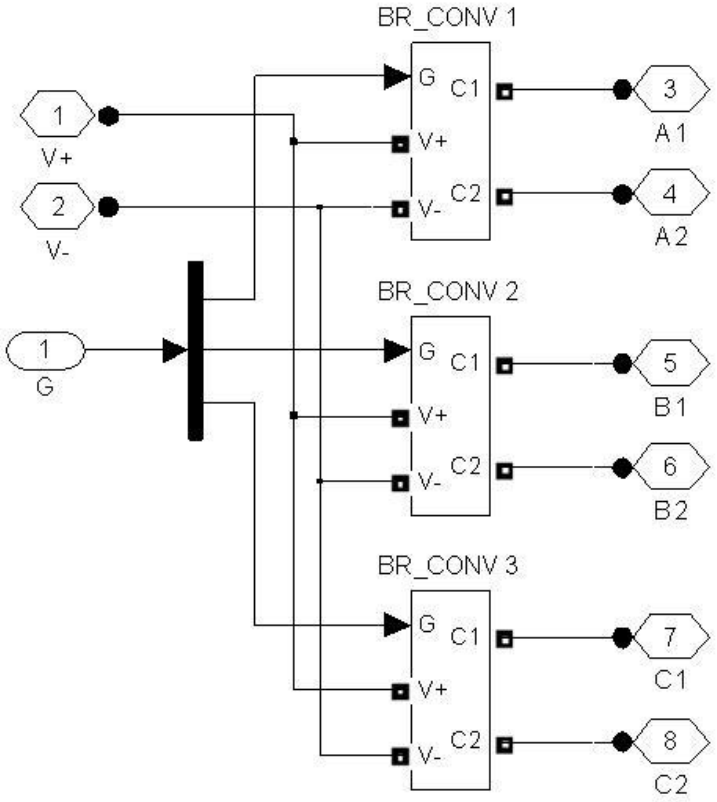

Figure D.5: Converter model from Power-sim toolbox.

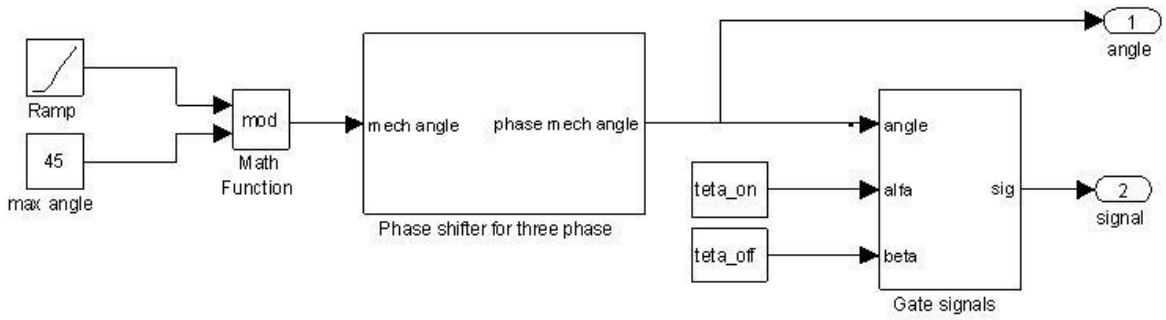

Figure D.6: Generation of gate signals.

Appendix E: Solidworks drawings of the demonstrator machine.

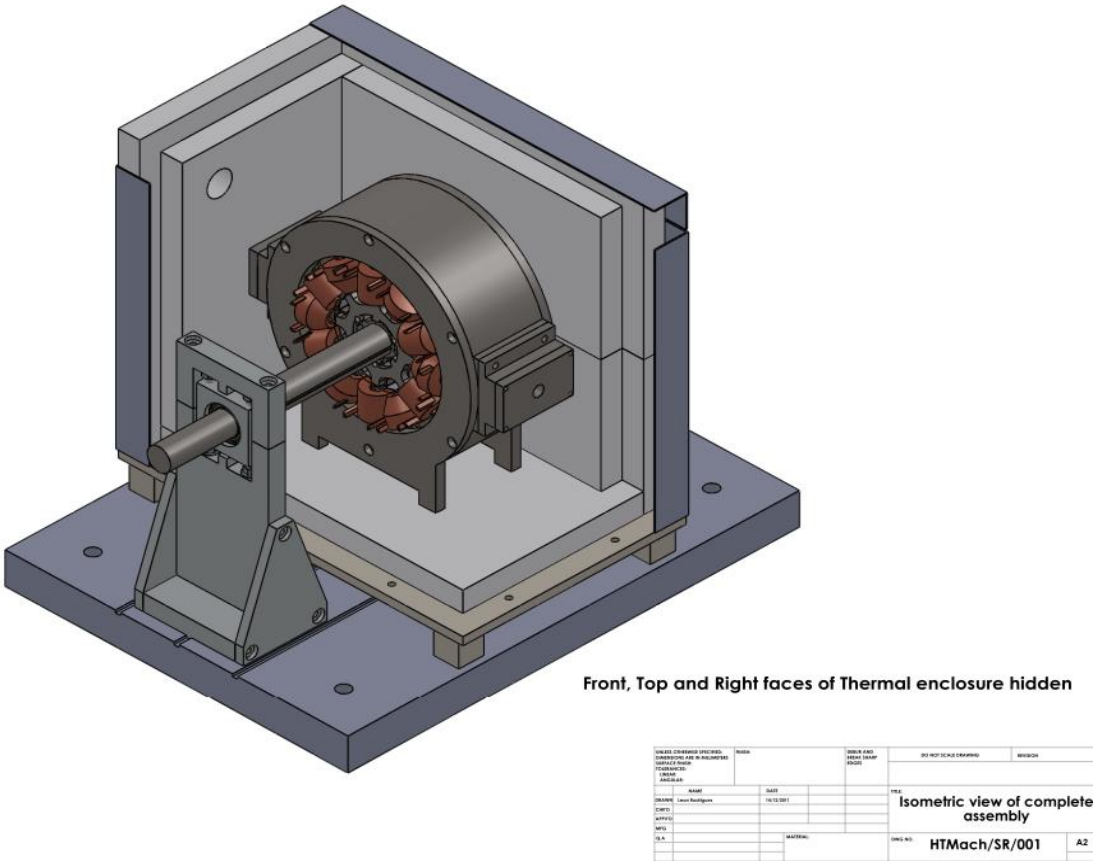

Figure E.1: Isometric view of high temperature SR machine demonstrator.

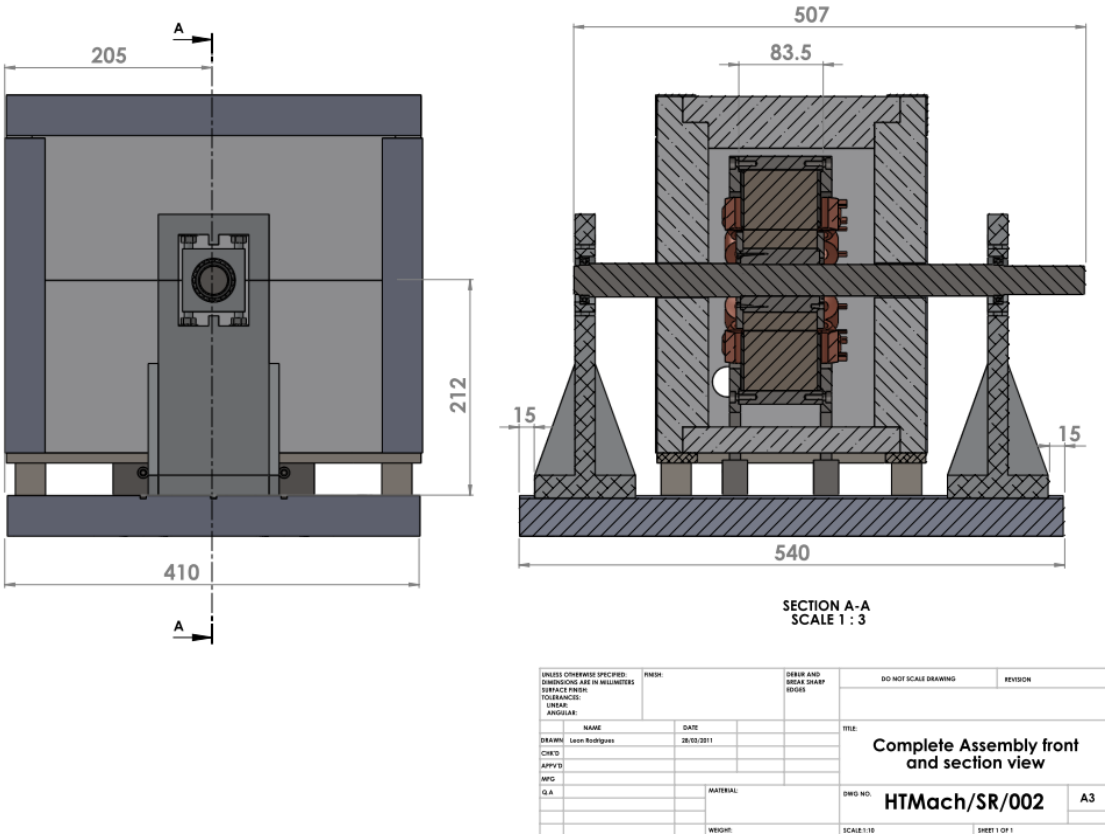

Figure E.2: Front and section view of high temperature SR machine demonstrator.

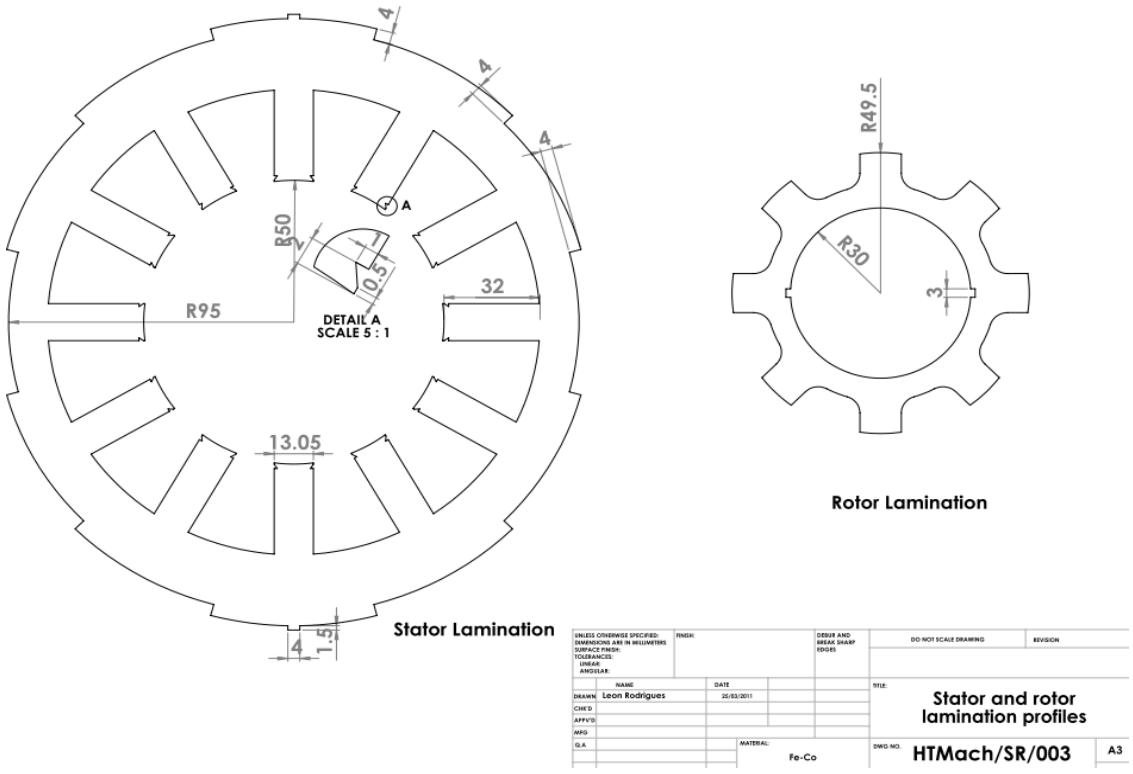

Figure E.3: Stator and rotor lamination profiles.

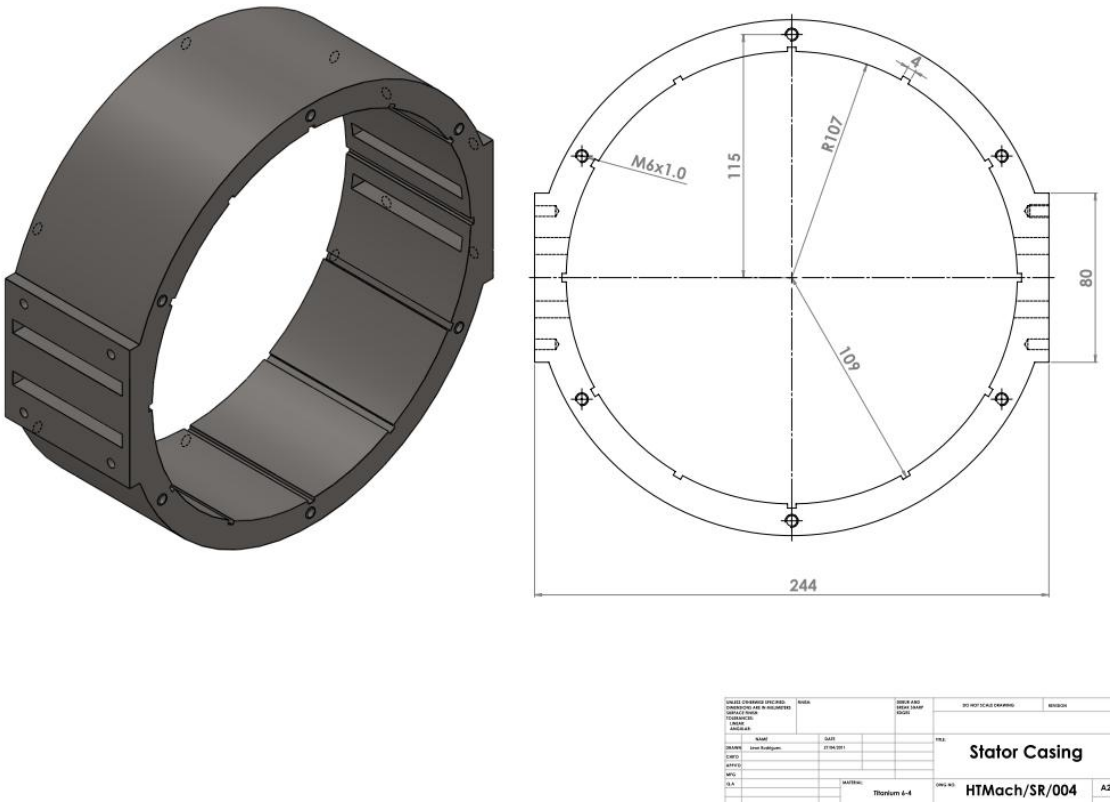

Figure E.4: Stator casing.

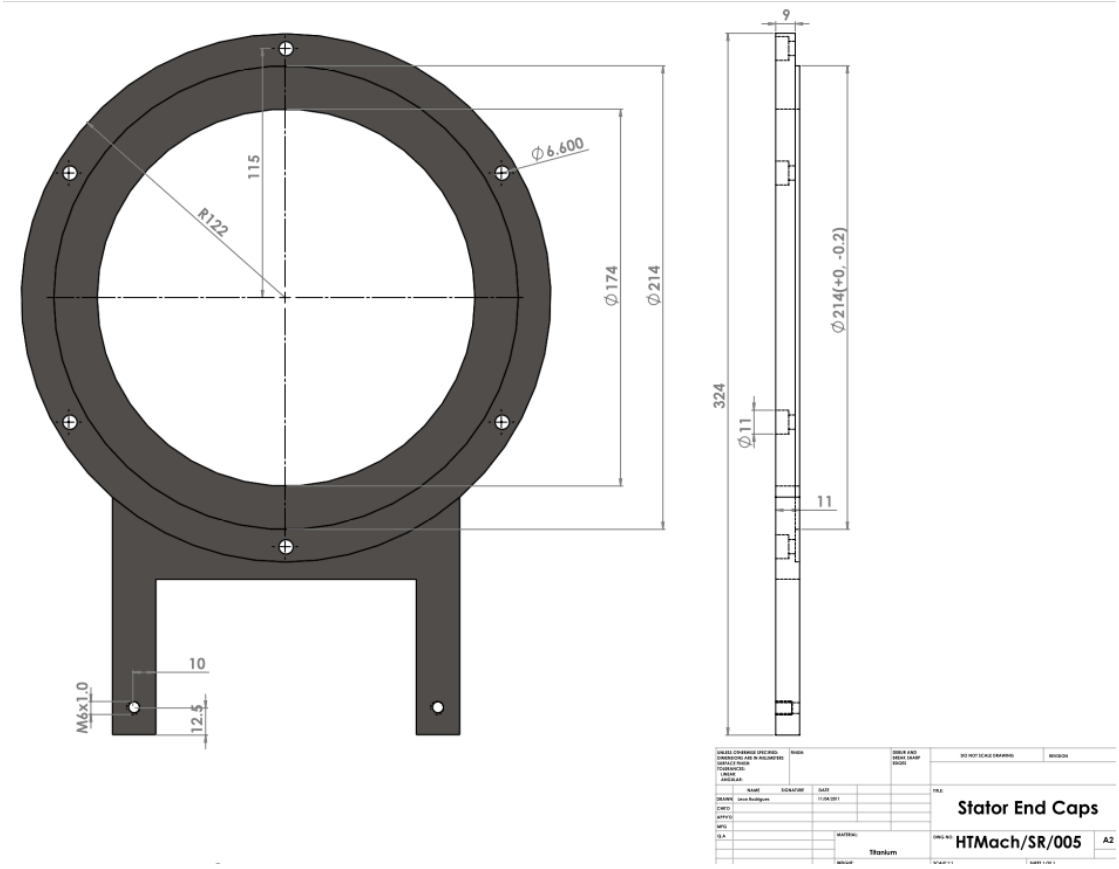

Figure E.5: Stator casing end-plates.

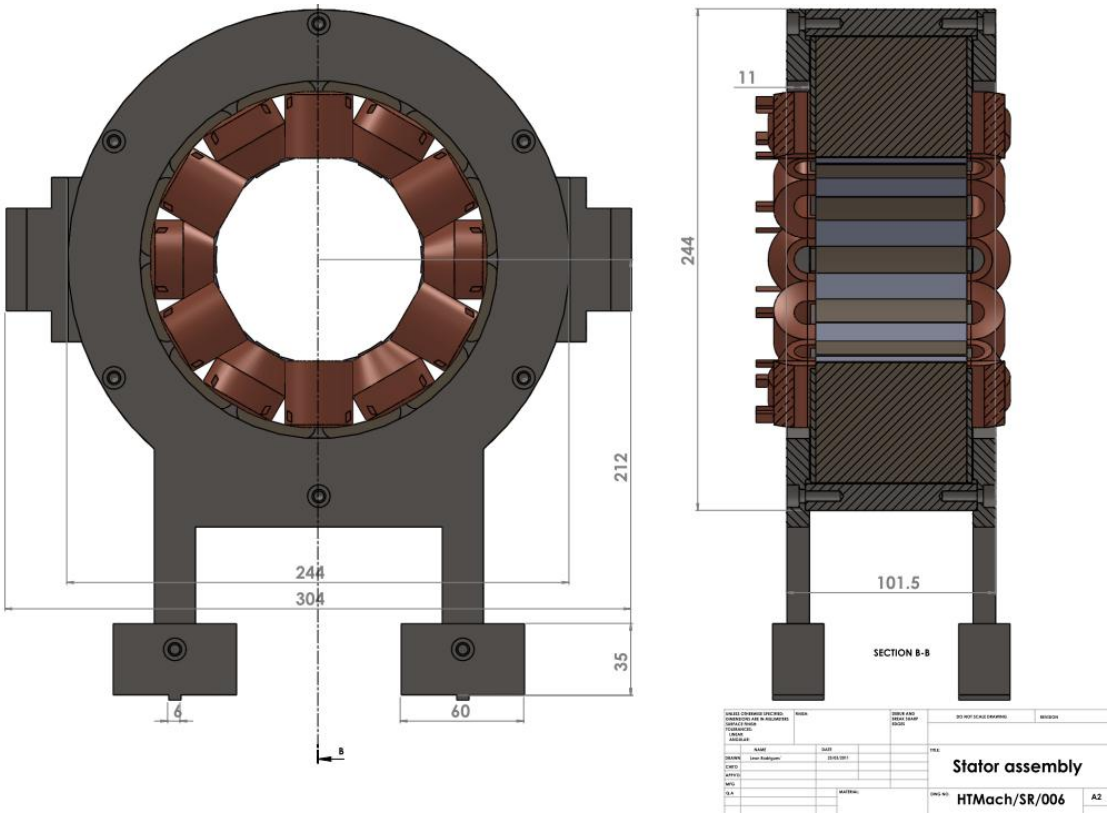

Figure E.6: Stator Assembly with windings.

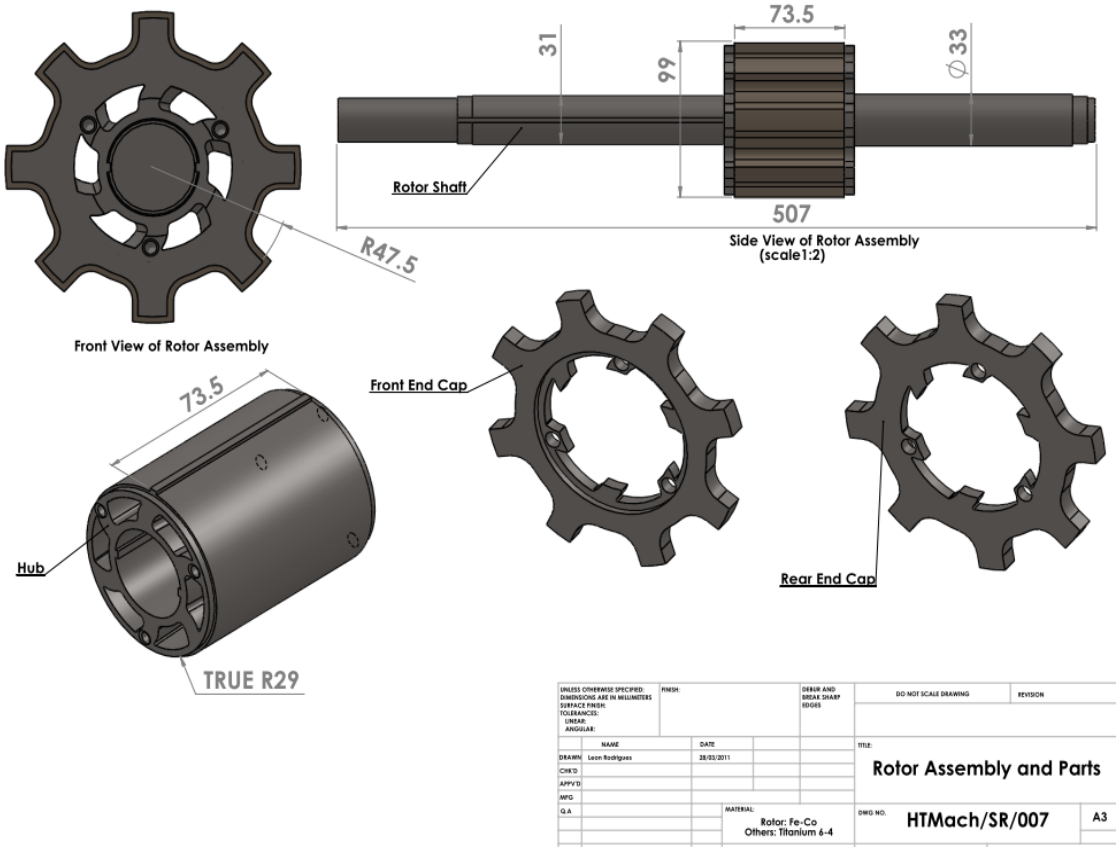

Figure E.7: Rotor assembly and parts.

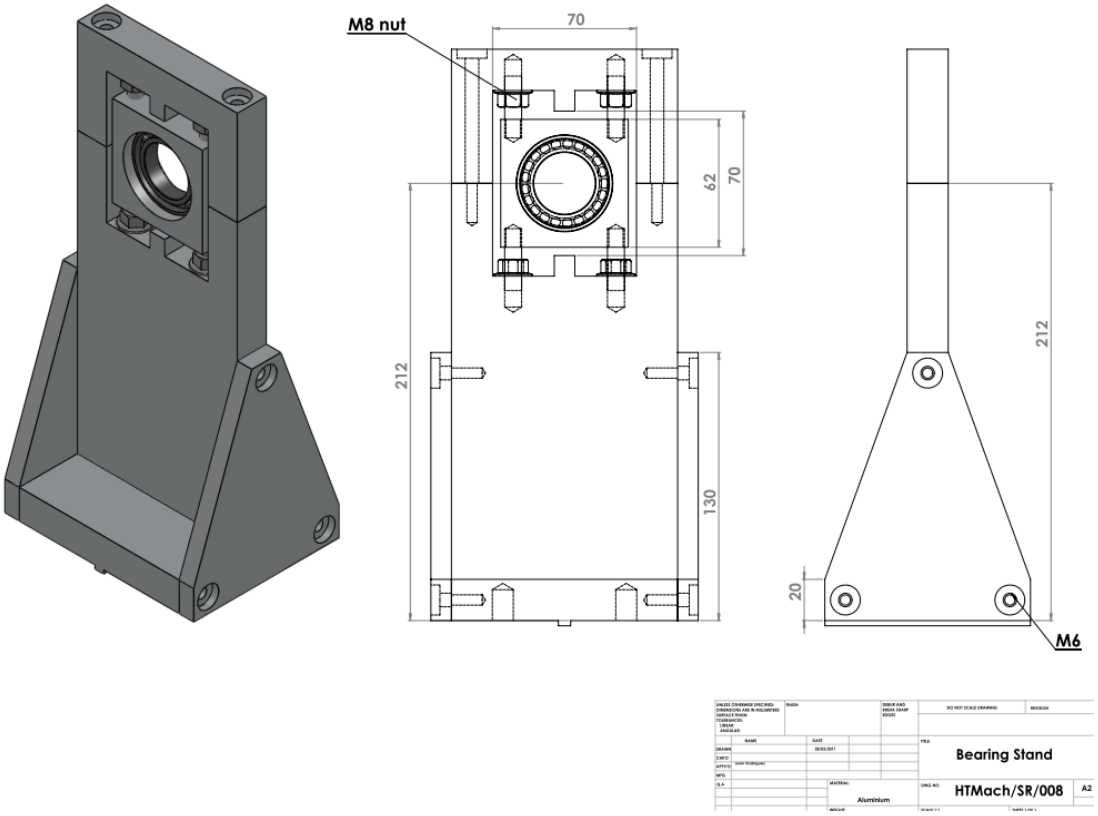

Figure E.8: Bearing stands.

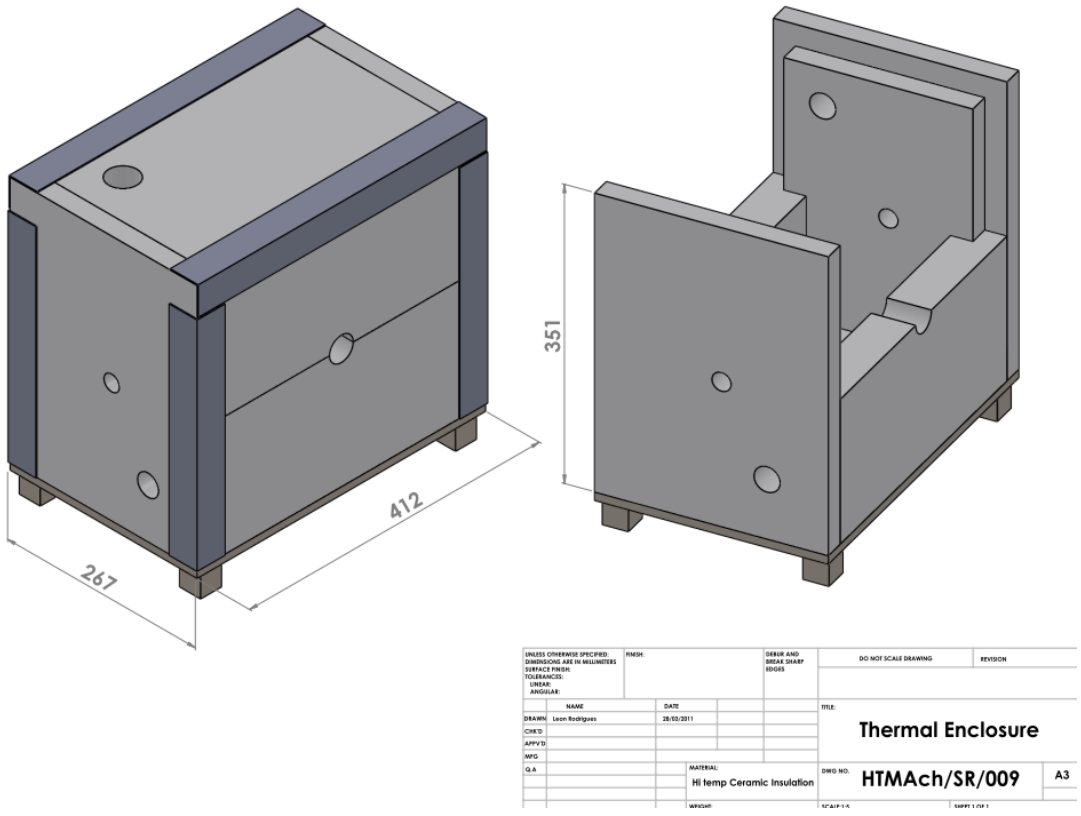

Figure E.9: Thermal enclosure.

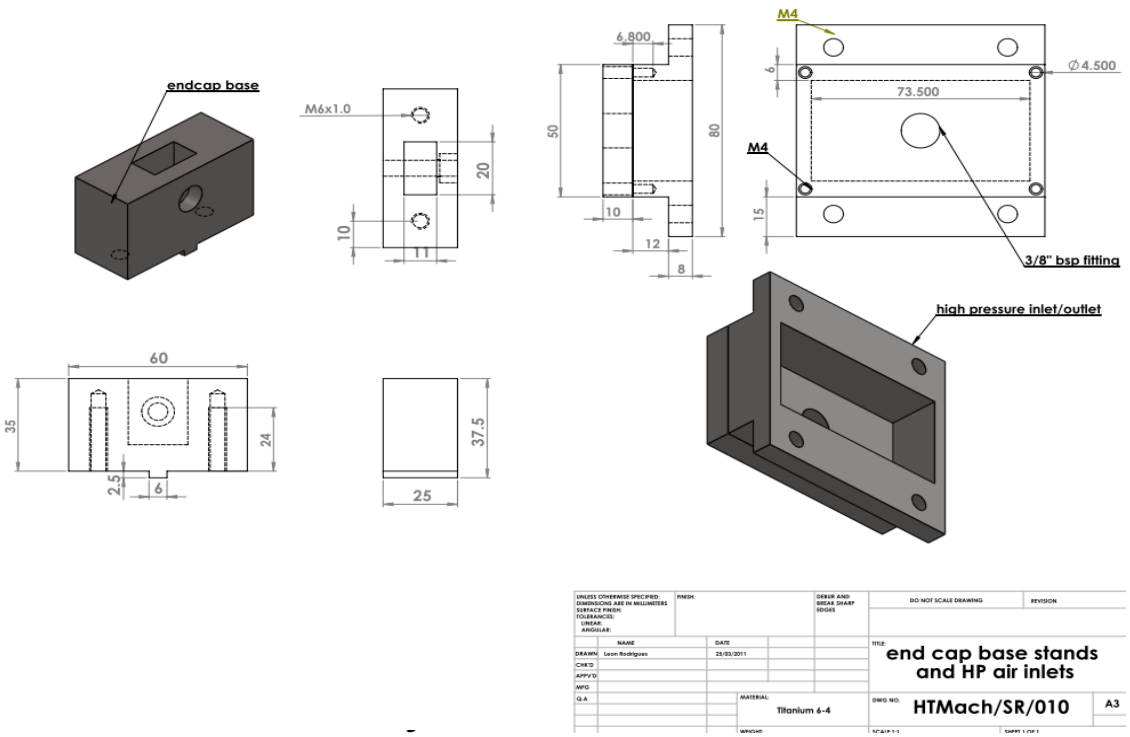

Figure E.10: Stator end plate base stands and HP air inlet/outlet.

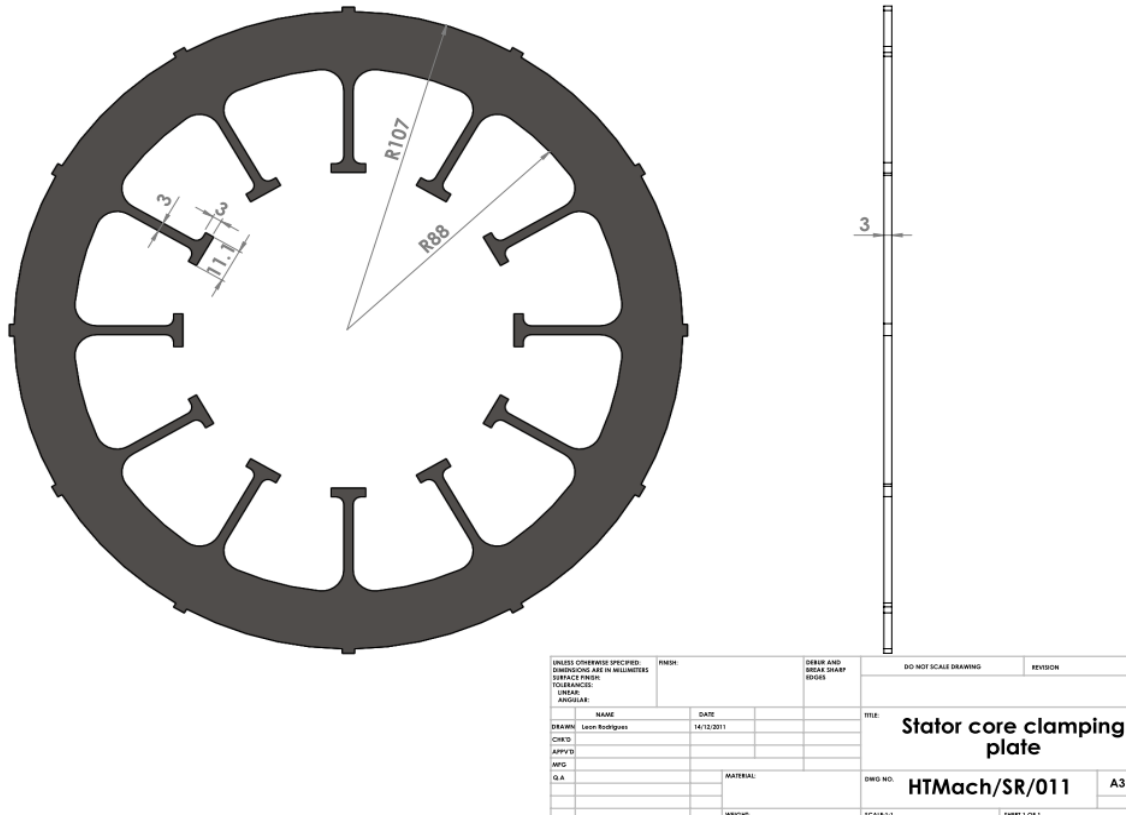

Figure E.11: Stator core clamping plates.

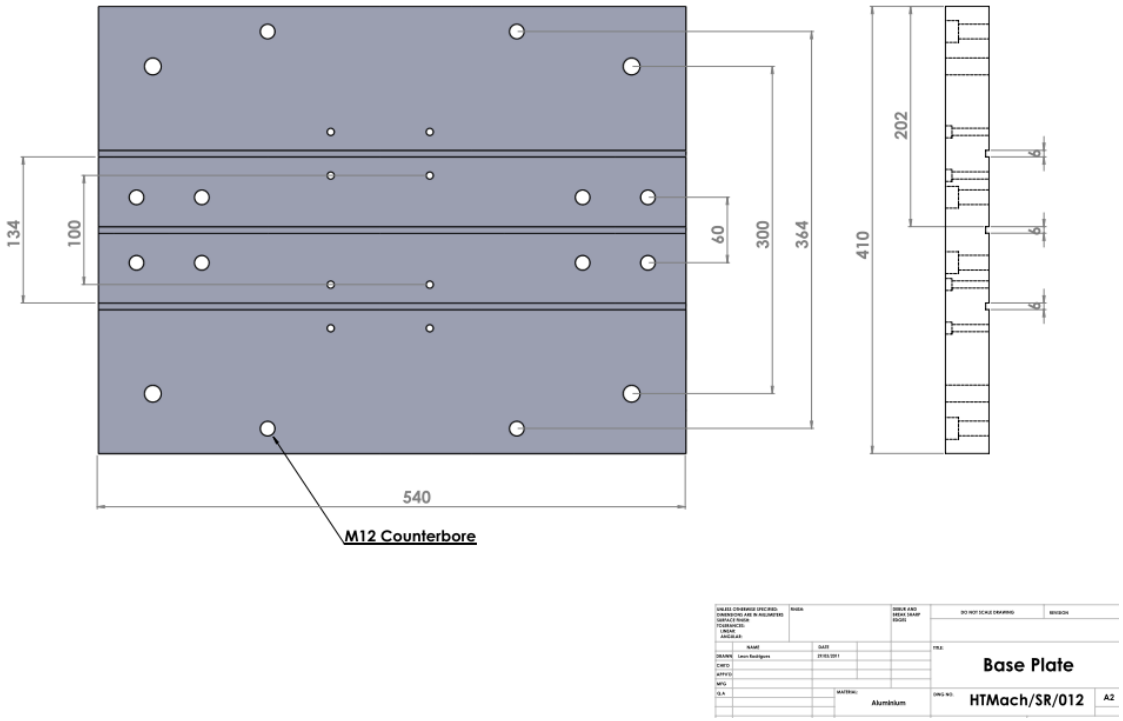

Figure E.12: Base plate.

Appendix F: Photographs of demonstrator machine in course of build.

Figure F.1: Single stator core lamination

Figure F.2: Indexing of laminations along length to form the stator core.

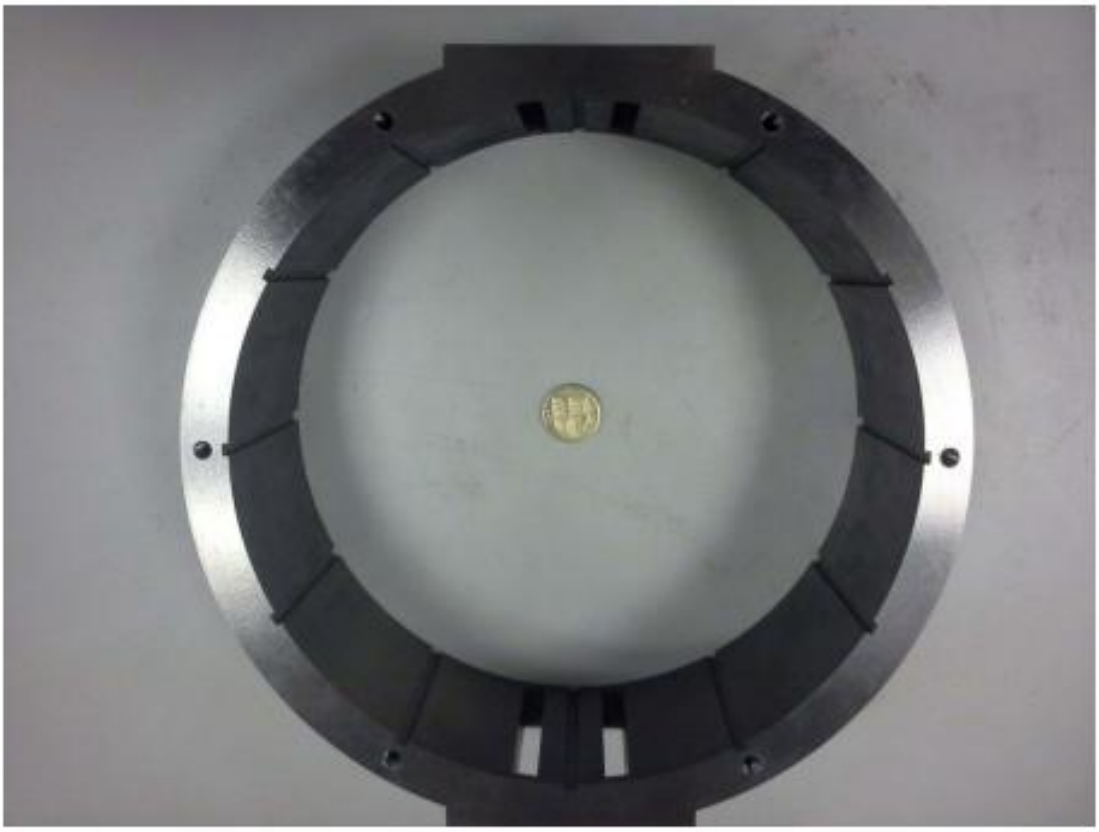

Figure F.3: Tubular section of stator casing

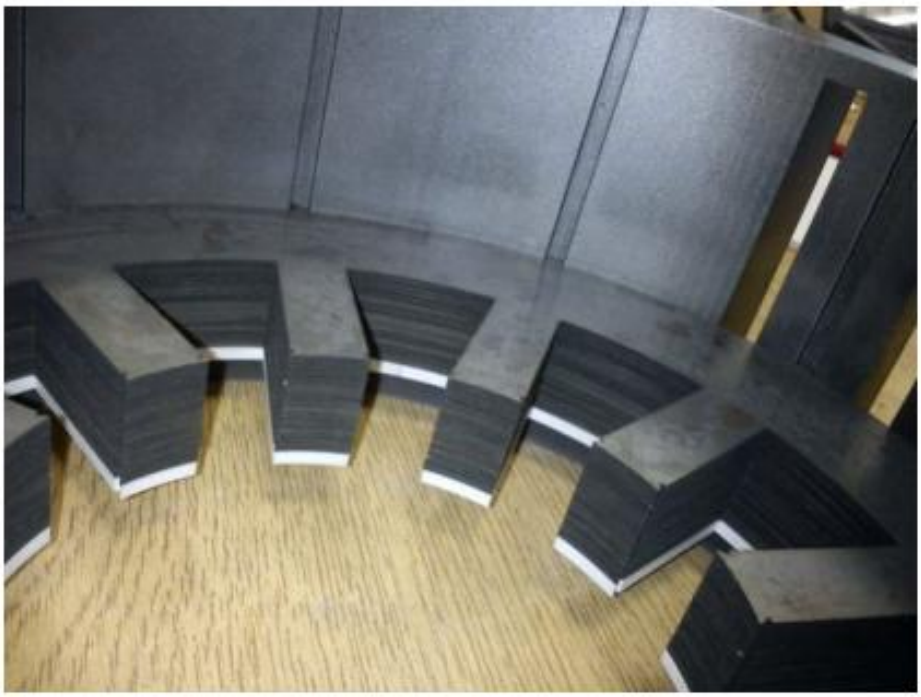

Figure F.4: Stator core part-way through assembly

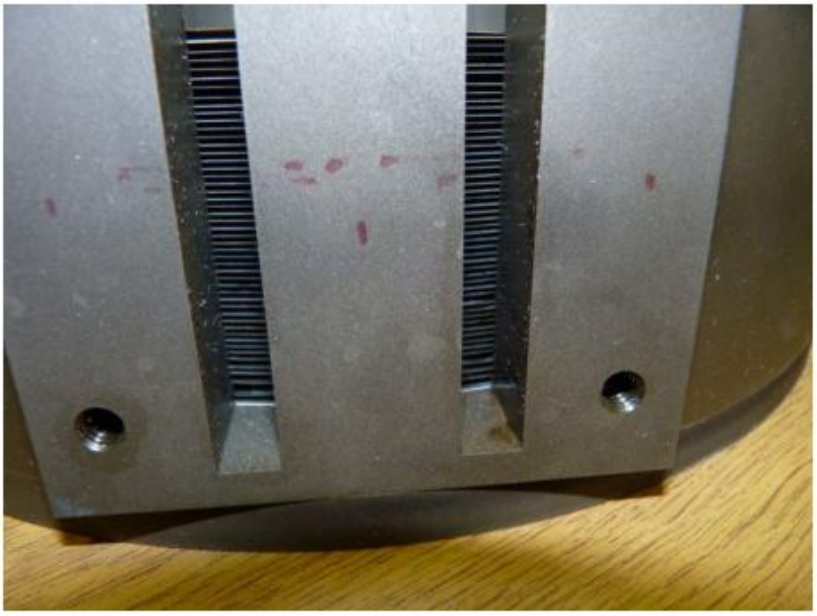

Figure F.5: Close up of cooling apertures illustrating the cooling channels realised in the stator core.

Figure F.6: Titanium casing end-caps.

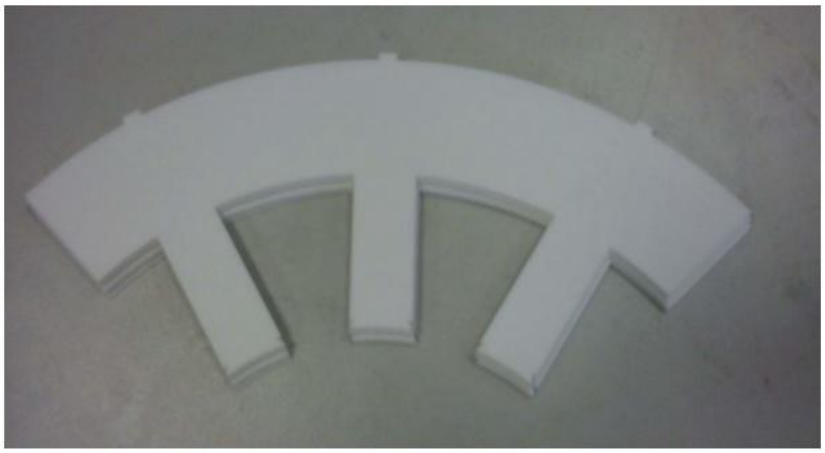

Figure F.7: Laser-cut Alumina clamping-plates.

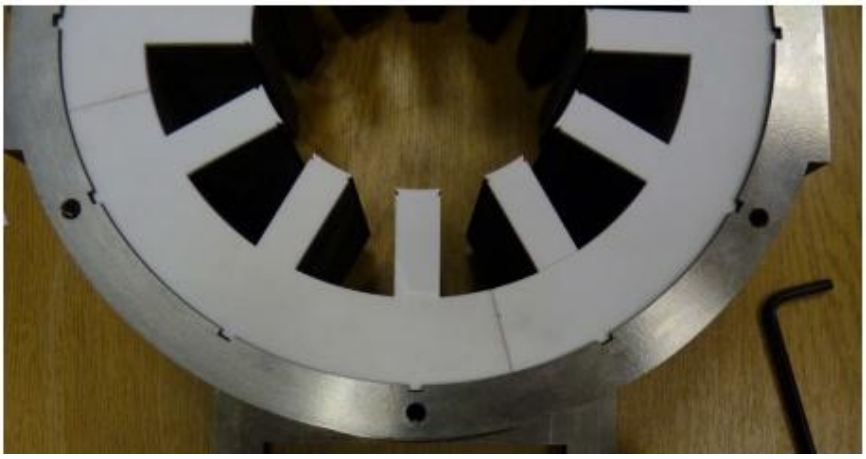

Figure F.8: Alumina clamping plates prior to fitting of Titanium end-cap.

Figure F.9: Failed Alumina clamping plates.

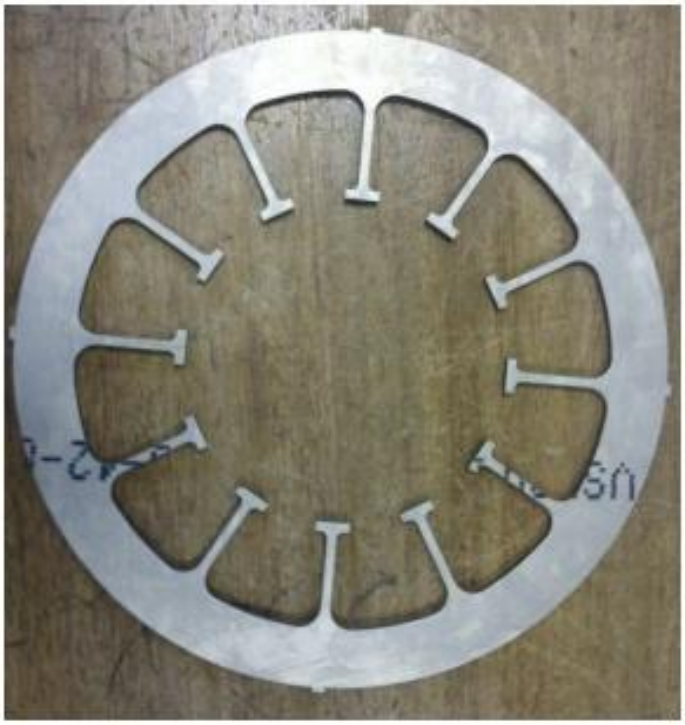

Figure F.10: Titanium clamping plate prior to insertion into the stator casing.

Figure F.11: Assembled stator casing, core and Titanium clamping plates.

Figure F.12: Cooling ports.

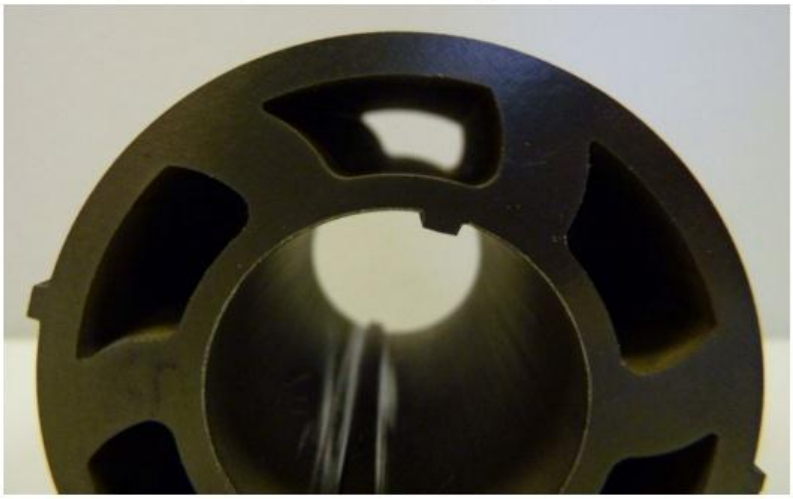

Figure F.13: Titanium rotor hub

Figure F.14: Titanium rotor clamping plate.

Figure F.15: Completed rotor assembly.

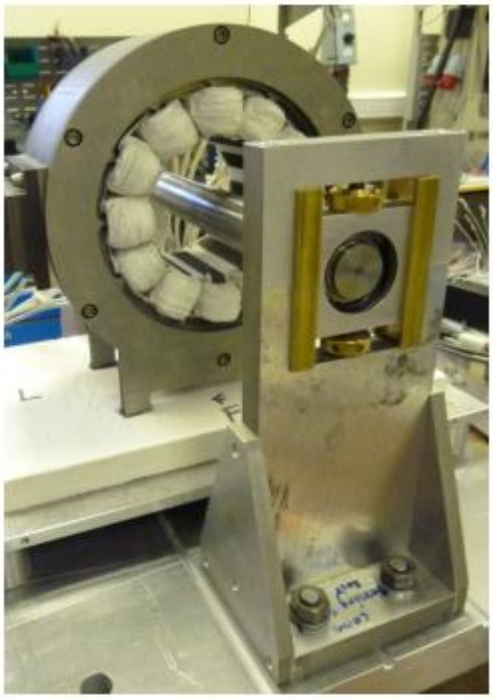

Figure F.16: Adjustable bearing stand

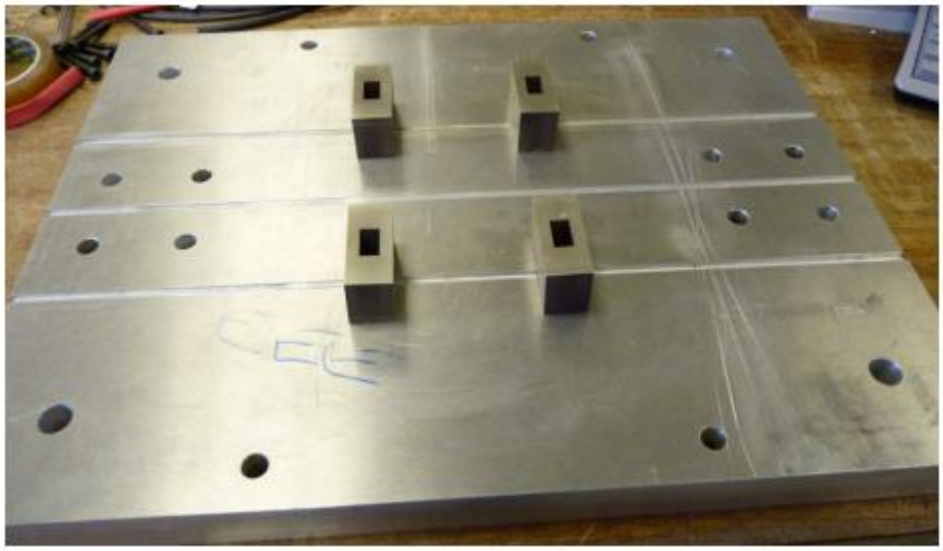

Figure F.17: Test-rig base-plate.

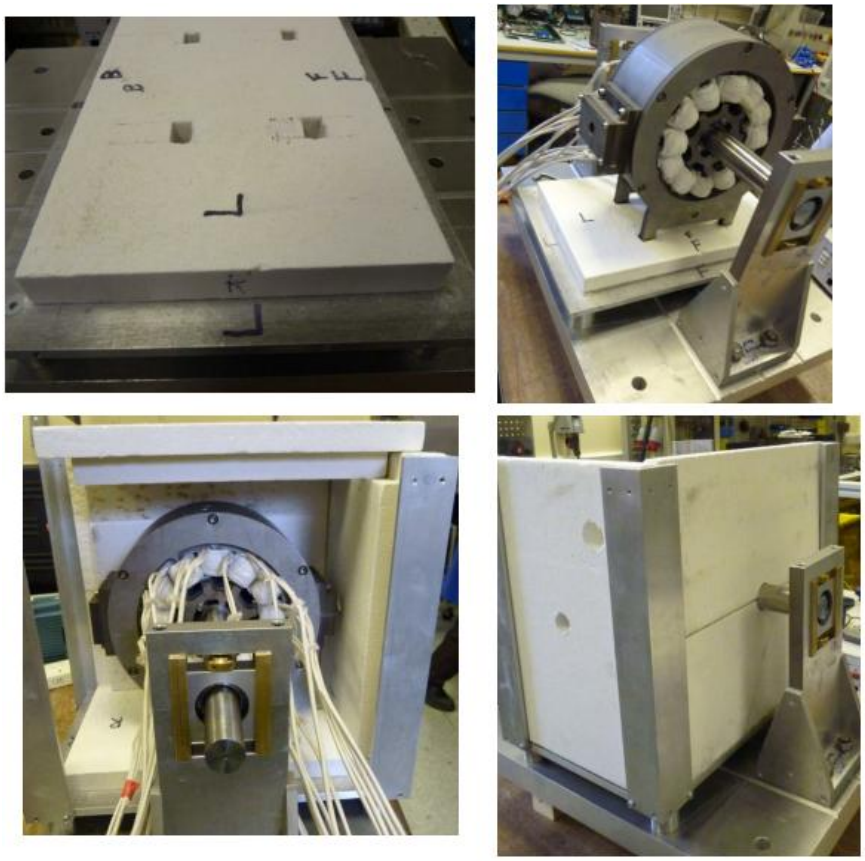

Figure F.18: Thermal enclosure during construction.